Title
High-Pressure Studies of Structural and Mechanical Properties of Superhard Metal Borides

Permalink
https://escholarship.org/uc/item/5965m437

Author
Hu, Shanlin

Publication Date
2022

Peer reviewed|Thesis/dissertation

UNIVERSITY OF CALIFORNIA

Los Angeles

High-Pressure Studies of Structural and Mechanical Properties of

Superhard Metal Borides

A dissertation submitted in partial satisfaction of the

requirements for the degree Doctor of Philosophy

in Chemistry

by

Shanlin Hu

2022

ABSTRACT OF THE DISSERTATION

High-Pressure Studies of Structural and Mechanical Properties of

Superhard Metal Borides

by

Shanlin Hu

Doctor of Philosophy in Chemistry

University of California, Los Angeles, 2022

Professor Sarah H. Tolbert, Co-Chair

Professor Richard B. Kaner, Co-Chair

Ultra-incompressible and superhard materials are good candidates for applications in cutting, grinding, polishing tools and coatings. It has been found that transition metal borides, combining highly incompressible transition metals with strong covalently bonded boron network, are potential candidates for machining tools due to good thermal stability and great mechanical properties. In the course of our studies involving a family of metal borides, such as tungsten diboride (WB_2), rhenium diboride (ReB_2), tungsten tetraborides (WB_4) and dodecaborides (MB_{12}, M = metal), and its solid solutions, we demonstrated that hardness could be enhanced through both intrinsic (chemical bonding) and extrinsic (grain boundary) approaches. In this thesis, a complete discussion was made for each diboride-, tetraboride- and dodecaboride- system, aiming to study the deformation mechanism in a lattice specific manner and the intrinsic hardening effects. In addition to intrinsically modify the crystal structure to improve the hardness, extrinsic hardening

effect, specifically modifying grain boundaries, was investigated in ReB_2 system to understand the

size dependence of strength and texture in the nano-system.

The dissertation of Shanlin Hu is approved.

Abby Kavner

Anastassia N. Alexandrova

Richard B. Kaner, Committee Co-Chair

Sarah H. Tolbert, Committee Co-Chair

University of California, Los Angeles

2022

Dedicated to my family

TABLE OF CONTENTS

Chapter 1 Introduction

Chapter 2 Enhanced Hardening Effects in Molybdenum-Doped WB$_2$ and WB$_2$-SiC/B$_4$C

Composites

Chapter 6 Synthesis and High-Pressure Mechanical Properties of Superhard Rhenium/Tungsten Diboride Nanocrystals

Chapter 7 High-Pressure Studies of Size Dependent Yield Strength in Rhenium Diboride Nanocrystals

Chapter 8 Future Work

xiv

obtain by integration over an 5° slice center at the magic angle of $\varphi = 54.7°$. Indexing for relevant peaks is included on the image (note that the stick pattern is for ReB$_2$, in both figures). Diffraction from the boron/epoxy gasket is indicated with an open star and an impurity in the n-Re$_{0.52}$W$_{0.48}$B$_2$ is labeled with a closed star. All diffraction peaks other than those form the gasket shift to higher angle with increase pressure----

LIST OF TABLES

ACKNOWLEDGEMENT

VITA

Education

University of California, Los Angeles
- Ph.D. in Materials Chemistry

Los Angeles, CA
Anticipated Jun 2022

Boston University
- B.A. in Chemistry, *Cum Laude*
- Minor in Psychology, Biology

Boston, MA
May 2017

Research Interests

Design ultra-incompressible superhard materials and study the mechanical properties of these materials using *in-situ* high-pressure X-ray diffraction.

Research Experience

- Designed and synthesized ultra-incompressible superhard materials using arc-melting and flux growth methods
- Performed synchrotron-based *in-situ* X-ray diffraction at Lawrence Berkeley National Lab and Argonne National Lab to investigate the mechanical properties of materials such as yield strength, bulk modulus and strength anisotropy
- Estimated material's mechanical strength and bonding motifs from 2-dimensional X-ray diffraction images using non-linear model in IGOR
- Performed Rietveld refinement and texture analysis in MAUD to deconvolute diffraction data to visualize grain preferred orientation in molecular level and to investigate plastic deformation mechanism

Teaching and Volunteering

- Taught Organic Chemistry for 10+ quarters and prepared weekly discussion worksheet and keynotes/review materials.
- Structured discussion to accommodate to virtual teaching and designed polls and interactive games to engage students in collaborative learning on Zoom
- Organized booth at *UCLA's Explore Your Universe* outreach to encourage younger students to study science

PUBLICATIONS AND PRESENTATIONS

1. Lei, J.; Hu, S.; Turner, C.L.; Zeng, K.; Yeung, M.T.; Yan, J.; Kaner, R.B.; Tolbert, S.H. Synthesis and High-Pressure Mechanical Properties of Superhard Rhenium/Tungsten Diboride Nanocrystals. *ACS Nano.* 2019, 13, 10036–10048.

2. Pangilinan, L.E.; Hu, S.; Cabrera, S.C.; Akopov, G.; Yeung, M.T.; Mohammadi, R.; Tolbert, S.H.; Kaner, R.B. Superhard Materials: Advances in the Search and Synthesis of New Materials. In Encyclopedia of Inorganic and Bioinorganic Chemistry, 2021.

3. Pangilinan, L.E.; Hu, S.; Hamilton, S.G.; Tolbert, S.H.; Kaner, R.B. Hardening Effects in Superhard Transition Metal Borides. *Acc. Mater. Res.* 2022, 3, 1, 100–109.

4. Pangilinan, L.E.; Hu, S.; Turner, C.L.; Yan, J.; Kavner, A.; Mohammadi, R.; Tolbert, S.H.; Kaner, R.B. Enhanced Hardening Effects in Molybdenum-Doped WB_2 and WB_2-SiC/B_4C Composites. *Chem. Mater.* 2022, 34, 12, 5461-5470.

5. Hu, S.; Lei, J.; Kaner, R.B.; Tolbert, S. H. "High-Pressure Studies of Nanostructured Ultra-incompressible Superhard Materials" Presented at Materials Research Society, 2021.

6. Hu, S.; Pangilinan, L.E.; Akopov, G.; Kaner, R.B.; Tolbert, S. H. "High-Pressure Studies of Ultra-incompressible Superhard Materials" Presented at North American Solid State Chemistry Conference, 2021.

7. Hu, S.; Hamilton, S.G.; Pangilinan, L.E.; Akopov, G.; Kaner, R.B.; Tolbert, S. H. "High-Pressure Studies of Solid-solution and High-entropy effects of Ultra-Incompressible Superhard Metal Dodecaborides" Presented at ACS Meeting, Spring 2022.

Chapter 1

Introduction

1.1 Microindentation Hardness Test

Hardness is a complex physical property that includes both intrinsic and extrinsic effects, which depends on chemical bond strength and dissipation of energy at grain boundaries, respectively. Back in the 19th century, Mohs hardness was used to evaluate a material's resistance to deformation through scratch resistance test with a scale ranging from 1 (soft materials such as talc) to 10 (diamond).[1] Due to its lack of precision, the Mohs scale does not gauge the performance of hard materials in an industrial setting. To quantify hardness, several indentation tests based on the size of imprint left on the surface of a sample by pressing a diamond indenter at a constant applied load were developed. The size of the imprint is then correlated with a hardness value, and indenters of different shapes produce different values. For example, in the Vickers micro-indentation test,[2] the hardness is quantified by the average diagonal length of the impression made by a regular pyramidal indenter at a constant applied force (**FIG. 1.1**) as following:

$$H_v = \frac{1.8544F}{d^2} \qquad (1.1)$$

Here, F is the applied force ranging from 0.49 N to 4.9 N and d is the diagonal length of the indentation.

Many materials exhibit an inverse relationship between hardness and applied load, which is referred to as the indentation size effect (ISE). Higher Vickers hardness is predominantly observed at low load, likely arising from the localization of dislocations near the indenter-material surface interface. Low load hardness values offer insight into the hardening behavior of a material along an applied load range. Materials that exceed a threshold Vickers hardness value ($H_v \geq 40$ GPa) under low load (0.49 N) are classified as superhard.[3]

1

The applications of hard materials are most evident in the manufacturing and machining industries, for example, cutting, polishing or grinding. Currently, diamond and cubic boron nitride, are the most commercially relevant hard materials. Although diamond is the hardest known material (H_v = 115 GPa at a load of 4.9 N for synthetic single-crystal diamond),[4] it is not suitable for cutting ferrous materials due to its poor thermal stability and tendency to form carbides.[5] The alternative, cubic boron nitride (c-BN) is much softer (H_v = 62 GPa at 4.9 N for single-crystal c-BN).[6] Most importantly, both materials require high-pressure high temperature (HPHT) conditions to form and are therefore expensive. Thus, the focus of superhard materials research is to create materials with high hardness, enhanced chemical stability, and low cost of production.

Inspired by the highly covalent bonding network found in diamond, our group has focused its efforts on designing new superhard materials by combining incompressible transition metal atoms with light elements (e.g. boron and carbon).[7] A range of superhard transition metal borides, including ReB_2,[8] WB_4,[9] and MB_{12},[10] have been synthesized. This work focuses on optimizing hardness of these boride systems from intrinsic (solid solution hardening) and extrinsic (grain-boundary effect) perspectives. One of the projects that I worked on is enhancing hardness in tungsten diboride (WB_2) system through solid solution and composite effect, which promotes non-superhard diboride into superhard regime (Chapter 2).

1.2 High Pressure X-Ray Diffraction

In-situ high-pressure radial diffraction reveals a lattice specific view of intrinsic hardness, which is based on the basic bonding of the material. In radial diffraction, the incident X-ray beam is perpendicular to the compression direction, and the sample is directly packed inside an x-ray transparent boron gasket, as shown in **FIG. 1.2**. When the material is under uniaxial compression, the lattice planes undergo deformation and the shift of the corresponding d-spacings along different

stress directions, commonly known as differential strain (t/G), reveal the degree to which each lattice plane can resistance a shear force. Upon compression, the differential stress (t), which is related to the differential strain by the shear modulus (G), eventually plateaus at the yield strength, the maximum stress that the lattice plane can withstand before bonds break.[11] The yield point thus indicates the onset of plastic deformation. As mentioned in the previous section, intrinsic effects can be optimized through formation of solid solutions, where a metal dopant of different size and electron density results in a local distortion pinning dislocation in the parent structure and prevents slip, thus I study the bonding motifs in ReB_2 (Chapter 3) and WB_4 (Chapter 4) solid solutions and their contributions to the intrinsic hardening. I also explore the unit cell packing in dodecaboride system (Chapter 5), where I come up with a theory for designing novel superhard dodecaboride solid solutions and high-entropy alloys.

At the opposite end of the spectrum, extrinsic effects can be optimized by grain boundary strengthening, where the grain boundaries impede the propagation of dislocations. When grains reach the nanoscale, significant enhancements in hardness can be achieved.[12] In fine grained materials, the peak intensity variation with stress directions in the high-pressure radial diffraction experiment also correlates with the slip systems and grain texture.[13] The texture can be plotted in an inverse pole figure to provide a direct map of the accessible slip systems, both as a function of pressure and as a function of composition and domain size. To understand the grain boundaries hardening effects, I work on nanoengineering ReB_2 (Chapter 6) and studying size-dependent mechanical properties in nano-ReB_2 system (Chapter 7).

Through the combined efforts of Vickers micro-indentation and high-pressure studies, we have obtained both direct hardness measurements and lattice-specific insight into various superhard materials. By understanding the elastic and plastic deformation mechanisms in different

transition metal systems under high pressure, we can have a comprehensive knowledge of fundamental physics that contributes to their high hardness and design new approaches to synthesizing next generation superhard materials. For the future work, more attempts would be made to optimize the hardness of currently synthesized materials and a broader regime of nanostructured materials would be explored (Chapter 8).
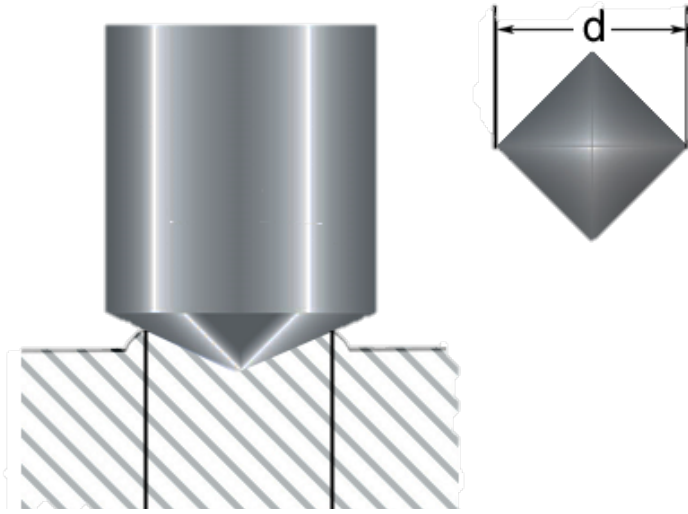
FIG. 1.1. Schematic figure for the micro-indentation hardness test.
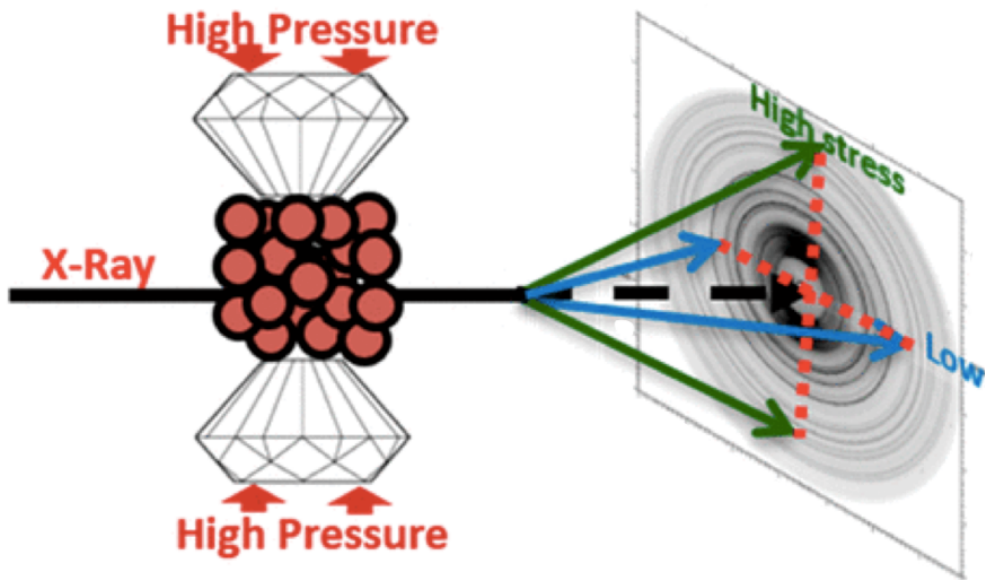
FIG. 1.2. Experimental geometry for radial diffraction.

1.3 References:

1. Yeung, M. T., Mohammadi, R. & Kaner, R. B. Ultraincompressible, Superhard Materials. *Annu. Rev. Mater. Res.* **46**, 465–485 (2016).

2. Smith, R. L. & Sandly, G. E. An Accurate Method of Determining the Hardness of Metals, with Particular Reference to Those of a High Degree of Hardness. *Proc. Inst. Mech. Eng.* **102**, 623–641 (1922).

3. Vepřek, S. The search for novel, superhard materials. *J. Vac. Sci. Technol. A* **17**, 2401–2420 (1999).

4. Novikov, N. V. & Dub, S. Fracture toughness of diamond single crystals. *J Hard Mater* **2**, (1992).

5. Komanduri, R. & Shaw, M. C. Wear of synthetic diamond when grinding ferrous metals. *Nature* **255**, 211–213 (1975).

6. Novikov, N. V., Dub, S. N. & Mal'nev, V. I. Microhardness and fracture toughness of cubic boron nitride single crystals. *Sov. J. Superhard Mater.* **5**, 16–21 (1983).

7. Kaner, R. B., Gilman, J. J. & Tolbert, S. H. Designing Superhard Materials. *Science* **308**, 1268–1269 (2005).

8. Chung, H.-Y. *et al.* Synthesis of Ultra-Incompressible Superhard Rhenium Diboride at Ambient Pressure. *Science* **316**, 436–439 (2007).

9. Mohammadi, R. *et al.* Tungsten tetraboride, an inexpensive superhard material. *Proc. Natl. Acad. Sci.* **108**, 10958–10962 (2011).

10. Akopov, G., Roh, I., Sobell, Z. C., Yeung, M. T. & Kaner, R. B. Investigation of ternary metal dodecaborides (M1M2M3)B12 (M1, M2 and M3 = Zr, Y, Hf and Gd). *Dalton Trans.* **47**, 6683–6691 (2018).

11. He, D., Shieh, S. R. & Duffy, T. S. Strength and equation of state of boron suboxide from radial x-ray diffraction in a diamond cell under nonhydrostatic compression. *Phys. Rev. B* **70**, 184121 (2004).

12. Hall, E. O. The Deformation and Ageing of Mild Steel: III Discussion of Results. *Proc. Phys. Soc. Lond. Sect. B* **64**, 747–753 (1951).

13. Chen, B. *et al.* Detecting grain rotation at the nanoscale. *Proc. Natl. Acad. Sci.* **111**, 3350–3353 (2014).

Chapter 2

Enhanced Hardening Effects in Molubdenum-Doped WB$_2$ and WB$_2$-Sic/B$_4$C Composites

"Reprinted (adapted) with permission from (Pangilian, L.E.; Hu, S.; Turner, C.L.; Yan, J.; Kavner, A.; Mohammadi.; Tolbert, S.H.; Kaner, R.B. Chem. Mater. 2022, 34, 12, 5461-5470).

Copyright (2022) American Chemistry Society."

2.1 Introduction

The search for novel superhard materials is motivated by the demand for high-performance cutting tools and abrasives with enhanced mechanical properties and thermal stability.[1,2] While frequently reported at the high load asymptotic limit, superhardness (Vickers hardness, H$_v \geq 40$ GPa) is often observed at lower load (0.49 N), which are more compatible with real world applications. Hardness values reported over a range of low and high loads can be utilized to understand the origin of hardness in bulk material and to assess a material's utility at the applied loads required for various industrial cutting operations. Although diamond is the most commercially relevant superhard material, diamond's use is limited by its cost prohibitive synthesis (requiring both high temperature and high pressure) as well as its high reactivity to ferrous alloys (resulting in poor cutting performance and poor stability above 700 °C).[3,4] These shortcomings have inspired the creation of new superhard materials that are readily synthesized, thermally stable, and made from less expensive elements.[5,6]

Due to their highly covalent bonding networks, several metal boride systems (e. g., ReB$_2$ and WB$_4$) have been identified as superhard at low load.[7,8] The intrinsic hardness of these materials can be further increased through the formation of solid solutions, where an alloying element with valence electron count and/or size that is different from the parent metal is substituted into the host structure.[9] These solid solutions employ the Hume-Rothery rules, where the parent metal and

dopant atoms need to: (1) be less than 15% different in atomic radius, (2) adopt similar crystal structures, (3) have similar electronegativity values, and (4) be close in valence electron density.[10–12] When atom mixtures fall outside of these bounds, two-phase coexistence generally results, preventing favorable solid solution-hardening. Two-phase mixtures can, however, show increased hardness due to extrinsic effects, include grain boundary strengthening and precipitation hardening, where the reduction in average grain size and precipitation of secondary phase(s) increase the degree of grain boundaries and dislocation pinning in bulk material.[13,14]

Transition metal diborides have been extensively studied for their superconductivity, electrocatalytic performance, and high hardness.[15–18] Most diborides, such as TiB_2 and ZrB_2, exhibit the AlB_2-type structure (*P6/mmm*), which contains flat boron sheets and 12-coordinate metal layers.[19,20] Such materials tend not to be terribly hard, due to easy slip parallel to the flat boron sheets. In the ReB_2 structure (*P6₃/mmc*), boron sheets adopt a corrugated, chair configuration that impedes slip plane motion.[21,22] With a hybrid structure containing alternating flat and corrugated boron sheets between metal layers, tungsten diboride (WB_2, *P6₃/mmc*) is a candidate structure in the design of new superhard materials (**FIG. 2.1**).[23,24] Although pure WB_2 is not intrinsically superhard, substitutional solid solutions of WB_2 have been characterized with hardness values measuring in the superhard regime.[25]

In addition to single-phase systems, many studies have examined the microstructure and properties of multi-phase composites based on metal diborides.[26] For instance, secondary additives, such as boron carbide (B_4C) and/or silicon carbide (SiC), have been shown to decrease the grain size of metal diborides, such as ZrB_2 and TiB_2, in ultra-high temperature ceramics and enhance bulk mechanical properties.[27,28] Thus, it is of great interest to identify the contributions of both

intrinsic and extrinsic hardening effects in order to optimize a material's grain morphology and mechanical properties.

In this study, we synthesize molybdenum (Mo)-doped WB_2 solid solutions and characterize their mechanical properties as a function of solubility. Given that Mo (1.45 Å)[29] has the same number of valence electrons (group 6) and a close atomic radius to W (1.35 Å),[29] we have obtained an extended range of solid solutions. The material is phase pure at concentrations up to and including 30 at. % Mo in WB_2, but higher Mo incorporation levels can be achieved in materials that contain small amounts of β-MoB_2 mixed with the $W_xMo_{1-x}B_2$. Vickers hardness measurements, high-pressure data, and SEM images are discussed in further detail to demonstrate that the addition of Mo enhances bulk material hardness through both solid solution formation, as well as additional extrinsic affects through a change in surface morphology. Additionally, we study the effects of secondary phases, SiC and B_4C, in both unsubstituted WB_2 and 30 at. % Mo substituted WB_2 ($W_{0.70}Mo_{0.30}B_2$), the hardest WB_2 solid solution created to date. These two-phase composites show extrinsic hardening through the inhibition of grain growth, and increased oxidation resistance through enhanced phase stability and protective oxide formation during thermal cycling.

2.2 Experimental Procedure

Samples were prepared using: tungsten (99.95%, Strem Chemicals, U.S.A.), amorphous boron (99+%, Strem Chemicals, U.S.A.), molybdenum (99.95%, Strem Chemicals, U.S.A.), silicon (99.9%, American Elements, U.S.A.), and carbon (graphite, 99+%, Strem Chemicals, U.S.A.). Elemental boron and metal powders were weighed and mixed according to the following nominal compositions: $W_{1-x}Mo_xB_{2.0}$, where x = 0.02-0.50. Composites were prepared by weighing and mixing elemental powders according to the compositions: $WB_{2.0}$-B_4C, $WB_{2.0}$-SiC, $W_{0.70}Mo_{0.30}B_{2.0}$-B_4C, and $W_{0.70}Mo_{0.30}B_{2.0}$-SiC, where the weight percentage of B_4C or SiC in each

total composition was varied (10, 20, and 30 wt. %). The powder mixtures were pressed into 12.7 mm (0.5 in) diameter pellets under a 10-ton load using a hydraulic jack press (Carver). The pressed pellets were arc-melted on a water-cooled copper hearth in an argon atmosphere with a maximum current of approximately 140 amps for 1-2 minutes. Each sample was arc-melted until molten, subsequently flipped and re-melted, totaling three times to ensure homogeneity.

The sample ingots were dissected using a diamond saw (Ameritool Inc., U.S.A.). One half of each sample was crushed into <45 μm powder (-325 mesh) for powder X-ray diffraction analysis (PXRD) and thermogravimetric analysis (TGA) using a tool steel Plattner-style mortar and pestle set (Humboldt Mfg., model H-17270). The other half was cold-mounted in epoxy using an epoxy/hardener set (Buehler, U.S.A.) and polished on a semi-automated polishing station (Buehler, U.S.A.). To produce an optically flat surface, each sample was polished with silicon carbide disks (120 – 600 grit sizes, Buehler, U.S.A.) followed by polishing cloths coated in polycrystalline diamond suspensions with particle sizes ranging from 15 to 0.25 micron (Buehler, U.S.A.). Polished samples were used for scanning electron microscopy (SEM), energy dispersion spectroscopy (EDS), and Vickers hardness testing.

PXRD was performed on a Bruker D8 Discover Powder X-ray Diffractometer (Bruker Corporation, Germany) to determine the composition and phase purity of the crushed powder samples. Data were acquired using a $Cu_{K\alpha}$ X-ray beam (λ = 1.5418 Å) in the 5-100° 2θ range. PXRD data were compared with the International Centre for Diffraction Data (ICDD) patterns, formerly known as the Joint Committee on Powder Diffraction Standards (JCPDS), in order to identify the phases present in each sample. Unit cell refinements were performed using GSAS-II.[30] An FEI Nova 230 high-resolution scanning electron microscope (FEI Company, U.S.A.) equipped with a backscattered electron detector (BSED) and an UltraDry EDS detector (Thermo Scientific,

U.S.A.) was used to analyze the surface morphology and elemental composition of the polished samples.

Vickers hardness measurements were performed by a multi-Vickers hardness tester (Leco, U.S.A.) with a pyramidal diamond indenter. Indentations were made on polished samples with applied force loads of: 0.49, 0.98, 1.96, 2.94, and 4.9 N. The lengths of the diagonals of each indent were measured under 500x magnification using a high-resolution optical microscope, Zeiss Axiotech 100HD (Carl Zeiss Vision GmbH, Germany). Vickers hardness values (H_v in GPa) were calculated and averaged for ten indents per load using the following formula (Equation 2.1):

$$H_v = \frac{1854.4F}{d^2} \tag{2.1}$$

where F is the applied load (in Newtons) and d is the average length of the diagonals for an indent (in micrometers). A minimum of 10 indentations were performed in pseudo-random locations throughout the polished sample surface. Hardness values were reported at loads ranging from 0.49 N to 4.9 N (low to high) in order to gain insight into the origin and load-dependency of a material's hardness.

A Pyris Diamond TGA/DTA unit (TG-DTA, PerkinElmer Instruments, U.S.A.) was used to study thermal stability (up to 1000 °C in standard nonmedical compressed air) under the following parameters: heat in air from 25 to 200 °C at a rate of 20 °C/min, hold at 200 °C for 30 minutes, heat from 200 to 1000 °C at 2 °C/min, hold at 1000 °C for 2 hr, and cool from 1000 to 25 °C at 5 °C/min. PXRD was used to identify the resulting phase(s) of the heated samples.

Nonhydrostatic *in-situ* high-pressure radial X-ray diffraction was performed in a diamond anvil cell at synchrotron beamline 12.2.2 of the Advanced Light Source (ALS, Lawrence Berkeley National Laboratory). Crushed powder of the sample ($W_{0.70}Mo_{0.30}B_2$) was loaded into a laser-drilled hole (~60 μm in diameter, ~60 μm in depth) in a ~400 μm diameter boron gasket made of

amorphous boron and epoxy. A small piece of Pt foil (~20 μm diameter) was placed on top of the sample to serve as an internal pressure standard. A monochromatic X-ray beam (λ = 0.4959 Å, spot size = 20 μm × 20 μm) was passed through the sample, which was compressed between two diamond tips up to 60 GPa of pressure, and 2-D diffraction data were collected using an MAR-345 image plate and FIT2D software. A cerium dioxide (CeO_2) standard was used to calibrate the detector distance and orientation. The angle-dispersive diffraction patterns were converted from elliptical to rectangular coordinates using FIT2D. The integrated "cake" patterns, azimuthal angle (η) versus diffraction angles (2θ), were then analyzed using Igor Pro (WaveMetrics, Inc.). Peak positions were manually picked for three easily resolvable diffraction peaks (004, 101, 110). The 1-dimensional diffractions of X-ray intensity as a function of 2θ was obtained at the magic angle (φ = 54.7°, effectively hydrostatic condition). All peaks were indexed to hexagonal phases with no indication of phase transition throughout the measured pressure range.

The stress in the sample under uniaxial compression is described by Equation (2.2):

$$\sigma = \begin{bmatrix} \sigma_1 & 0 & 0 \\ 0 & \sigma_1 & 0 \\ 0 & 0 & \sigma_3 \end{bmatrix} = \begin{bmatrix} \sigma_p & 0 & 0 \\ 0 & \sigma_p & 0 \\ 0 & 0 & \sigma_p \end{bmatrix} + \begin{bmatrix} -t/3 & 0 & 0 \\ 0 & -t/3 & 0 \\ 0 & 0 & -2t/3 \end{bmatrix} \tag{2.2}$$

where σ_1 is the minimum stress along the radial direction, σ_3 is the maximum stress in the axial direction, σ_P is the hydrostatic stress component, and t is the differential stress, which gives a lower-bound estimate of yield strength. The d-spacing is calculated by:

$$d_m(hkl) = d_p(hkl)[1 + (1 - 3\cos^2\varphi)Q(hkl)] \tag{2.3}$$

where d_m is the measured d-spacing, d_p is the d-spacing at hydrostatic peak position, φ is the angle between the diffraction normal and axial directions, and $Q(hkl)$ is the lattice strain under the uniaxial stress condition. The differential stress, t, is directly related to the differential strain, $t(hkl)/G(hkl)$, by:

$$t(hkl) = 6G(hkl)Q(hkl) \qquad\qquad (2.4)$$

where $G(hkl)$ is the shear modulus of the specific lattice plane.

Incompressibility can be determined using the third-order Birch-Murnaghan equation-of-state (EOS), which is written as:

$$P = \frac{3}{2}K_0\left(\left(\frac{V_0}{V}\right)^{7/3} - \left(\frac{V_0}{V}\right)^{5/3}\right)\left(1 + \frac{3}{4}(K_0' - 4)\left(\left(\frac{V_0}{V}\right)^{2/3} - 1\right)\right) \qquad (2.5)$$

where P is the pressure, K_0 is the bulk modulus at ambient pressure, V is the volume, V_0 is the undeformed unit cell volume, and K_0' is the derivative of K_0 with respect to P. Equation (2.5) can be simplified to second-order by fixing $K_0' = 4$. The Birch-Murnaghan equation-of-state can also be rewritten in terms of normalized pressure (F) and Eulerian strain (f), as shown in the following:

$$F = \frac{P}{3f(1+2f)^{5/2}} \qquad\qquad (2.6)$$

$$f = \frac{1}{2}\left(\left(\frac{V_0}{V}\right)^{2/3} - 1\right) \qquad\qquad (2.7)$$

Equations (2.6) and (2.7) can be combined to give a linear regression, where the zero-intercept yields the bulk modulus at ambient pressure (K_0) and the slope gives the pressure derivatives of the bulk modulus (K_0').

2.3 Results and discussion

Intrinsic properties of Mo doped-WB$_2$

Here, we investigate the effects of molybdenum substitution in WB$_2$ solid solutions (W$_{1-x}$Mo$_x$B$_2$). For a structure to be a solid solution, it must exhibit a linear change in the unit cell volume with increasing solute concentration. The concentration of atomic substitution (at. % of solute) before secondary phase precipitation appears indicates the substitution threshold, or solubility limit, for that particular solute. **FIG. 2.1** shows PXRD patterns for W$_{1-x}$Mo$_x$B$_2$, where the solubility limit of Mo in WB$_2$ is below 40 at. % Mo. Rietveld refinement was performed using

15

GSAS-II software to calculate the unit cell parameters of Mo-substituted solid solutions through comparison with the WB_2 structure (*P6₃/mmc*). The *c/a* axial ratio and unit cell volume for the WB_2-Mo system from 0 – 50 at. % Mo addition are presented in **FIG. 2.2**. As the percentage of Mo increases, the *c/a* ratio decreases while the overall volume increases. These results indicate a higher rate of unit cell expansion along the *a*-axis with increasing Mo substitution. The observed lattice expansion is in adherence with Vegard's law and substitutional solid solution formation as Mo substitutes for W in W sites in the WB_2 lattice across all concentrations, despite the appearance of a small amount of β-MoB_2 in the higher Mo samples.

The systematic shift in the WB_2 peaks across all 2θ values and the collective change in c/a ratio, shown in **FIG. 2.1** and **FIG. 2.2**, respectively, indicating the formation of solid solutions. Moreover, the refined diffraction patterns in **FIG. S2.1** indicate that no MoB_2 (R-3m) is present at or below 30% Mo doping. Some additional peaks do appear in the diffraction patterns at lower Mo concentrations, however, the fact that the impurity peaks appear at the same positions in all three samples, including pure WB_2 sample, indicates that the impurity is not a Mo-containing phase. Indeed, the peak positions are in good agreement with the WB diffraction pattern, and the relative intensity of the WB peaks to WB_2 peaks suggests the samples contain less than 5 wt % of the WB phase.

SEM images and elemental maps of $W_{0.70}Mo_{0.30}B_2$, the composition of maximum Mo solubility, show an even distribution of Mo up to 30 at. % substitution and indicate no secondary phase formation (**FIG. 2.2**). Above the solubility limit, a secondary phase, β-MoB_2 (*P6/mmm*) precipitates upon cooling from the melt. While XRD analysis demonstrates the presence of MoB_2 precipitates above 30 at. % Mo (**FIG. 2.1**), the WB_2 lattice still continues to expand linearly with 40 and 50 at. % Mo substitution (**FIG. 2.2**). This volume expansion past the solubility limit

suggests that many of the Mo atoms may still further substitute into the WB_2 structure in addition to forming a secondary MoB_2 phase.

Vickers micro-indentation hardness measurements from low to high load (0.49 to 4.9 N) for the WB_2-Mo system are shown in **FIG. 2.3**. All solid solutions exhibit load-dependent hardness values, where the hardness increases as the applied load decreases. This phenomenon, known as the indentation size effect, has been observed in the hardness of other systems and is likely due to the fact that more slip systems become accessible at higher load.[31] A gradual increase in hardness was observed from 29.5 ± 1.7 GPa at 0.49 N for unsubstituted WB_2 to a maximum value of 45.7 ± 2.5 GPa at 0.49 N with 30 at. % Mo. Above 30 at. % Mo, the hardness abruptly decreases due to the precipitation of the softer AlB_2-type β-MoB_2 phase (11.77 GPa at 0.49 N).[32]

Unlike ReB_2, which adopts a puckered boron structure that impedes dislocation slip, WB_2 contains alternating flat and puckered boron sheets, resulting in lower shear resistance than ReB_2. *In situ* X-ray radial diffraction was conducted under non-hydrostatic compression up to 60 GPa to probe changes in bond length and strength within $W_{0.70}Mo_{0.30}B_2$ upon pressure. The "cake" patterns recorded at the lowest and highest pressures (3 and 60 GPa, respectively) and the integrated 1-dimensional diffraction patterns are shown in **FIG. 2.4**. At low pressure (~3 GPa), the diffraction lines are almost straight due to hydrostatic stress state. However, at high pressure, the diffraction lines deviate to higher angle (2θ) in the high stress direction ($\varphi = 0°$) and to lower angle (2θ) in the low stress direction ($\varphi = 90°$). The sinusoidal variations of the diffraction lines at high pressure indicate the lattice-supported strains (**FIG. 2.4b**). In the integrated 1-dimensional diffraction pattern obtained at the magic angle $\varphi = 54.7°$, all peaks can be indexed to the WB_2 structure throughout the measured pressure range (**FIG. 2.4a**). A clear shift to the higher angle is observed at the higher pressure, indicating a decrease in the lattice spacing with greater

17

compression. The peak broadening is due to strain inhomogeneity. The peak positions at $\varphi = 54.7°$ are used to determine the lattice parameters and volume, as summarized in **Table S2.2** and **FIG. S2.2**. The pressure for each compression step was determined from the equation-of-state of Au standard, using its d-spacing at $\varphi = 54.7°$.

As shown in **FIG. 2.5a**, in the pressure range between 10 and 15 GPa, the c/a ratio undergoes a dramatic expansion, much large in magnitude than the contraction that occurs upon Mo substitution (**FIG. 2.2**). This sharp change in c/a ratio is indicative of a pressure induced second order phase transition. Such transitions have not been observed in other layered diborides that we have studied, such as ReB_2,[33] but they have been observed in more structurally constrained metal borides that contain boron cages crosslinking the layers, such as WB_4 and its solid solutions.[34,35] Past studies have associated such pressure induced changes in c/a ratio with rigid structures that also tend to show high hardness. In addition to providing a probe of phase behavior, the hydrostatic compression curve is fit to extract the bulk modulus or volume incompressibility. Because of the low phase transition pressure and the small number of points below the phase transition, the data can only be fit in the high-pressure phase, at pressures above 15 GPa. A fit of volume change to the second-order Birch-Murnaghan equation-of-state is shown in **FIG. S2.2c** and a normalized pressure versus Eulerian strain plot is shown in **FIG. 2.5b**, yielding a bulk modulus of 355 ± 2 GPa ($K_0' = 4$) and 368.5 ± 3.6 GPa ($K_0' = 3.2$) for second-order and third-order Birch-Murnaghan equations-of-state, respectively.

To calculate the differential strain and stress, the measured d-spacing is plotted versus the orientation function $(1-3\cos^2\varphi)$ for each lattice planes of interest; a linear correlation is observed to the highest pressures, as shown in **FIG. S2.3** and in good agreement with lattice strain theory (Equation 2.3). The hydrostatic d-spacings, obtained from zero-intercepts of linear fits like those

shown in **FIG. S2.2**, is found to shift smoothly with pressure, as shown in **FIG. S2.4**. The ratio of the slope of the line in **FIG. S2.3** to the zero-intercept is directly related to the differential strain, $Q(hkl)$, as given by Equation (2.3). As shown in **FIG. 2.6**, the measured differential strain for each lattice plane, presented here as t/G according to Equation (2.4), increases linearly with pressure and then appears to level off. The linear increase is associated with elastic behavior, including the second order phase transition, and the plateau is interpreted to imply that the lattice plane can no longer sustain additional differential strain, and presumably indicates the onset of plastic deformation (which is not clearly identifiable in the X-ray diffraction measurements). The plane with the lowest differential strain plateau value supports the least deformation, while planes with higher differential strain plateau values resist more shear and dislocation movement. The (004) plane, parallel to the boron layers, is prone to slip and therefore exhibits the lowest differential strain, particularly at the highest pressures. The (101) and (110) planes, which both cut through the metal-boron layers, support more lattice deformation (**FIG. 2.6a**). Interestingly, at lower pressures, $t(101)/G$ tracks almost perfectly with $t(004)/G$. However, part way through the (004) plateau, $t(101)/G$ deviates from $t(004)/G$ and eventually reaches a second plateau with the same value as $t(110)/G$ at 60 GPa. Data for the hardest pure metal diboride, ReB_2, is included for comparison. The ReB_2 generally supports much lower differential strain, and specifically shows a much lower plateau value for the (004) plane. The ReB_2 also does not show strain hardening in the (101) plane. Together, these factors combine to indicate that substituting Mo into WB_2 may strengthen the metal-boron bonds in $W_{0.70}Mo_{0.30}B_2$.

The differential stress (t) value at the plateau indicates the yield strength of the plane upon shear and is directly correlated to hardness. Unfortunately, the appropriate choice of a shear modulus, G, requires knowledge of the stress state in the sample chamber during measurement.

The differential stress can be calculated under Reuss (iso-stress) and Voigt (iso-strain) conditions using the elastic stiffness constants provided in the paper by Ding *et al.*[36] Since the real differential stress is likely a weighted average of the Reuss and Voigt conditions, both values were calculated as upper and lower limits of the true differential stress. The differential stress of the (110) plane plateaus at 19 GPa and 14 GPa under Voigt and Reuss conditions, respectively, suggesting that the plane has reached its yield strength at the pressure achieved in this experiment (**FIG. 2.6b**). The plateau in differential stress supported by (004), the weakest plane, reaches 11-16 GPa, which is higher than the strongest plane in ReB_2 (9-10 GPa).[33] The strain hardening the (101) plane is also preserved under both Reuss and Voight conditions. Although $W_{0.70}Mo_{0.30}B_2$ adopts the WB_2 structure, which deforms more readily than ReB_2, the presence of Mo dopant atoms in WB_2 apparently strengthen the covalent bonds and enable $W_{0.70}Mo_{0.30}B_2$ to support higher differential stress. These results indicate that increased hardness upon 30 at. % Mo substitution in WB_2 is largely the result of intrinsic solid-solution strengthening in the single-phase system.

Previous calculations have predicted that the WB_2-type MoB_2 (WB_2-MoB_2, $P6_3/mmc$) is more energetically favorable than the experimentally synthesized rhombohedral ($R\overline{3}m$) and hexagonal AlB_2-type MoB_2 ($P6/mmm$) structures.[36] The theoretically calculated strong covalency of the B-Mo bond in the WB_2-MoB_2 structure can provide insight into the observed high solubility of Mo in WB_2 and corresponding high hardness values.

Extrinsic properties of WB_2-Mo composites with SiC/B_4C

Once the solubility and Vickers hardness of the WB_2-Mo system were optimized, B_4C and SiC were incorporated as additives to both unsubstituted WB_2 and 30 at. % Mo substituted WB_2 in order to examine the effects of B_4C and SiC precipitation on surface morphology and hardness in multi-phase composites. The formation and stability of a phase from liquidus via arc melting is

dependent on the heat of formation as well as the melting point of each respective phase. In general, a phase is more likely to precipitate first upon cooling if it has a higher melting point than another phase and more likely to be stable if it has a highly negative heat of formation.[37] Both carbides have higher melting points than WB_2 (~2450 °C for B_4C[38] and ~2700 °C for SiC[39] versus ~2365 °C for WB_2[40]) and exhibit high thermodynamic stability. As a result, the addition of these secondary phases can be used to template subsequent WB_2 nucleation and grain growth.

FIG. 2.7 shows SEM images of arc-melted samples with increasing SiC content in both WB_2 and $W_{0.70}Mo_{0.30}B_2$ composites. As the amount of elemental Si and C collectively increase in the WB_2 system, the SiC grains increase in size and density. The addition of SiC to WB_2 led to an overall increase in hardness at 0.49 N from 29.5 ± 1.7 GPa for WB_2 to 45.7 ± 6.6 GPa for WB_2 with 30 wt. % SiC (**FIG. 2.8a, Table S2.3**). The reasonably large statistical variation in the measurements may be attributed to variations in grain orientations and the fact that the WB_2 crystal structure is anisotropic. To make sure that this did not bias the data, many different crystallographic orientations were indented. In previously studied from our group, the Vicker's hardness of ReB_2 was measured as a function of crystallographic orientation, and statistically significant differences were found in the hardness values measured using indentations parallel to the hexagonal c-axis, compared to those perpendicular to it.[7] Therefore, in this work, the hardness indentation locations were chosen pseudo-randomly to avoid selecting any particular grains. Despite the variation in measured values, the hardness was found to be significantly enhanced relative to pure WB_2 even considering the scatter in the measurements. The hardness value of 45.7 ± 6.6 GPa for WB_2 with 30 wt. % SiC is comparable to the hardness achieved in the hardest solid solution, $W_{0.70}Mo_{0.30}B_2$ (45.7 ± 2.5 GPa). SiC has a Vickers hardness range of 21-29 GPa at varying load.[31,41] Therefore, the individual SiC grains do not provide any additional hardening in the WB_2-SiC system. Instead,

the SiC precipitates apparently impede the dislocation of smaller WB_2 grains and additional stress must be added for plastic deformation to occur, resulting in a harder bulk material. Interestingly, hardness enhancement occurs only in the unsubstituted WB_2. For the $W_{0.70}Mo_{0.30}B_2$ system, SiC addition resulted in no change in average hardness (**FIG. 2.8b, Table S2.3**). This could be because more dramatic grain structure changes were observed in the pure WB_2 with increasing SiC content, or it may be due to the inherent solid solution hardening and grain boundary strengthening already present in the single-phase $W_{0.70}Mo_{0.30}B_2$ material. These results demonstrate that hardening effects are not necessarily additive, particularly when both intrinsic and extrinsic effects contribute to the overall material properties.

SEM images of WB_2 and $W_{0.70}Mo_{0.30}B_2$ composites with B_4C are shown in **FIG. 2.9**. Both systems show increasing grain size and B_4C precipitation as the amount of elemental B and C increases. Unlike SiC, the excess elemental boron added to form the WB_2-B_4C-based composites results in the formation of a WB_4 impurity in addition to B_4C (**FIG. 2.10**). PXRD data also indicate that less WB_4 is present in $W_{0.70}Mo_{0.30}B_2$ composites, where the substitution of Mo results in less W available for WB_4 formation (**FIG. S2.5**). Similar to the WB_2-SiC composites, increased hardness was observed in the WB_2-B_4C system (**FIG. 2.8c, Table S2.4**). However, the WB_2-B_4C system showed greater hardness enhancement, going from 29.5 ± 1.7 GPa with no B_4C addition to 53.8 ± 6.0 GPa with 30 wt. % B_4C addition. This average increase in hardness is due to two additional phases: WB_4 (43.3 ± 2.9 GPa at 0.49 N[42]) and B_4C ($\sim$38 GPa[43]), both of which are harder than the parent WB_2 system. In $W_{0.70}Mo_{0.30}B_2$-B_4C, the system again plateaus to a hardness value of approximately 45 GPa at all B_4C percentages (**FIG. 2.8d, Table S2.4**). The fact that the hardness of the $W_{0.70}Mo_{0.30}B_2$-B_4C shows no enhanced hardness despite significant grain size changes suggests that grain size is not the primary factor resulting in increased hardness. The explanation

more likely lies in the inherent solid solution hardening and grain boundary strengthening already present in the single-phase $W_{0.70}Mo_{0.30}B_2$ material.

Both oxidation resistance and hardness are important factors in cutting tools, where the lifetime and wear resistance of a material greatly affect its performance. To compare the thermal stability of the hardest samples, thermogravimetric studies were performed on fine powders of unsubstituted WB_2 and 30 at. % Mo-substituted WB_2 as well as the two hardest composites, WB_2-30 wt. % SiC and WB_2-30 wt. % B_4C. **FIG. 2.11** shows the oxidation behavior of the four samples up to 1000 °C in air. $W_{0.70}Mo_{0.30}B_2$ reaches 10% mass change at the lowest temperature (~580 °C), followed by WB_2-30 wt. % B_4C and WB_2 (~640 °C). WB_2-30 wt. % SiC does not gain 10% mass until 660 °C. At 700 °C, both $W_{0.70}Mo_{0.30}B_2$ and WB_2-30 wt. % B_4C have 20% increased mass, while WB_2 and WB_2-30 wt. % SiC do not reach 20% mass change until 740 °C and 800 °C, respectively. At 30% mass change, the corresponding temperature for WB_2-30 wt. % B_4C is 760 °C, much lower than the other three systems. While all systems increase the hardness of unsubstituted WB_2, their effects on oxidation resistance vary. WB_2-30 wt. % SiC exhibits the slowest oxidation rate, followed by $W_{0.70}Mo_{0.30}B_2$, WB_2 and WB_2-30 wt. % B_4C up until 30% mass change. While the composite effect for enhancing oxidation resistance is not fully understood, the presence of SiC and B_4C enhances both hardness and oxidation resistance in the WB_2 system. Understanding the grain morphology, hardness, and thermal stability of these systems provides valuable information towards tailoring boride-based materials for industrial applications.

2.4 Conclusions

The development of materials with high hardness, thermal stability, and cost-effectiveness remains a challenge in the manufacturing and machining industries. In this study, the substitution of 30 at. % Mo increased the hardness of the parent WB_2 structure, largely due to intrinsic solid

solution effects. These effects are observed both through Vickers hardness measurements and through plateau differential stress values that are both high and remarkably isotropic for a layered crystal structure. Multi-phase materials (WB_2 with B_4C and SiC) exhibited additional extrinsic hardening through grain size reduction and phase precipitation. This combination of results indicates that the hardness of WB_2 can be increased both through solid solutions effects, which is considered a form of intrinsic hardening, and via composite formation, which is often described as an extrinsic effect. Interestingly, for the WB_2 system, these two mechanisms do not appear to be additive, as the addition of B_4C and SiC to $W_{0.70}Mo_{0.30}B_2$ did not result in increased hardness. These strategies demonstrate the ability to design boride-based materials with enhanced mechanical properties through microstructure and composition, while using less expensive alloying additives.
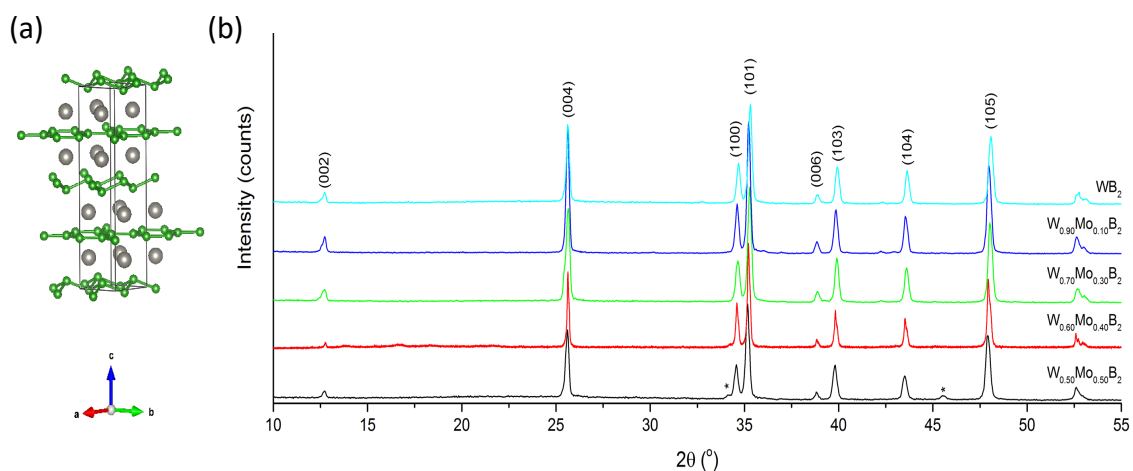
FIG. 2.1. (a) Crystal structure of tungsten diboride, WB_2 [*P6₃/mmc*, Inorganic Crystal Structure Database (ICSD) 023716], where the unit cell is indicated by the black box. Boron atoms are represented in green as flat and puckered alternating sheets. Tungsten atoms are represented in gray. (b) Selected PXRD data of tungsten diboride (WB_2) solid solutions with up to 50 at. % molybdenum (Mo). The solubility limit is below 40 at. % Mo. WB_2 (JCPDS 00-043-1386) is present at all concentrations of Mo, while β- MoB_2 (JCPDS 01-075-1046) appears in the 40 and 50 at. % Mo samples, denoted by an asterisk (*).
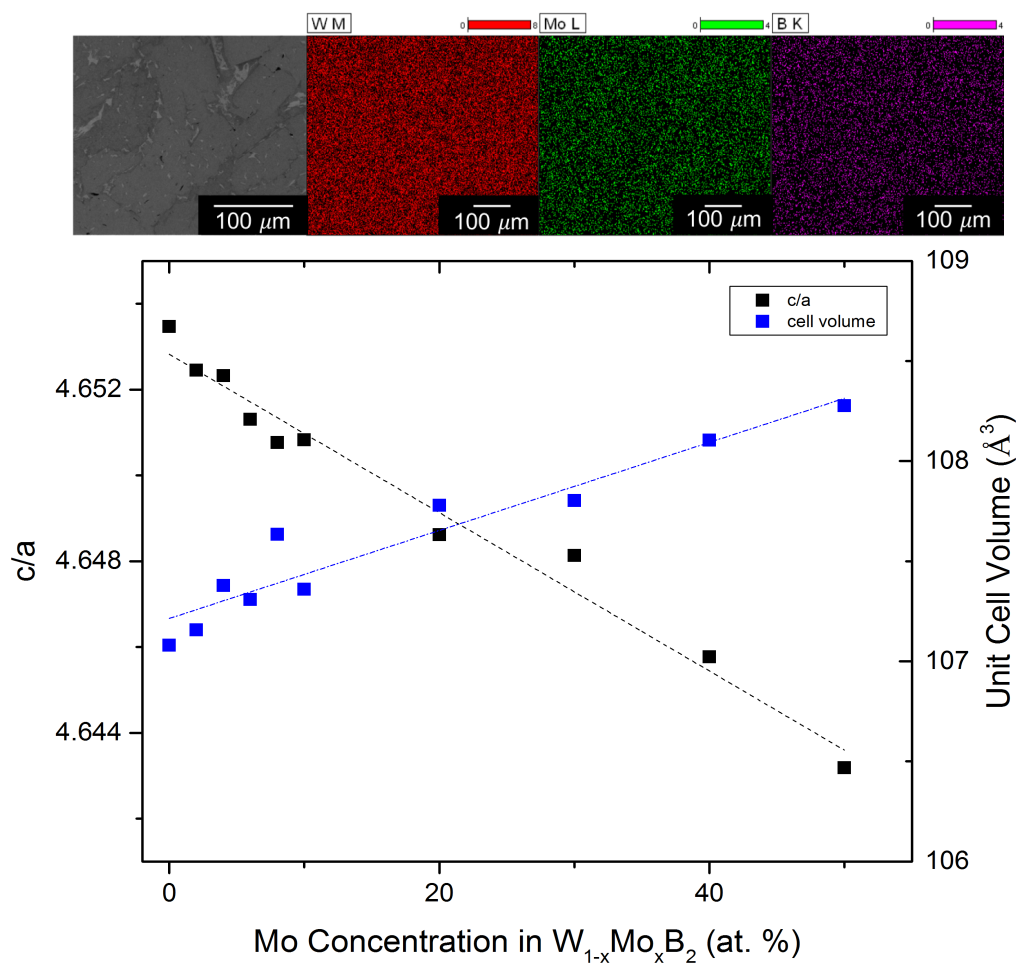
FIG. 2.2. (Top) SEM BSED image and elemental maps for tungsten (M line), molybdenum (L line), and boron (K line) for $W_{0.70}Mo_{0.30}B_2$ showing a uniform distribution of tungsten and molybdenum throughout the grains. (Bottom) Plot of (black) axial ratio, *c/a*, calculated from XRD cell refinement and (blue) unit cell volume calculated from $W_{1-x}Mo_xB_2$ lattice parameters versus Mo concentration in atomic percentage. Dashed lines represent linear trendlines as a function of Mo concentration. Unit cell parameters of all compositions are provided in **Table S2.1**.
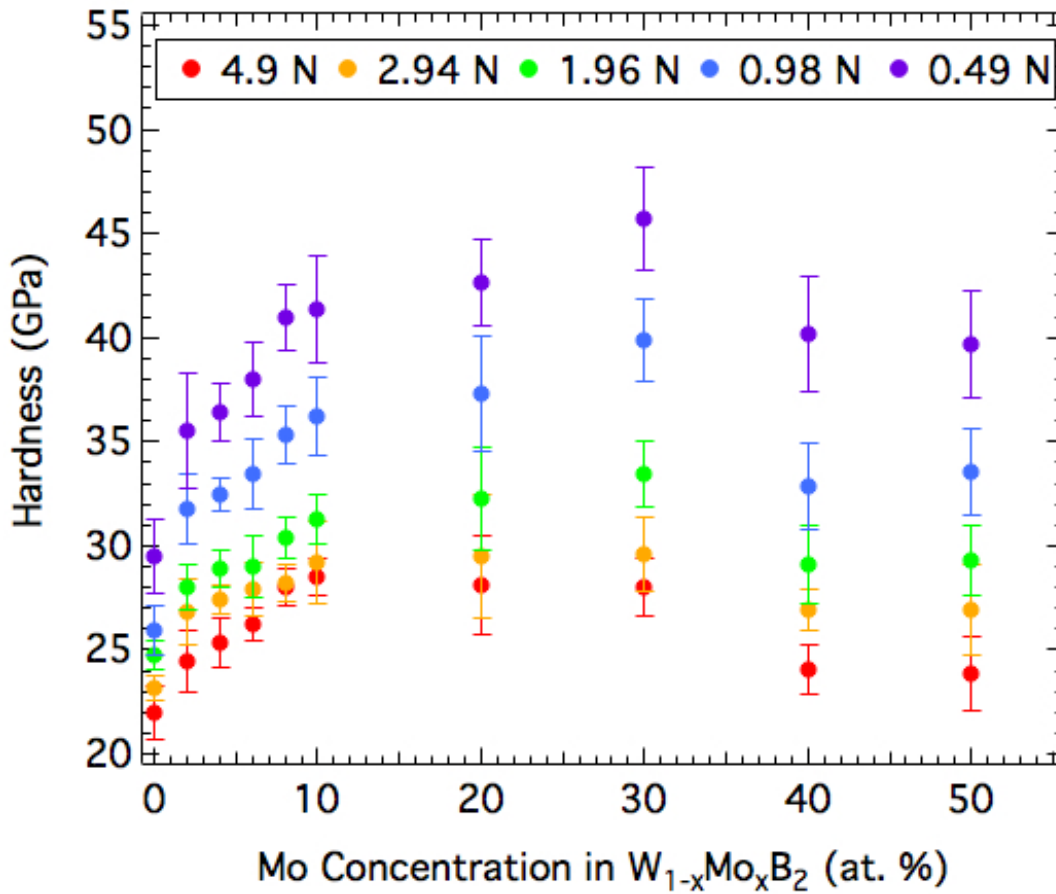
FIG. 2.3. Vickers micro-indentation hardness versus atomic percentage of Mo in WB$_2$-Mo solid solutions from low (0.49 N) to high (4.9 N) load. Concentrations of Mo were varied by increasing the substitution of Mo from 0-50 at. % on a metals basis.
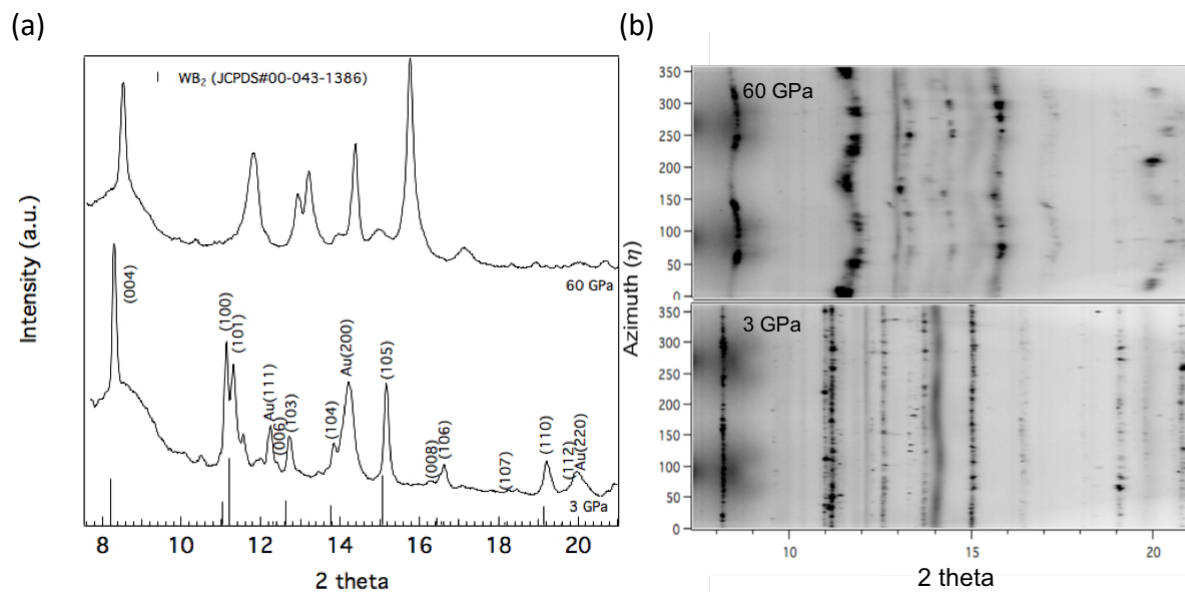
FIG. 2.4. Representative synchrotron (a) 1-D X ray diffraction patterns and (b) 2-D cake pattern of $W_{0.70}Mo_{0.30}B_2$ for low and high pressure. Cake patterns were obtained by integration over a 5° slice centered at the magic angle ($\varphi=54.7°$).
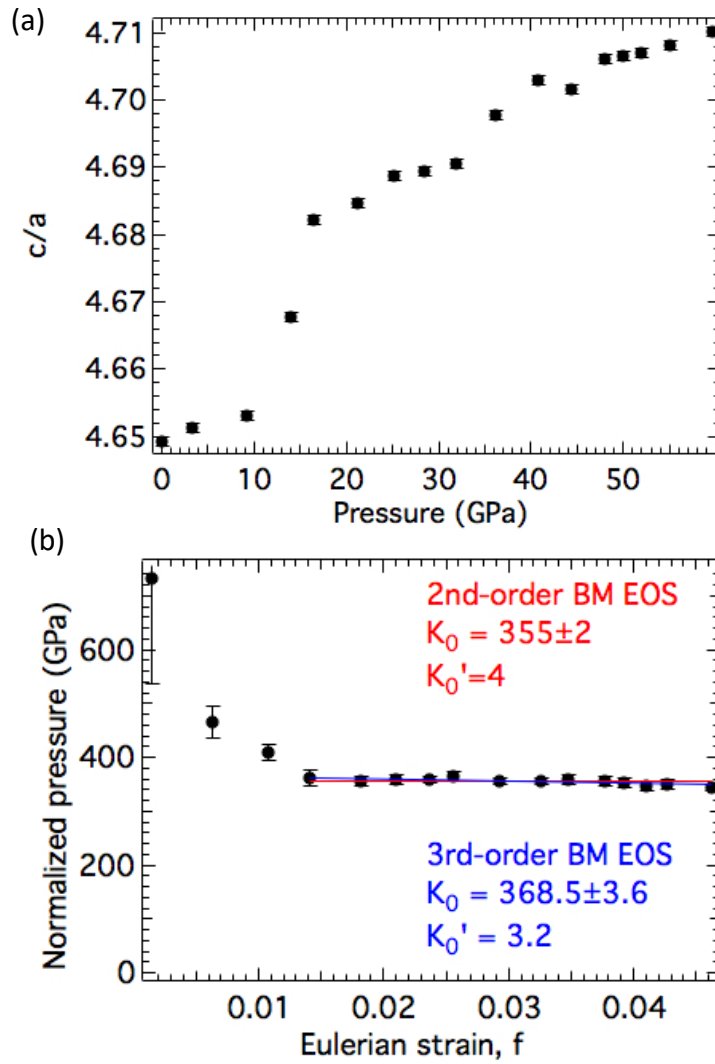
FIG. 2. 5. (a) Evolution of c/a upon pressure for $W_{0.70}Mo_{0.30}B_2$ obtained at the magic angle. (b) Normalized pressure (F) as a function of Eulerian strain (f). Second-order (red) and third-order (blue) Birch-Murnaghan equation-of-state fits.
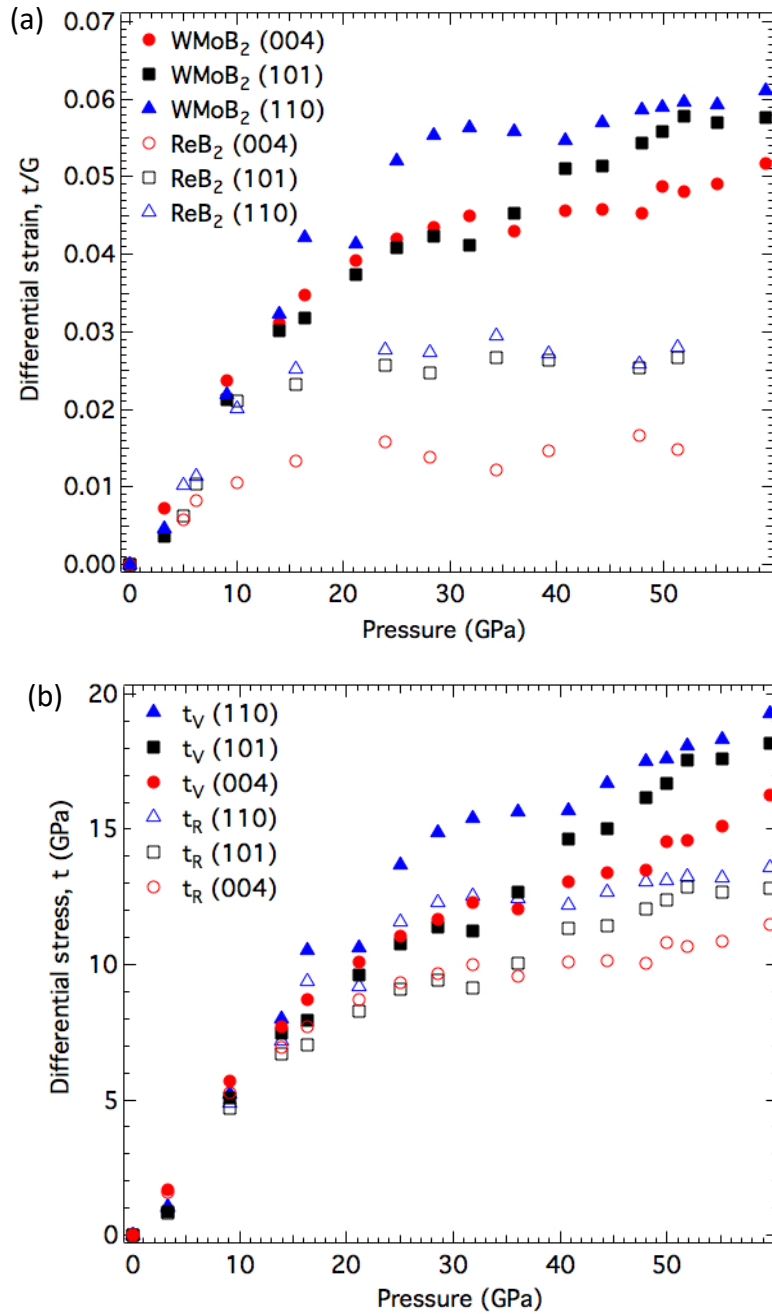
FIG. 2.6. (a) Comparison of the differential strain, given by the ratio of the differential stress (t) to shear modulus (G), as a function of pressure for both $W_{0.70}Mo_{0.30}B_2$ (WMoB$_2$) and ReB$_2$. (b) Differential stress (t) calculated under Reuss (isostress, t_R) and Voigt (isostrain, t_V) conditions for WMoB$_2$.
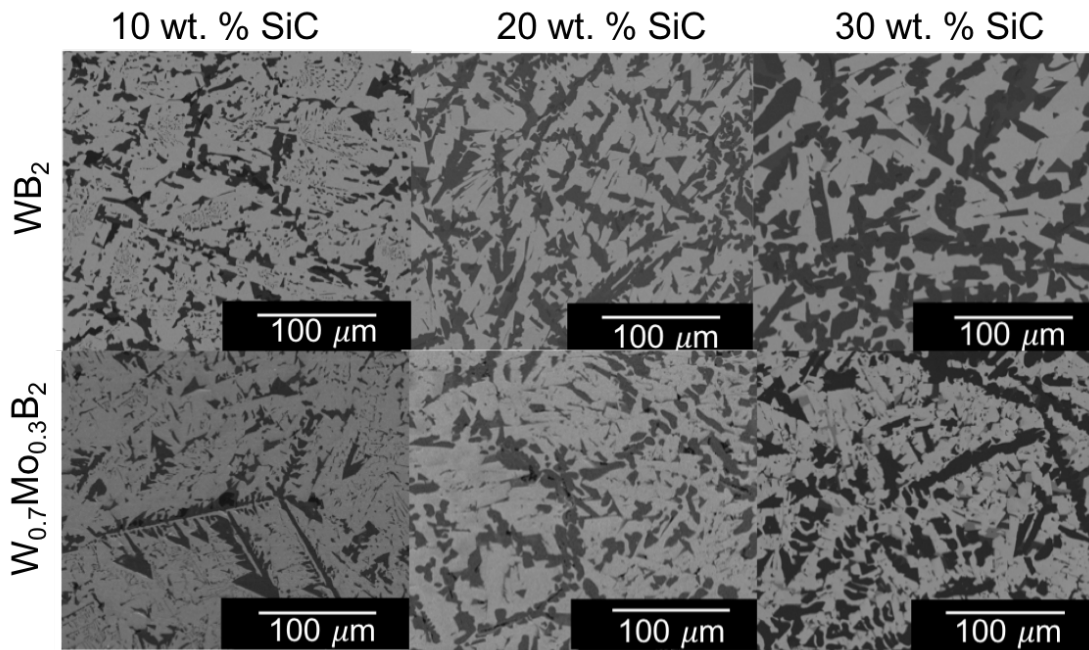
FIG. 2.7. SEM images of (top) WB_2 and (bottom) $W_{0.70}Mo_{0.30}B_2$ with 10, 20, and 30 wt. % SiC addition. Light gray regions represent areas of WB_2 and $W_{0.70}Mo_{0.30}B_2$, while dark gray regions represent SiC grains.
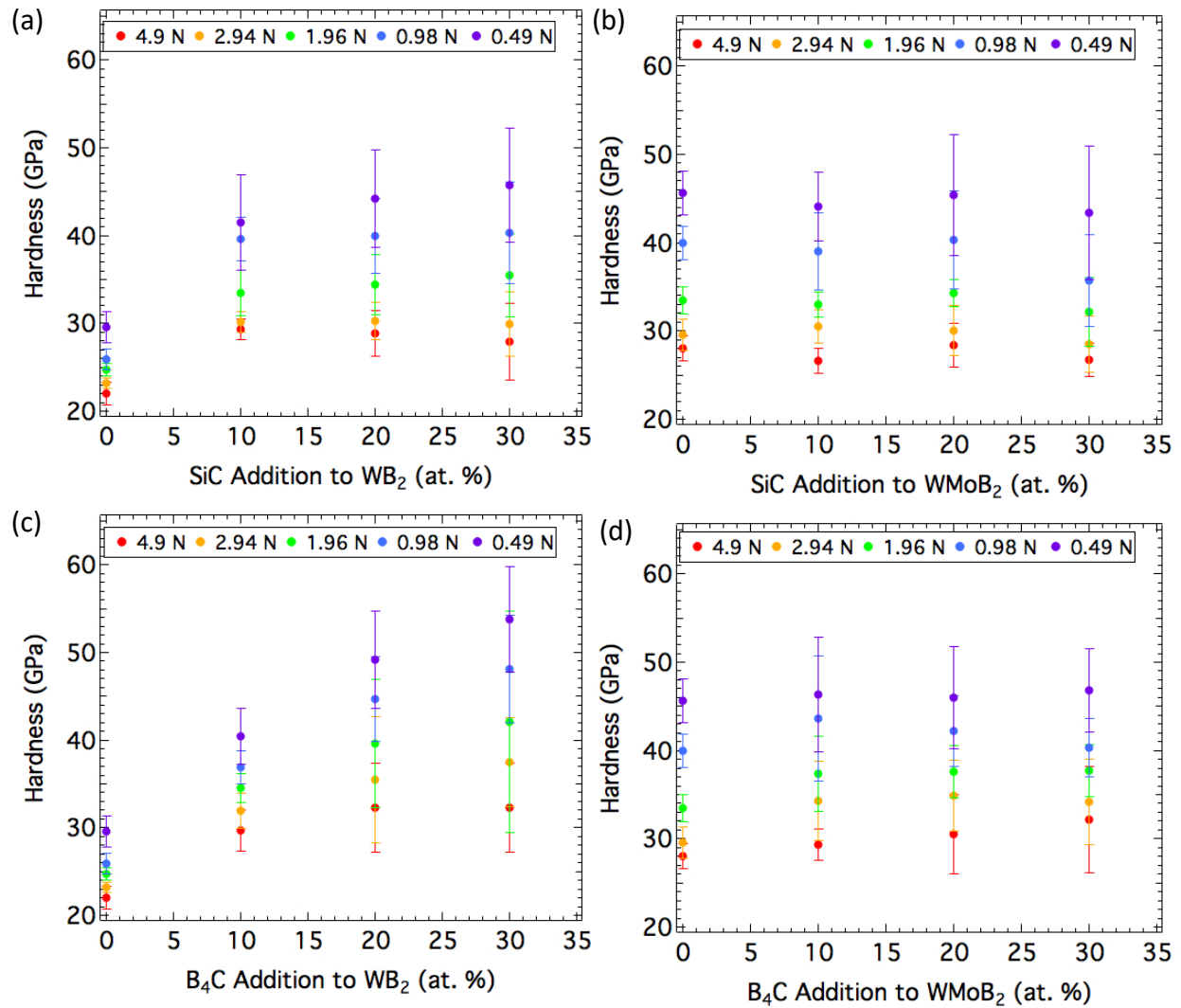
FIG. 2.8. Vickers micro-indentation hardness versus weight percentage (0-30 wt. %) of SiC addition in: (a) WB$_2$ and (b) W$_{0.70}$Mo$_{0.30}$B$_2$ using loads ranging from low (0.49 N) to high (4.9 N). Vickers micro-indentation hardness versus weight percentage (0-30 wt. %) of B$_4$C addition in: (c) WB$_2$ and (d) W$_{0.70}$Mo$_{0.30}$B$_2$ from low (0.49 N) to high (4.9 N) load.
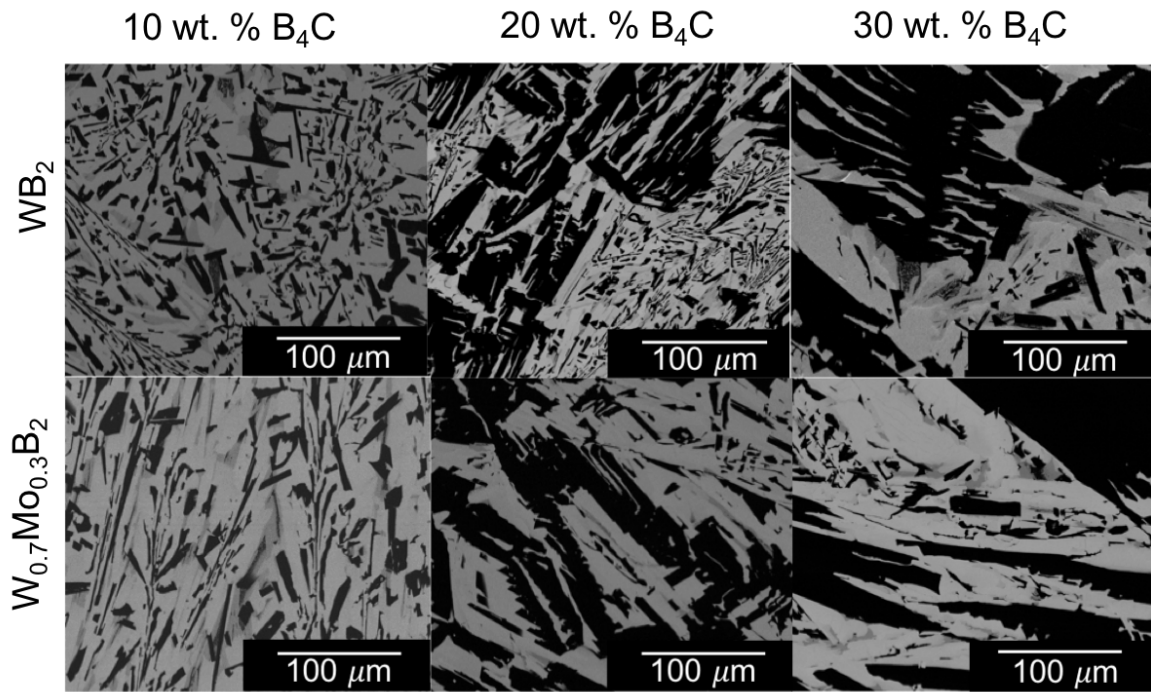
FIG. 2.9. SEM images of (top) WB_2 and (bottom) $W_{0.70}Mo_{0.30}B_2$ with 10, 20, and 30 wt. % B_4C additions. Light gray regions represent areas of WB_2 and $W_{0.70}Mo_{0.30}B_2$, while black regions represent B_4C grains. A higher content of additional WB_4 impurity (shown as gray areas surrounding WB_2 and B_4C) occurs in the WB_2 system, where more W is available for tetraboride formation.
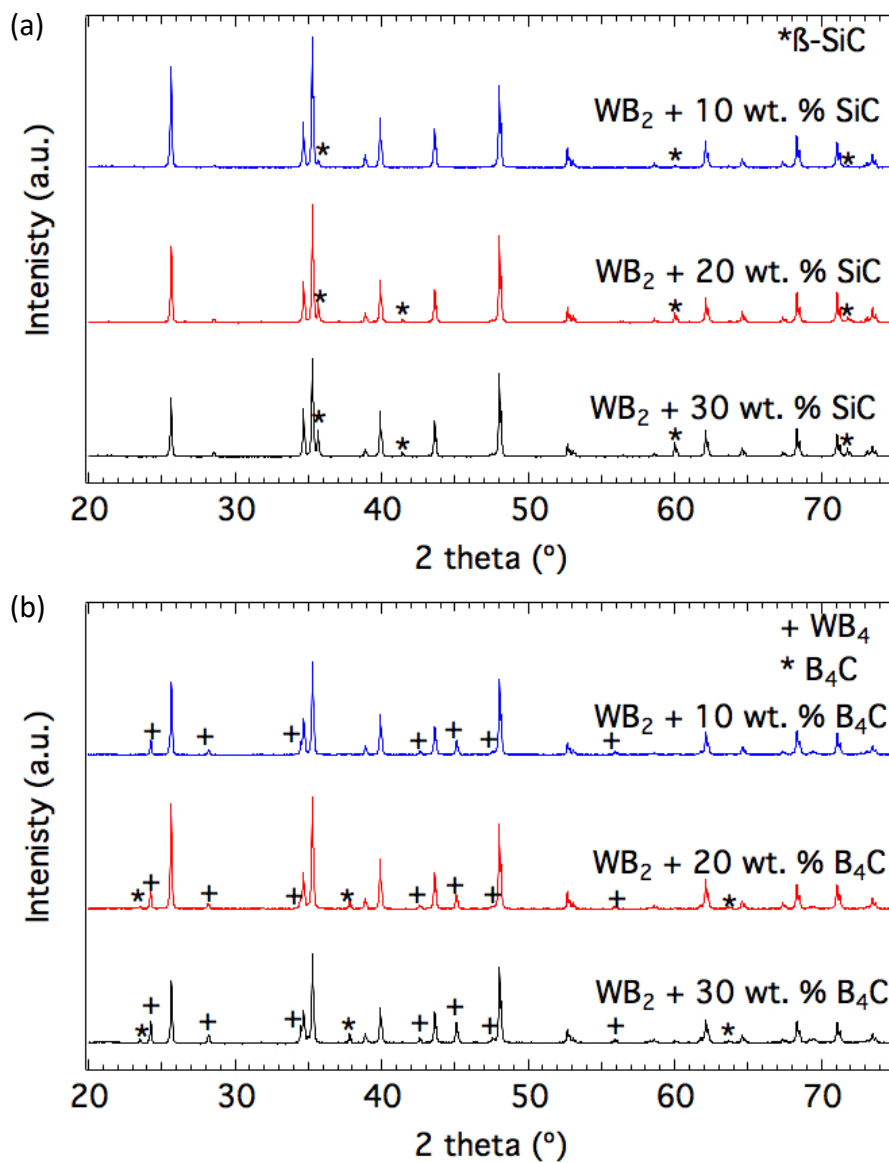
FIG. 2.10. PXRD data of: WB$_2$ with 10, 20, and 30 wt. % (a) SiC addition and (b) B$_4$C. The growth of the secondary β-SiC phase (JCPDS 03-065-0360) is denoted by an asterisk (*) in (a). All patterns show (+) WB$_4$ (JCPDS 00-019-1373) and (*) B$_4$C (JCPDS 00-035-0798) in (b).
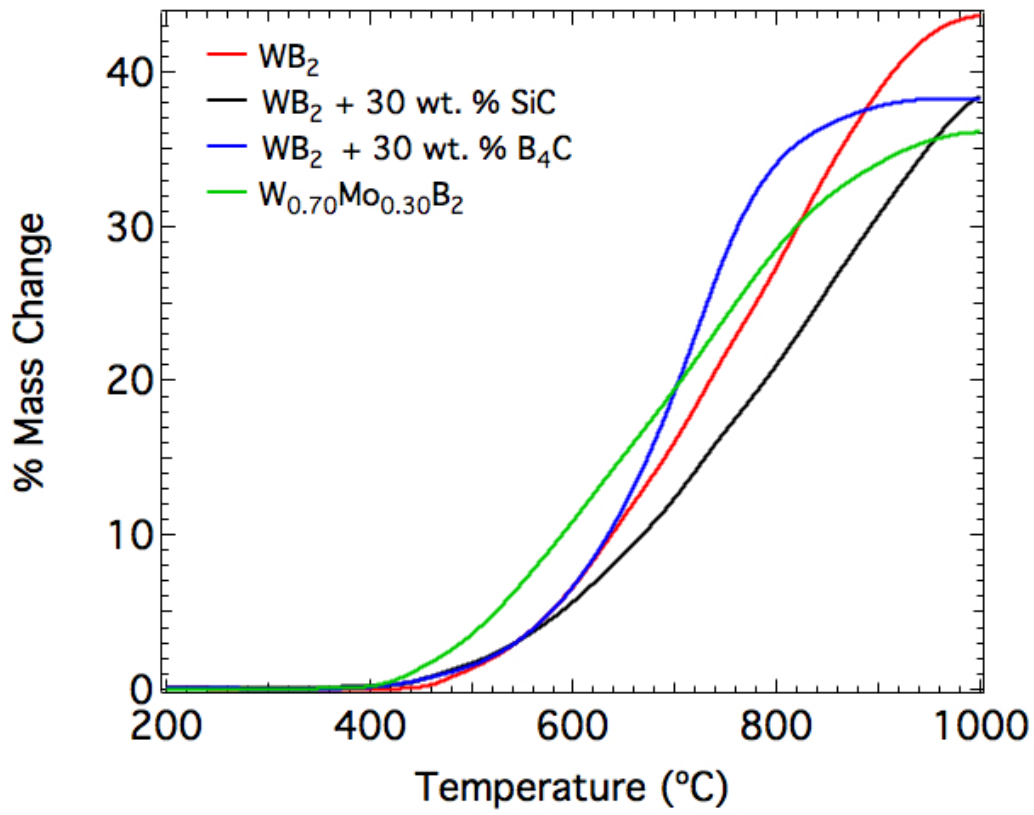
FIG. 2.11. Thermogravimetric analysis of unsubstituted WB_2 and the three hardest compositions studied in this work.

2.5 Supporting information

Table S2.1. Unit Cell Data[a,b] and Vickers Hardness for WB_2 with Variable Mo Substitution

at. % Mo	a (Å)	c (Å)	H_v (4.9 N)	H_v (2.94 N)	H_v (1.96 N)	H_v (0.98 N)	H_v (0.49 N)
0	2.9840(2)	13.8861(7)	22.0 ± 1.3	23.2 ± 0.6	24.7 ± 0.7	25.9 ± 1.2	29.5 ± 1.7
2	2.9849(2)	13.8873(7)	24.5 ± 1.5	26.9 ± 1.6	28.0 ± 1.1	31.7 ± 1.7	35.5 ± 2.8
4	2.9870(2)	13.8966(6)	25.4 ± 1.2	27.4 ± 0.7	28.9 ± 0.9	32.5 ± 0.8	36.4 ± 1.4
6	2.9866(3)	13.8916(8)	26.3 ± 0.8	27.9 ± 1.3	29.0 ± 1.5	33.4 ± 1.7	38.0 ± 1.8
8	2.9897(2)	13.9045(7)	28.0 ± 0.9	28.2 ± 0.9	30.4 ± 1.0	35.3 ± 1.3	40.9 ± 1.6
10	2.9872(2)	13.8928(8)	28.5 ± 0.8	29.2 ± 2.0	31.3 ± 1.2	36.2 ± 1.9	41.3 ± 2.6
20	2.9915(2)	13.9065(7)	28.1 ± 2.3	29.5 ± 3.0	32.2 ± 2.5	37.3 ± 2.8	42.6 ± 2.1
30	2.9918(3)	13.9065(6)	28.0 ± 1.4	29.6 ± 1.7	33.4 ± 1.6	39.9 ± 1.9	45.7 ± 2.5
40	2.9951(1)	13.9148(3)	24.1 ± 1.1	26.9 ± 0.9	29.1 ± 1.9	32.9 ± 2.1	40.1 ± 2.8
50	2.9972(1)	13.9170(3)	23.9 ± 1.7	26.9 ± 2.1	29.3 ± 1.7	33.5 ± 2.1	39.7 ± 2.6

[a]Standard deviations are indicated in parentheses.

[b]Cell parameters were calculated on GSAS-II software through comparison with WB_2 ICSD-023716 (a = 2.9831 Å; c = 13.879 Å).

Table S2.2. Lattice parameters and volume of $W_{0.70}Mo_{0.30}B_2$ as a function of pressure[a]

Pressure (GPa)	a (Å)	c (Å)	V (Å³)
0	2.99382(18)	13.9190(19)	108.041(20)
3.2(2)	2.98903(19)	13.9027(20)	107.570(21)
9.1(2)	2.97418(19)	13.8392(20)	106.017(20)
14.0(1)	2.95808(19)	13.8075(20)	104.632(20)
16.4(5)	2.9455(19)	13.7913(20)	103.622(20)
21.2(2)	2.93347(18)	13.7425(20)	102.414(19)
25.1(3)	2.92447(18)	13.7124(20)	101.564(19)
28.5(3)	2.91718(18)	13.6796(20)	100.816(19)
31.8(6)	2.91135(18)	13.6561(20)	100.241(19)
36.1(5)	2.89964(18)	13.6221(19)	99.189(19)
40.8(6)	2.88965(18)	13.5899(19)	98.274(19)
44.3(9)	2.88402(18)	13.5594(19)	97.671(18)
48.1(12)	2.87538(18)	13.5317(19)	96.889(18)
49.9(11)	2.8711(18)	13.5131(19)	96.468(18)
51.9(10)	2.86627(17)	13.4917(19)	95.991(18)
55.1(14)	2.86166(17)	13.4735(19)	95.554(18)
59.6(8)	2.85190(17)	13.4329(19)	94.617(17)

[a]Standard deviations are indicated in parentheses.

Table S2.3. Vickers Hardness for WB_2 and $W_{0.70}Mo_{0.30}B_2$ with Variable Weight Percentage (wt. %) of SiC[a]

	wt. % SiC	H_v (4.9 N)	H_v (2.94 N)	H_v (1.96 N)	H_v (0.98 N)	H_v (0.49 N)
WB_2	0	22.0 ± 1.3	23.2 ± 0.6	24.7 ± 0.7	25.9 ± 1.2	29.5 ± 1.7
	10	29.3 ± 1.2	30.2 ± 1.2	33.4 ± 2.6	39.6 ± 2.6	41.5 ± 5.4
	20	28.9 ± 2.6	30.3 ± 2.1	34.4 ± 3.4	39.9 ± 4.2	44.2 ± 5.5
	30	27.9 ± 4.3	30.0 ± 3.7	35.5 ± 4.7	40.3 ± 5.8	45.7 ± 6.6
$W_{0.70}Mo_{0.30}B_2$	0	28.0 ± 1.4	29.6 ± 1.7	33.4 ± 1.6	39.9 ± 1.9	45.7 ± 2.5
	10	26.7 ± 1.5	30.5 ± 1.9	33.0 ± 1.4	39.0 ± 4.4	44.1 ± 3.9
	20	28.4 ± 2.5	30.0 ± 2.9	34.3 ± 1.6	40.3 ± 5.6	45.4 ± 6.9
	30	26.7 ± 1.9	28.5 ± 3.2	32.2 ± 3.8	35.7 ± 5.2	43.4 ± 7.6

[a]Weight percentage of SiC was determined by nominal composition of elemental Si and C (1:1 molar Si:C) added during synthesis.

Table S2.4. Vickers Hardness for WB_2 and $W_{0.70}Mo_{0.30}B_2$ with Variable Weight Percentage (wt. %) of B_4C[a]

	wt. % B_4C	H_v (4.9 N)	H_v (2.94 N)	H_v (1.96 N)	H_v (0.98 N)	H_v (0.49 N)
WB_2	0	22.0 ± 1.3	23.2 ± 0.6	24.7 ± 0.7	25.9 ± 1.2	29.5 ± 1.7
	10	29.7 ± 2.3	31.9 ± 2.1	34.6 ± 1.6	36.9 ± 1.9	40.4 ± 3.2
	20	32.3 ± 5.1	35.5 ± 7.3	39.6 ± 7.4	44.7 ± 4.8	49.1 ± 5.6
	30	32.3 ± 5.0	37.5 ± 5.1	42.1 ± 5.6	48.1 ± 6.2	53.8 ± 6.0
$W_{0.70}Mo_{0.30}B_2$	0	28.0 ± 1.4	29.6 ± 1.7	33.4 ± 1.6	39.9 ± 1.9	45.7 ± 2.5
	10	29.3 ± 1.8	34.3 ± 4.5	37.3 ± 4.2	43.6 ± 7.1	46.3 ± 6.5
	20	30.5 ± 4.5	34.9 ± 4.0	37.6 ± 2.9	42.2 ± 4.0	46.0 ± 5.8
	30	32.2 ± 6.0	34.2 ± 4.8	37.7 ± 2.9	40.3 ± 3.3	46.8 ± 4.7

[a]Weight percentage of B_4C was determined by nominal composition of elemental B and C (4:1 molar B:C) added during synthesis.
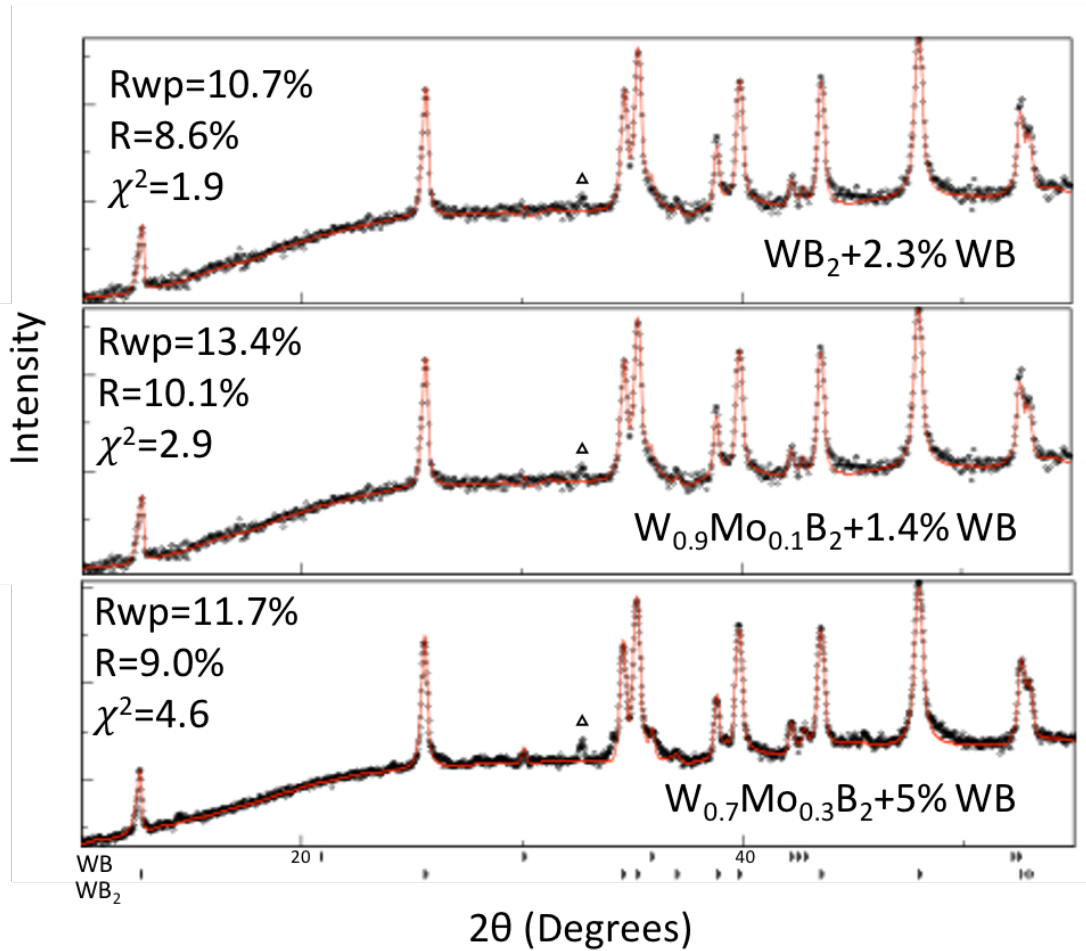
FIG. S2.1. Rietveld refinement of PXRD data of: WB_2 with 0, 10, and 30% Mo. The peak labelled as Δ is the background peak from the silicon substrate. Error analysis (Rwp%, R%, χ^2) is included in the plots. The percentage of WB impurity is included in the fit.
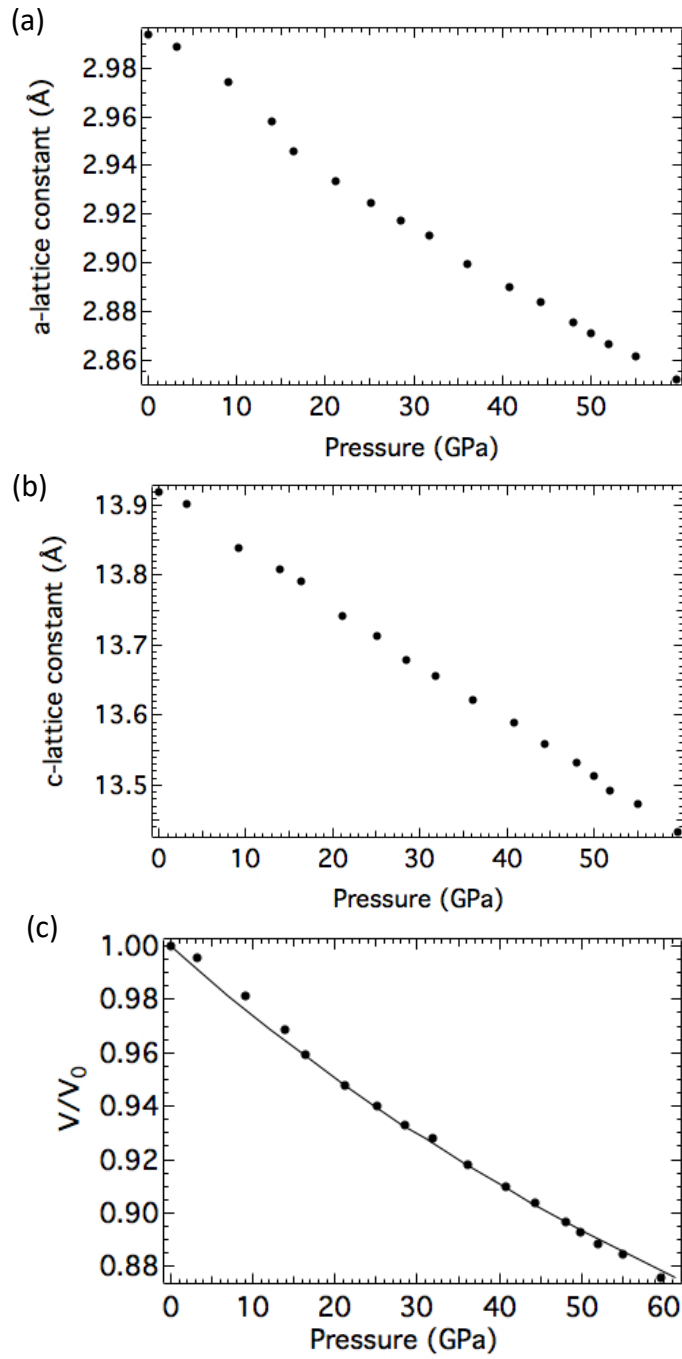
FIG. S2.2. Evolution of: (a) a-lattice constant, (b) c-lattice constant and (c) plot of volume change versus pressure for $W_{0.70}Mo_{0.30}B_2$. The curve is calculated from the second order Birch-Murnaghan equation of state, where K_0' is fixed at 4.
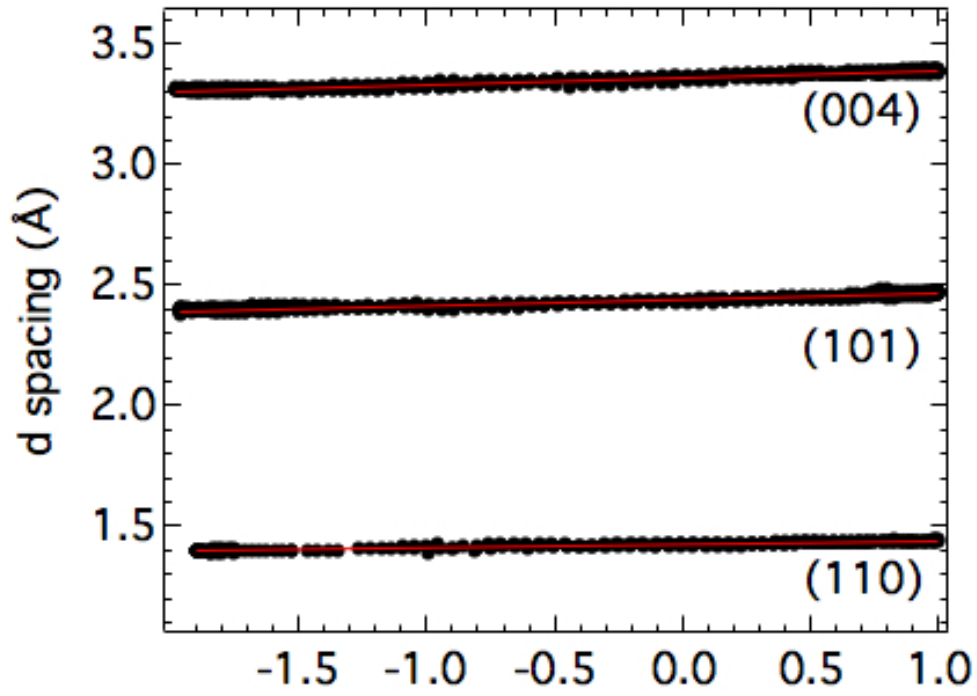
FIG. S2.3. Linearized plot of d-spacings as a function of φ angle at the highest pressure (60 GPa).
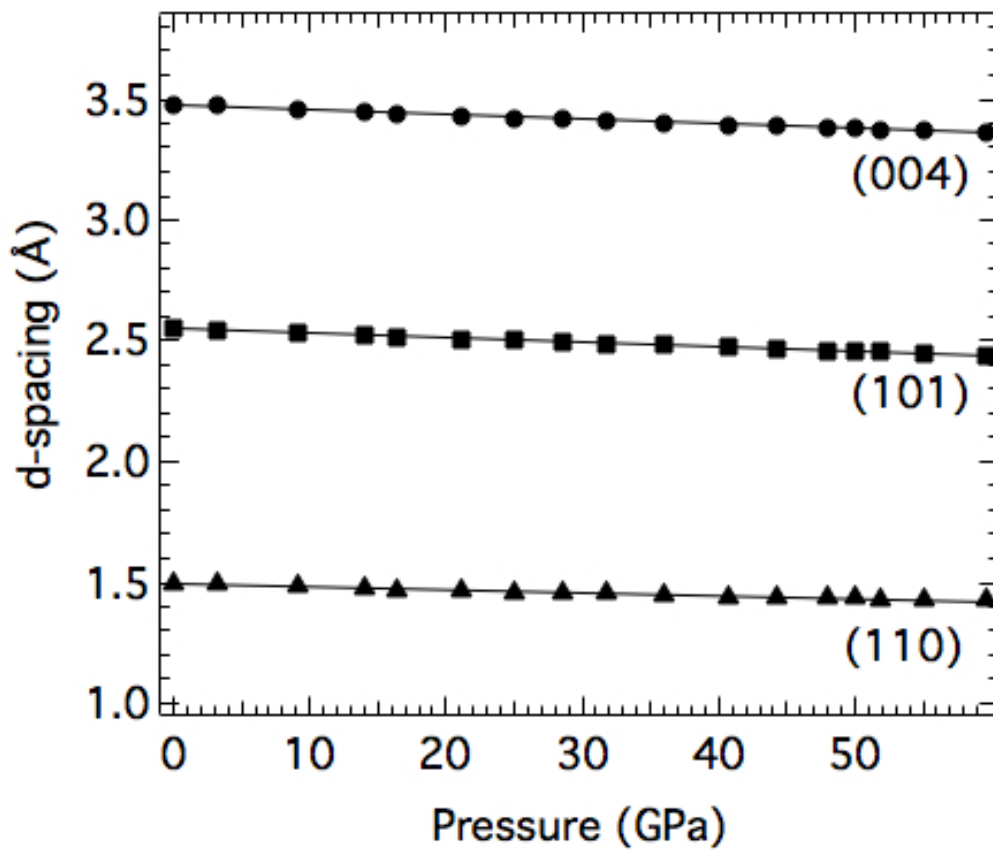
FIG. S2.4. Measured d-spacings for selected lattice planes as a function of pressure. Error bars that are smaller than the size of the markers have been omitted. The solid lines are the best linear fit of the data.
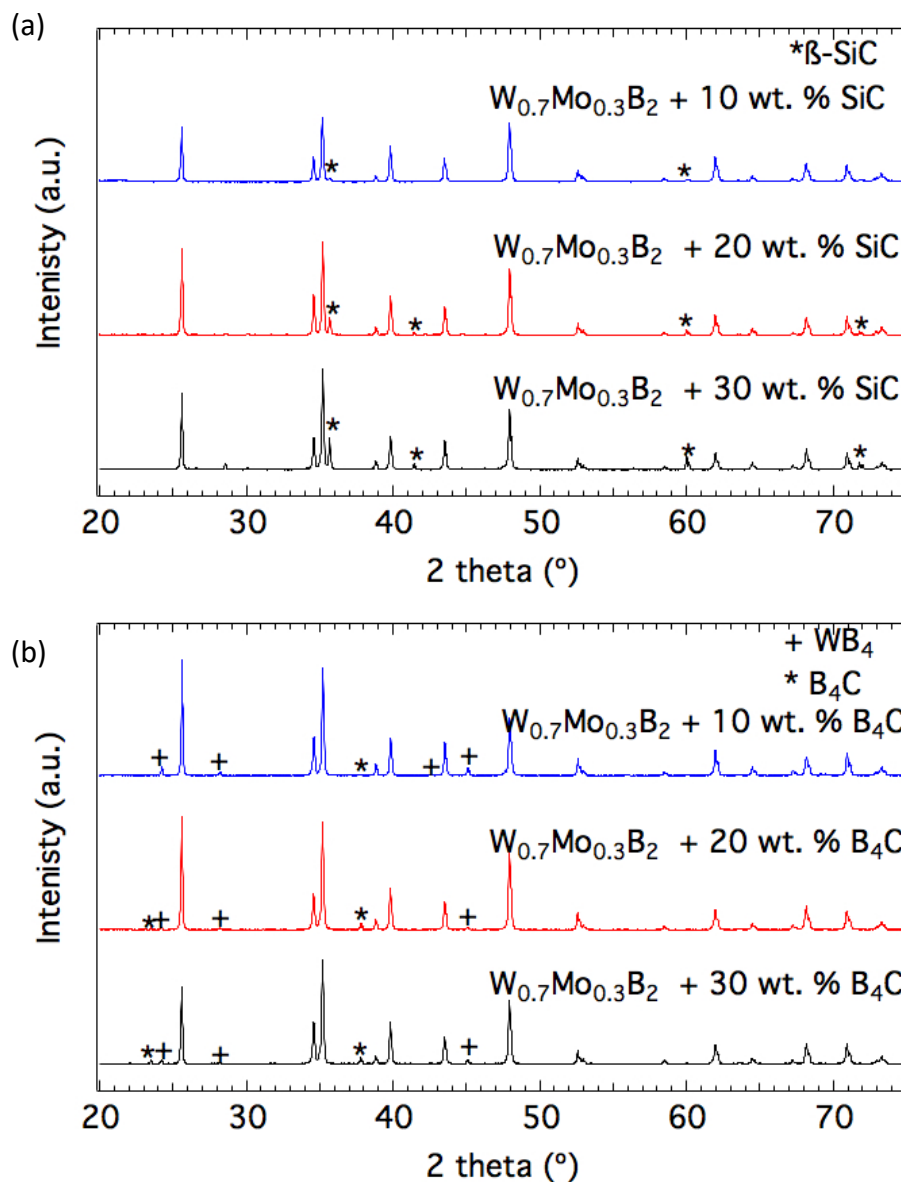
FIG. S2.5. PXRD data for: $W_{0.70}Mo_{0.30}B_2$ with 10, 20, and 30 wt. % (a) SiC addition and (b) B_4C. The growth of the secondary β-SiC phase (JCPDS 03-065-0360) is denoted by an asterisk (*) in (a). All patterns show (+) WB_4 (JCPDS 00-019-1373) and (*) B_4C (JCPDS 00-035-0798) in (b).

2.6 References

1. Ezugwu, E. O. Key Improvements in the Machining of Difficult-to-Cut Aerospace Superalloys. *Int. J. Mach. Tools Manuf.* **45** (12–13), 1353–1367 (2005).

2. Mohammadi, R. & Kaner, R. B. *Superhard Materials*; R.A. Scott ed., John Wiley and Sons, Inc., (2012).

3. Komanduri, R. & Shaw, M. C. Wear of Synthetic Diamond When Grinding Ferrous Metals. *Nature* **255** (5505), 211–213 (1975).

4. Westraadt, J. E., Sigalas, I. & Neethling, J. H. Characterisation of Thermally Degraded Polycrystalline Diamond. *Int. J. Refract. Met. Hard Mater.* **48**, 286–292 (2015).

5. Kaner, R. B.; Gilman, J. J.; Tolbert, S. H. Designing Superhard Materials. *Science.* **308**, 1268–1269 (2005).

6. Mansouri Tehrani, A., Ghadbeigi, L., Brgoch, J. & Sparks, T. D. Balancing Mechanical Properties and Sustainability in the Search for Superhard Materials. *Integr. Mater. Manuf. Innov.* **6**, 1–8 (2017).

7. Chung, H.-Y. *et al*. Synthesis of Ultra-Incompressible Superhard Rhenium Diboride at Ambient Pressure. *Science.* **316**, 436–439 (2007).

8. Mohammadi, R. *et al.* Tungsten Tetraboride, an Inexpensive Superhard Material. *Proc. Natl. Acad. Sci.* **108**, 10958–10962 (2011).

9. Akopov, G., Pangilinan, L. E., Mohammadi, R. & Kaner, R. B. Perspective: Superhard Metal Borides: A Look Forward. *APL Mater.* **6**, 070901 (2018).

10. Hume-Rothery, W. *Atomic Theory for Students of Metallurgy*, 5th ed.; The Institute of Metals: London (1969).

11. Hume-Rothery, W. & Powell, H. M. On the Theory of Super-Lattice Structures in Alloys.

Z. Krist. **91**, 23 (1935).

12. Hume-Rothery, W., Smallman, R. W. & Haworth, C. W. *The Structure of Metals and Alloys*; The Institute of Metals: London (1969).

13. Wu, D., Zhang, J., Huang, J. C., Bei, H. & Nieh, T. G. Grain-Boundary Strengthening in Nanocrystalline Chromium and the Hall–Petch Coefficient of Body-Centered Cubic Metals. *Scr. Mater.* **68**, 118–121 (2013).

14. Akopov, G., Yeung, M. T., Turner, C. L., Mohammadi, R. & Kaner, R. B. Extrinsic Hardening of Superhard Tungsten Tetraboride Alloys with Group 4 Transition Metals. *J. Am. Chem. Soc.* **138**, 5714–5721 (2016).

15. Nagamatsu, J., Nakagawa, N., Muranaka, T., Zenitani, Y. & Akimitsu, J. Superconductivity at 39K in Magnesium Diboride. *Nature* **410**, 63–64 (2001).

16. Park, H., Encinas, A., Scheifers, J. P., Zhang, Y. & Fokwa, B. P. T. T. Boron-Dependency of Molybdenum Boride Electrocatalysts for the Hydrogen Evolution Reaction. *Angew. Chemie - Int. Ed.* **56**, 5575–5578 (2017).

17. Lech, A. T. *et al*. Superhard Rhenium/Tungsten Diboride Solid Solutions. *J. Am. Chem. Soc.* **138**, 14398–14408 (2016).

18. Park, H., Zhang, Y., Lee, E., Shankhari, P. & Fokwa, B. P. T. High-Current-Density HER Electrocatalysts: Graphene-like Boron Layer and Tungsten as Key Ingredients in Metal Diborides. *ChemSusChem* **12**, 3726–3731 (2019).

19. Burdett, J. K., Canadell, E. & Miller, G. J. Electronic Structure of Transition-Metal Borides with the AlB2 Structure. *J. Am. Chem. Soc.* **108**, 6561–6568 (1986).

20. Aronsson, B., Lundström, T. & Engström, I. Some Aspects of the Crystal Chemistry of Borides, Boro-Carbides and Silicides of the Transition Metals. In *Anisotropy in Single-Crystal*

Refractory Compounds: Proceedings of an International Symposium on Anisotropy in Single-Crystal Refractory Compounds, Springer US: Boston, (1968).

21. La Placa, S. J. & Post, B. The Crystal Structure of Rhenium Diboride. *Acta Crystallogr.* **15**, 97–99 (1962).

22. Frotscher, M., Hölzel, M. & Albert, B. Crystal Structures of the Metal Diborides ReB2, RuB2, and OsB2 from Neutron Powder Diffraction. *Zeitschrift fur Anorg. und Allg. Chemie* **636**, 1783–1786 (2010).

23. Lundström, T. The Structure of Ru2B3 and WB2.0 as Etermined by Single-Crystal Diffractometry, and Some Notes on the W-B System. *Ark. Kemi* **30**, 115–127 (1968).

24. Frotscher, M. *et al.* M2B5 or M2B4? A Reinvestigation of the Mo/B and W/B System. *Zeitschrift für Anorg. und Allg. Chemie* **633**, 2626–2630 (2007).

25. Pangilinan, L. E. *et al*. Superhard Tungsten Diboride-Based Solid Solutions. *Inorg. Chem.* **57**, 15305–15313 (2018).

26. Zhao, F. *et al.* Synthesis and Characterization of WB2-WB3-B4C Hard Composites. *Int. J. Refract. Met. Hard Mater.* **82**, 268–272 (2019).

27. Neuman, E. W., Brown-Shaklee, H. J., Hilmas, G. E. & Fahrenholtz, W. G. Titanium Diboride-Silicon Carbide-Boron Carbide Ceramics with Super-High Hardness and Strength. *J. Am. Ceram. Soc.* **101**, 497–501 (2018).

28. Asl, M. S., Kakroudi, M. G. & Noori, S. Hardness and Toughness of Hot Pressed ZrB2–SiC Composites Consolidated under Relatively Low Pressure. *J. Alloys Compd.* **619**, 481–487 (2015).

29. Slater, J. C. Atomic Radii in Crystals. *J. Chem. Phys.* **41**, 3199–3204 (1964).

30. Toby, B. H. & Von Dreele, R. B. *GSAS-II* : The Genesis of a Modern Open-Source All

Purpose Crystallography Software Package. *J. Appl. Crystallogr.* **46**, 544–549 (2013).

31. Quinn, J. B. & Quinn, G. D. Indentation Brittleness of Ceramics: A Fresh Approach. *J. Mater. Sci.* **32**, 4331–4346 (1997).

32. Ivankov, A. A. *Handbook of Hardness Data*; Naukova Dumka: Kiev (1968).

33. Lei, J. *et al.* Synthesis and High-Pressure Mechanical Properties of Superhard Rhenium/Tungsten Diboride Nanocrystals. *ACS Nano* **13**, 10036–10048 (2019).

34. Xie, M. *et al*. Exploring the High-Pressure Behavior of Superhard Tungsten Tetraboride. *Phys. Rev. B - Condens. Matter Mater. Phys.* **85**, 1–8 (2012).

35. Xie, M. *et al*. Exploring Hardness Enhancement in Superhard Tungsten Tetraboride-Based Solid Solutions Using Radial X-Ray Diffraction. *Appl. Phys. Lett.* **107**, 041903 (2015).

36. Ding, L.-P. *et al*. Crystal Structures, Stabilities, Electronic Properties, and Hardness of MoB_2 : First-Principles Calculations. *Inorg. Chem.* **55**, 7033–7040 (2016).

37. Niessen, A. K. & De Boer, F. R. The Enthalpy of Formation of Solid Borides, Carbides, Nitrides, Silicides and Phosphides of Transition and Noble Metals. *J. Less Common Met.* **82**, 75–80 (1981).

38. Morosin, B.; Aselage, T. L.; Feigelson, R. S. Crystal Structure Refinements of Rhombohedral Symmetry Materials Containing Boron-Rich Icosahedra. *MRS Proc.* **97**, 145 (1987).

39. Wright, W. V. J. & Bartels, F. T. C. Considerations of the Ternary System Carbon-Silicon-Germanium. In *Proceedings of the Conference on Silicon Carbide*; O'Connor, J. R., Smiltens, J., Eds.; Pergamon Press: New York (1960).

40. Duschanek, H. *et al.* Critical Assessment and Thermodynamic Calculation of the Binary System Boron-Tungsten (B-W). *J. Phase Equilibria* **16**, 150–161 (1995).

41. Brazhkin, V. V., Lyapin, A. G. & Hemley, R. J. Harder than Diamond: Dreams and Reality. *Philos. Mag. A Phys. Condens. Matter, Struct. Defects Mech. Prop.* **82**, 231–253 (2002).

42. Mohammadi, R.; Xie, M.; Lech, A. T.; Turner, C. L.; Kavner, A.; Tolbert, S. H.; Kaner, R. B. Toward Inexpensive Superhard Materials: Tungsten Tetraboride-Based Solid Solutions. *J. Am. Chem. Soc.* **134**, 20660–20668 (2012).

43. Crouch, I. G., Franks, G. V., Tallon, C., Thomas, S. & Naebe, M. Glasses and Ceramics. In *The Science of Armour Materials*; Elsevier (2017).

Chapter 3

Exploring the Hardness and High-Pressure Behavior of Osmium and Rhenium-Doped

Rhenium Diboride Solid Solutions

3.1 Introduction

Materials with superior hardness are desirable in the machining and manufacturing industries, where higher hardness affords higher wear resistance and longer lifetimes of cutting tools and abrasives.[1-3] Traditional superhard materials (Vickers hardness, $H_v \geq 40$ GPa), such as diamond and cubic boron nitride (c-BN), are both difficult and expensive to synthesize due to the required high pressure and high temperature conditions.[4-6] These shortcomings have motivated the search for alternative superhard materials that are readily synthesized and capable of cutting materials at lower costs.[7-10]

Transition metal borides are a class of materials that have attracted significant interest among materials researchers due to their remarkable magnetic, thermal, and mechanical properties.[11-13] More specifically, several transition metal boride systems exhibit exceptionally high hardness, making them an attractive alternative to traditional hard materials for industrial applications.[14] Rhenium diboride (ReB_2) is an example of an exceptionally hard transition metal boride system, with Vickers hardness reaching as high as 40.5 GPa under a low applied load (0.49 N).[15] Since the investigation of ReB_2, the scope of hard metal boride research has widened towards higher borides, such as tungsten tetraboride (WB_4)[16,17] and metal dodecaborides (MB_{12})[18], along with their complementary alloys and solid solutions.[19,20] Studies based on the metal boride systems demonstrate both atomistic or intrinsic routes to increasing hardness (e.g. solid solution formation) and composite or extrinsic routes to hardness enhancement (e.g. grain boundary strengthening and precipitation hardening) can lead to improved hard materials.[21-24]

The ReB$_2$ structure is one of three structurally related yet distinct diboride structure types: AlB$_2$, ReB$_2$, and RuB$_2$ (**FIG. 3.1**).[25,26] A vast majority of diborides (e.g., TiB$_2$ and ZrB$_2$) adopt the AlB$_2$-type structure (*P6/mmm*) of planar boron sheets that alternate with 12-coordinate metal layers. In the case of the ReB$_2$ and RuB$_2$ systems, the boron sheets corrugate in chair and boat conformations for ReB$_2$ (*P6$_3$/mmc*) and RuB$_2$ (*Pmmn*) structures, respectively. Among these three diboride structure types, only ReB$_2$ has been experimentally measured as superhard at low load. Theoretical investigation of the diboride structures show that only ReB$_2$ has the right electron count to show only bonding metal-boron (M-B) interactions with no antibonding M-B bonds.[27] Moreover, the same study indicates that the hypothetical chair OsB$_2$ configuration should be harder than the existing boat OsB$_2$ counterpart, emphasizing the significance of the boron configuration in determining hardness. These results accurately describe the hardness of the known phases, and identify specific chemical bonding environments that facilitate high hardness in metal borides.

Previous studies have examined the ReB$_2$ structure type in other diboride solid solutions (e.g., W$_{0.5}$Ru$_{0.5}$B$_2$ and W$_{0.5}$Os$_{0.5}$B$_2$).[28,29] With the exception of solid solutions of tungsten in ReB$_2$ (Re$_{1-x}$W$_x$B$_2$)[30] and a limited number of Re-M-B phase diagrams, no other ReB$_2$-based solid solutions with the ReB$_2$ structure have been extensively studied or reported for their mechanical properties. Given the high incompressibility of both osmium (Os) and ruthenium (Ru) and their close proximity to rhenium (Re) on the periodic table, the Re-Os-B and Re-Ru-B diboride systems merit further examination of their solubility and hardness.

In this study, we report the Vickers hardness of two ReB$_2$ solid solutions (Re$_{0.98}$Os$_{0.02}$B$_2$ and Re$_{0.9}$Ru$_{0.02}$B$_2$) and probe changes in bond length and strength within the solid solutions using high pressure diffraction. Although both Os and Ru exhibit limited solubility in the ReB$_2$ structure (< 5 at. % for both metals), our results indicate that substituting low concentrations of these metals for

51

Re in the ReB_2 lattice significantly increases both the hardness and resistance to deformation upon pressure.

3.2 Experimental Procedure

Samples were prepared using elemental powders of: rhenium (99.99%), ruthenium (99.9%), osmium (99.8%), and amorphous boron (99+%). All powders were purchased from Strem Chemicals, U.S.A. Solid solutions of rhenium diboride were weighed and mixed according to the nominal composition: $Re_{1-x}M_xB_{2.3}$, where x = 0, 0.02, and 0.05 and M = Ru or Os with the total M:B ratio maintained at 1:2.3. The extra boron was added to compensate for its loss during the synthesis and to ensure the complete formation of the compounds. The mixed powders were pressed into pellets under a 10 ton load using a hydraulic jack press (Carver). Each pellet (~1g) was arc-melted in an argon atmosphere (I ≥ 70 A; t = 1-2 min) until molten three times, flipping in between each melt.

The cooled ingots were then bisected, where one half was crushed into powder (-325 mesh) for powder X-ray diffraction (PXRD) analysis. The other half was mounted in epoxy using an epoxy/hardener set (Buehler, U.S.A.) before being polished on a semi-automated polishing station (Buehler, U.S.A.). Each sample was polished using the following abrasives: silicon carbide disks (120 – 600 grit size, Buehler, U.S.A.) and polishing cloths coated in polycrystalline diamond suspensions (15 – 0.25 μm, Buehler, U.S.A.). Once an optically flat surface was achieved, the polished samples were analyzed through scanning electron microscopy (SEM), energy-dispersive X-ray spectroscopy (EDS), and Vickers hardness testing.

PXRD patterns of the powder samples were collected on an X'Pert Pro powder X-ray diffraction system (PANalytical, Netherlands) using a $Cu_{K\alpha}$ X-ray beam (λ = 1.5418 Å) in the 5-100° 2θ range. The collected data were compared to reference patterns in the Joint Committee on

Powder Diffraction Standards (JCPDS) database, now known as the International Center for Diffraction Data (ICDD), for phase identification in each sample. Rietveld refinement was performed on GSAS-II in order to determine unit cell parameters.[31] The surface morphology and elemental composition of the polished samples were determined on an FEI Nova 230 high resolution scanning electron microscope (FEI Company, U.S.A.) with a backscattered electron detector (BSED) and an UltraDry EDS detector (Thermo Scientific, U.S.A.).

The Vickers hardness of each sample was measured using a multi-Vickers hardness tester (Leco, U.S.A.) with a pyramid diamond tip. Ten indentations per load were made on polished samples under applied force loads ranging from low to high: 0.49, 0.98, 1.96, 2.94, and 4.9 N. The indentation diagonal lengths were measured with a high-resolution Axiotech 100 HD optical microscope (Carl Zeiss Vision GmbH, Germany) under 500x magnification. Vickers hardness (H_v in GPa) was calculated and averaged at each load using Equation (3.1):

$$H_v = \frac{1854.4F}{d^2}$$
(3.1)

where F is the applied force in Newtons (N) and d is the average diagonal length for each indent in micrometers (μm).

Nonhydrostatic *in-situ* high pressure radial X-ray diffraction was performed in a diamond anvil cell at synchrotron beamline 12.2.2 of the Advanced Light Source (ALS, Lawrence Berkeley National Laboratory). Crushed powder of the samples ($Re_{0.98}Os_{0.02}B_2$ and $Re_{0.98}Ru_{0.02}B_2$) were loaded into a laser-drilled hole (~60 μm in diameter, ~130 μm in depth) in a ~400 μm diameter boron gasket made of amorphous boron and epoxy. A small piece of Pt foil (~25 μm diameter) was placed on top of the sample to serve as an internal pressure standard. A monochromatic X-ray beam (λ = 0.4959 Å, spot size = 20 μm × 20 μm) was passed through the sample, which was compressed between two diamond tips up to 60 GPa of pressure, and 2-dimensional (2-D)

diffraction data were collected using an MAR-345 image plate and FIT2D software. A cerium

dioxide (CeO_2) standard was used to calibrate the detector distance and orientation.

The angle-dispersive diffraction patterns were converted from elliptical to rectangular

coordinates using FIT2D. The integrated "cake" patterns, azimuthal angle (η) versus diffraction

angles (2θ), were then analyzed using Igor Pro (WaveMetrics, Inc.). Peak positions were manually

picked for four easily resolvable diffraction peaks (002, 100, 101, and 110). All peaks of the 1-

dimensional (1-D) diffraction patterns of X-ray intensity as a function of 2θ obtained at the magic

angle (φ=54.7°, effectively hydrostatic condition) were indexed to hexagonal phases with no

indication of first-order phase transition throughout the measured pressure range. The pressure for

each compression step was determined from the equation-of-state of Pt standard, using its d-

spacing at φ=54.7°.

The stress in the sample under uniaxial compression is described by Equation (3.2):

$$\sigma = \begin{bmatrix} \sigma_1 & 0 & 0 \\ 0 & \sigma_1 & 0 \\ 0 & 0 & \sigma_3 \end{bmatrix} = \begin{bmatrix} \sigma_p & 0 & 0 \\ 0 & \sigma_p & 0 \\ 0 & 0 & \sigma_p \end{bmatrix} + \begin{bmatrix} -t/3 & 0 & 0 \\ 0 & -t/3 & 0 \\ 0 & 0 & -2t/3 \end{bmatrix} \tag{3.2}$$

where σ_1 is the minimum stress along the radial direction, σ_3 is the maximum stress in the axial

direction, σ_P is the hydrostatic stress component, and t is the differential stress, which gives a

lower-bound estimate of yield strength.[32] The d-spacing is calculated by:

$$d_m(hkl) = d_p(hkl)[1 + (1 - 3\cos^2\varphi)Q(hkl)] \tag{3.3}$$

where d_m is the measured d-spacing, d_p is the d-spacing under the hydrostatic component of the

stress, φ is the angle between the diffraction normal and axial directions, and $Q(hkl)$ is the lattice

strain under the uniaxial stress condition.[33] The differential stress, t, is directly related to the

differential strain, $t/G(hkl)$, by:

$$t(hkl) = 6G(hkl)Q(hkl) \tag{3.4}$$

where $G(hkl)$ is the shear modulus of the specific lattice plane. Incompressibility was determined using the generalized Birch-Murnaghan equation-of-state (EOS), which can be written as:

$$P = \frac{3}{2} K_{0T} \left(\left(\frac{V_0}{V}\right)^{7/3} - \left(\frac{V_0}{V}\right)^{5/3} \right) \left(1 + \frac{3}{4}(K_{0T}' - 4)\left(\left(\frac{V_0}{V}\right)^{2/3} - 1 \right) \right) \quad (3.5)$$

where P is the pressure, K_{0T} is the bulk modulus at ambient pressure, V is the volume, V_0 is the undeformed unit cell volume, and K_{0T}' is the derivative of K_{0T} with respect to P.[34]

3.3 Results and discussion

Here, we investigate the effects of osmium and ruthenium substitution in ReB_2 ($Re_{1-x}Os_xB_2$ and $Re_{1-x}Ru_xB_2$) on Vickers hardness and deformation of the ReB_2 structure upon pressure. According to the Hume-Rothery rules, a thermodynamically favorable substitutional solid solution forms when the host and dopant atoms are: (1) < 15% different in atomic radius; (2) similar in crystal structure; (3) similar in oxidation state (valency); and (4) similar in electronegativity.[35–37] Although both Os (1.35 Å) and Ru (1.34 Å) are similar to Re (1.37 Å) in atomic radius, valence electron count, and electronegativity, they form solid solutions with ReB_2 only at low percentages, with solubility limits of less than 5 atomic percentage (at. %) for both metals.[38] The low solubility of Os and Ru in the hexagonal ReB_2 ($P6_3/mmc$) structure can be largely explained by the fact that both of these metals form metal diborides of the orthorhombic RuB_2-structure type ($Pmmn$).[26,39] When ReB_2 is substituted with >2 at. % Os or Ru, OsB_2 ($Pmmn$) and RuB_2 ($Pmmn$) appear as secondary phases, respectively (**FIG. S3.1**). In order to isolate intrinsic solid solution effects from the presence of any potential extrinsic effects (e.g., secondary phase precipitation hardening), we discuss the properties of only the two low concentration solid solutions, $Re_{0.98}Os_{0.02}B_2$ and $Re_{0.9}Ru_{0.02}B_2$, in further detail below.

Rietveld refinement of $Re_{0.98}Os_{0.02}B_2$ and $Re_{0.9}Ru_{0.02}B_2$ (hereon noted as "$ReOsB_2$" and "$ReRuB_2$", respectively) was performed through comparison with the ReB_2 structure using GSAS-

II software. **Table 3.1** compares the refined unit cell parameters of $ReOsB_2$ and $ReRuB_2$ with that of pure ReB_2 synthesized under the same conditions. While Os substitution shrinks the unit cell along the *c*-axis, it expands $ReOsB_2$ along the *a*-axis, resulting in the lowest *c/a* axial ratio between the three compositions and less volume compression than that observed with Ru substitution in the ReB_2 unit cell. In the $ReRuB_2$ system, both *a* and *c* lattice parameters decrease in comparison to unsubstituted ReB_2, indicating an overall unit cell compression and decrease in volume as a result of Ru substitution. These materials are know to slip along the layering direction,[40] and so the decreased *c*-axis spacing in the $ReOsB_2$ is noteworthy.

Subsequent Vickers micro-indentation hardness measurements were performed on both $ReOsB_2$ and $ReRuB_2$ to study the effects of Os and Ru on ReB_2 hardness. Hardness measurements of unsubstituted ReB_2, also synthesized in this study, are in agreement with literature values for ReB_2 and serve as a basis for comparison between the two solid solutions.[15,30] Measured values from low to high load (0.49 to 4.9 N) for the three compositions are given in tabular form and compared to literature values for OsB_2 and RuB_2 in **Table S3.1** and are plotted in **FIG. 3.2** . While both Os and Ru adopt the same orthorhombic diboride structure, studies have measured higher hardness for OsB_2 than RuB_2, suggesting that the increase in hardness for OsB_2 is due to increased bond strength for Os-B bonds compared to Ru-B bonds.[41–43] In the current study, a similar trend of higher hardness in the Os-based system is observed. The hardness increases from 40.3 ± 1.6 GPa for unsubstituted ReB_2 to 47.4 ± 1.5 GPa with 2 at. % Os addition under an applied load of 0.49 N, while the same amount of Ru addition (2 at. % Ru) results in a hardness of 43.0 ± 2.8 GPa (at 0.49 N).

SEM images and elemental maps of $ReOsB_2$ and $ReRuB_2$ indicate homogenous elemental distribution across the samples with no secondary phase formation (**FIG. S3.2**). It should be noted

that the two compositions exhibit no significant difference from one another in surface grain morphology. Therefore, any difference in hardness between the two compositions likely arise solely due to solid solution effects, with no extrinsic contributions from precipitation hardening or grain size reduction. Although Os and Ru are similar to one another in their atomic properties and their effects on ReB$_2$ morphology, our results suggest that the two metals differ in how they bond to other atoms in the ReB$_2$ lattice and enhance Vickers hardness.

In general, superhard materials show high resistance to volume change.[44,45] The bulk modulus (incompressibility) of a material reflects the resistance to volume change upon compression and correlates to valence electron count and structure. Radial X-ray diffraction was conducted under non-hydrostatic compression up to 56 GPa to study the deformation mechanisms of ReOsB$_2$ and ReRuB$_2$ upon pressure. **FIG. 3.3 (a)** shows representative "cake" patterns and the integrated 1-D diffraction patterns of ReRuB$_2$ recorded at the lowest and highest pressures (~2 and 56 GPa, respectively). The nearly straight diffraction lines of the "cake" patterns at low pressure (~2 GPa) are due to the hydrostatic stress state. However, at high pressure, sinusoidal variations of the diffraction lines occur due to nonhydrostatic stress, so that the diffraction lines deviate to higher angle (2θ) in the high stress direction ($\varphi=0°$) and to lower angle (2θ) in the low stress direction ($\varphi=90°$). The waviness of the diffraction lines indicates the lattice-supported strains, which will be further discussed in the next paragraph. In the 1-D diffraction patterns, a clear shift of the peaks to higher angles at higher pressure indicates a decrease in the lattice spacing with greater compression, and the peak broadening implies strain inhomogeneity. Similar representative diffraction patterns for ReOsB$_2$ can be found in **FIG. S3.3**.

The d-spacing data as a function of φ-angle from FIG. 3.3a and FIG. S3.3 can then be plotted as ($1-3\cos^2\varphi$) to generate a linear trend (**Equation 3.3** and **FIG. 3.3b,c**,), with the minimum d-

spacing in the high stress direction ($\varphi=0°$ and 180°), and the maximum d-spacing in the low stress direction ($\varphi=90°$ and 270°). The zero-intercept of the linear regression at $\varphi=54.7°$ (the magic angle) gives the d-spacing under hydrostatic condition, which we use to determine the hydrostatic lattice parameters and volume, as summarized in **Table S3.2 & FIG. S3.4a** and **FIG. 3.4a**. For all lattice planes, a steady decrease in d-spacings as a function of increasing pressure is observed (**FIG. 3.3d).** Moreover, we observe a continuous increase in the c/a ratio upon compression, as shown in **FIG. S3.4b**, indicating that no phase transitions occur in either solid solutions.[46] The general trend of increasing c/a ratio with increasing pressure has been observed previously across many members of this family of compounds.[47]

We then analyzed volume change upon pressure to determine the bulk modulus using the Birch-Murnaghan EOS (**Equation 3.5**). Interestingly, the best fit to the overall data shows very high bulk moduli for both solid solutions, with $K_{0T}=413.2\pm22.8$ ($K_{0T}'=1\pm0.7$) for ReOsB$_2$ and $K_0=447.5\pm14.8$ ($K_{0T}'=1.5\pm0.5$) for ReRuB$_2$ (**FIG 3.4a**). We note that based on the Birch-Murnaghan EOS, the bulk modulus (K_{0T}) is significantly affected by the pressure derivative of the bulk modulus (K_{0T}'), with lower a lower K_{0T} resulting as K_{0T}' increases. This interplay has been mapped out in **FIG. S3.5** to emphasize the potential for error in reported K_{0T} values. In comparison, the bulk modulus of ReB$_2$, obtained from various experiments and calculations, falls between $317-383$ GPa.[48] Both solid solutions present similarly high bulk moduli, indicating great incompressibility attributed to high valence electron concentration with Ru or Os substitution.

The differential strain (t/G) is obtained by taking the ratio of the slope of the linear fit to the zero-intercept in **FIG. 3.3 (b,c)**, according to **Equation 3.4**. The measured differential strain for each lattice plane increases linearly with pressure and then appears to level off, as shown in **FIG. 3.4 (b,c)**. This plateau implies the onset of plastic deformation where the lattice plane can no longer

sustain additional differential strain and the deformation is no longer reversible. The plane with the lowest plateau value, or lowest differential strain (t/G), supports the strain before the onset of plastic deformation, while planes with higher differential strain plateau values support more strain before plastic deformation ensues. For all materials studied here, the (002) plane, which is parallel to the boron layers, is prone to slip and therefore supports the least lattice deformation, while the (100), (101) and (110) planes, which cut through the metal-boron layers, exhibit higher differential strain (**FIG. 3.4 b,c**). Due to the puckered boron sheets in the ReB_2 structure, ReB_2 exhibits great resistance to dislocation slip than other MB_2 materials, but the (002) plain remains the primary slip system.

In the current study, we investigate the effects of metal substitution on enhancing resistance to dislocation by doping 2 at. % transition metals (Os and Ru) in ReB_2 solid solutions. Both $ReOsB_2$ and $ReRuB_2$ in the ReB_2 structure and show higher differential strain values than that of pure ReB_2. For example, the plateaued t/G values of all lattice planes in the $ReOsB_2$ system are higher than that of the strongest plane in ReB_2, the (110) plane, which is found to be approximately 0.03, or ~3%, at 50 GPa. The t(hkl)/G(hkl) plateau values for $ReOsB_2$ are in the range of 3.4% to 4.3%, while ReB_2 shows a much lower range from 1.5% to 2.8%. Unlike ReB_2, where the t(002)/G(002) plateaued value is lower than that of other ReB_2 lattice planes by almost 50%, the plateaued t(002)/G(002) value of $ReOsB_2$ (~0.034) is almost as high as t(110)/G(110), indicating that the (002) plane is significantly strengthened in $ReOsB_2$. In addition, the differential strain in $ReOsB_2$ does not plateau until higher pressure than those observed in ReB_2. The (100), (101) and (110) planes in $ReOsB_2$ do not plateau until 30 GPa, while the (002) plane does not reach its plateau value of t/G until 50 GPa (**FIG. 3.4 b,c).** Overall, $ReOsB_2$ shows both higher plateau values and higher plateau pressures for all lattice planes, indicating significantly improved mechanical

properties from doping a small percentage of Os in ReB_2, in good agreement with measured enhancement in Vicker's hardness. These effects like arise in part from the compressed *c*-axis distance in the material, which should facilitate metal-boron bonding between the layers.

In $ReRuB_2$, only the (002) plane is significantly enhanced. All other lattice planes exhibit similar trends in t/G to ReB_2. In the elastic region, the t(hkl)/G(hkl) values for all lattice planes in $ReRuB_2$ increase similarly as those for ReB_2 planes. Starting from the onset of plastic deformation for ReB_2 at ~20 GPa, t(002)/G(002) of $ReRuB_2$ begins to deviate from the trend of the differential strain of ReB_2, while t(101)/G(101) and t(110)/G(110) remain similar to those of ReB_2. Above 30 GPa, the differential strain of the (002) plane in $ReRuB_2$ yields a plateau value ~48% higher than that of ReB_2. Thus, while the differential strain data in $ReRuB_2$ is not as dramatically different from ReB_2 as $ReOsB_2$, the strength of the primary slip system is enhanced, likely resulting in the observed increase in Vicker's hardness.

It is noteworthy that solid solution effects are significant as even 2 at. % dopant, and can change strain anisotropy and enhance differential strain in the ReB_2 system. The addition of metal dopant atoms that differ from rhenium in atomic size and valence electron count leads to stronger dislocation barriers that enhance the solid solution's resistance to slip. High-pressure studies demonstrate that doping enhances the bond strength between the boron interlayers of ReB_2 and consequently improves Vickers hardness. More specifically, doping Os into ReB_2 enhances resistance to dislocation slip in all lattice planes, whereas doping Ru enhances only the weakest plane in the ReB_2 system. These results offer insight into the lattice specific strengthening mechanisms that lead to higher hardness with solid solution formation.

3.4 Conclusions

ReB$_2$-structured solid solutions (ReOsB$_2$ and ReRuB$_2$) were synthesized via arc melting and characterized for their mechanical properties. Vickers micro-indentation measurements demonstrate a greater increase (>17%) in hardness for ReOsB$_2$ than for ReRuB$_2$. To understand the lattice specific changes induced by metal doping in ReB$_2$, the high-pressure behavior of ReOsB$_2$ and ReRuB$_2$ were examined and compared to ReB$_2$ using synchrotron based X-ray diffraction under non-hydrostatic compression. The equations of states for these two solid solutions were determined from the hydrostatic volume data measured at the magic angle (φ=54.7°). Both ReOsB$_2$ (K$_{0T}$=413.2±22.8, K$_{0T}$'=1±0.7) and ReRuB$_2$ (K$_0$=447.5±14.8, K$_{0T}$'=1.5±0.5) exhibit higher bulk modulus than pure ReB$_2$, indicating enhanced incompressibility upon doping. Lastly, lattice-dependent strength anisotropy suggests that Os doping enhances resistance to slip in all lattice planes, while Ru doping only strengthens slip plane (002) in the ReB$_2$ structure.

Table 3.1. Unit Cell Data[a,b] for *P6₃/mmc* ReB$_2$, ReOsB$_2$, and ReRuB$_2$

Composition	a (Å)	c (Å)	c/a	volume (Å^3)
ReB$_2$	2.9008(1)	7.4781(2)	2.5779	54.496
Re$_{0.98}$Os$_{0.02}$B$_2$	2.9010(1)	7.4754(1)	2.5768	54.482
Re$_{0.98}$Ru$_{0.02}$B$_2$	2.9006(1)	7.4762(3)	2.5775	54.472

[a]Standard deviations are indicated in parentheses.

[b]Cell parameters were calculated on GSAS-II software through comparison with ReB$_2$ ICSD-243627 (a = 2.90047 Å; c = 7.47734 Å).
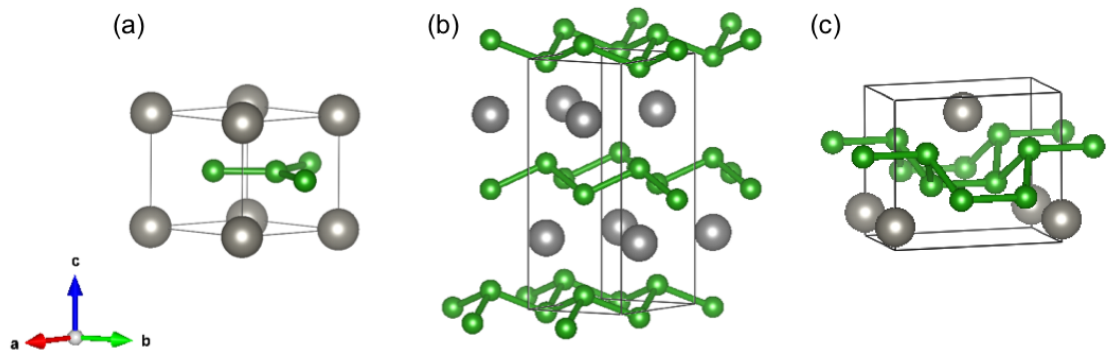
FIG. 3.1. Comparison of diboride structure types: (a) AlB_2, (b) ReB_2, and (c) RuB_2. The unit cell for each structure is indicated by the black box. The gray spheres represent metal atoms, while the green spheres represent boron atoms arranged in different sheet conformations.
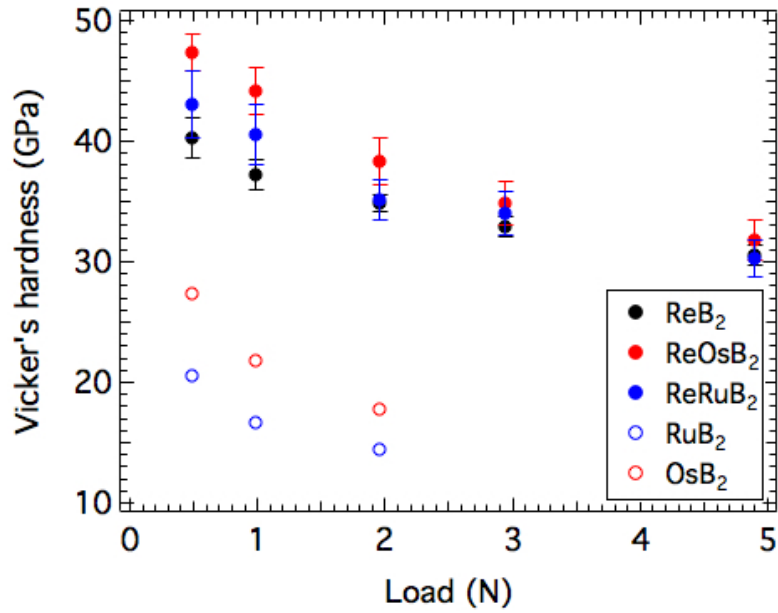
FIG. 3.2. Vickers Hardness for ReB_2, $Re_{0.98}Os_{0.02}B_2$, $Re_{098}Ru_{0.02}B_2$, OsB_2, and RuB_2 at various

loads. The two ReB_2 solid solutions are abbreviated as $ReOsB_2$ and $ReRuB_2$ for simplicity.
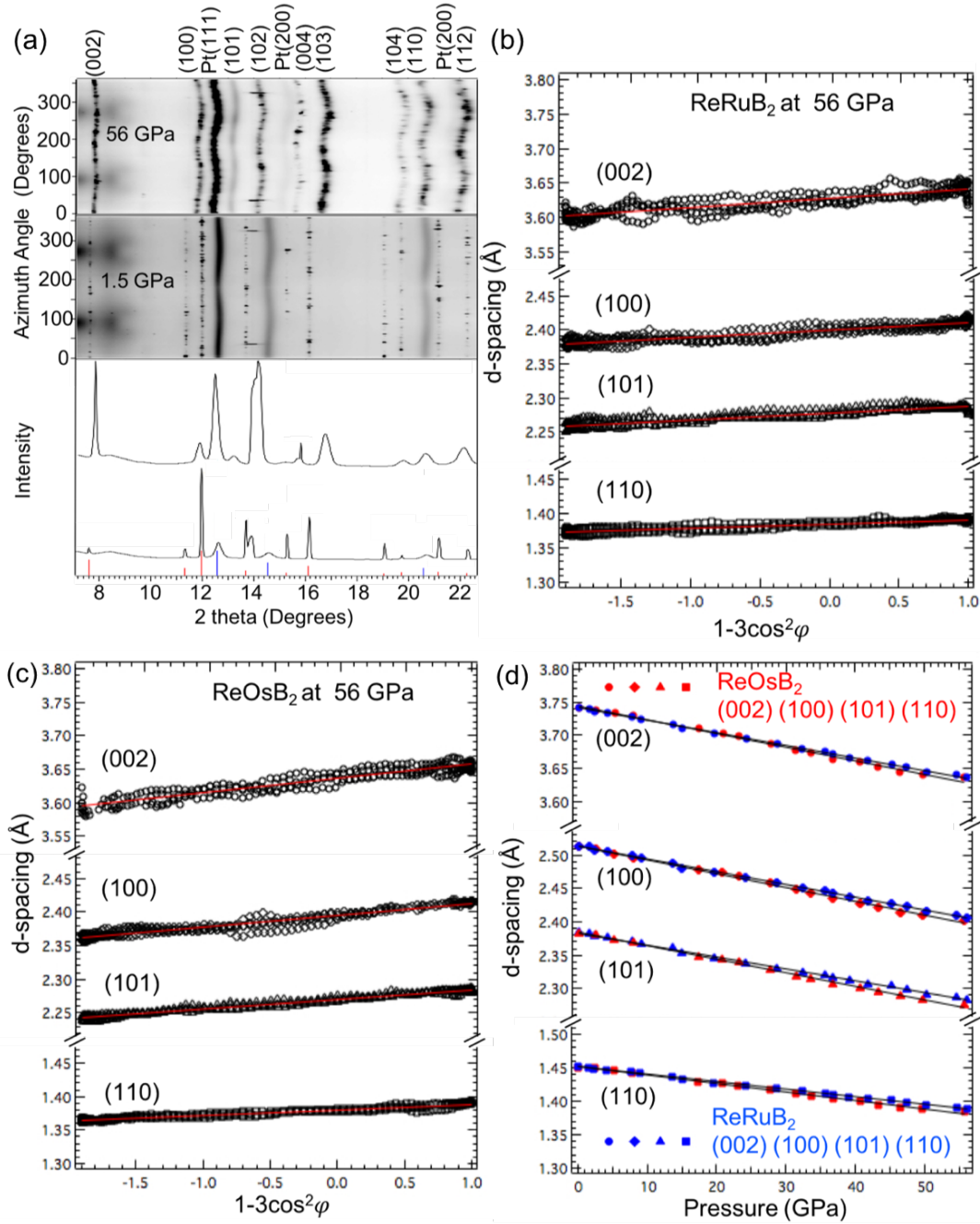
FIG. 3.3. (a) Representative synchrotron 1-D X-ray diffraction patterns and 2-D cake patterns for ReRuB$_2$. Linearized plot of d-spacings for ReRuB$_2$ (b) and ReOsB$_2$ (c) as a function of φ angle at the highest pressure. (d) Measured d-spacings under hydrostatic condition (φ=54.7°) for selected lattice planes of ReOsB$_2$ (red) and ReRuB$_2$ (blue) as a function of pressure. The solid lines are the best linear fit to the data.
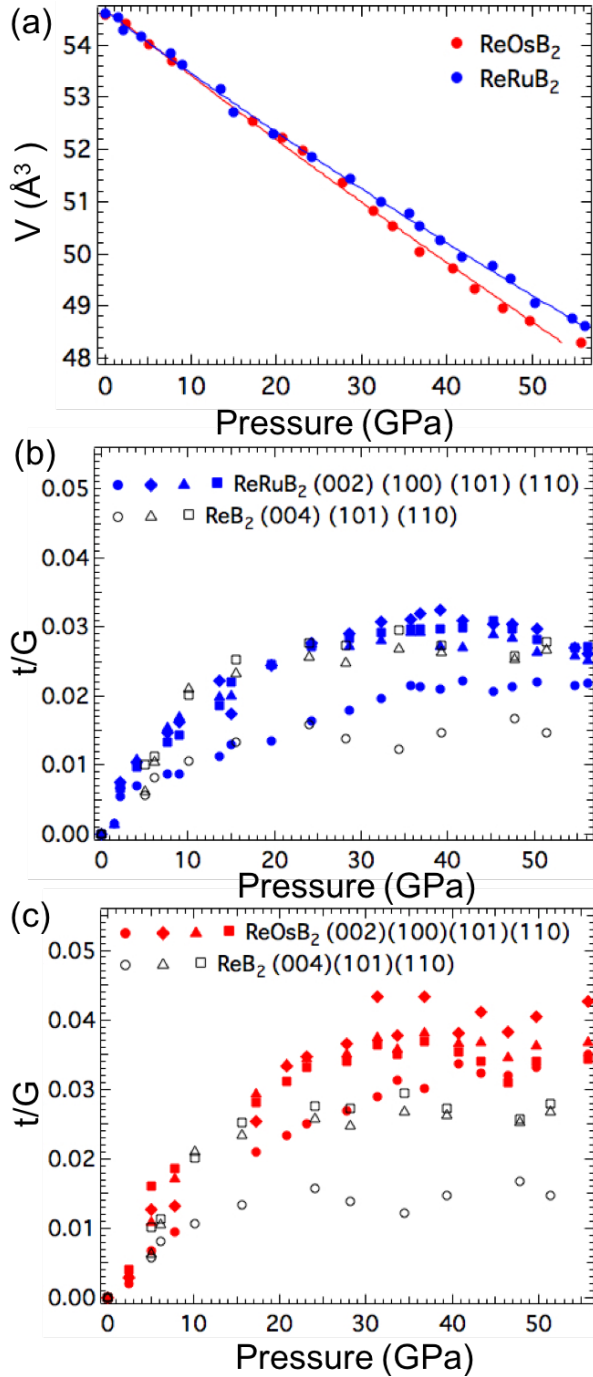
FIG. 3.4. Evolution of volume (a) of ReOsB₂ (red) and ReRuB₂ (blue) obtained at the magic angle

φ=54.7° upon pressure. The best fit lines to the Birch-Murnaghan equation-of-state on the volume

are indicated by solid lines. Linear relationship between c/a ratio and pressure indicates no phase

transition. Differential strain (t/G) as a function of pressure of ReRuB₂ (b) and ReOsB₂ (c),

comparing with ReB₂ (open symbols).

3.5 Supporting information

Table S3.1. Vickers Hardness Measurements for ReB_2, $ReOsB_2$, $ReRuB_2$, OsB_2, and RuB_2

Composition	H_v (GPa at 4.9 N)	H_v (GPa at 2.94 N)	H_v (GPa at 1.96 N)	H_v (GPa at 0.98 N)	H_v (GPa at 0.49 N)
ReB_2	30.6 ± 0.9	32.9 ± 0.9	34.8 ± 0.7	37.2 ± 1.3	40.3 ± 1.6
$Re_{0.98}Os_{0.02}B_2$	31.8 ± 1.7	34.9 ± 1.8	38.4 ± 1.9	44.1 ± 1.9	47.4 ± 1.5
$Re_{0.98}Ru_{0.02}B_2$	30.3 ± 1.5	34.0 ± 1.8	35.2 ± 1.6	40.5 ± 2.5	43.0 ± 2.8
OsB_2[a]	-	-	17.8	21.8	27.4
RuB_2[b]	-	-	14.4	16.7	20.6

[a]Ref. 41

[b]Ref. 39

Table S3.2. Compression data for $ReOsB_2$ and $ReRuB_2$.

ReOsB$_2$			ReRuB$_2$		
Pressure (GPa)	Constant a (Å)	Constant c (Å)	Pressure (GPa)	Constant a (Å)	Constant c (Å)
55.8(8)	2.769(3)	7.272(7)	56.2(9)	2.7779(4)	7.274(1)
49.7(6)	2.780(2)	7.281(6)	54.6(9)	2.7813(2)	7.279(1)
46.5(5)	2.785(2)	7.290(5)	50.3(10)	2.7878(4)	7.290(1)
43.3(4)	2.792(3)	7.303(7)	47.5(7)	2.7976(2)	7.305(1)
40.7(4)	2.801(2)	7.319(4)	45.3(6)	2.8030(2)	7.313(1)
36.8(5)	2.808(3)	7.326(7)	41.8(7)	2.8068(6)	7.321(2)
33.6(5)	2.818(2)	7.348(5)	39.2(6)	2.8135(8)	7.332(2)
31.4(9)	2.825(3)	7.355(8)	36.9(5)	2.8193(4)	7.341(1)
27.7(5)	2.836(2)	7.375(5)	35.7(4)	2.8240(3)	7.351(1)
23.1(4)	2.848(2)	7.397(4)	32.4(4)	2.8286(9)	7.358(2)
20.8(3)	2.853(2)	7.406(5)	28.7(4)	2.8380(9)	7.373(2)
17.3(4)	2.859(1)	7.421(3)	24.2(4)	2.8468(6)	7.389(2)
7.8(3)	2.883(1)	7.458(2)	19.6(4)	2.8555(8)	7.404(2)
5.1(3)	2.891(1)	7.466(3)	15.0(4)	2.8643(3)	7.419(1)
2.4(1)	2.899(1)	7.476(2)	13.6(2)	2.8740(4)	7.432(1)
0	2.903(1)	7.482(2)	9.0(2)	2.8832(5)	7.447(1)
			7.6(2)	2.8873(5)	7.458(1)
			4.1(2)	2.8937(3)	7.469(1)
			2.2(2)	2.8964(1)	7.473(3)
			1.5(3)	2.9013(6)	7.481(2)
			0	2.9027(6)	7.483(2)
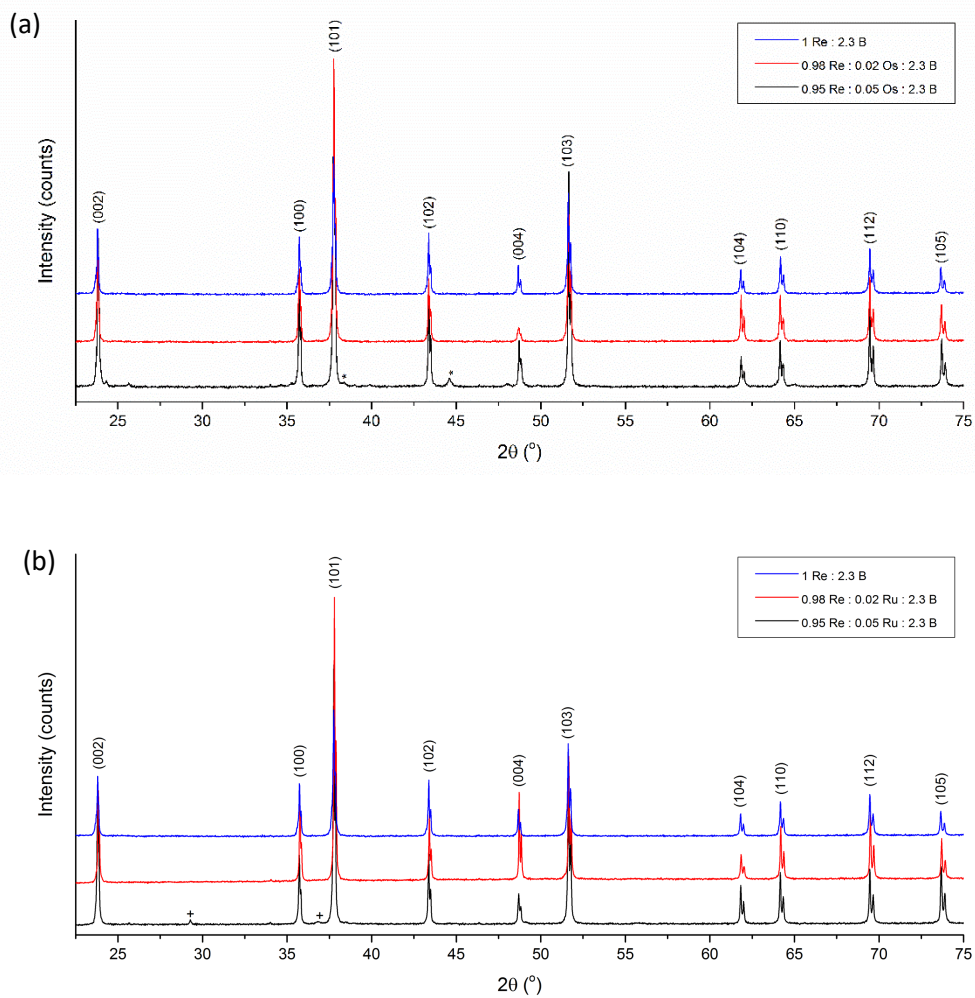
FIG. S3.1. PXRD data of: (a) $Re_{1-x}Os_xB_2$ and (b) $Re_{1-x}Ru_xB_2$, where x = 0 – 0.05 and the total metal to boron ratio (M : B) used was 1 : 2.3. Peaks were assigned using ReB_2 (JCPDS 00-011-0581). Additional phases, OsB_2 (JCPDS 01-089-2672) and RuB_2 (JCPDS 01-089-2671) are denoted as (*) and (+), respectively.
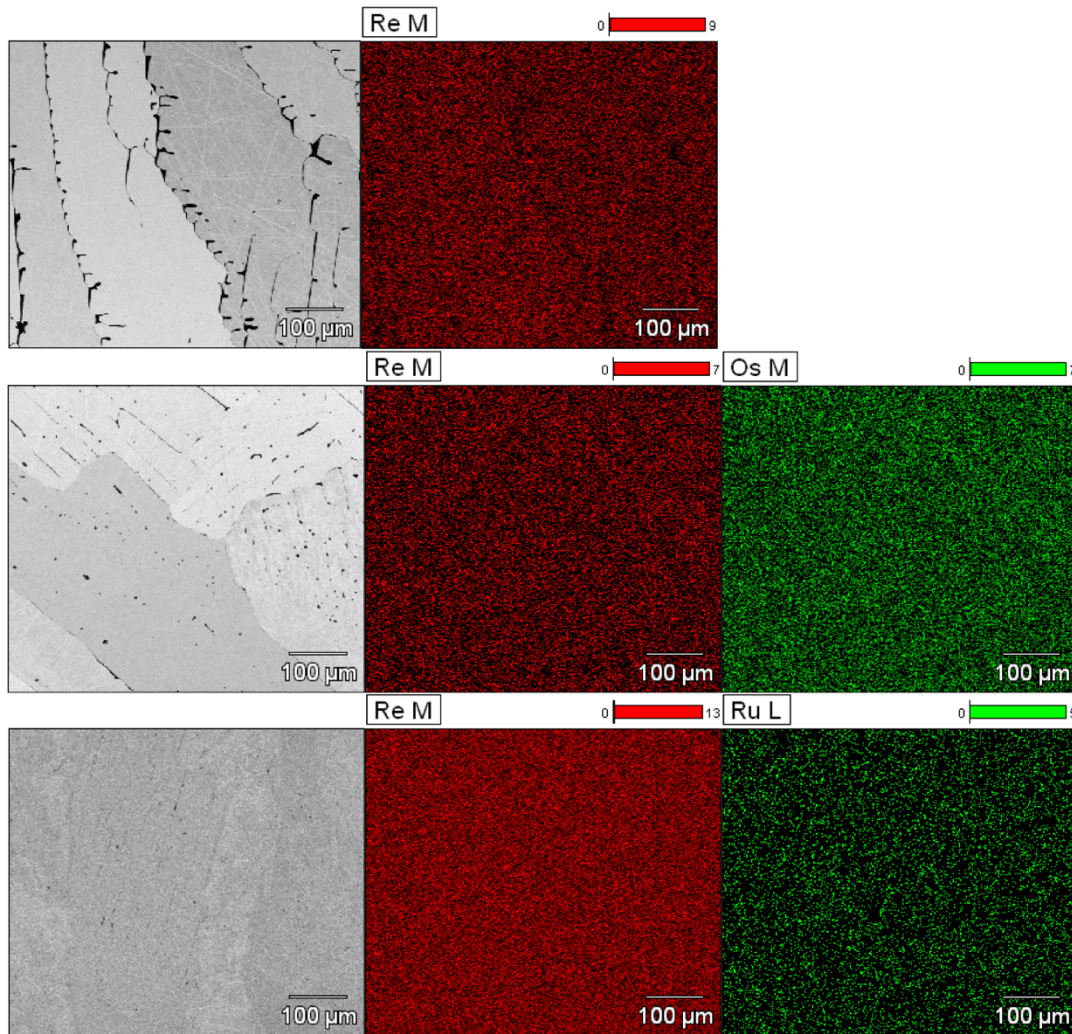
FIG. S3.2. SEM images and elemental maps for rhenium (M line), osmium (M line), and ruthenium (L line) for: (top) ReB_2, (middle) $ReOsB_2$, and (bottom) $ReRuB_2$. The image and corresponding elemental maps were taken at 1000x magnification at 15 keV with scale bars of 100 µm.
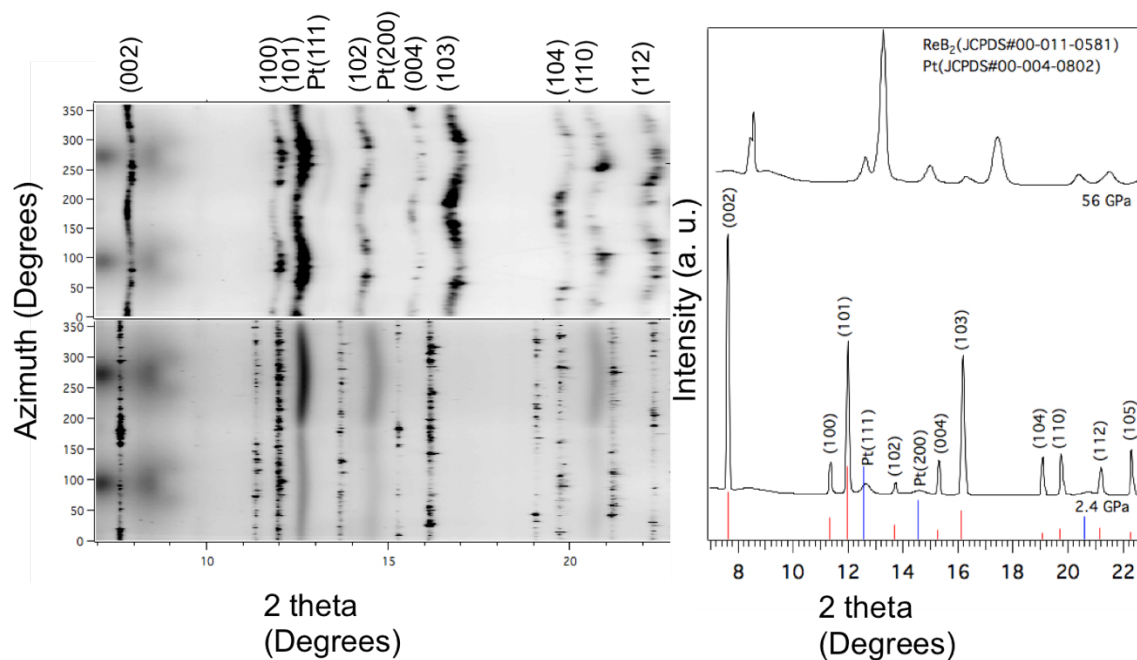
FIG. S3.3. Representative synchrotron 1-D X-ray diffraction patterns and 2-D cake patterns for ReOsB$_2$. Indices for relevant peaks are included on the image. All diffraction peaks shift to higher angle with increased pressure.
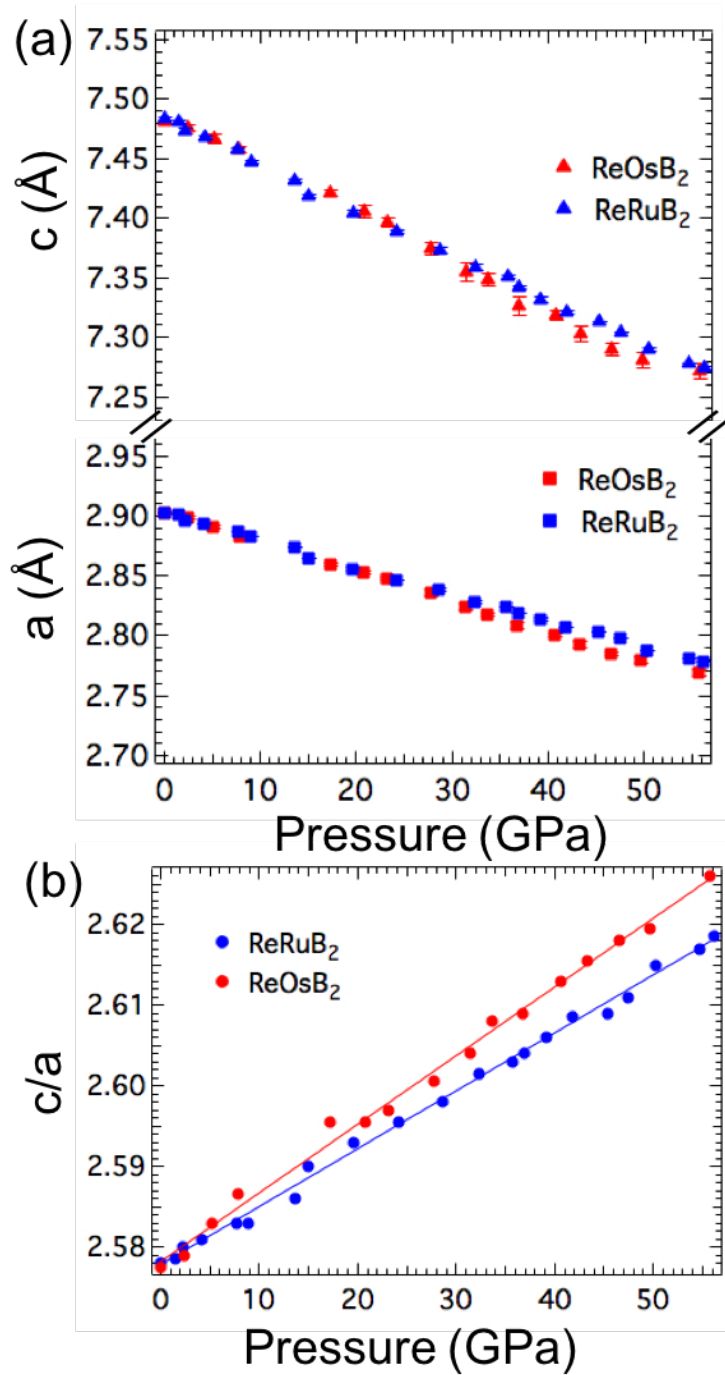
FIG. S3.4. Evolution of lattice constants (a) and c/a ratio (b) of $ReOsB_2$ (red) and $ReRuB_2$ (blue) obtained at the magic angle $\varphi=54.7°$ upon pressure. The error bar is shown on the graph.
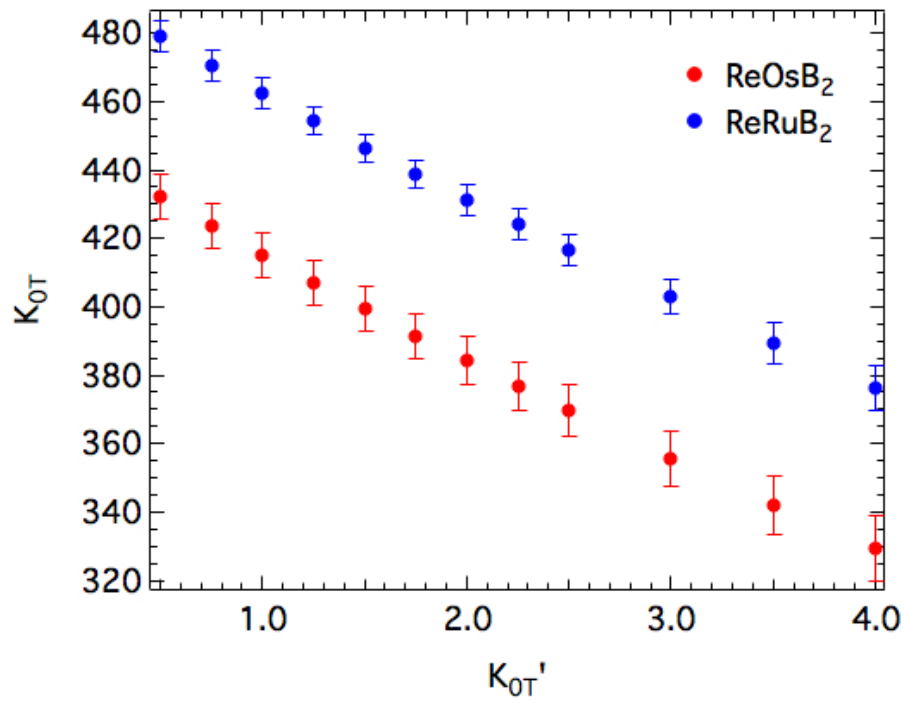
FIG. S3.5. Bulk modulus (K_{0T}) vs. pressure derivatives of bulk modulus (K_{0T}') for $ReOsB_2$ and $ReRuB_2$. K_{0T} and K_{0T}' are obtained from Birch-Murnaghan EOS by fitting unit cell volume vs. pressure, as shown in **FIG. 3.4 (a)**.

3.6 References

1. Ezugwu, E. O. Key improvements in the machining of difficult-to-cut aerospace superalloys. *Int. J. Mach. Tools Manuf.* **45**, 1353–1367 (2005).

2. Sung, C.-M. & Sung, M. Carbon nitride and other speculative superhard materials. *Mater. Chem. Phys.* **43**, 1–18 (1996).

3. Wentorf, R. H., DeVries, R. C. & Bundy, F. P. Sintered superhard materials. *Science.* **208**, 873–880 (1980).

4. Westraadt, J. E., Sigalas, I. & Neethling, J. H. Characterisation of thermally degraded polycrystalline diamond. *Int. J. Refract. Met. Hard Mater.* **48**, 286–292 (2015).

5. Komanduri, R. & Shaw, M. C. Wear of synthetic diamond when grinding ferrous metals. *Nature* **255**, 211–213 (1975).

6. Wentorf, R. H. Cubic Form of Boron Nitride. *J. Chem. Phys.* **26**, 956–956 (1957).

7. Kaner, R. B., Gilman, J. J. & Tolbert, S. H. Designing Superhard Materials. *Science.* **308**, 1268–1269 (2005).

8. Mansouri Tehrani, A. *et al.* Machine Learning Directed Search for Ultraincompressible, Superhard Materials. *J. Am. Chem. Soc.* **140**, 9844–9853 (2018).

9. Mansouri Tehrani, A., Ghadbeigi, L., Brgoch, J. & Sparks, T. D. Balancing Mechanical Properties and Sustainability in the Search for Superhard Materials. *Integr. Mater. Manuf. Innov.* **6**, 1–8 (2017).

10. Zhang, Z., Mansouri Tehrani, A., Oliynyk, A. O., Day, B. & Brgoch, J. Finding the Next Superhard Material through Ensemble Learning. *Adv. Mater.* 2005112 (2020).

11. Akopov, G., Yeung, M. T. & Kaner, R. B. Rediscovering the Crystal Chemistry of Borides. *Adv. Mater.* **29**, 1604506 (2017).

12. Scheifers, J. P., Zhang, Y. & Fokwa, B. P. T. T. Boron: Enabling Exciting Metal-Rich Structures and Magnetic Properties. *Acc. Chem. Res.* **50**, 2317–2325 (2017).

13. Fokwa, B. P. T. Borides: Solid-State Chemistry. *Encycl. Inorg. Bioinorg. Chem.* 1–14 (2014).

14. Akopov, G., Pangilinan, L. E., Mohammadi, R. & Kaner, R. B. Perspective: Superhard metal borides: A look forward. *APL Mater.* **6**, 070901 (2018).

15. Chung, H.-Y. *et al.* Synthesis of Ultra-Incompressible Superhard Rhenium Diboride at Ambient Pressure. *Science.* **316**, 436–439 (2007).

16. Mohammadi, R. *et al.* Tungsten tetraboride, an inexpensive superhard material. *Proc. Natl. Acad. Sci.* **108**, 10958–10962 (2011).

17. Lech, A. T., Turner, C. L., Mohammadi, R., Tolbert, S. H. & Kaner, R. B. Structure of superhard tungsten tetraboride: A missing link between MB 2 and MB 12 higher borides. *Proc. Natl. Acad. Sci.* **112**, 3223–3228 (2015).

18. Akopov, G. *et al.* Superhard Mixed Transition Metal Dodecaborides. *Chem. Mater.* **28**, 6605–6612 (2016).

19. Mohammadi, R. *et al.* Toward inexpensive superhard materials: Tungsten tetraboride-based solid solutions. *J. Am. Chem. Soc.* **134**, 20660–20668 (2012).

20. Akopov, G. *et al.* Synthesis and Characterization of Single-Phase Metal Dodecaboride Solid Solutions: Zr1-xYxB12 and Zr1-xUxB12. *J. Am. Chem. Soc.* **141**, 9047–9062 (2019).

21. Zhang, Z., Tehrani, A. M. & Brgoch, J. Tailoring the Mechanical Properties of Earth-Abundant Transition Metal Borides via Bonding Optimization. *J. Phys. Chem. C* **124**, 4430–4437 (2020).

22. Akopov, G., Yeung, M. T., Turner, C. L., Mohammadi, R. & Kaner, R. B. Extrinsic

Hardening of Superhard Tungsten Tetraboride Alloys with Group 4 Transition Metals. *J. Am. Chem. Soc.* **138**, 5714–5721 (2016).

23. Pangilinan, L. E. *et al.* Superhard Tungsten Diboride-Based Solid Solutions. *Inorg. Chem.* **57**, 15305–15313 (2018).

24. Mansouri Tehrani, A. *et al.* Atomic Substitution to Balance Hardness, Ductility, and Sustainability in Molybdenum Tungsten Borocarbide. *Chem. Mater.* **31**, 7696–7703 (2019).

25. Lundström, T. Preparation and Crystal Chemistry of some refractory Borides and Phosphides. *Ark. Kemi* **31**, 227–266 (1969).

26. Frotscher, M., Hölzel, M. & Albert, B. Crystal structures of the metal diborides ReB2, RuB2, and OsB2 from neutron powder diffraction. *Zeitschrift fur Anorg. und Allg. Chemie* **636**, 1783–1786 (2010).

27. Robinson, P. J. *et al.* Mystery of Three Borides: Differential Metal − Boron Bonding Governing Superhard Structures. *Chem. Mater.* **29**, 9892–9896 (2017).

28. Rogl, P. F., Nowotny, H. & Benesovsky, F. Ternary Complex Borides in the Systems: (Mo,W)--(Ru,Os)--B and W--Ir--B. *Monatsh. Chem.* **101**, 850–854 (1970).

29. Gu, Q., Krauss, G. & Steurer, W. Transition Metal Borides: Superhard versus Ultra-incompressible. *Adv. Mater.* **20**, 3620–3626 (2008).

30. Lech, A. T. *et al.* Superhard Rhenium/Tungsten Diboride Solid Solutions. *J. Am. Chem. Soc.* **138**, 14398–14408 (2016).

31. Toby, B. H. & Von Dreele, R. B. *GSAS-II* : the genesis of a modern open-source all purpose crystallography software package. *J. Appl. Crystallogr.* **46**, 544–549 (2013).

32. Ruoff, A. L. Stress anisotropy in opposed anvil high-pressure cells. *J. Appl. Phys.* **46**, 1389–1392 (1975).

33. Singh, A. K., Balasingh, C., Mao, H.-K., Hemley, R. J. & Shu, J. Analysis of lattice strains measured under nonhydrostatic pressure. *J. Appl. Phys.* **83**, 7567 (1998).

34. Birch, F. Finite strain isotherm and velocities for single-crystal and polycrystalline NaCl at high pressures and 300°K. *J. Geophys. Res.* **83**, 1257 (1978).

35. Hume-Rothery, W. *Atomic Theory for Students of Metallurgy*. (The Institute of Metals, 1969).

36. Hume-Rothery, W. & Powell, H. M. On the Theory of Super-Lattice Structures in Alloys. *Z. Krist.* **91**, 23 (1935).

37. Hume-Rothery, W., Smallman, R. W. & Haworth, C. W. *The Structure of Metals and Alloys*. (The Institute of Metals, 1969).

38. Egami, T. & Waseda Y. Atomic size effect on the formability of metallic glasses. *J. Non. Cryst. Solids* 113–134 (1984).

39. Aronsson, B. The Crystal Structure of RuB2, OsB2, and IrB1.35 and Some General Comments on the Crystal Chemistry of Borides in the Composition Range MeB-MeB3. *Acta Chem. Scand.* **17**, 2036–2050 (1963).

40. Wang, C. *et al.* WB2: Not a superhard material for strong polarization character of interlayer W-B bonding. *Phys. Chem. Chem. Phys.* **19**, 8919–8924 (2017).

41. Weinberger, M. B. *et al.* Incompressibility and Hardness of Solid Solution Transition Metal Diborides: Os $_{1-x}$ Ru $_x$ B $_2$. *Chem. Mater.* **21**, 1915–1921 (2009).

42. Kanoun, M. B., Hermet, P. & Goumri-Said, S. Structure, Elastic Stiffness, and Hardness of Os $_{1-x}$ Ru $_x$ B $_2$ Solid Solution Transition-Metal Diborides. *J. Phys. Chem. C* **116**, 11746–11751 (2012).

43. Chung, H.-Y., Yang, J.-M., Tolbert, S. H. & Kaner, R. B. Anisotropic mechanical

properties of ultra-incompressible, hard osmium diboride. *J. Mater. Res.* **23**, 1797–1801 (2008).

44. Yeung, M. T., Mohammadi, R. & Kaner, R. B. Ultraincompressible, Superhard Materials. *Annu. Rev. Mater. Res.* **46**, 465–485 (2016).

45. Haines, J., Léger, J. & Bocquillon, G. Synthesis and Design of Superhard Materials. *Annu. Rev. Mater. Res.* **31**, 1–23 (2001).

46. Xie, M. *et al.* Lattice stress states of superhard tungsten tetraboride from radial x-ray diffraction under nonhydrostatic compression. *Phys. Rev. B* **90**, 104104 (2014).

47. Xie, M. *et al.* Exploring the high-pressure behavior of superhard tungsten tetraboride. *Phys. Rev. B - Condens. Matter Mater. Phys.* **85**, (2012).

48. Xie, M. *et al.* Exploring the high-pressure behavior of superhard tungsten tetraboride. **85**, (2012).

Chapter 4

Hardening in Tungsten Tetraboride with the Addition of Carbon and Zirconium: Intrinsic vs Extrinsic Effects

4.1 Introduction

Transition metal borides possess a large variety of crystal structures,[1] which results in the ability to tune many useful materials characteristics, including their electronic, magnetic, optical, thermal, and mechanical properties.[1–7] The most commonly used mechanical property is hardness, and, as a consequence, superhard materials (possessing a Vickers hardness of greater than 40 GPa) and ultra-incompressible materials (possessing a bulk modulus greater than 300 GPa) are increasingly more popular subjects of research.[8–11]

Diamond, the hardest naturally occurring material, is expensive and cannot be readily used in processing of iron-containing alloys due to the formation of iron carbide. Cubic boron nitride, the second hardest material, requires high-pressure and high temperature to synthesize its hard polymorph. Boron carbide, the third hardest material, has a similar disadvantage as diamond in the cutting of iron, as well an expensive manufacturing process. Transition metal borides are thus interesting alternatives as more cost effective and easily synthesizable superhard materials.

In the last decade, the field of metal borides has seen a host of phases, their alloys and solid solutions: ReB_2 (the first reported superhard metal boride),[8,9] $W_{1-x}Ta_xB$ (having an enhanced bulk modulus compared to WB),[11,12] tungsten tetraboride (providing a cost-effective alternative to ReB_2),[13–18] metal dodecaborides (MB_{12})[19–22] (possessing a true 3D network of boron atoms) and ternary metal borides (featuring complex atomic arrangements).[23] The hardness of these metal borides can be enhanced through both intrinsic and extrinsic hardening effects. Intrinsic hardness

generally involves solid-solution formation and novel chemical bonding effects, while extrinsic hardness is governed by surface grain hardening (Hall-Petch), patterning, and nano-size effects.[24]

WB$_4$ is an incongruently melting phase traditionally synthesized with excess boron (W : B $\approx$ 1 : 12), as this suppresses the formation of the softer tungsten diboride (WB$_2$, *P6$_3$/mmc*). However, the formation of WB$_4$ through the use of excess boron is accompanied by crystalline β-rhombohedral boron ($R\bar{3}m$).[10,14,25] Due to the presence of the two phases (WB$_4$ and β-rhombohedral boron), it is possible to control the size and shape of the grains and as a result influence bulk mechanical properties through extrinsic effects.[14,17] Alternatively, by substituting some of the tungsten atoms with tantalum it is possible to stabilize the WB$_4$ structure at near-stoichiometric amounts of boron, with a nominal composition of (W$_{0.67}$Ta$_{0.33}$) : 4.5B.[18]

Tungsten tetraboride (WB$_4$, *P6$_3$/mmc*) has a unique structure among borides that contains partially filled metal and boron sites as well as voids (**FIG. 4.1**). This defect structure enables WB$_4$ to host both substitutional and interstitial dopants in voids and partial occupancy sites.[13–15,17] The addition of dopants leads to an enhancement of hardness. The hardening appears to be intrinsic in the case of Ta, Mo, Ti and Hf,[13–15] and some combination of intrinsic and extrinsic effects in the case of Zr, Y, Sc and some lanthanides.[14,17]

In the current study, we investigated the effects of adding carbon and silicon on the mechanical properties of WB$_4$. It was found that both elements have a similar effect on surface morphology to the addition of zirconium studied previously.[14] Tungsten tetraboride (WB$_4$) has a pseudo-cage structure that consists of alternating hexagonal layers of boron and tungsten with some partially occupied tungsten sites. Boron trimers sitting at those unoccupied sites combine with the boron layers to form "hourglass" structures; when the boron trimers above and below the boron layer correlate, they form distorted cuboctahedral cages. Therefore, WB$_4$ is able to accommodate

dopants by either substitutional or interstitial doping into the partially filled metal and boron sites or into the voids. The defect structure allows the hardness of WB_4 to be tuned by doping with other transition metals, such as tantalum (Ta), manganese (Mn), and chromium (Cr).[16] However, little is known about the dopant positions in the WB_4 cage structure. Our goal here is to use a combination of high-pressure studies and computational chemistry to understand the mechanisms for enhanced hardness upon doping WB_4 with boron-like light elements (C and Si) as well as with transition metals (Zr) and whether the enhancement is intrinsic or extrinsic (or some combination of both) in nature.

4.2 Experimental Procedure

Metal boride samples were synthesized by arc-melting stoichiometric amounts of metal and boron. The prepared phases were partly crushed into powder and analyzed by laboratory powder X-ray diffraction (PXRD) and partly encased into epoxy resin and polished. The polished samples were used for Vickers hardness micro-indentation, scanning electron microscopy (SEM) and energy-dispersive X-ray spectroscopy (EDS). Samples were further analyzed using nonhydrostatic *in situ* high-pressure radial X-ray diffraction performed in a diamond anvil cell at synchrotron beamline 12.2.2 of the Advanced Light Source (ALS, Lawrence Berkeley National Laboratory).

Alloys of WB_4 with carbon and silicon were prepared using: tungsten (99.95%, Strem Chemicals, U.S.A.), amorphous boron (99+%, Strem Chemicals, U.S.A.), tantalum (99.9%, Strem Chemicals, U.S.A.), silicon (99.9%, American Elements, U.S.A.), and tungsten carbide (99.5%, Strem Chemicals, U.S.A.). For these alloys the M : B ratio was kept at 1 : 4.5 and 1 : 11.6. For samples with a nominal composition of $(W_{1-x}C_x)$: 4.5B, $(W_{0.67}Ta_{0.33})$: C_x : 4.5B, x = 0.00, 0.02, 0.04, 0.06, 0.08, 0.10, 0.15, 0.20, 0.30, 0.40, 0.50; samples with a nominal composition of $(W_{1-z}C_z)$: 11.6B, $(W_{0.92}Zr_{0.08})$: C_z : 11.6B, z = 0.00, 0.02, 0.04, 0.05, 0.06, 0.08, 0.10, 0.20, 0.25, 0.30,

81

0.40, 0.50; and for samples with a nominal composition of $(W_{1-t}Si_t) : 4.5B$, $(W_{1-t}Si_t) : 11.6B$, t = 0.00, 0.02, 0.04, 0.06, 0.08, 0.10, 0.20, 0.25, 0.30, 0.40, 0.50.

Boron and metal powders in appropriate ratios were mixed in an agate mortar with a pestle to ensure homogeneity. A hydraulic press (Carver) was used to press the mixtures of powders into pellets with a diameter of 1.27 cm (0.5 in) under a 10-ton load. The pressed pellets were then placed into an arc-melting chamber on top of a water-cooled copper hearth. The chamber was then sealed and evacuated under vacuum for 20 minutes, followed by filling with argon; this was repeated at least 4 times. Before arc-melting the samples, getters made of titanium and zirconium were melted in order to "absorb" any trace oxygen and finally the samples were then arc melted using I > 70 amps (typically 145 amps) for 1 - 2 min. The samples were heated until molten, flipped and re-arced at least 2 times to ensure homogeneity.

The prepared samples were separated into two halves using a diamond saw (Ameritool Inc., U.S.A.), with one half crushed into sub-40 μm powder for powder X-ray diffraction analysis (PXRD) using a Plattner-style crusher, while the other half was encapsulated into epoxy for scanning electron microscopy (SEM)/energy dispersion spectroscopy (EDS) and Vickers hardness testing using an epoxy/hardener set (Allied High Tech Products Inc., U.S.A.).

In order to polish the samples to an optically flat surface, SiC papers (120 – 1200 grit sizes, Allied High Tech Products Inc., U.S.A.) and diamond films with particle sizes ranging from 30 to 1 micron (South Bay Technology Inc., U.S.A.) were used on a semi-automated polishing station (South Bay Technology Inc., U.S.A.).

To establish the purity and phase composition of the samples, PXRD and SEM techniques were used. PXRD was performed on a Bruker D8 Discover Powder X-ray Diffractometer (Bruker Corporation, Germany) using a Cu Kα X-ray beam (λ = 1.5418 Å) in the 5 - 100° 2θ range with a

step size of 0.0353º, scan speed of 0.1055º/sec and time per step of 0.3 sec. The Joint Committee on Powder Diffraction Standards (JCPDS) database was used to identify the phases present in the samples. *Maud* software was used to perform the unit cell refinements.[26–30] The phase purity was further verified on the polished samples using an UltraDry EDS detector (Thermo Scientific, U.S.A.) attached to a FEI Nova 230 high-resolution scanning electron microscope (FEI Company, U.S.A.).

Vickers hardness test

Hardness measurements were performed on polished samples using a load-cell type multi-Vickers hardness tester (Leco, U.S.A.) with a pyramidal diamond indenter tip. Under each applied load: 0.49, 0.98, 1.96, 2.94 and 4.9 N, 10 indents were made in randomly chosen spots on the sample surface. The lengths of the diagonals of the indents were measured using a high-resolution optical microscope, Zeiss Axiotech 100HD (Carl Zeiss Vision GmbH, Germany) with a 500x magnification. Vickers hardness values (H_v in GPa) were calculated using the following formula (Equation 1) and the values of all 10 indents per load were averaged:

$$H_v = \frac{1854.4F}{d^2} \qquad (4.1)$$

where *d* is the arithmetic average length of the diagonals of each indent in microns and F is the applied load in Newtons (N).

High-Pressure experiment

Nonhydrostatic *in situ* high-pressure radial X-ray diffraction was performed in a diamond anvil cell at synchrotron beamline 12.2.2 of the Advanced Light Source (ALS, Lawrence Berkeley National Laboratory). Crushed powder of the samples ($W_{0.96}C_{0.04}$: 11.6 B and $W_{0.92}Zr_{0.08}$: 11.6 B) was loaded into a laser-drilled hole (~60 μm in diameter, ~60 μm in depth) in a ~400 μm diameter boron gasket made of amorphous boron and epoxy. Both samples adopt the WB_4 structure,

therefore we abbreviate them as $W_{0.96}C_{0.04}B_4$ and $W_{0.92}Zr_{0.08}B_4$ when we mention these two samples in the text. A small piece of Pt foil (~20 μm diameter) was placed on top of the sample to serve as an internal pressure standard. A monochromatic X-ray beam ($\lambda = 0.4959$ Å, spot size = 30 μm × 30 μm) was passed through the sample, which was compressed between two diamond tips up to 60 GPa of pressure, and 2-D diffraction data were collected using an MAR-345 image plate and FIT2D software. A cerium dioxide (CeO_2) standard was used to calibrate the detector distance and orientation. The stress state of the sample under nonhydrostatic compression was analyzed by Igor Pro (WaveMetrics, Inc.) based on lattice strain theory.

In the radial geometry, the X-rays are directed onto the sample through the boron gasket and between the diamond culets. The collected 2-dimensional diffraction patterns contain information on the d-spacings in the low and high stress directions, and at all intermediate angles. The stress in the sample under uniaxial compression is described by Equation (4.2):

$$\sigma = \begin{bmatrix} \sigma_1 & 0 & 0 \\ 0 & \sigma_1 & 0 \\ 0 & 0 & \sigma_3 \end{bmatrix} = \begin{bmatrix} \sigma_p & 0 & 0 \\ 0 & \sigma_p & 0 \\ 0 & 0 & \sigma_p \end{bmatrix} + \begin{bmatrix} -t/3 & 0 & 0 \\ 0 & -t/3 & 0 \\ 0 & 0 & -2t/3 \end{bmatrix} \tag{4.2}$$

where σ_1 is the minimum stress along the radial direction, σ_3 is the maximum stress in the axial direction, σ_P is the hydrostatic stress component, and t is the differential stress, which gives a lower-bound estimate of yield strength. Each line in the two-dimensional cake pattern corresponds to a d-spacing and starts as a straight line at low pressure, indicating a hydrostatic stress state. At high pressure, the lines deviate to lower angles in the low stress direction (σ_1) and to higher angles in the high stress direction (σ_3) (**FIG. S4.7-9**). The integrated one-dimensional diffraction pattern at the magic angle shifts to higher angles with increasing pressure, as the lattice spacing decreases upon compression (**FIG. S4.7-9**). The d-spacing is calculated by:

$$d_m(hkl) = d_p(hkl)[1 + (1 - 3\cos^2\varphi)Q(hkl)] \tag{4.3}$$

where d_m is the measured d-spacing, d_p is the d-spacing under the hydrostatic component of the stress, φ is the angle between the diffraction normal and axial directions, and Q(hkl) is the lattice strain under the uniaxial stress condition. The differential stress, t, is directly related to the differential strain, $t(hkl)/G(hkl)$, by:

$$t(hkl) = 6G(hkl)Q(hkl) \tag{4.4}$$

where *G(hkl)* is the shear modulus of the specific lattice plane. The lattice parameters at each pressure calculated from the d-spacings at φ = 54.7° are summarized in **Table S4.1 & S4.2**. Incompressibility was then determined using the third order Birch-Murnaghan equation-of-state (EOS), which can be written as:

$$P = \tfrac{3}{2}K_0 \left(\left(\tfrac{V_0}{V} \right)^{7/3} - \left(\tfrac{V_0}{V} \right)^{5/3} \right) \left(1 + \tfrac{3}{4}(K_0' - 4)\left(\left(\tfrac{V_0}{V} \right)^{2/3} - 1 \right) \right) \tag{4.5}$$

where *P* is the pressure, K_0 is the bulk modulus, *V* is the volume, V_0 is the undeformed unit cell volume, and K_0' is the derivative of K_0 with respect to *P*.

Computation details

The sampling of the B_3-cluster distributions within a 3×2×1-supercell was performed with Site Disorder Occupancy.[31] All quantum mechanical calculations in this work were performed within the GGA PBE[32,33] functional, as implemented in VASP.[34–36] The kinetic energy cutoff of 750 eV together with the 2nd order Methfessel-Paxton approximation with $\sigma = 0.2$ were used. The first Brillouin zone was sampled using Gamma-centered Monkhorst-Pack Grids with k-point mesh density of $2\pi \times 0.025 \text{Å}^{-1}$. All structures were relaxed until the forces on each atom were ≤0.01 eV.

Quantum Theory of Atoms and Molecules (QTAIM) calculations were performed using Critic2 software.[37,38] A recursive subdivision of the Wigner-Seitz cell algorithm was used to locate critical points such that the Morse number of the resulting graph equals to zero. The integration of

atomic basins for Bader charge calculations the Yu and Trinkle (YT)[39] method was utilized. QTAIM is a method to analyze the topology of the electron density, $\rho(\vec{r})$. In QTAIM, each atom is associated with a nuclear critical point (NCP) — a local maximum in $\rho(\vec{r})$, and an atomic basin — a portion of space surrounded by a zero-flux surface ($\nabla\rho(\vec{r})$). A Bader charge of an atom is the difference between the number of valence electrons and integral of $\rho(\vec{r})$ within the atomic basin. $\rho(\vec{r})$ contains four types of critical points: nuclear critical points (NCP) have three negative eigenvalues of the Hessian (local maxima); bond critical points (BCP) have two negative and one positive eigenvalues of the Hessian (saddle points); ring critical point (RCP) have one positive and two negative eigenvalues of the Hessian (second order saddle points); cage critical points (CCP) have three positive eigenvalues of the Hessian (local minima). Paths that trace the direction of maximum gradient of $\rho(\vec{r})$ between two NCPs are called bond paths, defining a bond. A point of the intersection of a bond path and an atomic basin surface is a BCP, and it determines the properties of the bond. In this work, we used the electron density, $\rho(\vec{r})$, at a BCP (linked with the occupation of the bond, and the bond strength for metallic systems), and the Laplacian of electron density, $\nabla\rho(\vec{r})$, at a BCP (associated with the electron depletion: the more negative $\nabla\rho(\vec{r})$ — the more stable the bond is).

All *ab initio* quantum mechanical calculations were carried out using Density Functional Theory (DFT), and the GGA PBE[40,41] functional implemented in VASP.[42–45] The sampling of the B_3-cluster distributions within a 3×2×1-supercell was performed with Site Disorder Occupancy.[46] Analysis of electron density was performed using the Quantum Theory of Atoms and Molecules (QTAIM) methodology implemented in Critic2.[47,48] Specific parameters for these calculations can be found in the Supporting Information.

4.3 Results and discussion

FIG. 4.2 and FIG. S4.1 show the powder X-ray diffraction data for alloys with nominal compositions of $(W_{1-x}C_x) : 4.5B$, $(W_{1-x}Si_x) : 4.5B$, $(W_{1-x}C_x) : 11.6B$ and $(W_{1-x}Si_x) : 11.6B$. For the first two cases, the main WB_4 phase is accompanied by the lower boride phase (WB_2) at all concentrations of carbon and silicon addition. This can be explained by the fact that at $1 : 4.5$ metal to boron ratio, the liquid peritectically decomposes into WB_4 and WB_2 upon cooling.[18,25,49] This further suggests that neither carbon or silicon stabilize the WB_4 phase without the formation of the lower boride, which suggests that they do not substitute for the tungsten positions in the structure, being non-metals by nature. For the second two cases, the main WB_4 phase is present, while the lower boride is absent, due to the stoichiometry used. At $1 : 11.6$ metal to boron ratio, the liquid peritectically decomposes upon cooling to form WB_4 and crystalline β-rhombohedral boron.[49–51] For both carbon and silicon at high concentrations, the powder diffraction data indicates the formation of insoluble impurities, suggesting a clear solubility limit.[13–15,17,18] Secondary phases can be seen in all four cases at high addition fraction, and more prominently in the case of added carbon, where with increasing concentration, peaks corresponding to boron carbide can be seen. This is further corroborated by the changes in lattice parameters a and c for the alloys of WB_4 with carbon and silicon prepared at $1 : 4.5$ and $1 : 11.6$ metal to boron ratios (**FIG. 4.3**). The lattice parameters do not change dramatically with the increased concentration of carbon and silicon, from which we can deduce that neither of these elements substitute for tungsten in any significant amounts. They can, however, substitute for the partially occupied boron atoms in the WB_4 structure.[51]

To identify the preferred positions of Zr, C, and Si impurities, and corroborate the experimental observations, we used DFT calculations. First, we computationally identified the

most stable realization of $WB_{4.2}$ with respect to the B_3-trimer distribution. Next, that structure was used to compute the placement and formation enthalpies of the doped materials.

The $WB_{4.2}$ unit cell structure with unit *P6/mmc* symmetry was taken as the foundation for future calculations.[51] However, as it was shown by Lech *et al*. that the crystal structure of $WB_{4.2}$ is disordered with a ~2/3 chance of a B_3-trimer substituting a W-atom in the Wyckoff 2(b) position. Therefore, to account for fractional occupancy sites, a 3×2×1-supercell was chosen, since it is the smallest supercell that guarantees an integer number - four - of B_3-trimers in the structure. Within this supercell, a set of structures was sampled, including but not limited to, structures of high symmetry, high bulk modulus, low energy, etc. (**FIG. S4.10**). The structure shown in **FIG. 4.4** is the one on which we focus the discussion, as it is the structure with not only the highest symmetry, *Cmcm*, but also the highest calculated bulk modulus (B_0 = ~293 GPa). Furthermore, the *Cmcm* structure was found to be the most stable at finite temperature with inclusion of configurational entropy.[43]

To identify the preferred positions of C, Si, Zr in the structure shown in **FIG. 4.4**, the formation enthalpies, H_0, were calculated (**Table 4.1. Calculated** *thermodynamic* and mechanical properties of model structures. B0 is bulk modulus and H0 is formation enthalpy. By this metric, the preferential position for C is in the B_{hex}-layer in the [001] plane, in agreement with the hypothesis derived from the experiment. Si preferentially substitutes the entire B_3-trimer. Zr substitutes W in the Wyckoff 2(c) position (next to the edge of the B_3-trimer), and there is an only slightly less preferred structure where Zr substitutes for W in the Wyckoff 2(c) position (next to the vertex of the B_3-trimer). Indeed, *ab initio* DFT calculations support experimental findings regarding the location of impurities within $WB_{4.2}$.

The DFT calculations make it clear that C, Si, and Zr can substitute into the $WB_{4.2}$ lattice, resulting in intrinsic changes to the material hardness. These intrinsic effects do not preclude additional extrinsic effects based on changes in grain structure, and so in addition to diffraction and computation studies, we examined the grain morphology of a range of carbon-doped WB_4 alloy compound. **FIG. 4.5 and S4.2** show the SEM images of the surface of the alloys of WB_4 with carbon and silicon. In the case of 1 : 4.5 metal to boron ratio, both carbon and silicon result in reduced grain sizes at low concentration, primarily manifesting at 6–8 at.% addition for carbon and 8–10 at.% for silicon, attributed to the rapid cooling caused by their addition. At high amounts of carbon addition, areas corresponding to boron carbide formation can be seen (**FIG. S4.2**).

FIG. 4.6 and FIG. S4.5 are graphs showing Vickers hardness of the alloys. For $(W_{1-x}C_x) : 11.6B$ (**FIG. 4.6 top**), the hardness increase at 5 at.% C to 52.2 ± 3.0 GPa, compared to 41.2 ± 1 GPa for the pure phase, correlates the formation of a fine grained morphology, but may also have an intrinsic component (**FIG. 4.5 top**), while the second increase at 50 at.% C to 51.8 ± 6.1 GPa appears to be the result of extrinsic effects due to the formation of boron carbide.[52] For $(W_{1-x}Si_x) : 11.6B$ (**FIG. 4.6 bottom**), the hardness maxima at 2 at.% Si of 50.5 ± 2.5 GPa again correlates with a changes in grain morphology (**FIG. 4.5 bottom panel**), while at higher amounts of silicon addition, the hardness plateaus at ~42 GPa. In the case of $(W_{1-x}C_x) : 4.5B$ (**FIG. S4.5 top**), similar trends are observed, but with lower absolute hardness values, where the hardness first increase to 38.0 ± 3.8 GPa at 6 at.% C, compared to 30.8 ± 2.8 GPa[18] for the pure phase, which correlates with changes in morphology and grain size (**FIG. S4.2 top panel**), while the second hardness increase to 53.4 ± 6.6 GPa at 50 at.% C clearly results from the formation of the superhard boron carbide phase.[52] Similarly for $(W_{1-x}Si_x) : 4.5B$ (**FIG. S4.5 bottom**), the hardness maxima at 8–10 at.% Si of 38.7 ± 3.0 and 40.0 ± 2.2 GPa, respectively, correspond to the

changes in grain morphology (**FIG. S4.2 bottom panel**), while at higher mounts of silicon addition, the hardness plateaus at ~36 GPa.

To complement the pure addition of C, Si, and Zr to $WB_{4.2}$, a few more-complex combinations were produces. Specifically, C was added to two WB_4 alloy compositions of interest: the single-phase alloy with a WB_4 structure prepared with a stoichiometric amount of boron - $(W_{0.67}Ta_{0.33}) : 4.5B;$[18] and an alloy with 8 at.% zirconium addition $-(W_{0.92}Zr_{0.08}) : 11.6B$[14] – which resulted in the most nano-structured grain morphology. In the case of $(W_{0.67}Ta_{0.33}) : 4.5B$, when carbon was added, a secondary lower boride (WB_2) started to form at about 20 at.% C, which can be explained by the fact that as boron carbide forms, it lowers the amount of available boron (**FIG. S4.3**). The grain morphology does not change drastically, until ~40 at.% carbon addition (**FIG. S4.4**), at which point, the boron carbide phase starts to generate a lamellar decomposition pattern.[53] In agreement with these observations, indentation data shows only a gradual increase in hardness to a maximum of 44.6 ± 7.5 GPa at 100 at.% C addition, mainly due to the formation of boron carbide. No peaks in the hardness as a function of C addition are observed, as in the case of C or Si substituted into $WB_{4.2}$, suggesting only grain size and compositional effects are at play. By contrast, in the case of $(W_{0.92}Zr_{0.08}) : 11.6B$, the nano-morphology is lost immediately upon the addition of carbon, resulting in a hardness decreases from 55.9 ± 2.8 GPa[14] for the pure phase, to ~45 GPa with low carbon addition, and back up to 52.4 ± 6.9 GPa at 100 at.% C, again due to the formation of boron carbide (**FIG. S4.6**). For $(W_{0.92}Zr_{0.08}) : 11.6B$, lower borides ($WB_2$) do not form until ~80 at.% C addition because of the large amount of excels boron (**FIG. S4.3**). These results make two things clear: (1) small compositional changes can produce dramatic morphological changes which can, in turn, dramatically change the bulk hardness of the composite

through extrinsic effects, and (2) adding substituents like carbon can dramatically change the phase composition of a sample, resulting in a complex mixture of effects.

Because of the large number of possible combinations and the interplay of intrinsic and extrinsic effects, we chose three of the hardest phases for further study. The Vickers hardness values and grain morphologies of these three compositions – WB_4 with 8 at.% Zr, 5 at.% C and 2 at.% Si – can be seen in **FIG. 4.7**. The metal and the two non-metals have a similar effect on the grain morphology, resulting in small grains for all substituted compositions. The key question is: to what extent is the increased hardness discussed above a result only of this decreased grain size, given that all elements have the potential to substitute into the host lattice?

Although Vickers micro-indentation provides a direct measurement of a material's hardness, it often does not afford sufficient mechanical insight into intrinsic properties or explain the effect of dopant position on the material's bonding motif. Our goal here is to use high-pressure studies to understand the mechanisms for tunable hardness from doping WB_4 with boron-like light elements (C and Si) as well as transition metals (Zr). Previously we have demonstrated that the WB_4 structure is stabilized by boron with a ratio of 1 : 11.6 and a small amount of secondary transition metal. Samples with nominal compositions of $(W_{0.96}C_{0.04})$: 11.6B and $(W_{0.92}Zr_{0.08})$: 11.6B, especially, exhibit the best homogeneity in morphologies, essentially single-phase WB_4 with remarkable hardness. For simplicity, we now abbreviate them as $W_{0.96}C_{0.04}B_4$ and $W_{0.92}Zr_{0.08}B_4$ to clarify the structure of the sample and the percentage of the dopants, ignoring the excess boron.

By compressing a sample under non-hydrostatic stress in a diamond anvil cell, radial X-ray diffraction can be readily collected at incremental pressure steps (up to 45 GPa) *in situ* to provide information about the evolution of unit cell volume, and also lattice specific measurements of

differential strain and predominant slip planes in the material. In the radial geometry, diffraction data is collected at a range of angles with respect to the low and high stress directions, and the stress state of the sample under non-hydrostatic compression can be determined according to lattice strain theory, as explained in the **FIG. S4.7-9**. The integrated "cake" patterns, azimuthal angle (η) versus diffraction angles (2θ) were reported in both low and high pressure. At low pressure, the nearly straight diffraction lines of the "cake" patterns are due to the hydrostatic stress state. However, at high pressure, sinusoidal variations of the diffraction lines occur due to nonhydrostatic stress, so that the diffraction lines deviate to higher angle (2θ) in the high stress direction ($\varphi=0°$) and to lower angle (2θ) in the low stress direction ($\varphi=90°$). The waviness of the diffraction lines indicates the lattice-supported strains, which will be further discussed in **FIG. 4.9**. In the 1-D diffraction patterns, a clear shift of the peaks obtained at $\varphi = 54.7°$ (magic angle) to higher angles at higher pressure indicates a decrease in the lattice spacing with greater compression, and the peak broadening implies strain inhomogeneity. The pressure dependent d spacings of the (002), (101) and (110) planes at the quasi-hydrostatic condition ($\varphi = 54.7°$, magic angle), are plotted in **FIG. 4.8**. Examples of the full description of the d-spacings at all angles are shown in **FIG. 4.9**, which demonstrate the linear correlation between d spacings and *(1-3cos²φ)* for the selected planes of WB$_4$ solid solutions at the highest pressure. According to Equation (4.3), the slope of each line yields the corresponding *Q(hkl),* and the intercept gives the d spacing under quasi-hydrostatic compression. The differential strain *(t/G)*, which is the ratio of differential stress *(t)* to shear modulus *(G)*, can be directly determined from the *Q(hkl)* value, as shown in Equation (4.4). In **FIG. 4.10**, the *t(hkl)/G* ratio increases linearly with pressure at the beginning, then levels off, increases slowly, and eventually plateaus at 30 GPa. The plateau indicates the onset of plastic deformation, where the bonding starts to break and the lattice dislocations become irreversible.

The planes with higher $t(hkl)/G$ plateau value (differential strain) can be deformed to a greater extent before undergoing plastic deformation, and the plane with lowest $t(hkl)/G$ plateau slips with the lowest deformation.

As seen in **FIG 4.10**, $W_{0.96}C_{0.04}B_4$ supports higher differential strain, $t(hkl)/G$, than pure WB_4 in all three lattice planes of choice, indicating lattice planes in $W_{0.96}C_{0.04}B_4$ can undergo more deformation before bond breaking and are less prone to slip than in in pure WB_4. In other words, $W_{0.96}C_{0.04}B_4$ is intrinsically harder than WB_4. In $W_{0.96}C_{0.04}B_4$, the (002) plane, parallel to the layers of boron and tungsten atoms, supports the highest differential strain followed by the (110) plane and then the (101) plane. In pure WB_4, however, the (110) and (101) planes have almost identical differential strain. The fact that the (002) plane is greatly enhanced and the (110) plane is less prone to slip than the (101) plane in $W_{0.96}C_{0.04}B_4$ suggests that the bonding in the c axis is particularly strengthened by doping with carbon and confirms the computational results that carbon substitution into the boron sheets right above the boron trimer, enhancing the C_{layer}-$B_{cluster}$ bonds. This suggests that adding carbon maintains the cage structure and strengthens the cross-links between the interlayers, contributing to the enhanced intrinsic hardness of $W_{0.96}C_{0.04}B_4$.

When 8 at.% zirconium is doped into WB_4, the resultant solid solution is the hardest of any of the materials discussed here, but radial diffraction studies show decreased differential strain in the (002), (100) and (101) planes compared to pure WB_4 (**FIG. 4.10**). The decrease of the differential strain in all three lattice planes in $W_{0.92}Zr_{0.08}B_4$ suggests that the pseudo-cage structure of WB_4 is disrupted by doping with Zr. In addition, the weakening in the c axis is also observed from strain anisotropy that indicates that the (101) plane supports higher differential strain than the (110) plane in $W_{0.92}Zr_{0.08}B_4$. This is consistent with computational results that Zr weakens bonding between interlayers by doping into the tungsten vacancies. The fact that $W_{0.92}Zr_{0.08}B_4$ has the highest

Vickers hardness among pure WB_4 and its solid solutions but has lower plateau differential strain values for all lattice planes suggests that the enhanced Vickers hardness by doping Zr largely results from improved extrinsic hardness due to the very small grain sizes found in this material. Vicker's hardness is sensitive to both intrinsic and extrinsic effects, while the high-pressure experiments explore only a material's microscopic deformation, which contributes to the intrinsic hardness.

The Si doped sample posed an experimental challenge because the highly elongated grains produced strong texture in the radial diffraction experiment, which resulted in insufficient data for some lattice planes to analyze the differential strain. As shown in **FIG. S4.9**, the Si doped sample exhibits strong texture even at pressure as low as 1.7 GPa. The few lattice planes that could be analyzed are plotted in **FIG. S4.10**, along with the data for the undoped, C-doped, and Zr-doped material. While the quality of the data is fairly poor, it is clear that the differential strain is similar to or lower than that of the pure WB4, indicating that, similar to the Zr doped case, the increase in hardness likely arises primarily from extrinsic effects.

The rigid cage structure along the *c*-direction in the WB_4 system not only supports a high differential strain, but also resists great hydrostatic compression (high bulk modulus). From fitting the third order Birch-Murnaghan equation-of-state in terms of normalized pressure and Eulerian strain, the bulk moduli for $W_{0.92}Zr_{0.08}B_4$ and $W_{0.96}C_{0.04}B_4$ were determined to be 329 ± 4 GPa ($K_0' = 2$) and 390 ± 9 GPa ($K_0' = 0.6$), respectively (**FIG. 4.11**). The bulk modulus of $W_{0.92}Zr_{0.08}B_4$ is within the range of the bulk modulus of WB_4 (326–339 GPa), and other borides,[54,55] while $W_{0.96}C_{0.04}B_4$ has a higher bulk modulus than WB_4. This finding also implies that the cage structure is strengthened in $W_{0.96}C_{0.04}B_4$. An accurate bulk modulus for the Si-doped sample, unfortunately, could not be calculated.

To validate these conclusions, and clarify the effects of C, Zr, and Si dopants on the local rigid cage structure and its influence on the mechanical properties of the material, we return to theoretical calculations. First, bulk moduli, B_0, were calculated for structures with the impurities in several different positions (**Table 4.1.** Calculated thermodynamic and mechanical properties of model structures. B0 is bulk modulus and H0 is formation enthalpy. The DFT-based B_0 values are significantly underestimated compared to the experimental values. The discrepancy can be attributed to the use of a GGA functional (PBE), which suffer from delocalization error resulting in underestimated B_0 by ~9%.[56] poor treatment of Van der Waals interactions, and disregard for relativistic effects in W. We have attempted to recalculated the bulk modulus for pure and C-doped structures with HSE06[57,58] hybrid functionals, and observed an increase in B_0, but still not to the level of the experimental results. We therefore used PBE functional for its greater computational efficiency. The inclusion of Si decreases the computed B_0 of $WB_{4.2}$, while the inclusion of C leaves the computed B_0 practically unchanged. The introduction of Zr in either position marginally increases the computed B_0.

A better measure of mechanical hardness is the shear modulus. Accessing it computationally for such a large supercell is prohibitively expensive, and thus, we infer information about stability against shear through the QTAIM bonding analysis. Since chemical bonding is a local effect, and also the bonding is largely covalent in $WB_{4.2}$, we used a smaller 2×2×1-supercell with a single B_3-trimer, isolated from other trimers. The relevant QTAIM graphs are shown in **FIG. 4.12** and the BCPs discussed are shown in **FIG. 4.13**. QTAIM analyzes the topology of the quantum mechanical charge density, ρ. Specifically, ρ is rigorously partitioned into atomic basins, defined by zero-flux surfaces where the normal vector at any point on the surface is orthogonal to the gradient of the electron density ($\nabla \rho(\mathbf{r}) \cdot \mathbf{n}(\mathbf{r}) = 0$). There are 4 types of critical points (CPs) in ρ: nuclear, bond,

ring, and cage CPs, defined by the curvature of $\rho(\mathbf{r})$ at that point. A bond CP (BCP), of most interest to this study, is a maximum in 2 spatial directions and a minimum in 1 spatial direction, a ring CP (RCP) is a maximum in 1 spatial direction and a minimum in 2 spatial directions, and a cage CP (CCP) is a minimum in all 3 spatial directions. Topological quantities include curvature and $\nabla^2\rho(\mathbf{r})$. Characteristics of ρ at CPs are telling of materials properties, such as mechanical stability.

Due to the pseudo-layered nature of the material, the weakest slip system in $WB_{4.2}$ is the shear in the [001] plane. Therefore, the bonds connecting hexagonal layers either through B_3-trimers or through metal atoms are essential for strengthening $WB_{4.2}$ against shear. The strongest bond formed in the C-doped $WB_{4.2}$ is the 2-center bond between B in the B_3-trimer and C in the B_{hex}-layer (**FIG. 4.12**). It has the highest electron density and lowest Laplacian in the entire structure. The formation of the strong C_{layer}-$B_{cluster}$ bond is likely related to the resistance of the material to shear. The bonds formed with other impurities generally have lower electron density and higher positive Laplacians, associated with bond weakening. For instance, the substitution of W with Zr in Wychoff 2c leaves the interlayer bonding unchanged or weakens it, while substitution of Zr in the W-vacancy always depletes the electron density of interlayer bonds (**Table 4.2**). This result is consistent with the experimental observation that the plateau differential strain observed through high pressure radial diffraction is actually lower in $W_{0.92}Zr_{0.08}B_4$ than in WB_4.

An extreme example of bond weakening is Si, upon substituting itself for the entire B_3-cluster. The bonds it forms with the B-sheets are characterized by small $\rho(\vec{r})$ and near-zero $\nabla\rho(\vec{r})$). While the metal dopants generally slightly weaken $B_{cluster}$-B_{sheet} (lower in $\rho(\vec{r})$ and higher in $\nabla\rho(\vec{r})$), the Si impurity replaces those bonds with significantly weaker bonds. This may explains why the hardness is only slightly increased in Si-doped $WB_{4.2}$, despite a dramatic reduction in grain size,

and suggests that hardness enhancement in Si-doped $WB_{4.2}$, like that in Zr-doped $WB_{4.2}$, is dominantly extrinsic/grain size induced in nature.

4.4 Conclusions

Tungsten tetraborides have been extensively explored due to its unique rigid pseudo-cage structure that results in high hardness. The partially occupied tungsten sites and voids in the crystal structure also make WB_4 a particularly interesting for enhancing hardness by doping heteroatoms into the WB_4 lattice. Because of this, extensive work has been done to enhance the hardness of WB_4 by doping heteroatoms into the crystal lattice, modifying the overall composition of composite materials, and introducing/modifying grain boundaries. The challenge, exemplified in this work, is that very often, all of these processes occur simultaneously. As a result, it is difficult to develop a predictive understanding of the most effect ways to enhance hardness. In the current study, significant decreases in grain size were observed in all solid solutions, and, in parallel, the hardness was greatly enhanced. While the significant decrease of grain size in these solid solutions suggests extrinsic or grain-boundary based hardening effect, lattice specific strain analysis indicates that such a conclusion is not uniformly true in these materials. High-pressure studies, together with computational work, demonstrate significant change of bonding upon doping, in both the positive and negative direction. Specifically, doping carbon into WB_4 strengthens the bonding in the cage structure, resulting in better resistance to plastic deformation. In contrast, doping Zr and Si into WB_4 disrupts the cage structure, consequently leading to weaker intrinsic strength. For both Zr and Si, however, the reduced grain size and potential improved grain boundary strength compensates for the reduced bond strength, resulting in enhanced hardness, but a reduction in the plateau value of the differential strain. This work thus shows that through a combination of morphological studies, high-pressure diffraction experiments, and first-principles calculations, the

hardening effects in a highly complex, multiphase material like doped WB$_4$ can be thoroughly understood from both an intrinsic and extrinsic perspectives.
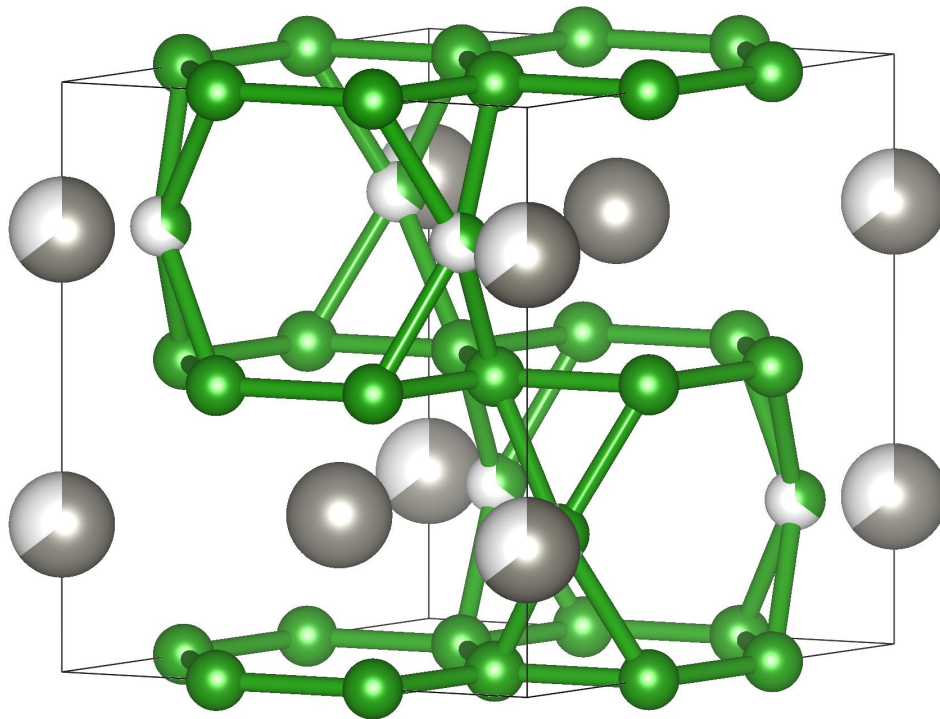
FIG. 4.1. Crystal structure of WB$_4$ with the *P6$_3$/mmc* space group (ICSD (Inorganic Crystal Structure Database) 291124).[51] Tungsten atoms are shown in gray, while boron atoms are in green; partially occupied positions are depicted by half-filled atoms.
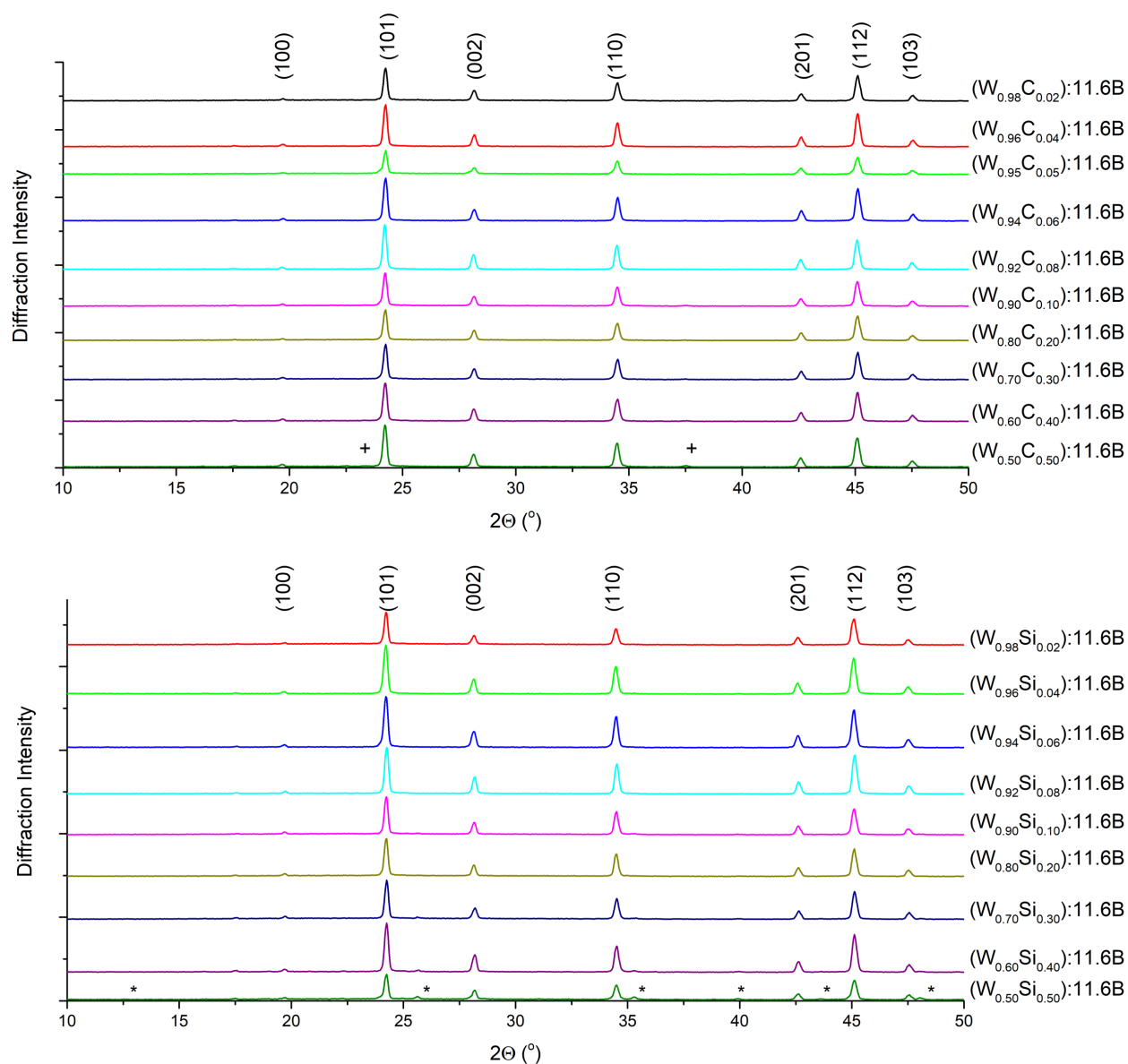
FIG. 4.2. Powder XRD patterns (10–50° 2Θ) of alloys of nominal composition **(top)** $(W_{1-x}C_x) : 11.6B$ and **(bottom)** $(W_{1-x}Si_x) : 11.6B$. WB_4 ($P6_3/mmc$, JCPDS 00-019-1373) is present at all concentrations of C and Si. Peaks corresponding to a boron carbide phase (denoted by (+), $R\bar{3}m$, JCPDS 00-035-0798) can be observed at heavy concentrations of carbon addition. Peaks corresponding to WB_2 (denoted by (*), $P6_3/mmc$, JCPDS 01-073-1244)) can be observed at heavy concentrations of silicon addition.
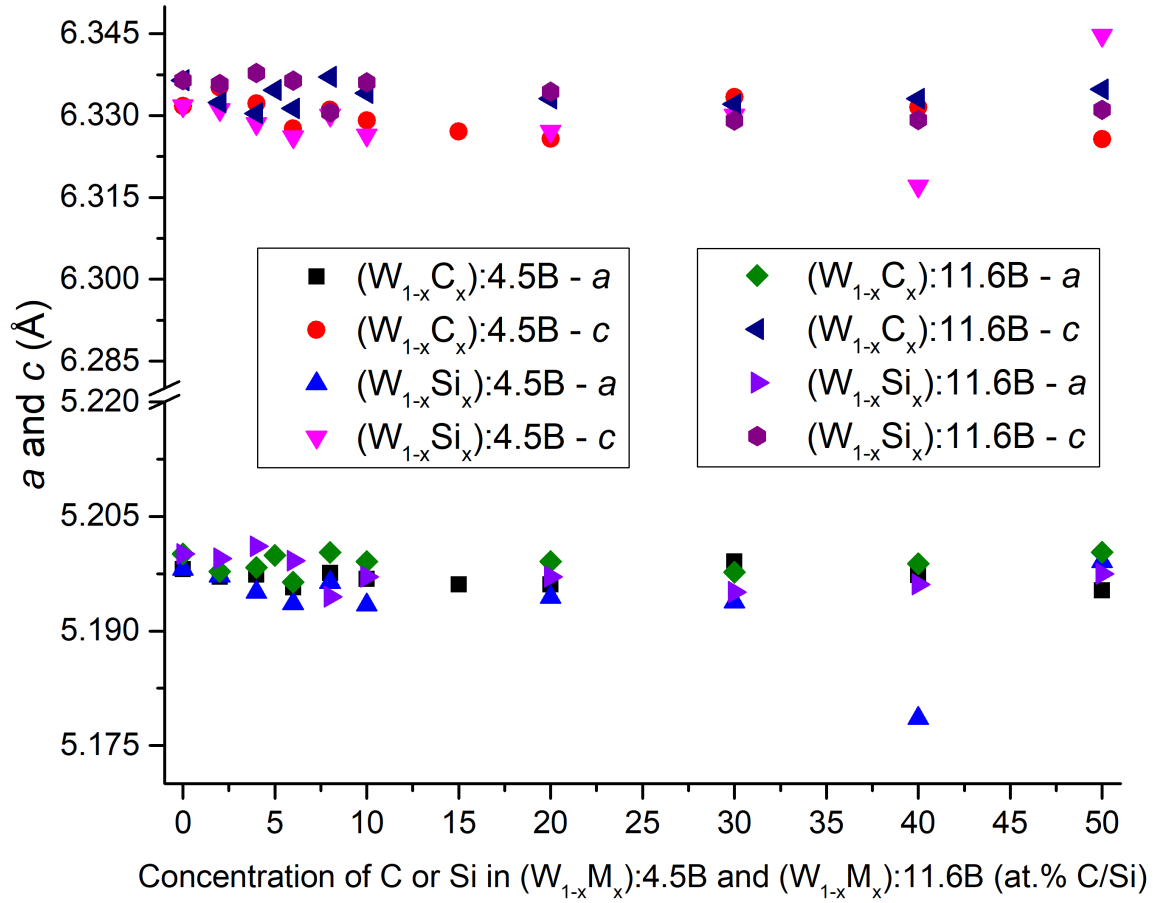
FIG. 4.3. Unit cell parameters *a* and *c* for alloys of WB₄ with C and Si, prepared at a nominal metal to boron composition of 1 to 4.5 and 1 to 11.6, calculated using *Maud*.[26–30] The literature value for the unit cell parameters of WB₄ are: *a* = 5.1998(15), *c* = 6.3299(19).[51]
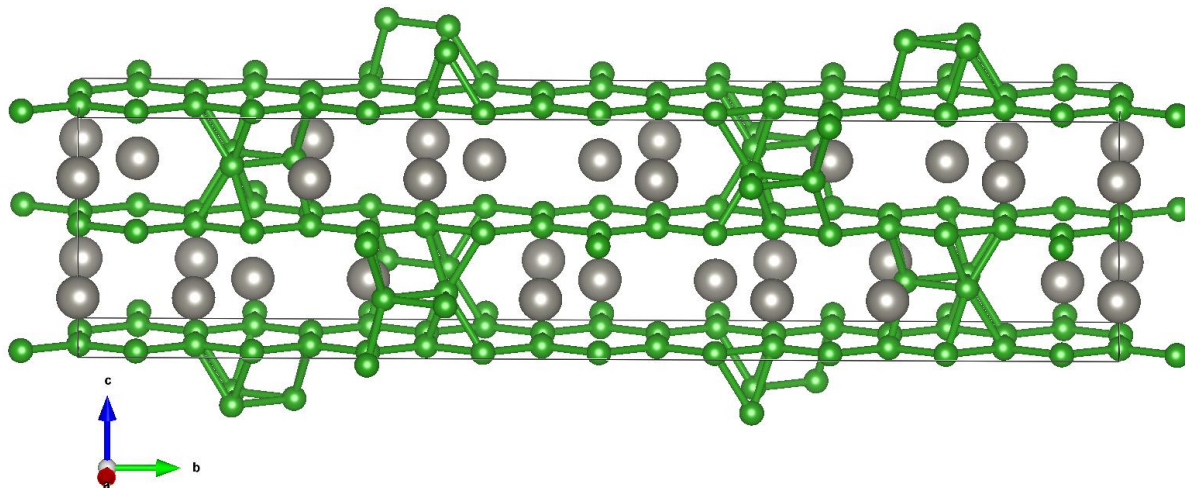
FIG. 4.4. Model *Cmcm* structure. A characteristic feature of this structure is alternating "rows" of B$_3$-trimers, "piercing" the material along the *a*-axis.
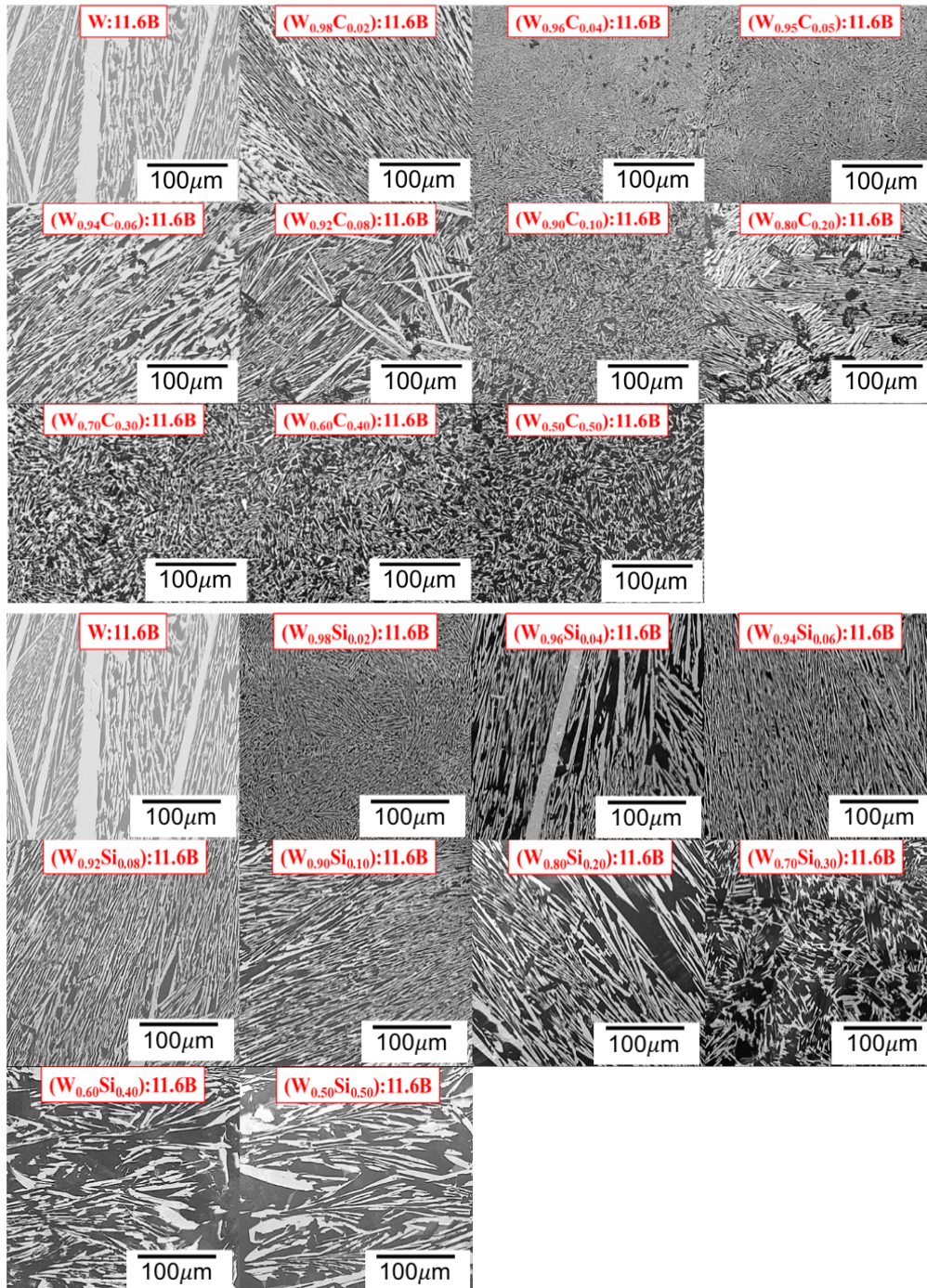
FIG. 4.5. SEM images for alloys of WB$_4$ with a nominal composition of **(top)** $(W_{1-x}C_x)$: 11.6B and **(bottom)** $(W_{1-x}Si_x)$: 11.6B showing a change in surface morphology associated with the effects of carbon and silicon and secondary phase formation. All SEM images were taken at 1000× magnification; the scale bars are 100 μm.
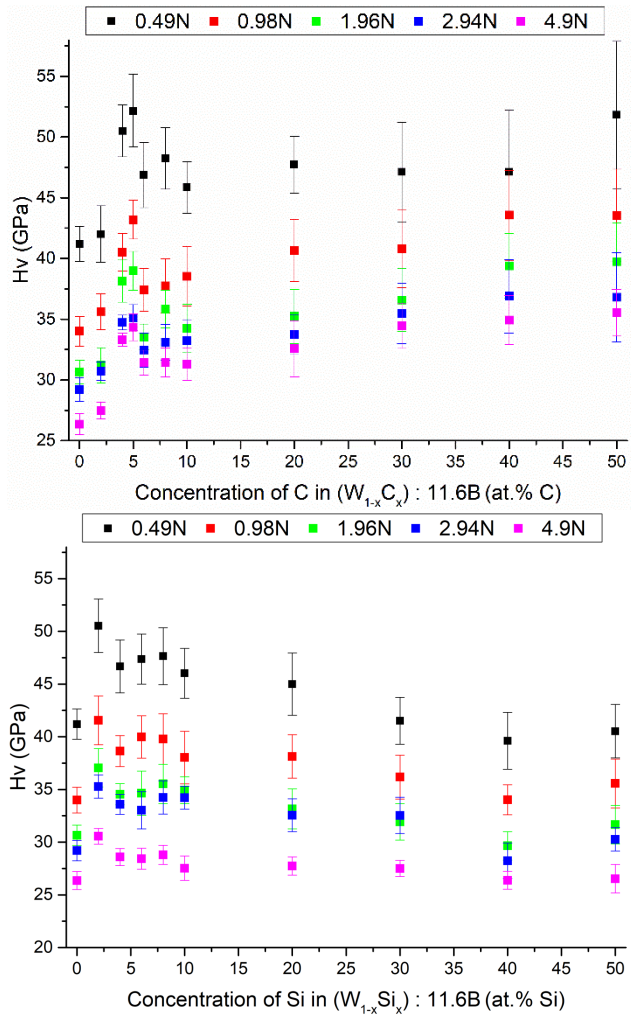
FIG. 4.6. Vickers micro-indentation hardness of alloys with a nominal composition of **(top)** $(W_{1-x}C_x) : 11.6B$ and **(bottom)** $(W_{1-x}Si_x) : 11.6B$ alloys at low (0.49 N) to high (4.9 N) loading.
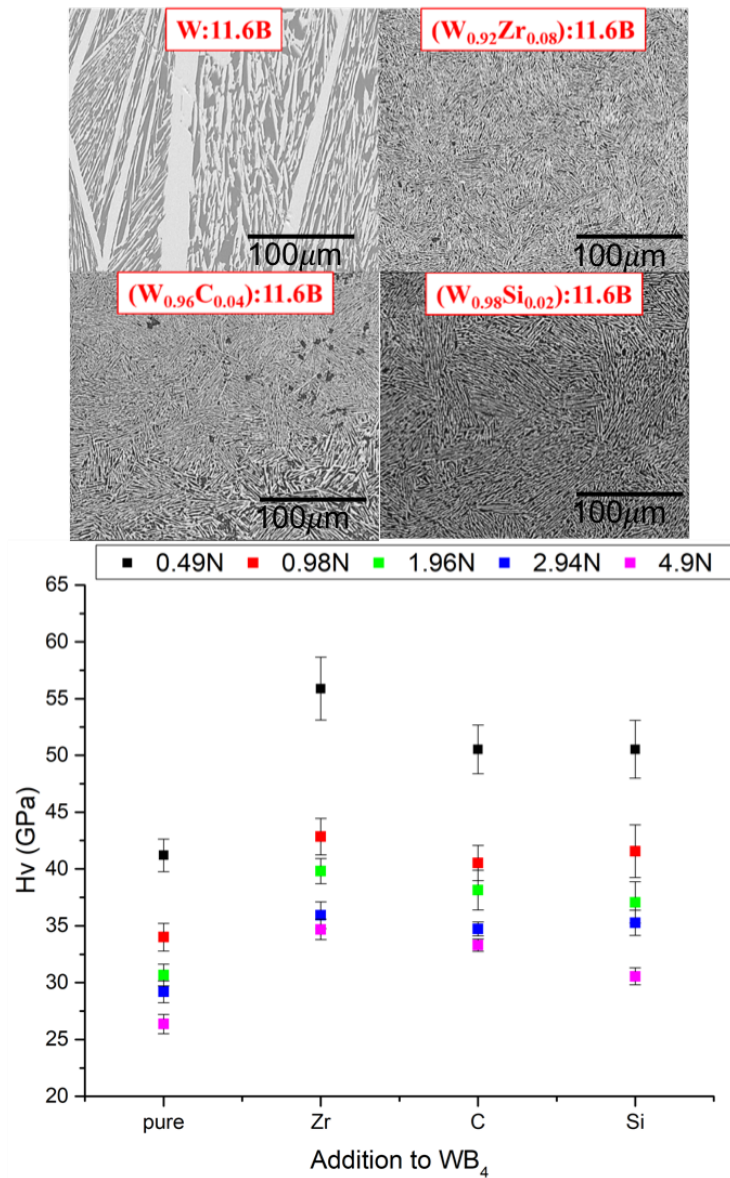
FIG. 4.7. Vickers micro-indentation hardness and SEM images of WB$_4$ alloys with a nominal composition of $(W_{1-x}M_x)$: 11.6B, where M = zirconium (x = 0.08), carbon (x = 0.04) and silicon (x = 0.02) at low (0.49 N) to high (4.9 N) loading. All SEM images were taken at 1000x magnification; the scale bars are 100 μm.
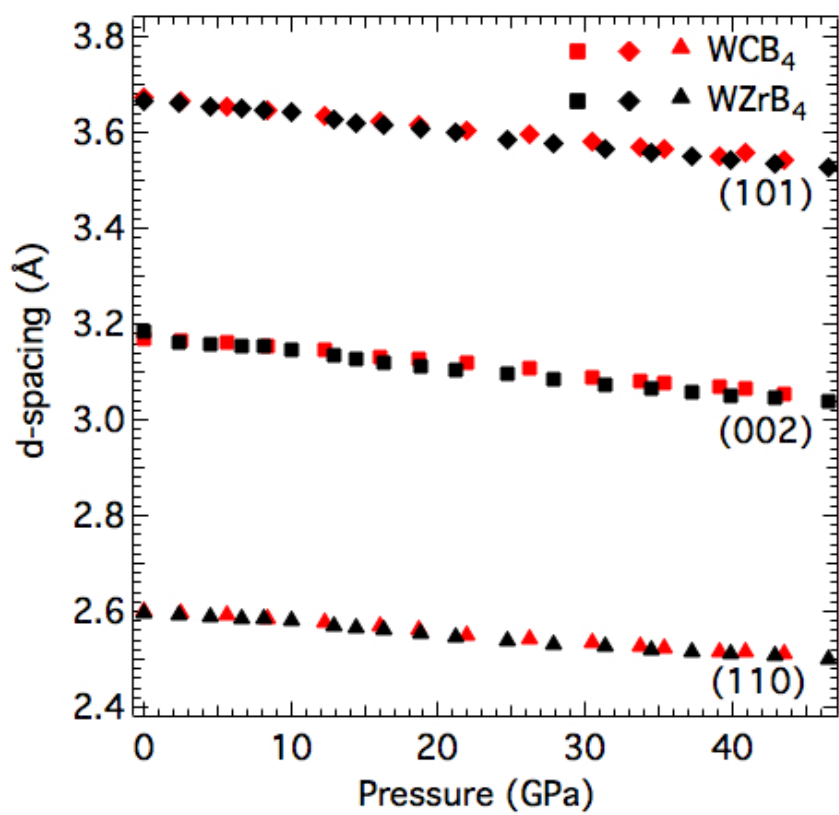
FIG. 4.8. Selected d spacings vs. pressure collected at $\varphi = 54.7°$ for $W_{0.96}C_{0.04}B_4$ and $W_{0.92}Zr_{0.08}B_4$.
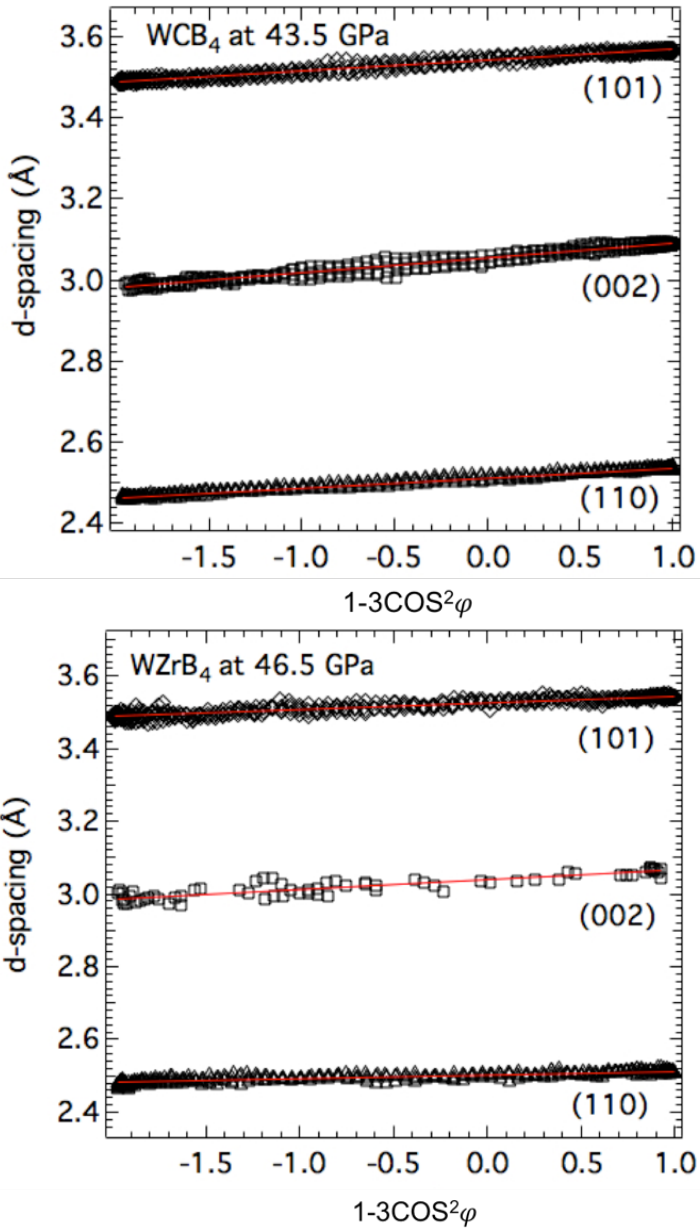
FIG. 4.9. Linearized plots of d spacings for $W_{0.96}C_{0.04}B_4$ (top) and $W_{0.92}Zr_{0.08}B_4$ (bottom) as a function of $(1\text{-}3cos^2\varphi)$ at the highest pressure. Solid lines are the best linear fit to the data.
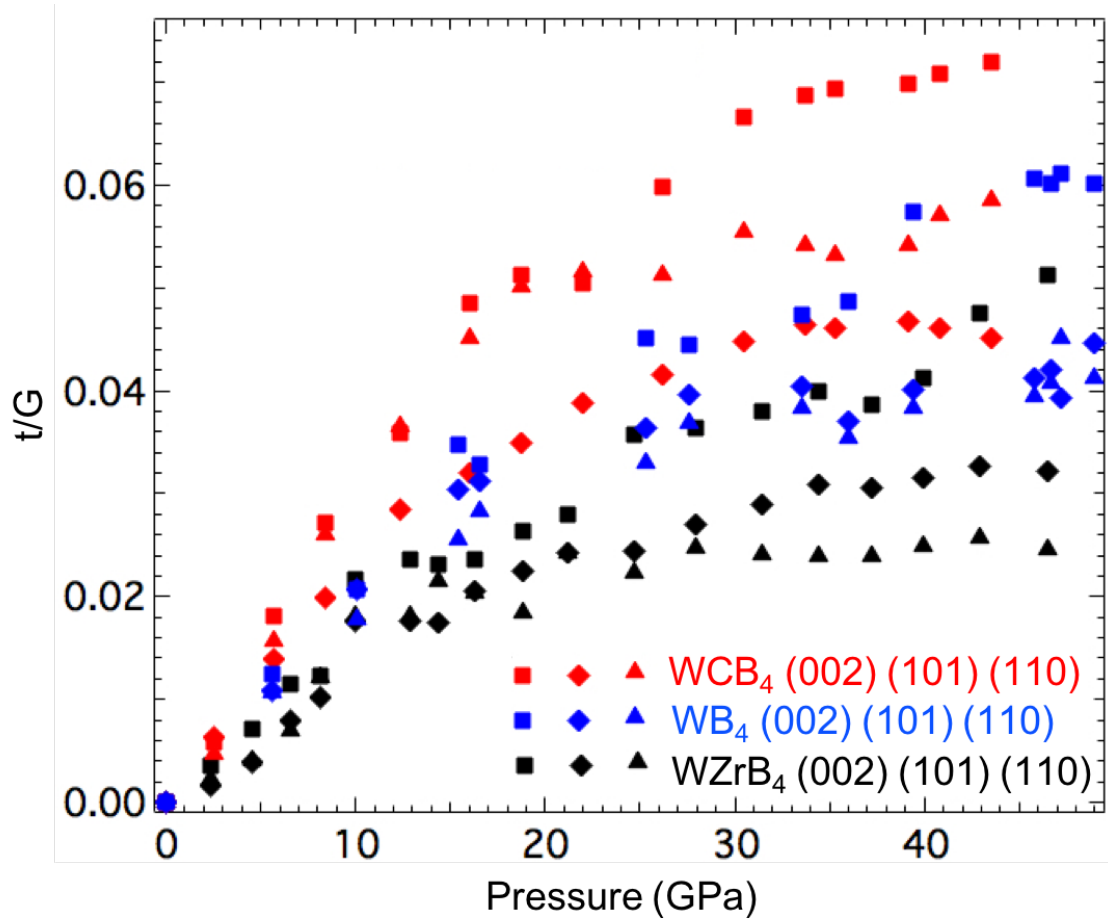
FIG. 4.10. The ratio of differential stress to shear modulus (t/G) for pure WB$_4$ (blue) compared to WB$_4$ with 8 at.% Zr (black) and 4 at.% C (red) addition.
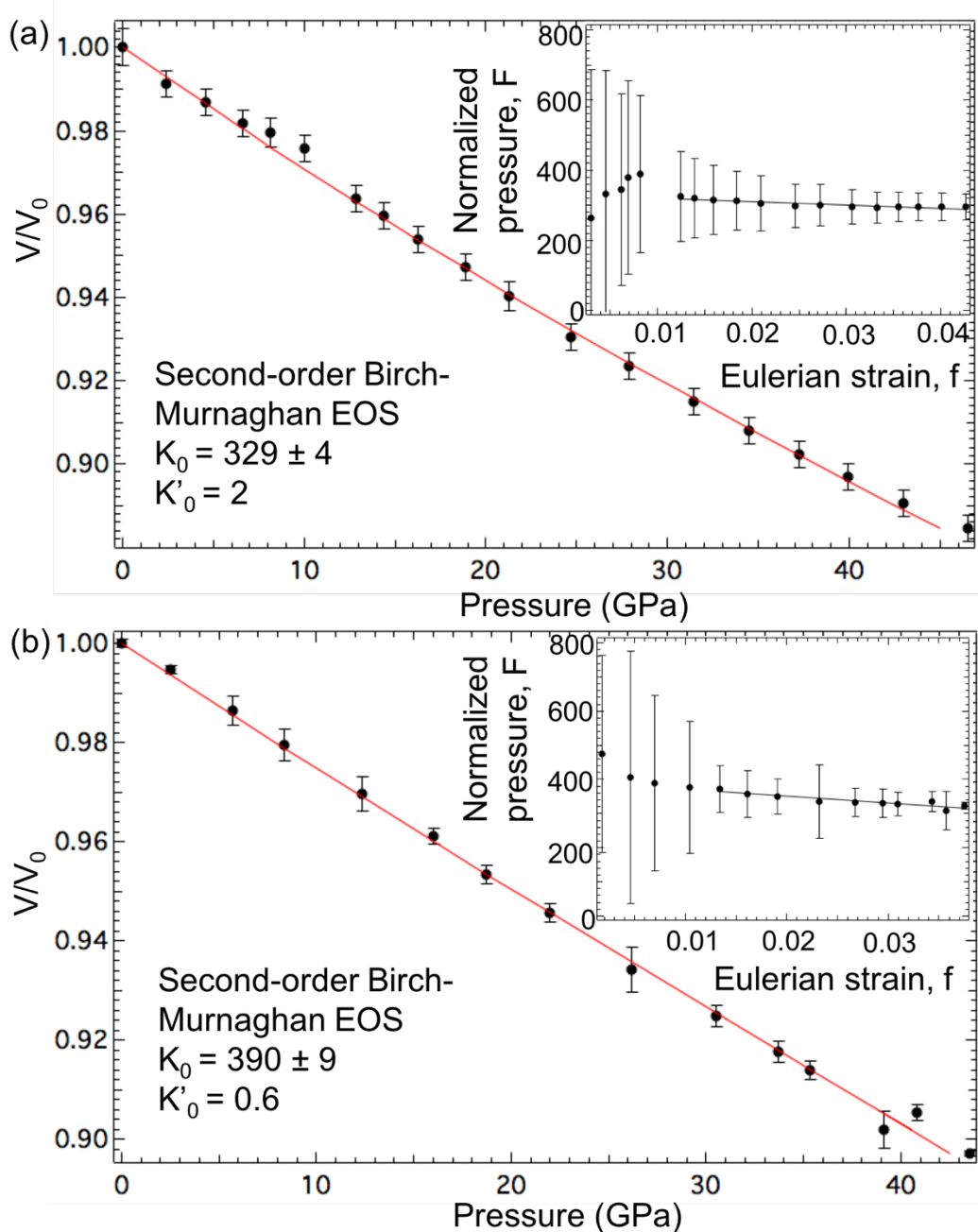
FIG. 4.11. Evolution of the unit cell volume for $W_{0.92}Zr_{0.08}B_4$ (**a**) and $W_{0.96}C_{0.04}B_4$ (**b**) as a function of pressure under nonhydrostatic compression. The volume was measured at $\varphi = 54.7°$. The red solid line is the best fit to the third-order Birch-Murnaghan equation-of-state (EOS). Inset is the third-order Birch-Murnaghan EOS plotted in terms of normalized pressure and Eulerian strain. The straight line in the inset plot yields the ambient pressure bulk modulus.
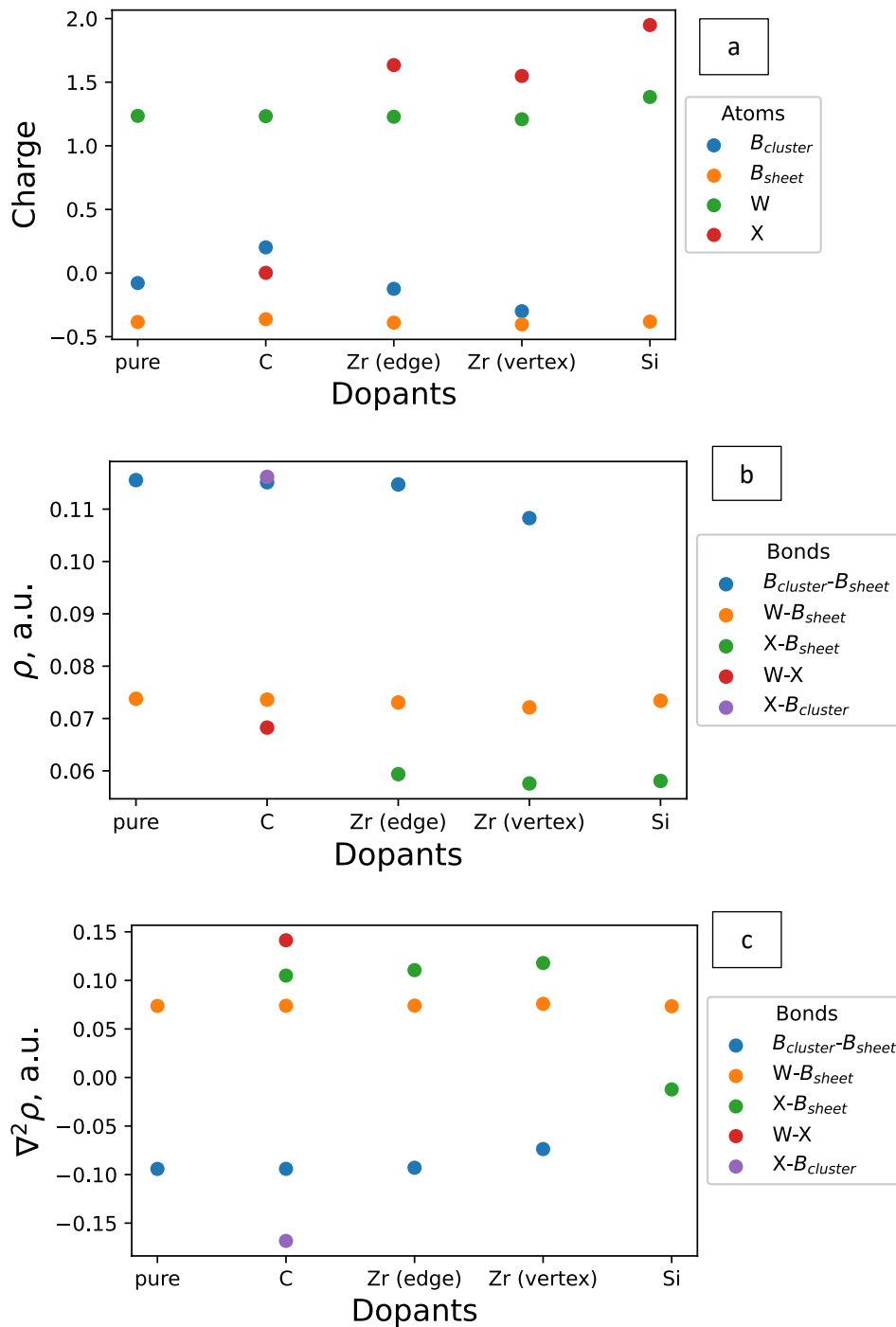
FIG. 4.12. QTAIM analysis of BCPs for model structures. (a) Average Bader atomic charges in model structures. (b) Average electron density at BCPs, connecting "layers" of the material. Average Laplacian at BCPs, connecting "layers" of the material.

(a) Pure WB$_{4.2}$

(b) Si substitutes B$_3$-trimer

(c) C in B$_{sheet}$

(d) Zr in W-occupied Wyckoff 2(c)

(e) Zr in unoccupied Wyckoff 2(d)
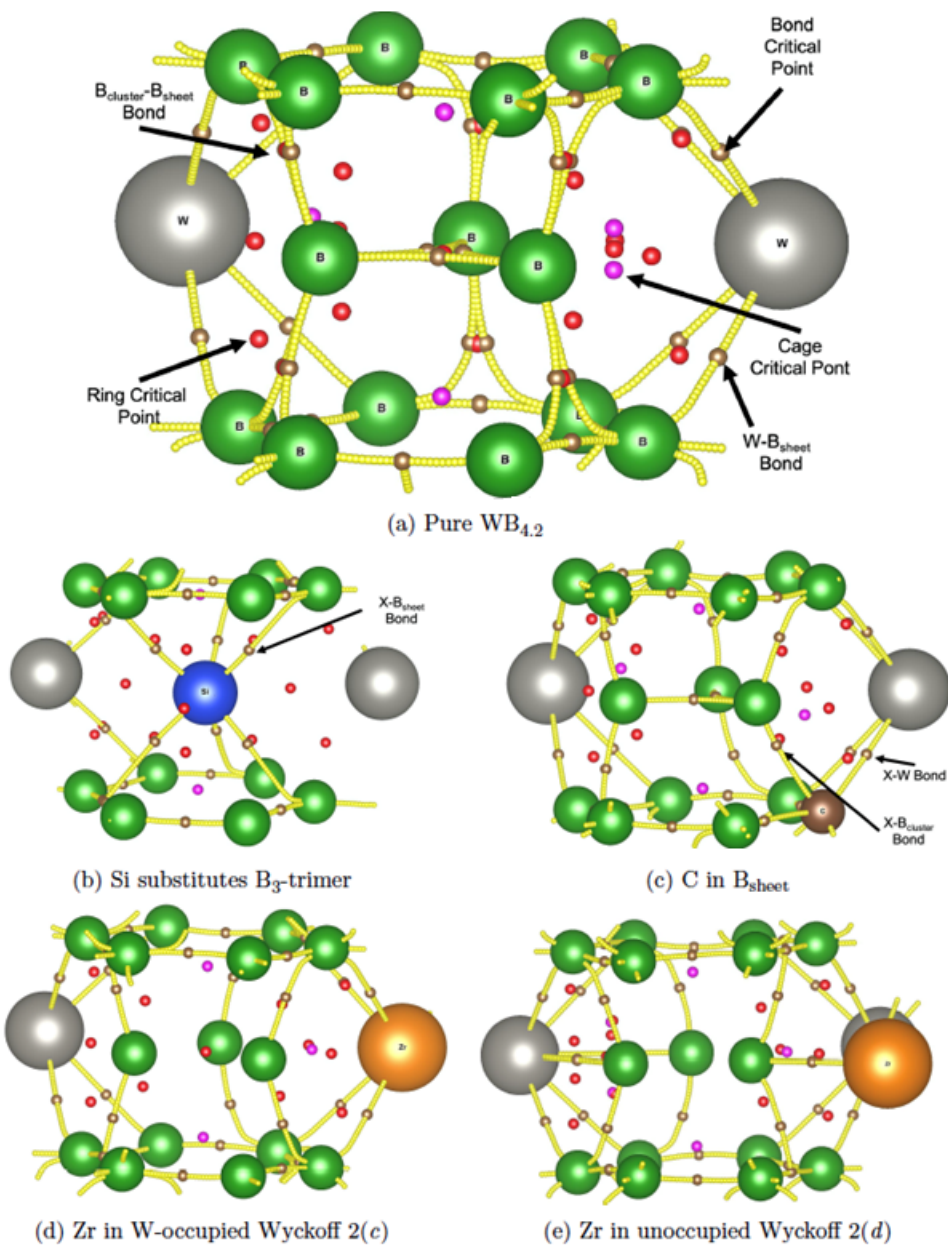
FIG. 4.13. Bonding QTAIM analysis of model structures with selected impurities. Point descriptions: Bond CPs—brown, Ring CPs—red, Cage CP—magenta. Lines of gold critical points depict bond paths.

Table 4.1. Calculated thermodynamic and mechanical properties of model structures. B_0 is bulk modulus and H_0 is formation enthalpy.

Impurity	Atoms Substituted	B_0, GPa	H_0, eV
Pure material	N/A	292.7	-12.6
C	Two B atoms in B_{hex}-layer above B_3-trimers	292.1	-8.7
	Four B atoms in B_{hex}-layer above B_3-trimers	289.8	-5.1
	One B atom in B_3-trimer	288.6	-7.3
Si	Two B atoms in B_{hex}-layer above B_3-trimer	274.9	-6.9
	One B atom in B_3-trimer	280.5	-9.2
	B_3-trimer	281.7	-10.4
Zr	W-occupancy	295.3	-12.9
	W-vacancy	292.0	-12.8

Table 4.2. Electron density and Laplacian of BCPs at $B_{cluster}$-B_{layer} bonds (or $B_{cluster}$-C_{layer} in case of C dopant).

	Electron Density, au	Laplacian, au
Pure	0.115	-0.996
C	0.117	-0.156
Zr (edge)	0.114	-0.998
Zr (vertex)	0.107	-0.06

4.5 Supporting information

Table S4.1. Lattice parameters of WCB$_4$ at corresponding pressure.

Pressure (GPa)	a (Å)	c (Å)
43.5(9)	5.0214(6)	6.1060(7)
40.8(14)	5.032(4)	6.135(5)
39.2(14)	5.023(9)	6.13(1)
35.3(11)	5.048(4)	6.154(5)
33.7(11)	5.055(5)	6.162(6)
30.5(10)	5.068(5)	6.178(6)
26.2(12)	5.08(1)	6.21(1)
22.0(9)	5.099(4)	6.241(5)
18.7(8)	5.116(4)	6.252(5)
16.0(6)	5.132(3)	6.261(4)
12.3(9)	5.145(8)	6.29(1)
8.4(8)	5.164(7)	6.305(9)
5.7(5)	5.177(6)	6.316(8)
2.5(2)	5.192(1)	6.334(1)
0	5.202(1)	6.341(2)

Table S4.2. Lattice parameters of $WZrB_4$ at corresponding pressure.

Pressure (GPa)	a (Å)	c (Å)
46.5(7)	4.999(3)	6.075(4)
42.9(6)	5.013(3)	6.085(4)
39.9(5)	5.023(2)	6.103(3)
37.2(5)	5.031(2)	6.118(3)
34.5(5)	5.042(2)	6.133(2)
31.4(5)	5.053(2)	6.150(3)
27.9(5)	5.070(3)	6.170(4)
24.7(4)	5.080(3)	6.192(4)
21.2(5)	5.100(3)	6.207(5)
18.8(4)	5.111(2)	6.225(3)
16.3(4)	5.125(2)	6.237(3)
14.4(2)	5.132(2)	6.256(3)
12.9(2)	5.139(2)	6.265(3)
10.0(3)	5.161(1)	6.291(1)
8.2(2)	5.164(3)	6.307(4)
6.6(2)	5.170(2)	6.307(3)
4.6(2)	5.178(1)	6.317(2)
2.4(1)	5.187(1)	6.323(2)
0	5.192(7)	6.370(9)
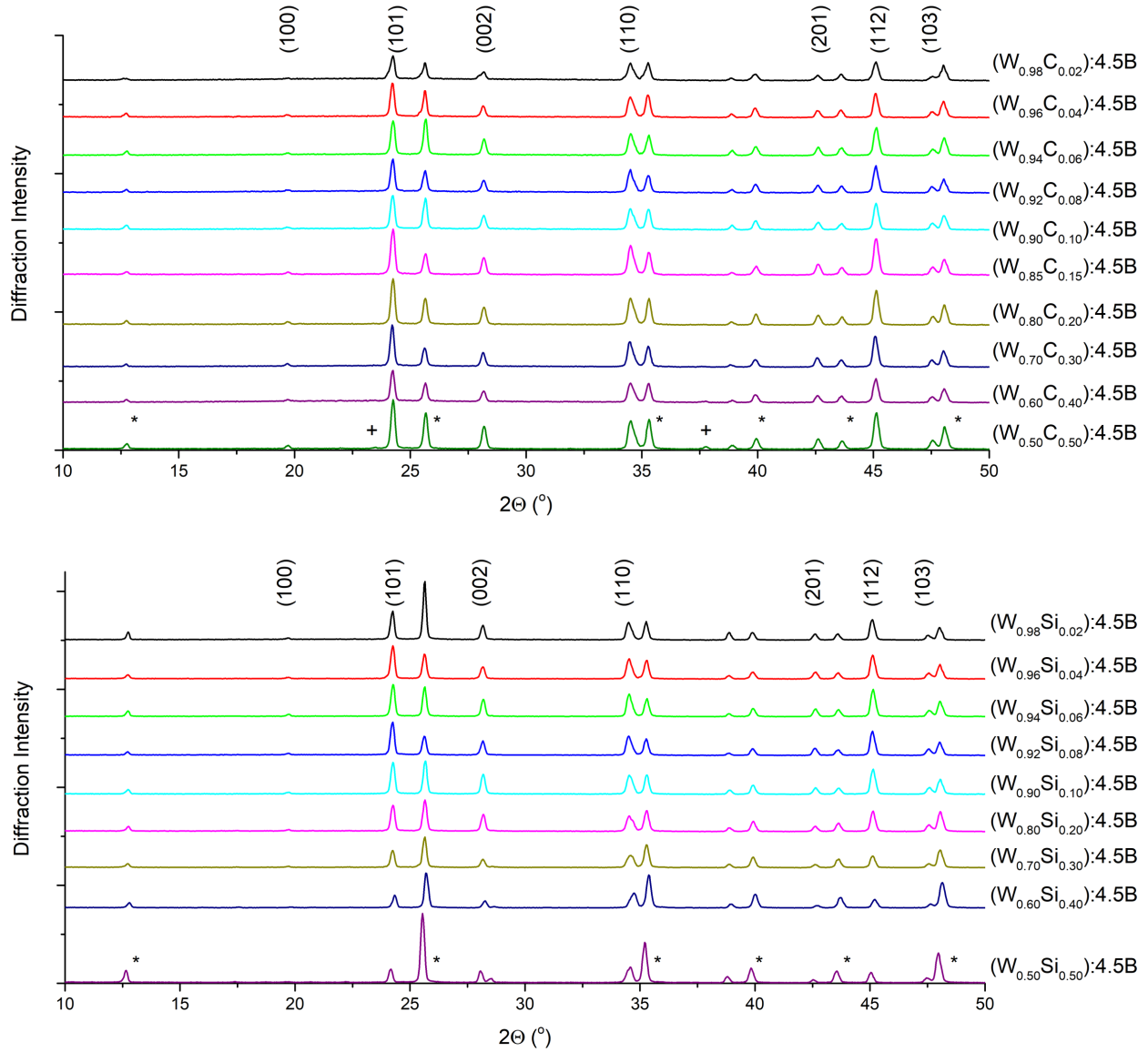
FIG. S4.1. Powder XRD patterns ($10 – 50^{\circ}$ 2Θ) of alloys of nominal composition **(top)** ($W_{1-x}C_x$) : 4.5B and **(bottom)** ($W_{1-x}Si_x$) : 4.5B. WB_4 (*$P6_3/mmc$*, JCPDS 00-019-1373) and WB_2 (denoted by (*), *$P6_3/mmc$*, JCPDS 01-073-1244) are present at all concentrations of C and Si. Peaks corresponding to a boron carbide phase (denoted by (+), $R\bar{3}m$, JCPDS 00-035-0798) can be observed at heavy concentrations of carbon addition.
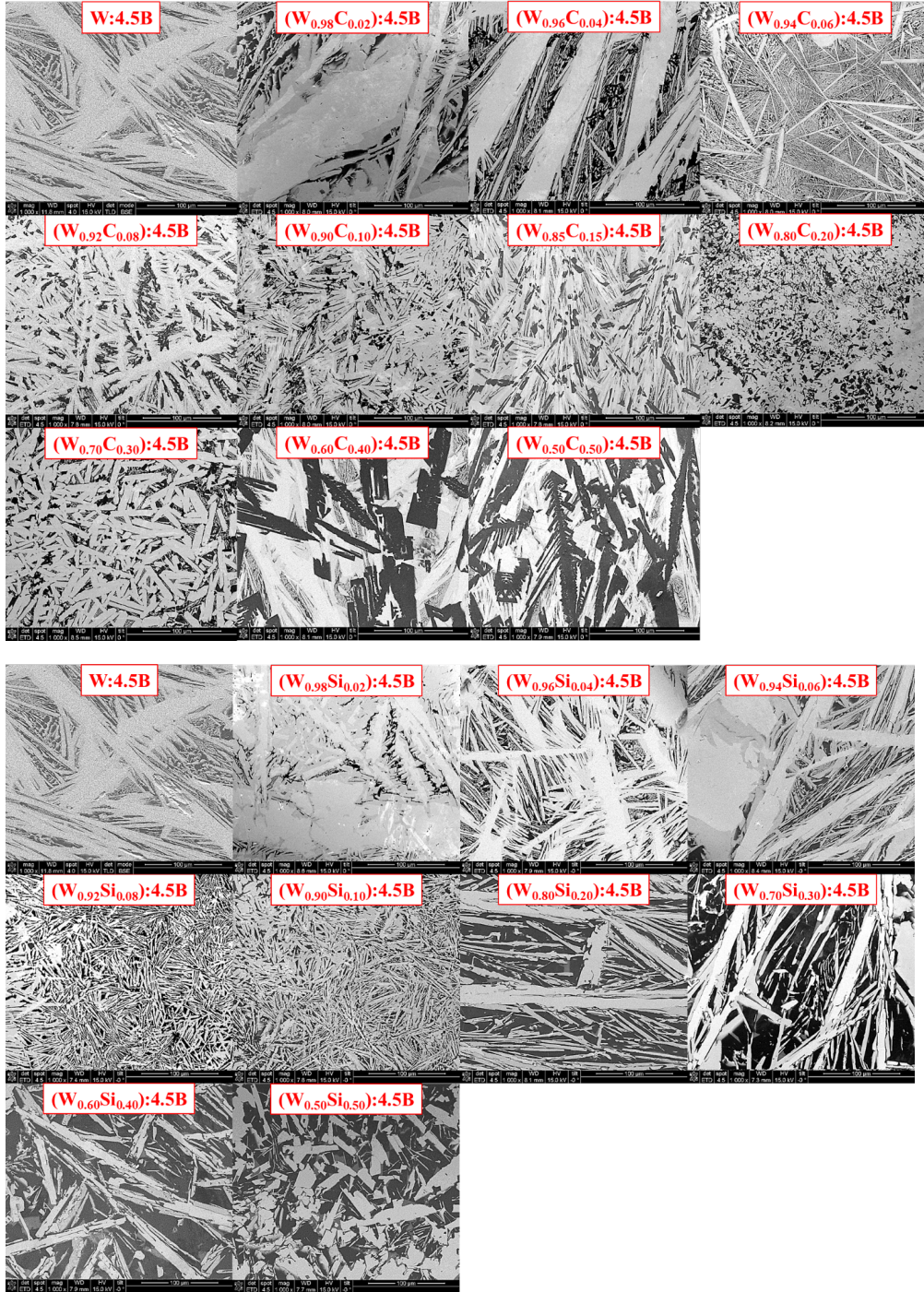
FIG. S4.2. SEM images for alloys of WB$_4$ with a nominal composition of **(top)** (W$_{1-x}$C$_x$) : 4.5B and **(bottom)** (W$_{1-x}$Si$_x$) : 4.5B showing a change in surface morphology associated with the effects of carbon and silicon and secondary phase formation. All SEM images were taken at 1000x magnification; the scale bars are 100 μm.
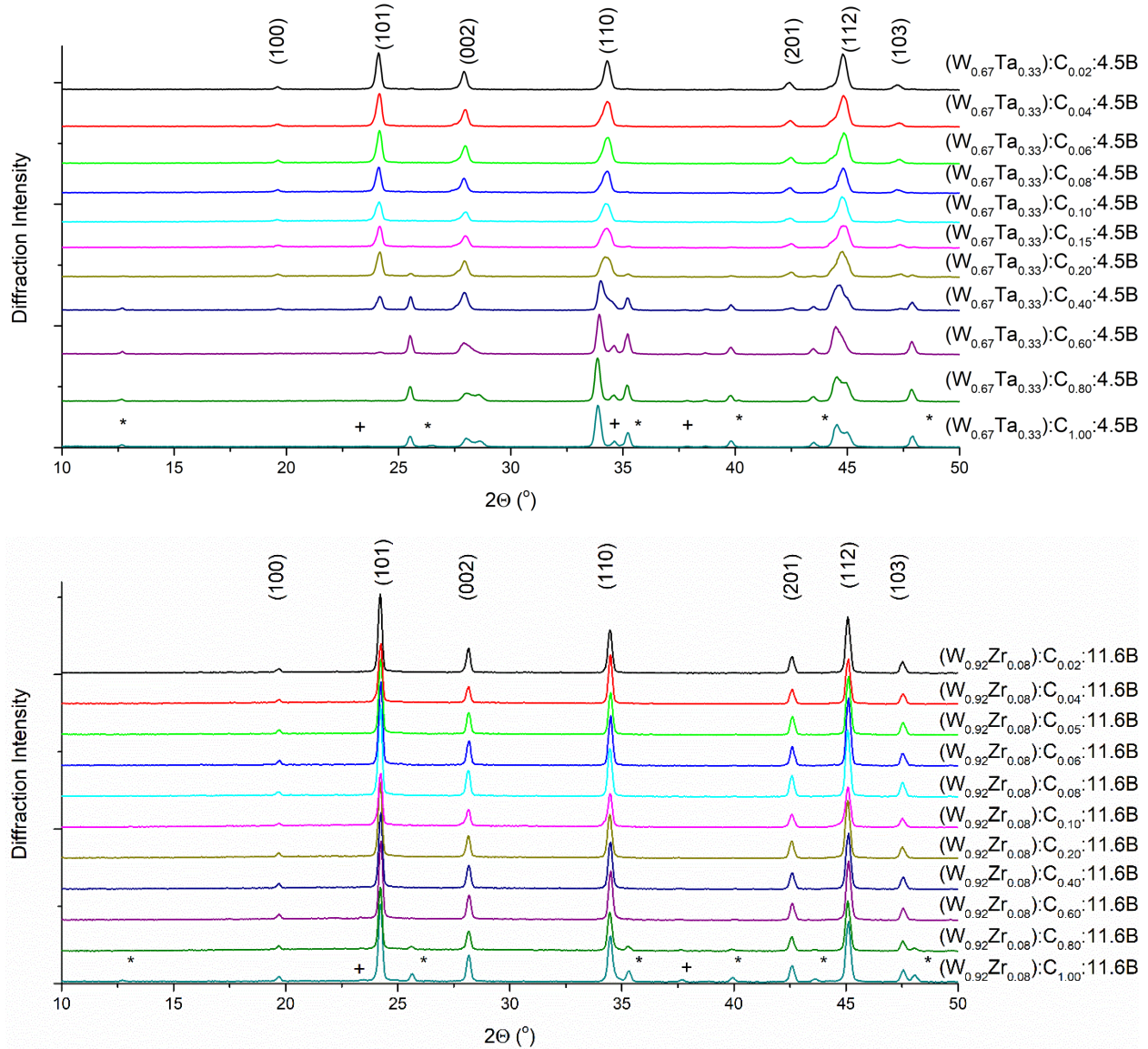
FIG. S4.3. Powder XRD patterns ($10 - 50°$ 2Θ) of alloys of nominal composition **(top)** ($W_{0.67}Ta_{0.33}$) : C_x : 4.5B and **(bottom)** ($W_{0.92}Zr_{0.08}$) : C_x :11.6B. Solid solutions of WB_4 (*P6₃/mmc*, JCPDS 00-019-1373) are present at all concentrations of C. Peaks corresponding to WB_2 (denoted by (*), *P6₃/mmc*, JCPDS 01-073-1244) and a boron carbide phase (denoted by (+), $R\bar{3}m$, JCPDS 00-035-0798) can be observed at heavy concentrations of carbon addition.

$(W_{0.67}Ta_{0.33}):4.5B$ $(W_{0.67}Ta_{0.33}):C_{0.02}:4.5B$ $(W_{0.67}Ta_{0.33}):C_{0.04}:4.5B$ $(W_{0.67}Ta_{0.33}):C_{0.06}:4.5B$

$(W_{0.67}Ta_{0.33}):C_{0.08}:4.5B$ $(W_{0.67}Ta_{0.33}):C_{0.10}:4.5B$ $(W_{0.67}Ta_{0.33}):C_{0.15}:4.5B$ $(W_{0.67}Ta_{0.33}):C_{0.20}:4.5B$

$(W_{0.67}Ta_{0.33}):C_{0.40}:4.5B$ $(W_{0.67}Ta_{0.33}):C_{0.60}:4.5B$ $(W_{0.67}Ta_{0.33}):C_{0.80}:4.5B$ $(W_{0.67}Ta_{0.33}):C_{1.0}:4.5B$
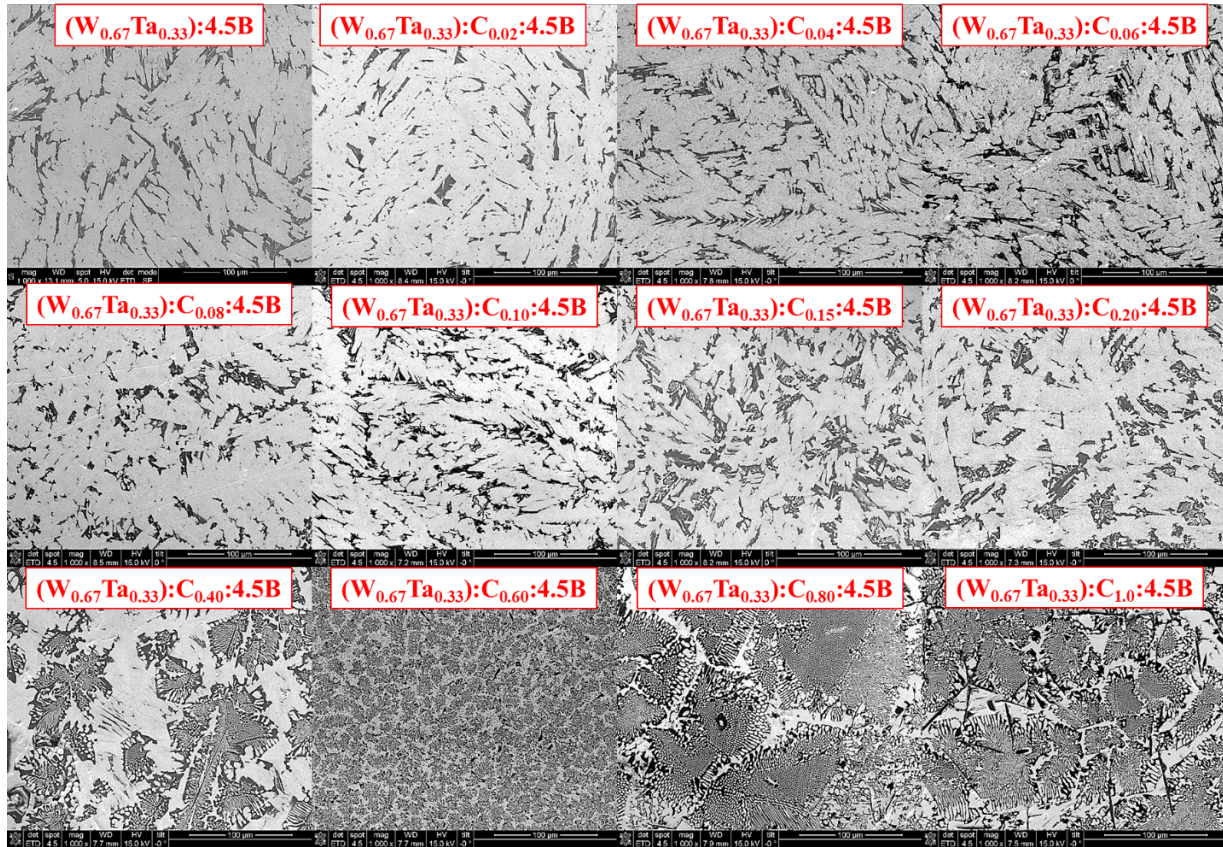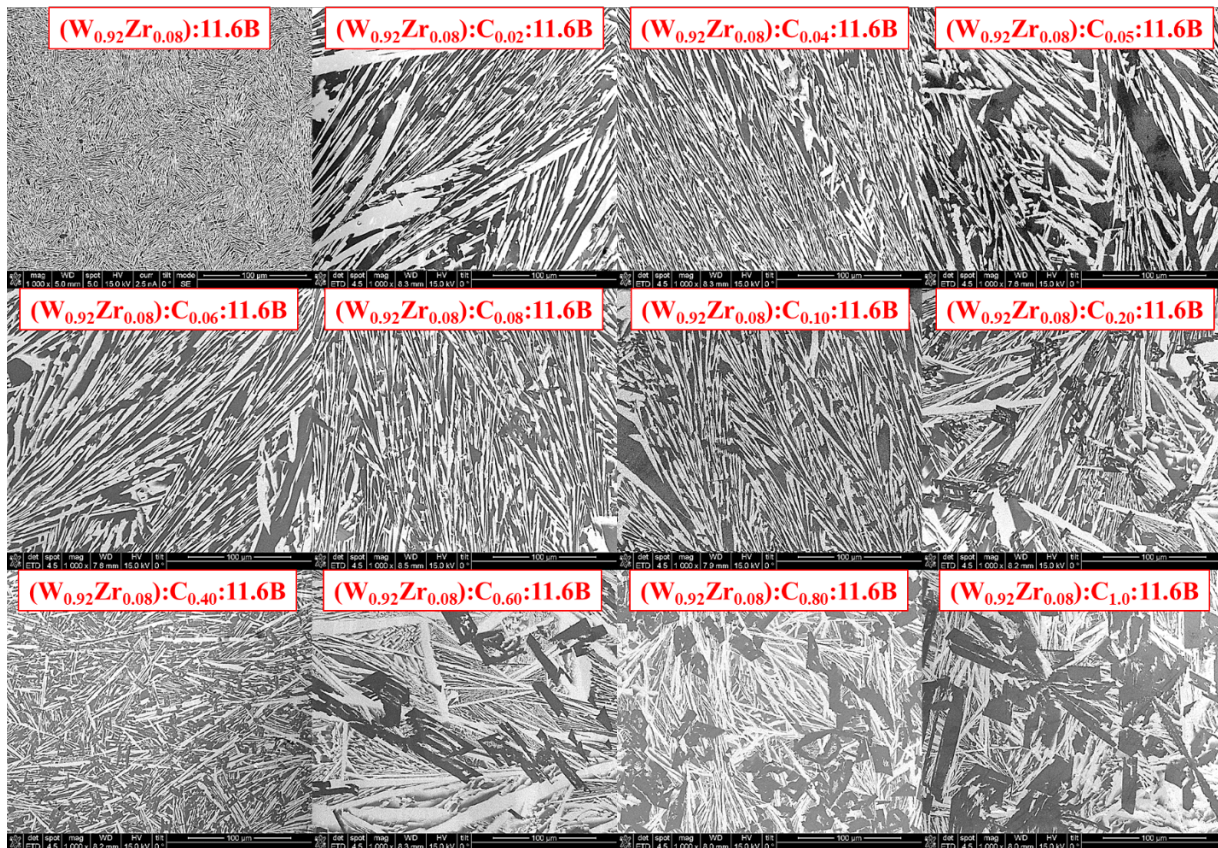
FIG. S4.4. SEM images for alloys of WB$_4$ with a nominal composition of **(top)** $(W_{0.67}Ta_{0.33})$: C$_x$: 4.5B and **(bottom)** $(W_{0.92}Zr_{0.08})$: C$_x$:11.6B showing a change in surface morphology associated with the effects of carbon and secondary phase formation. All SEM images were taken at 1000x magnification; the scale bars are 100 μm.
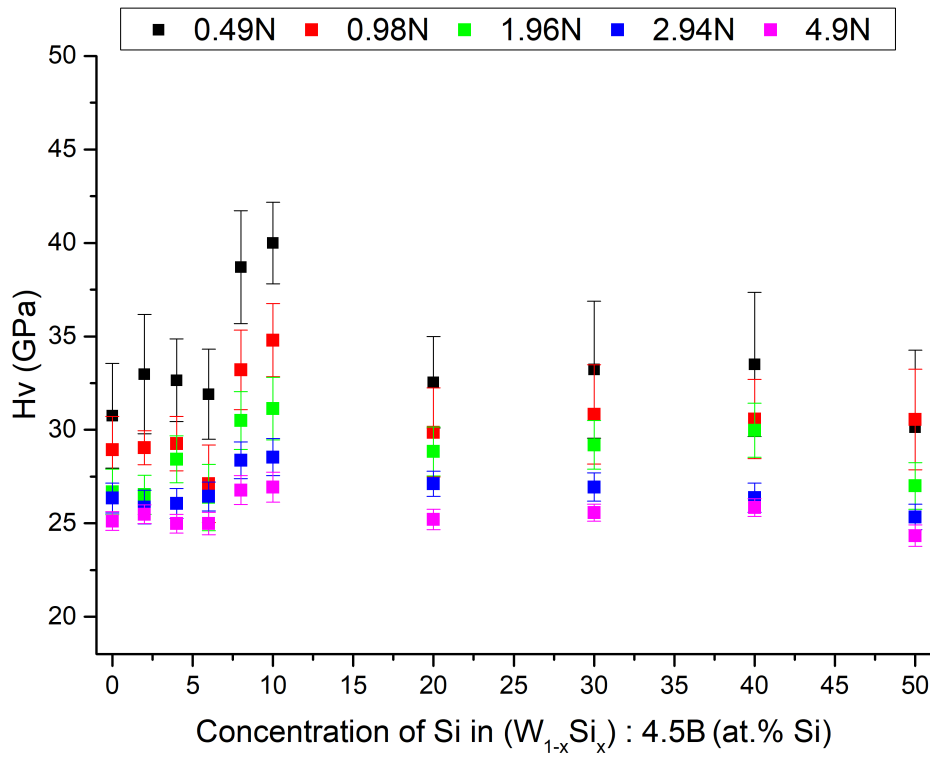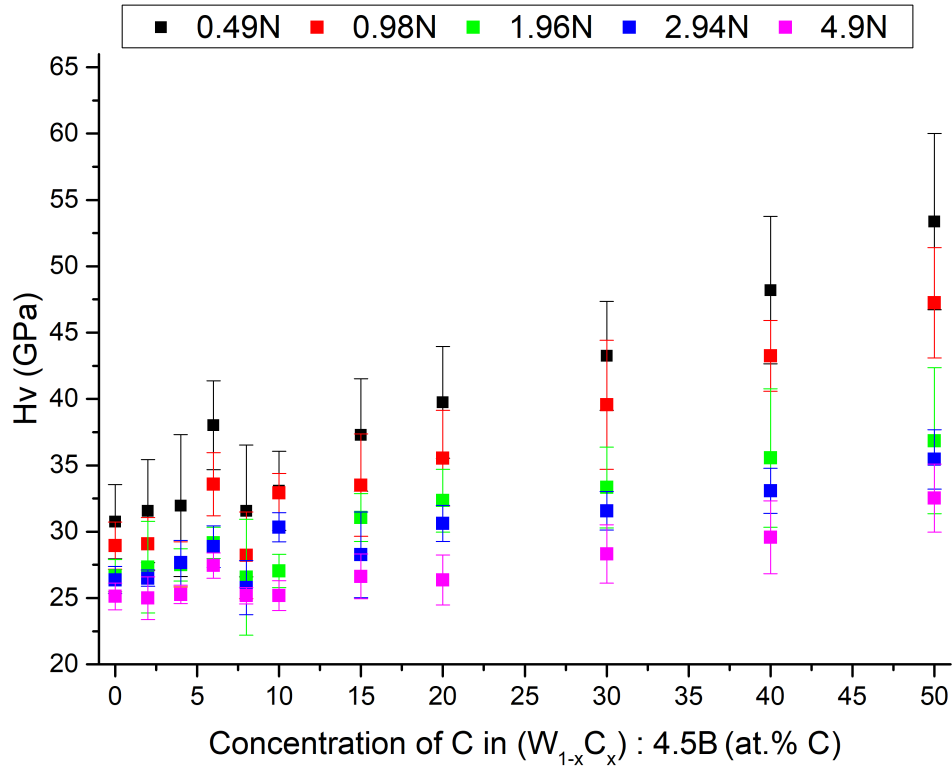
FIG. S4.5. Vickers micro-indentation hardness of alloys with a nominal composition of **(top)** $(W_{1-x}C_x)$: 4.5B and **(bottom)** $(W_{1-x}Si_x)$: 4.5B alloys at low (0.49 N) to high (4.9 N) loading.
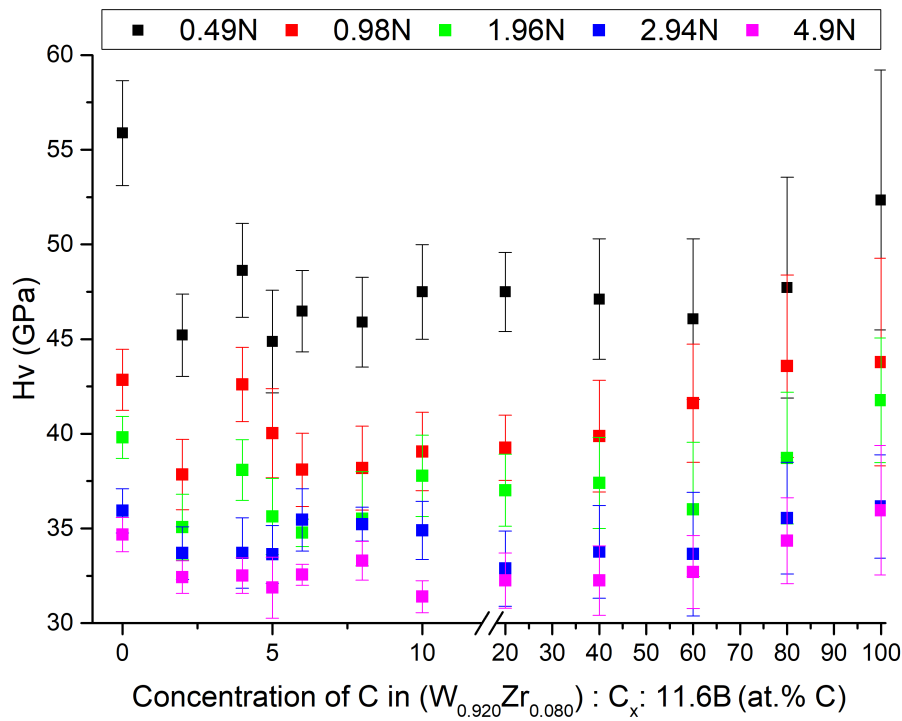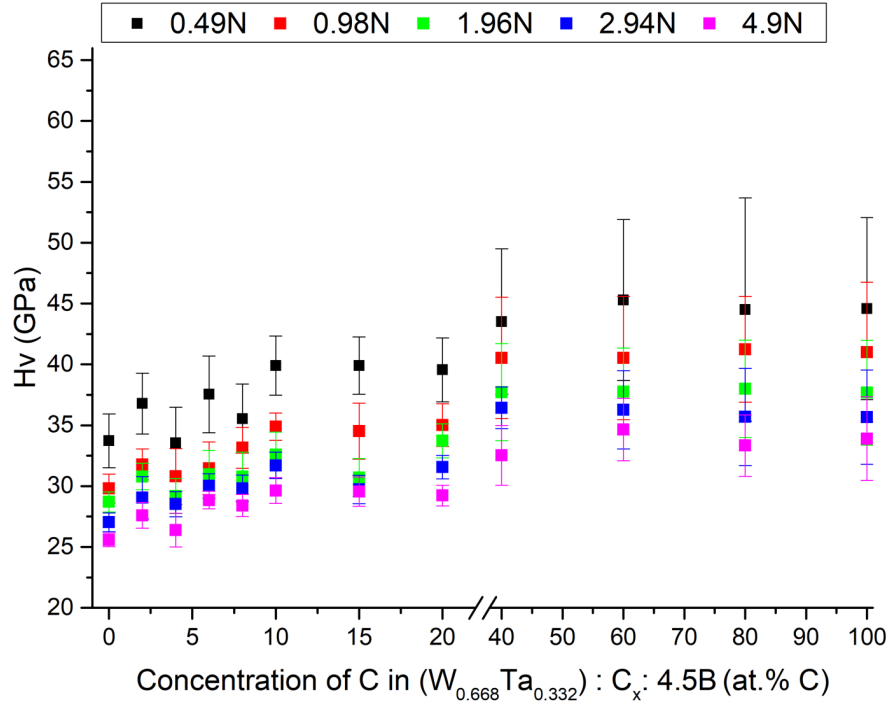
FIG. S4.6. Vickers micro-indentation hardness of alloys with a nominal composition of **(top)** $(W_{0.67}Ta_{0.33}) : C_x : 4.5B$ and **(bottom)** $(W_{0.92}Zr_{0.08}) : C_x : 11.6B$ alloys at low (0.49 N) to high (4.9 N) loading.
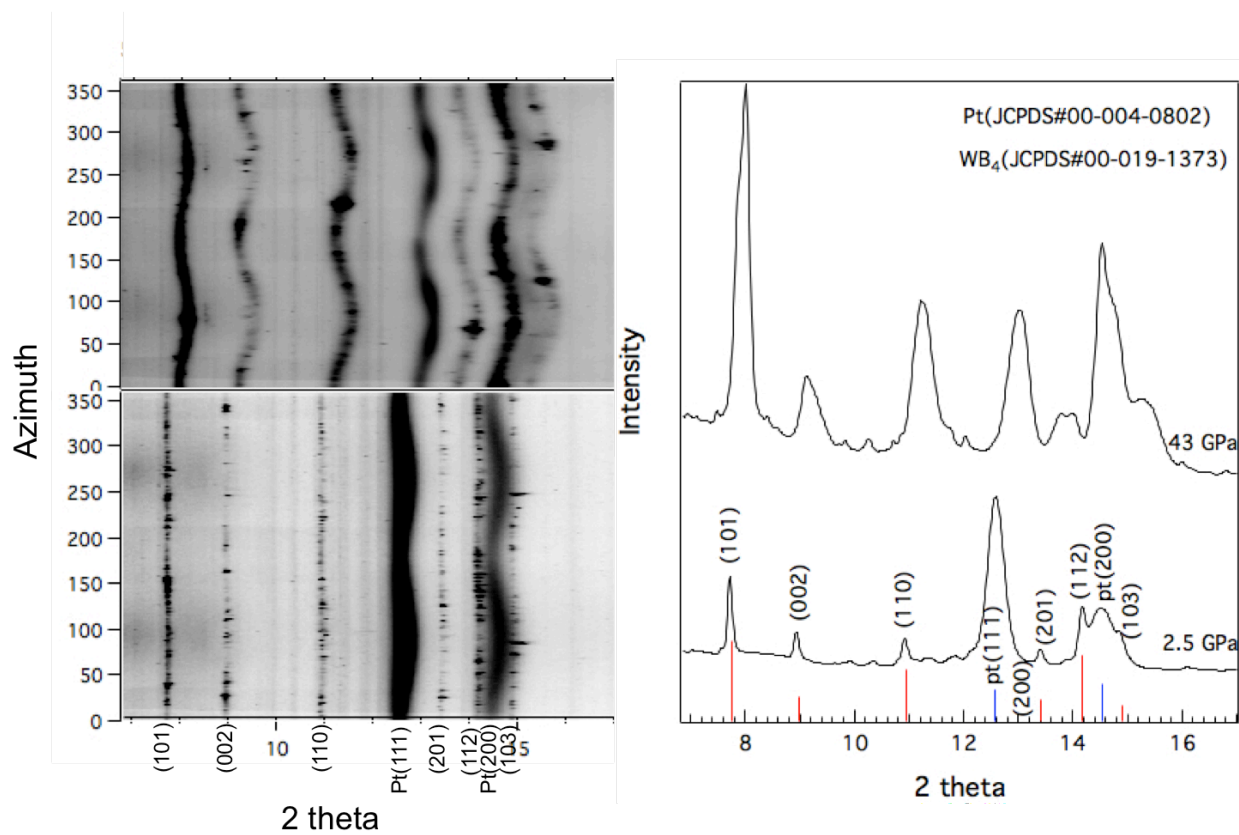
FIG. S4.7. Representative synchrotron 2-D azimuthally unrolled pattern (**left**) and 1-D X-ray diffraction pattern (**right**) with increasing pressure for WCB_4. 1-D diffraction pattern was obtained by integrating full pattern of the 2-D rings. Index for relevant peaks is included on the image as stick patterns.
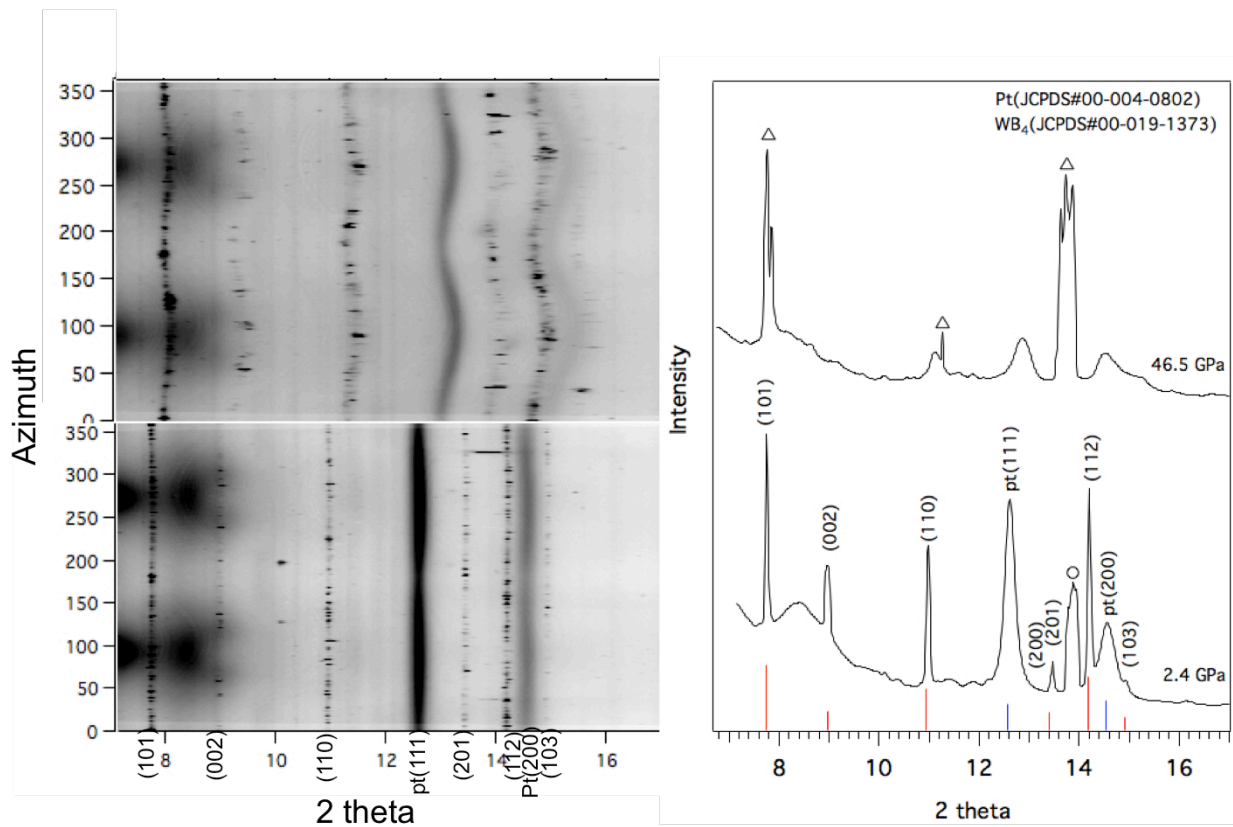
FIG. S4.8. Representative synchrotron 2-D azimuthally unrolled pattern (**left**) and 1-D X-ray diffraction pattern (**right**) with increasing pressure for $WZrB_4$. 1-D diffraction pattern was obtained by integrating the full pattern of the 2-D rings. Index for relevant peaks is included on the image as stick patterns. Open triangle is marked for large peaks, which are observed as big spots in the 2-D cake pattern.
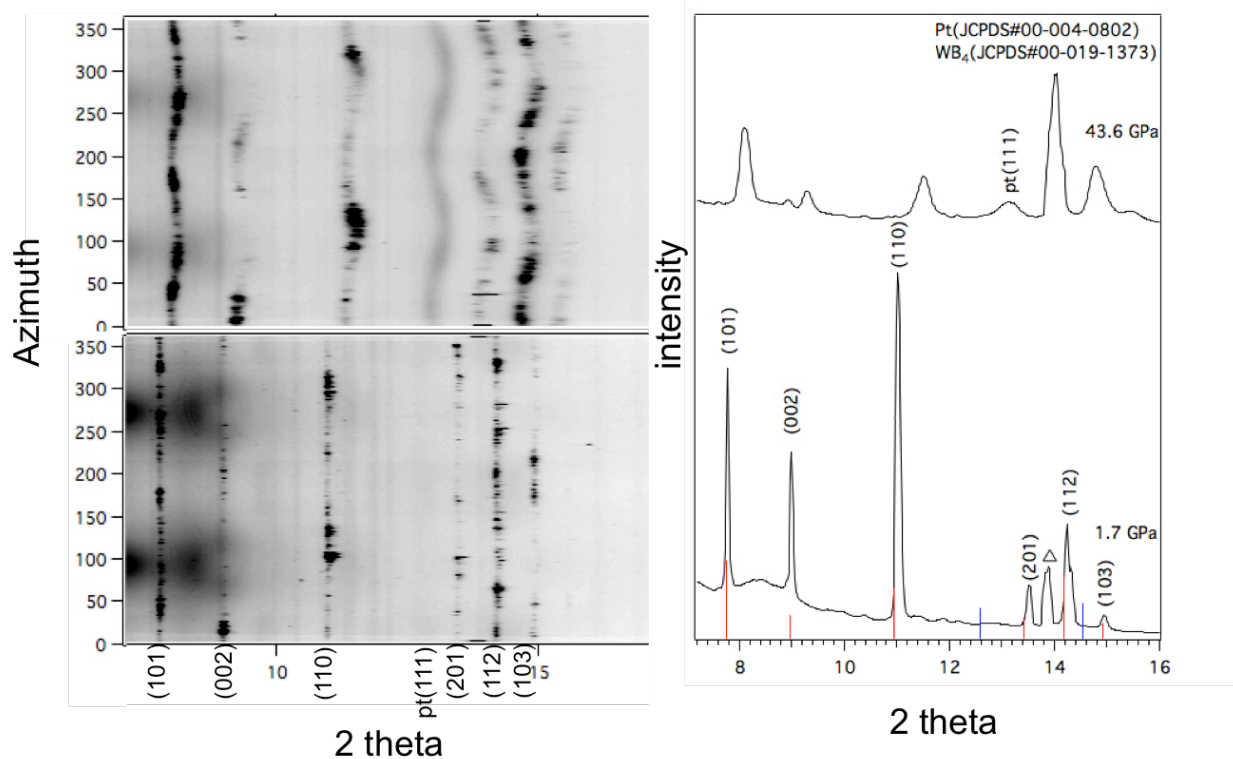
FIG. S4.9: Representative synchrotron 2-D azimuthally unrolled pattern (**left**) and 1-D X-ray diffraction pattern (**right**) with increasing pressure for $WSiB_4$. 1-D diffraction pattern was obtained by integrating the full pattern of the 2-D rings. Index for relevant peaks is included on the image as stick patterns. Open triangle is marked for large peaks, which are observed as big spots in the 2-D cake pattern.
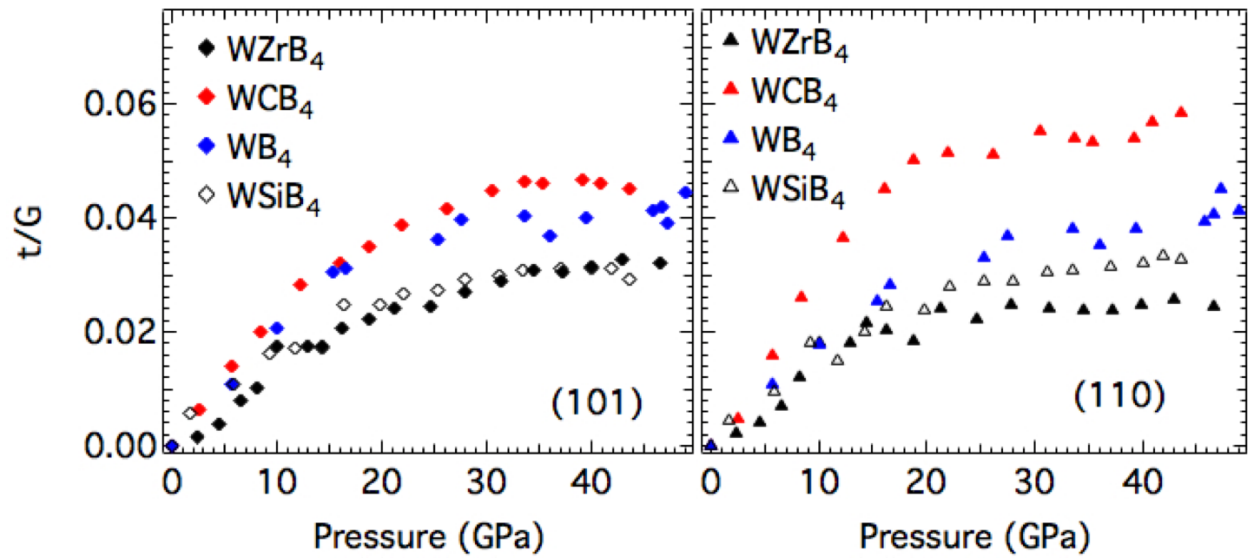
FIG. S4.10. Differential strain (t/G) of (101) and (110) lattice planes for pure WB$_4$ (blue) compared to WB$_4$ with 8 at.% Zr (black), 4 at.% C (red) addition and 2 at.% Si (open black).
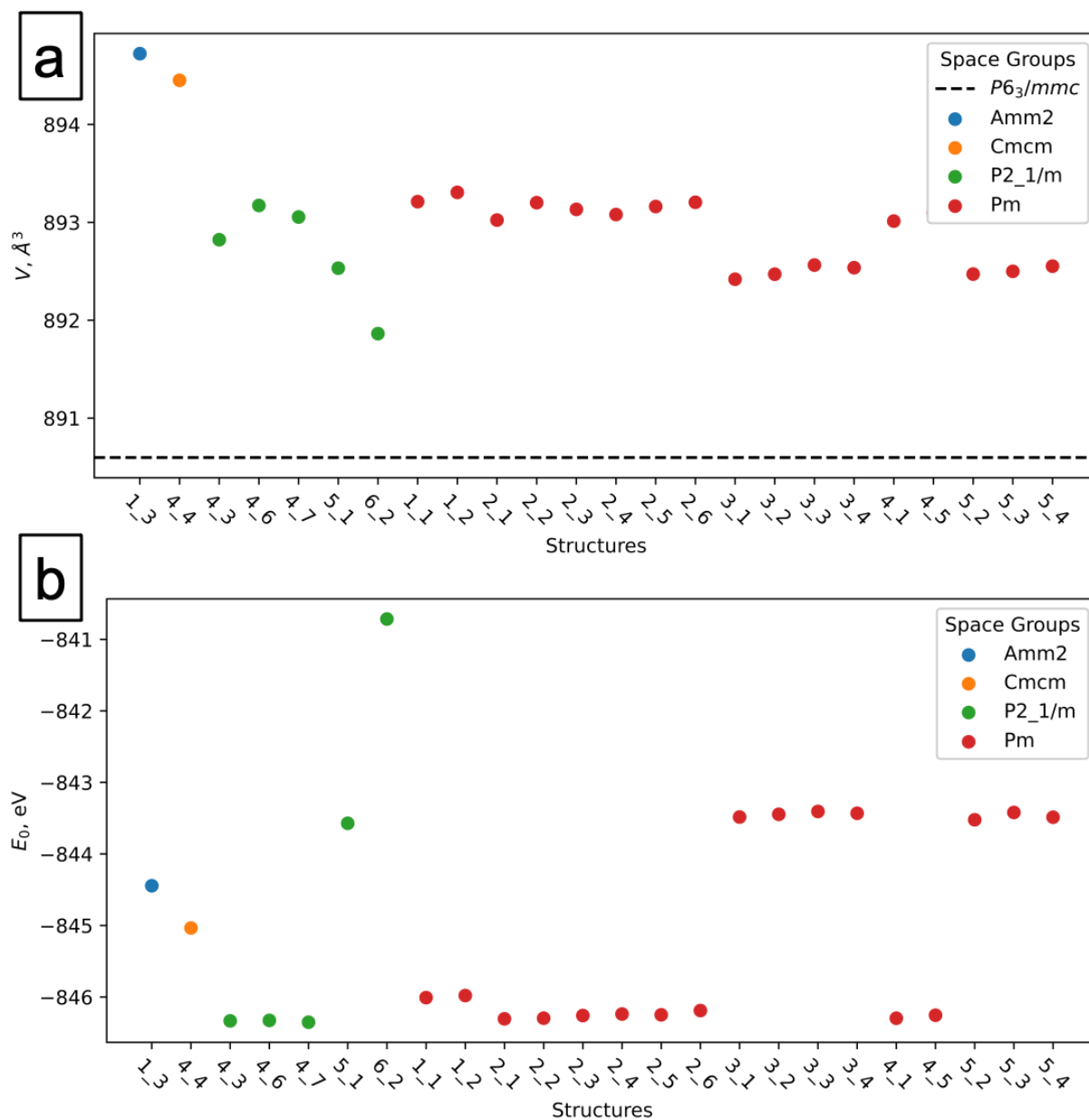
FIG. S4.11. Ensemble of $3 \times 2 \times 1$-supercell $WB_{4.2}$ realizations. (**a**) Volumes of various realizations. (**b**) Energies of various realizations.

4.6 References

1. Akopov, G., Yeung, M. T. M. T. & Kaner, R. B. R. B. Rediscovering the Crystal Chemistry of Borides. *Adv. Mater.* **29**, 1604506 (2017).

2. Fokwa, B. P. T. Borides: Solid-State Chemistry. *Encycl. Inorg. Bioinorg. Chem.* 1–14 (2014)

3. Samsonov, G. V., Markovskii, L. Ya., Zhigach, A. F. & Valyashko, M. G. *Boron, Its Compounds and Alloys [in Russian]*. (House of the Academy of the Sciences Ukrainian SSR, 1960).

4. Samsonov, G. V., Serebriakova, T. I. & Neronov, V. A. *Borides [in Russian]*. (Atomizdat, 1975).

5. Samsonov, G. V. & Vinitskii, I. M. *Refractory compounds [in Russian]*. (Atomizdat, 1975).

6. Buschow, K. H. J. Magnetic Properties of Borides. in *Boron and Refractory Borides* (ed. Matkovich, V. I.) 494–515 (Springer Berlin Heidelberg, 1977).

7. Scheifers, J. P., Zhang, Y. & Fokwa, B. P. T. Boron: Enabling Exciting Metal-Rich Structures and Magnetic Properties. *Acc. Chem. Res.* **50**, 2317–2325 (2017).

8. Chung, H.-Y. *et al.* Synthesis of Ultra-Incompressible Superhard Rhenium Diboride at Ambient Pressure. *Science* **316**, 436–439 (2007).

9. Chung, H.-Y. *et al.* Response to Comment on 'Synthesis of Ultra-Incompressible Superhard Rhenium Diboride at Ambient Pressure'. *Science* **318**, 1550 (2007).

10. Mohammadi, R. *et al.* Tungsten tetraboride, an inexpensive superhard material. *Proc. Natl. Acad. Sci.* **108**, 10958–10962 (2011).

11. Yeung, M. T. *et al.* Superhard Monoborides: Hardness Enhancement through Alloying in W1−xTaxB. *Adv. Mater.* **28**, 6993–6998 (2016).

12. Yeung, M. T. *et al.* Superhard W0.5Ta0.5B nanowires prepared at ambient pressure. *Appl. Phys. Lett.* **109**, (2016).

13. Mohammadi, R. *et al.* Enhancing the Hardness of Superhard Transition-Metal Borides: Molybdenum-Doped Tungsten Tetraboride. *Chem. Mater.* **28**, 632–637 (2016).

14. Akopov, G., Yeung, M. T., Turner, C. L., Mohammadi, R. & Kaner, R. B. Extrinsic hardening of superhard tungsten tetraboride alloys with group 4 transition metals. *J. Am. Chem. Soc.* **138**, 5714–5721 (2016).

15. Xie, M. *et al.* Exploring hardness enhancement in superhard tungsten tetraboride-based solid solutions using radial X-ray diffraction. *Appl. Phys. Lett.* **107**, 41903 (2015).

16. Mohammadi, R. *et al.* Toward Inexpensive Superhard Materials: Tungsten Tetraboride-Based Solid Solutions. *J. Am. Chem. Soc.* **134**, 20660–20668 (2012).

17. Akopov, G. *et al.* Effects of Dodecaboride-Forming Metals on the Properties of Superhard Tungsten Tetraboride. *Chem. Mater.* **30**, (2018).

18. Akopov, G. *et al.* Effects of Variable Boron Concentration on the Properties of Superhard Tungsten Tetraboride. *J. Am. Chem. Soc.* **139**, 17120–17127 (2017).

19. Akopov, G., Sobell, Z. C., Yeung, M. T. & Kaner, R. B. Stabilization of LnB12 (Ln = Gd, Sm, Nd, and Pr) in Zr(1− x)Ln(x)B12 under Ambient Pressure. *Inorg. Chem.* **55**, 12419–12426 (2016).

20. Akopov, G., Roh, I., Sobell, Z. C., Yeung, M. T. M. T. & Kaner, R. B. R. B. Investigation of ternary metal dodecaborides (M1M2M3)B12 (M1, M2 and M3 = Zr, Y, Hf and Gd). *Dalton Trans* **47**, 6683–6691 (2018).

21. Akopov, G., Yeung, M. T., Turner, C. L., Li, R. L. & Kaner, R. B. Stabilization of HfB12 in Y1-xHfxB12 under Ambient Pressure. *Inorg. Chem.* **55**, (2016).

22. Akopov, G. *et al.* Superhard mixed transition metal dodecaborides. *Chem. Mater.* **28**, 6605–6612 (2016).

23. Akopov, G., Yin, H., Roh, I., Pangilinan, L. E. & Kaner, R. B. Investigation of Hardness of Ternary Borides of the YCrB4, Y2ReB6, Y3ReB7, and YMo3B7 Structural Types. *Chem. Mater.* **30**, (2018).

24. Akopov, G., Pangilinan, L. E. L. E., Mohammadi, R. & Kaner, R. B. Superhard metal borides: A look forward. *APL Mater.* **6**, 070901 (2018).

25. Portnoi, K. I. I. *et al.* Phase diagram of the system tungsten-Boron. *Sov. Powder Metall. Met. Ceram.* **6**, 398–402 (1967).

26. Lutterotti, L., Chateigner, D., Ferrari, S. & Ricote, J. Texture, residual stress and structural analysis of thin films using a combined X-ray analysis. *Thin Solid Films* **450**, 34–41 (2004).

27. Lutterotti, L., Bortolotti, M., Ischia, G., Lonardelli, I. & Wenk, H. R. Rietveld texture analysis from diffraction images. *Z. Krist. Suppl.* **1**, 125–130 (2007).

28. Lutterotti, L. Maud Rev. 2.55. *Univ. Trento-Italy Dep. Ind. Eng. Trento Italy* (2015).

29. Lutterotti, L. Total pattern fitting for the combined size-strain-stress-texture determination in thin film diffraction. *Nucl. Instrum. Methods Phys. Res. Sect. B Beam Interact. Mater. At.* **268**, 334–340 (2010).

30. Lutterotti, L., Matthies, S., Wenk, H. R., Schultz, A. S. & Richardson, J. W. Combined texture and structure analysis of deformed limestone from time-of-flight neutron diffraction spectra. *J. Appl. Phys.* **81**, 594–600 (1997).

31. Grau-Crespo, R., Hamad, S., Catlow, C. R. A. & Leeuw, N. H. de. Symmetry-adapted configurational modelling of fractional site occupancy in solids. *J. Phys. Condens. Matter* **19**, 256201 (2007).

32. Perdew, J. P., Burke, K. & Ernzerhof, M. Generalized Gradient Approximation Made Simple. *Phys. Rev. Lett.* **77**, 3865–3868 (1996).

33. Perdew, J. P., Burke, K. & Ernzerhof, M. Generalized Gradient Approximation Made Simple [Phys. Rev. Lett. 77, 3865 (1996)]. *Phys. Rev. Lett.* **78**, 1396–1396 (1997).

34. Kresse, G. & Furthmüller, J. Efficiency of ab-initio total energy calculations for metals and semiconductors using a plane-wave basis set. *Comput. Mater. Sci.* **6**, 15–50 (1996).

35. Kresse, G. & Hafner, J. Ab initio molecular-dynamics simulation of the liquid-metal--amorphous-semiconductor transition in germanium. *Phys. Rev. B* **49**, 14251–14269 (1994).

36. Kresse, G. & Hafner, J. Ab initio molecular dynamics for liquid metals. *Phys. Rev. B* **47**, 558–561 (1993).

37. Otero-de-la-Roza, A., Blanco, M. A., Martín Pendás, A. & Luaña, V. Critic: a new program for the topological analysis of solid-state electron densities. *Comput. Phys. Commun.* **180**, 157–166 (2009).

38. Otero-de-la-Roza, A., Johnson, E. R. & Luaña, V. Critic2: A program for real-space analysis of quantum chemical interactions in solids. *Comput. Phys. Commun.* **185**, 1007–1018 (2014).

39. Yu, M. & Trinkle, D. R. Accurate and efficient algorithm for Bader charge integration. *J. Chem. Phys.* **134**, 064111 (2011).

40. Perdew, J. P., Burke, K. & Ernzerhof, M. Generalized Gradient Approximation Made Simple (vol 77, pg 3865, 1996). *Phys. Rev. Lett.* **78**, 1396–1396 (1997).

41. Perdew, J. P., Burke, K. & Ernzerhof, M. Generalized gradient approximation made simple. *Phys. Rev. Lett.* **77**, 3865–3868 (1996).

42. Kresse, G. & Furthmüller, J. Efficient iterative schemes for ab initio total-energy calculations using a plane-wave basis set. *Phys. Rev. B - Condens. Matter Mater. Phys.* **54**, 11169–11186 (1996).

43. Kresse, G. & Furthmüller, J. Efficiency of ab-initio total energy calculations for metals and semiconductors using a plane-wave basis set. *Comput. Mater. Sci.* **6**, 15–50 (1996).

44. Kresse, G. & Hafner, J. Ab initio molecular dynamics for liquid metals. *Phys. Rev. B* **47**, 558–561 (1993).

45. Kresse, G. & Hafner, J. Ab initio molecular-dynamics simulation of the liquid-metalamorphous- semiconductor transition in germanium. *Phys. Rev. B* **49**, 14251–14269 (1994).

46. Grau-Crespo, R., Hamad, S., Catlow, C. R. A. A., De Leeuw, N. H. & de Leeuw, N. H. Symmetry-adapted configurational modelling of fractional site occupancy in solids. *J. Phys. Condens. Matter* **19**, 256201 (2007).

47. Otero-de-la-Roza, A., Blanco, M. A., Pendás, A. M. & Luaña, V. Critic: a new program for the topological analysis of solid-state electron densities. *Comput. Phys. Commun.* **180**, 157–166 (2009).

48. Otero-de-la-Roza, A., Johnson, E. R. & Luaña, V. Critic2: A program for real-space analysis of quantum chemical interactions in solids. *Comput. Phys. Commun.* **185**, 1007–1018 (2014).

49. Bodrova, L. G., Koval'chenko, M. S. & Serebryakova, T. I. Preparation of tungsten tetraboride. *Sov. Powder Metall. Met. Ceram.* **13**, 1–3 (1974).

50. Samsonov, G. V. The Phases of the Tungsten-Boron System. *Dokl Akad Nauk SSSR* **113**, 1299–1301 (1957).

51. Lech, A. T., Turner, C. L., Mohammadi, R., Tolbert, S. H. & Kaner, R. B. Structure of superhard tungsten tetraboride: A missing link between MB2 and MB12 higher borides. *Proc. Natl. Acad. Sci.* **112**, 3223–3228 (2015).

52. Akopov, G. *et al.* Synthesis and Characterization of Single-Phase Metal Dodecaboride Solid Solutions: Zr1–xYxB12 and Zr1–xUxB12. *J. Am. Chem. Soc.* **141**, 9047–9062 (2019).

53. McCaughey, C. & Tsakiropoulos, P. Type of primary Nb5Si3and precipitation of Nbssin αNb5Si3in a Nb-8.3Ti-21.1Si-5.4Mo-4W-0.7Hf (at.%) near eutectic Nb-silicide-based alloy. *Materials* **11**, 1–25 (2018).

54. Lei, J. *et al.* Radial X-Ray Diffraction Study of Superhard Early Transition Metal Dodecaborides under High Pressure. *Adv. Funct. Mater.* **29**, 1900293 (2019).

55. Xie, M. *et al.* Exploring the high-pressure behavior of superhard tungsten tetraboride. *Phys. Rev. B* **85**, 064118 (2012).

56. Råasander, M. & Moram, M. A. On the accuracy of commonly used density functional approximations in determining the elastic constants of insulators and semiconductors. *J. Chem. Phys.* **143**, 144104 (2015).

57. Heyd, J., Scuseria, G. E. & Ernzerhof, M. Hybrid functionals based on a screened Coulomb potential. *J. Chem. Phys.* **118**, 8207–8215 (2003).

58. Heyd, J., Scuseria, G. E. & Ernzerhof, M. Erratum: "Hybrid functionals based on a screened Coulomb potential" [J. Chem. Phys. 118, 8207 (2003)]. *J. Chem. Phys.* **124**, 219906 (2006).

Chapter 5

High-Pressure Studies of Solid-Solution Effects in Ultra-incompressible Superhard Metal Dodecaborides

5.1 Introduction

With a booming economy, the demand for novel superhard materials has steadily increased in the past decades, not only due to expansion in construction and automotive industries, but also due to the limitations of traditional superhard materials. The traditional superhard materials, diamond and cubic boron nitride, require both high temperature and high pressure for their syntheses.[1,2] Moreover, diamond is not effective in cutting and drilling ferrous metals because of tendency to form carbides.[3] Despite this drawback, the incredible hardness of diamond inspired us to design new superhard materials with bond networks modeled after the 3D networks of strong covalent bonds found in diamond.

Transition metal borides are interesting potential candidates for superhard materials due to their combination of high-electron-density metals and strong covalent boron bonding.[4] Here, we focus on a family of intrinsically hard transition metal dodecaborides (MB_{12}, M = metal), which are a class of boron-rich compounds containing rigid cuboctahedron cages.[5] As shown in **FIG. 5.1(a)**, each 12-coordinated metal atom is surrounded by a 24-boron-atom cuboctahedron cage that occupies an octahedral site of the cubic unit cell; those octahedral sites sit at the cube corner or face center, forming an FCC lattice ($Fm\bar{3}m$).[6,7,8] The short covalent bond network mimics the bonding motif in diamond, contributing to the high hardnesses of MB_{12} compounds. Indeed, the Vicker's hardness of YB_{12} and ZrB_{12} both exceed 40 GPa at low load and therefore both materials are considered to be superhard.[9,10]

Since each metal atom is surrounded by a cuboctahedron cage, the size of the unit cell must fall within a very small range (~7.408 Å-7.500 Å) to maintain the cage structure, so that only two MB_{12} phases are found to be stable at ambient conditions (YB_{12} and ZrB_{12}). Recently, however, we showed that a range of binary and ternary metal dodecaborides can be stabilized by combining a mixture of a slightly bigger metal atom and a smaller metal atom in a framework, as long as the average size fits the constraint listed above.[6] Micro-indentation studies showed that all these solid solutions are superhard, with the highest hardness of 46.9 ± 2.4 GPa under low load (0.49 N) reached by $Y_{0.25}Zr_{0.5}Gd_{0.25}B_{12}$.

In these cases, all MB_{12} solid solutions showed structures in accordance with Vegard's law,[11] meaning that the lattice constant of each solid solution is in agreement with the weighted average of the lattice constants of its constituents.[6] As briefly mentioned above, the lattice parameter is closely related to the weighted metal atomic radii. In the cubic structure, the smallest metal, zirconium (r = 1.603 Å), forms a stabilized dodecaboride at ambient pressure with the smallest lattice parameter, while the largest metal, yttrium (r = 1.801 Å), exhibits the largest lattice parameter, and the rest of the solid solutions have lattice parameters within the required range.[12] From the previous data, however, there were no clear trends in which solid solutions showed higher or lower hardness, and hardness did not follow any simple Vegard's law type trends.

In this work, our goal is thus to gain a deeper understanding of the factors controlling hardness in MB_{12} solid solution. To do this, we turn to high-pressure studies deformation under nonhydrostatic compression. Deformation under these conditions can be related to the intrinsic hardness of a material, which is associated with covalent bonding and dislocation pinning due to atomic size mismatch or valence electron density differences, and thus should be tuned by solid solution effects. Micro- and nano-indentation experiments are sensitive to this intrinsic hardness,

but they can also be influenced by extrinsic hardness, which is governed by grain boundaries and precipitation of secondary phases.[13] As discussed above, there are lower and higher boride impurities in all of these samples, and so extrinsic hardening effects are likely to play a role. Although the Vickers hardness value is a standard parameter to report the overall hardness of a composite material, it fails to cleanly describe the intrinsic hardening effects and the deformation mechanism at the macroscopic level. Most importantly, the hardness enhancement in various MB_{12} solid solutions in terms of the nature of bonding and atomic packing within the unit cell is not fully understood. Therefore, understanding the bonding motif under compression and the contributing factors to enhanced hardness is important to shed light on design rules for next-generation light weight (high boron content) superhard materials.

Here, we have performed *in situ* high-pressure radial X-ray diffraction experiments in a radial geometry under nonhydrostatic compression on a wide range of MB_2 binary ($Y_{0.25}Hf_{0.75}B_{12}$, $Zr_{0.5}Gd_{0.5}B_{12}$) and ternary solid solutions ($Y_{0.25}Zr_{0.5}Gd_{0.25}B_{12}$, $Y_{0.5}Gd_{0.25}Hf_{0.25}B_{12}$, $Zr_{0.5}Gd_{0.25}Hf_{0.25}B_{12}$), and examined differential strain in a lattice specific manner up to 60 GPa. The differential strain is directly proportional to the differential stress through the shear modulus, and the plateau value of the differential stress corresponds to the yield strength of the material, which in turn directly reports on intrinsic hardness. While the shear modulus of these MB_{12} solid solutions is not known, we expect it to similar within dodecaboride family. As a result, the relative differential strain plateau value of these solid solutions should align with the relative plateau values of differential stress, thus providing a good estimation of relative yield strength that is directly related to the intrinsic hardness.[14,15,16,17] Our aim is thus to compare the differential strain plateau values to gain a better understanding of the factors controlling intrinsic hardness in this family of dodecaboride solid solutions.

5.2 Experimental Procedure

All dodecaboride samples ($Y_{0.25}Hf_{0.75}B_{12}$, $Zr_{0.5}Gd_{0.5}B_{12}$, $Y_{0.25}Zr_{0.5}Gd_{0.25}B_{12}$, $Y_{0.5}Gd_{0.25}Hf_{0.25}B_{12}$ and $Zr_{0.5}Gd_{0.25}Hf_{0.25}B_{12}$, ZrB_{12}, YB_{12} and $Zr_{0.5}Y_{0.5}B_{12}$) were prepared by arc melting from elements of zirconium (99.5%, Strem Chemicals, USA), yittrium (99.5%, Strem Chemicals, USA), hafmium (99.5%, Strem Chemicals, USA), gadolinium (99.5%, Strem Chemicals, USA), and amorphous boron (99+%, Strem Chemicals, USA) powder. The molar ratio of metal to boron was kept at 1:20 and the metal ratio follows the nominal composition of the sample. All components were thoroughly mixed together using an agate mortar and pestle and pressed into pellets using a hydraulic Caver pressure under ~10 tons. Subsequently, the pellets were arc melted under Argon, with an ~100 Amp DC current for 1-2 min. The resultant ingots were ground to fine powders using a Plattner-style hardened tool-steel mortar and pestle set (Humboldt Mfg., Model H-17270) followed by sifting by screening with a No. 635 mesh (20um) sieve (Humboldt Mfg.).

Nonhydrostatic *in situ* high-pressure radial X-ray diffraction was performed individually on $Y_{0.25}Hf_{0.75}B_{12}$, $Zr_{0.5}Gd_{0.5}B_{12}$, $Y_{0.25}Zr_{0.5}Gd_{0.25}B_{12}$ in a diamond anvil cell at synchrotron beamline 12.2.2 of the Advanced Light Source (ALS, Lawrence Berkeley National Laboratory) and on $Y_{0.5}Gd_{0.25}Hf_{0.25}B_{12}$ and $Zr_{0.5}Gd_{0.25}Hf_{0.25}B_{12}$ at synchrotron beamline 16-ID-B of the Advanced Photon Source (APS, Argonne National Laboratory). ZrB_{12}, YB_{12} and $Zr_{0.5}Y_{0.5}B_{12}$ previously studied in our group can be found in Ref 9. Crushed powder of each sample, together with a small piece of an Au pressure standard (~20 μm diameter), was loaded into a laser-drilled hole (~60 μm in diameter, ~60 μm in depth) in a ~400 μm diameter boron gasket made of amorphous boron and epoxy, sandwiched between two diamond tips.[18] In the radial geometry, a monochromatic X-ray beam ($\lambda = 0.4066$ Å, spot size = 10 μm × 10 μm) was passed through the sample, perpendicular to

the compression direction. The ambient samples were measured directly in capillary tubes. The angle-dispersive diffraction pattern was collected using an MAR-345 image plate, and the detector distance and orientation were calibrated by a cerium dioxide (CeO_2) standard using FIT2D software.[19]

The angle-dispersive diffraction patterns were converted from elliptical to rectangular coordinates using FIT2D. The converted plot of azimuthal angle (η) versus diffraction angles (2θ), known as a "cake" pattern, was then analyzed using Igor Pro (WaveMetrics, Inc.). Peak positions were manually picked out for three easily resolvable diffraction peaks (111, 200, and 311). The quasi-hydrostatic diffraction pattern as a function of 2θ was obtained at the magic angle ($\varphi = 54.7°$, effectively the hydrostatic condition). All peaks were indexed to the cubic phase with no indication of any phase transition throughout the measured pressure range.

The stress in the sample under uniaxial compression is described by Equation 5.1:

$$\sigma = \begin{bmatrix} \sigma_1 & 0 & 0 \\ 0 & \sigma_1 & 0 \\ 0 & 0 & \sigma_3 \end{bmatrix} = \begin{bmatrix} \sigma_p & 0 & 0 \\ 0 & \sigma_p & 0 \\ 0 & 0 & \sigma_p \end{bmatrix} + \begin{bmatrix} -t/3 & 0 & 0 \\ 0 & -t/3 & 0 \\ 0 & 0 & -2t/3 \end{bmatrix} \tag{5.1}$$

where σ_1 is the minimum stress along the incident x-ray beam, σ_3 is the maximum stress in the compression direction, σ_P is the hydrostatic stress component, and t is the differential stress, which gives a lower-bound estimate of yield strength.[20] The d-spacing is calculated by:

$$d_m(hkl) = d_p(hkl)[1 + (1 - 3\cos^2\varphi)Q(hkl)] \tag{5.2}$$

where d_m is the measured d-spacing, d_p is the d-spacing at the hydrostatic peak position, φ is the angle between the diffraction normal and compression directions, and $Q(hkl)$ is the lattice strain under the uniaxial stress condition.[14,21] The differential stress, t, is directly related to the differential strain, $t(hkl)/G(hkl)$, by:

$$t(hkl) = 6G(hkl)Q(hkl) \tag{5.3}$$

where $G(hkl)$ is the shear modulus of the specific lattice plane.[15]

Incompressibility can be determined using the third-order Birch-Murnaghan equation-of-state (EOS),[22] which is written as:

$$P = \frac{3}{2} K_0 \left(\left(\frac{V_0}{V} \right)^{7/3} - \left(\frac{V_0}{V} \right)^{5/3} \right) \left(1 + \frac{3}{4} (K_0' - 4) \left(\left(\frac{V_0}{V} \right)^{2/3} - 1 \right) \right) \tag{5.4}$$

where P is the pressure, K_0 is the bulk modulus at ambient pressure, V is the volume, V_0 is the undeformed unit cell volume, and K_0' is the derivative of K_0 with respect to P. The Birch-Murnaghan equation-of-state can be rewritten in terms of normalized pressure (F) and Eulerian strain (f),[23] as shown in the following equations:

$$F = \frac{P}{3f(1+2f)^{5/2}} \tag{5.5}$$

$$f = \frac{1}{2} \left(\left(\frac{V_0}{V} \right)^{2/3} - 1 \right) \tag{5.6}$$

Combining Equations (5.5) and (5.6) gives a linear regression, where the zero-intercept yields the bulk modulus at ambient pressure (K_0) and the slope yields the pressure derivatives of the bulk modulus (K_0').

5.3 Results and discussion

Dodecaborides were synthesized by resistive arc-melting with a 1: 20 metal to boron ratio to promote formation of the dodecaboride phase and suppress the formation of any lower diboride or hexaboride phases. Representative XRD patterns were fit using a Rietveld refinement method as implemented in the software package MAUD.[24,25,26] As shown in **FIG. 5.1(b,c)**, $Y_{0.25}Hf_{0.75}B_{12}$ and $Zr_{0.5}Gd_{0.5}B_{12}$ contain lower borides in addition to the MB_{12} phase and the boron-rich MB_{66} phase. This is because HfB_{12} and GdB_{12} are unstable high-pressure phases,[12,27] which can either be synthesized under high pressure or stabilized using a secondary atom with different atomic size ($Y_{1-x}Hf_xB_{12}$, $Zr_{1-x}Gd_xB_{12}$).[28,29] As previously mentioned, the boron cuboctahedron cage is stable

when the metal size falls within the range between zirconium and yttrium atomic radii (1.603-1.801 Å). A smaller hafnium atom (r = 1.580 Å) or a larger gadolinium atom (1.801 Å) disrupts the cage structure and thus results in favorable formation of lower boride phases.[12] In agreement with this idea, $Y_{0.5}Zr_{0.5}B_{12}$ and other solid solution of stable dodecaborides, do not form lower borides. Interestingly, a ternary solid solution ($Y_{0.25}Zr_{0.5}Gd_{0.25}B_{12}$) is able to stabilize the FCC structure with a wide variety of large and small metal atoms (**FIG. 5.1 d,e**) . In order to gain more insights into the crystal lattice of these dodecaborides, the diffraction pattern was fit to an orthorhombic structure, giving the refinement more freedom to exactly fit the lattice constants along the a, b and c axes. We found that all dodecaborides form approximately cubic structures with only slight deviations in the lattice constants (**Table 5.1**). The minor noncubic effects probably result from the atomic packing of metals with various sizes in the unit cell.

In order to gain more insights into solid solution formation, we plotted the measured volume with respect to the weighted average of the metal atomic radii (**FIG. 5.2**). As mentioned above, metal dodecaborides stable at ambient pressure have stringent requirements on the metal atomic radii, with Zr at the lower limit and Y at the upper limit. The unit cell expansion or contraction should be closely related to the weighted metal size. In **FIG. 5.2**, most of the dodecaborides fall on the line connecting YB_{12} and ZrB_{12}, with the exception of $Y_{0.25}Zr_{0.5}Gd_{0.25}B_{12}$ and $Y_{0.5}Zr_{0.5}B_{12,}$ which fall slightly below the line, and $Y_{0.25}Hf_{0.75}B_{12}$, which is observed above the line. The linear trend indicates a continuous unit cell expansion as the overall metal size increases, which confirms the solid solution formation in accordance with Vegard's law.[11] The fact that $Y_{0.25}Zr_{0.5}Gd_{0.25}B_{12}$ and $Y_{0.5}Zr_{0.5}B_{12}$ possess smaller unit cells than predicted from perfect solid solutions suggest that the distortion of the boron cage to optimize atomic packing leads to a more compact unit cell. The

same idea applies to $Y_{0.25}Hf_{0.75}B_{12}$, which results in a less compact unit cell due to the large atomic size mismatch between metals.

In situ high-pressure radial X-ray diffraction was performed on the MB_{12} binary ($Y_{0.25}Hf_{0.75}B_{12}$, $Zr_{0.5}Gd_{0.5}B_{12}$, $Zr_{0.5}Y_{0.5}B_{12}$) and the ternary solid solutions ($Y_{0.25}Zr_{0.5}Gd_{0.25}B_{12}$, $Y_{0.5}Gd_{0.25}Hf_{0.25}B_{12}$, $Zr_{0.5}Gd_{0.25}Hf_{0.25}B_{12}$) and compared to the pure materials (YB_{12} and ZrB_{12}). In radial geometry, the sample is compressed uniaxially under a nonhydrostatic condition in the diamond anvil cell, while the X-ray beam is passed perpendicular to the compression direction, is and diffraction data is collected as a function of compression.[18] A set of representative XRD data on a ternary alloy, taken at ambient, low, and high pressure is shown in **FIG. 5.3**. The 1-dimensional full integration patterns were indexed and compared to the stick reference patterns, and the peaks broaden as the pressure increases because the integration is averaging over the varying stress states within the high pressure cell. A clear shift to higher angles (2θ) at higher pressures suggests a decrease in the lattice spacing with greater compression. The pressure was determined from the equation-of-state of the Au standard, using its d-spacing at $\varphi = 54.7°$.[30] In the cake pattern (FIG. 5.3, top), the diffraction lines are nearly straight due to the hydrostatic stress state at ambient pressure, whereas at higher pressure, the diffraction lines start to deviate to higher angles (2θ) in the high stress direction ($\varphi = 0°$) and to lower angles (2θ) in the low stress direction ($\varphi = 90°$). The sinusoidal variations of the diffraction lines indicate the lattice-supported strains.

To calculate the differential strain, the measured d-spacing was plotted versus the orientation function ($1-3\cos^2\varphi$) for each lattice planes of interest (**FIG. 5.4a**). A linear correlation is observed to the highest pressure, which is in good agreement with lattice strain theory (Equation 5.2).[14,15] The hydrostatic d-spacings was obtained from the zero-intercepts of the line, and the orientation-dependent lattice strain, *Q(hkl)*, was determined from the ratio of the slope to the zero-

intercept.[31,32] Differential strain, $t/G(hkl)$, was then calculated from $Q(hkl)$, as given by Equation (5.3). The pressure-dependence of the hydrostatic d-spacings is shown in **FIG. 5.4b**. The continuous decrease of d-spacings with pressure indicates that no phase transition occurs at high pressure. The same data processing and strain analyses for $Y_{0.5}Zr_{0.5}B_{12}$, $Y_{0.25}Hf_{0.75}B_{12}$, $Zr_{0.5}Gd_{0.5}B_{12}$, $Y_{0.5}Gd_{0.25}Hf_{0.25}B_{12}$ and $Zr_{0.5}Gd_{0.25}Hf_{0.25}B_{12}$ are shown in **FIGS. S5.1-S5.3** and previously published in reference 9.

As shown in **FIG. 5.5**, the measured differential strain for each lattice plane increases linearly with pressure and then appears to level off. The linear increase is associated with elastic deformation, and the plateau is an indication of plastic deformation. The corresponding differential strain at the plateau is the maximum deformation that a lattice plane can sustain before bond breaking. The plane with the lowest plateau value supports the least deformation, while planes with higher plateau values resist more shear and dislocation movement. Given by Equation (5.3), the differential stress, t, can be determined from differential strain (t/G) if the shear modulus (G) is known. Therefore, the intrinsic hardness can be directly obtained from the plateau value of differential stress, which is known as the yield strength. Since the shear modulus, G, does not generally change very much across a family of metal borides,[33] the plateau differential strain value, t/G, which is proportional to the yield strength, can be a good indication of hardness.

In **FIG. 5.5**, $Y_{0.25}Zr_{0.5}Gd_{0.25}B_{12}$ shows the highest plateau t/G value in all three lattice planes and $Y_{0.5}Zr_{0.5}B_{12}$ shows the second highest values. These are the two compounds that showed unusually compact unit cell volumes in FIG. 5.2. The tight atomic packing in $Y_{0.25}Zr_{0.5}Gd_{0.25}B_{12}$ and $Y_{0.5}Zr_{0.5}B_{12}$ may optimize the stacking of the boron cages and contributes to the higher differential strain. On the other hand, $Y_{0.25}Hf_{0.75}B_{12}$ is a solid solution with a large amount of substitutional doping of smaller atoms, and this material has both a less compact than expected

142

structure and shows the lowest plateau t/G value. It appears that the $Y_{0.25}Hf_{0.75}B_{12}$ crystal structure fails to optimize the distance between Hf and the boron cages while accommodating the repulsion between Y and the cages. Consequently, the large empty space present in $Y_{0.25}Hf_{0.75}B_{12}$ disrupts the cage structure, resulting in the least compact unit cell and the lowest differential strain. This is in good agreement with the Vickers hardness results (**Table 5.1**) and suggests that $Y_{0.25}Zr_{0.5}Gd_{0.25}B_{12}$ is indeed intrinsically the hardest dodecaboride in the current study.

We then associate the extrinsic hardness with the intrinsic hardness by comparing Vickers hardness with differential strain. Since the indentation hardness is influenced by the crystallographic orientations of the indented grains, a small deviation from the perfect isotropic structure might result in variations in Vickers hardness values.[34] Therefore, the hardness indentations were performed pseudo-randomly to avoid selecting any particular grains. W note that the differential strain also varies with lattice plane. Of the three lattice planes (111, 200, 311) that we analyzed in this study, the (311) lattice plane is a weighted combination of the (111) and (200) planes and should thus be most representative of the overall deformation behavior. Therefore, we plotted the Vickers hardness with respect to differential strain of the (311) plane, as shown in **FIG. 5.6**. We have found that the Vickers hardness is linearly proportional to the differential strain, confirming the solid solution effect in this dodecaboride system. In addition, the fact that all solid solutions show both higher hardness and higher differential strain suggests that doping metal atoms with atomic size mismatch and valence electron density differences enhances the intrinsic hardness through dislocation pinning.

To better compare the trends in **FIG. 5.5** and to speculate about the solid solution effect in the dodecaboride family, we calculated the averaged differential strain of the (111), (200) and (311) lattice planes for all the dodecaborides studied, including those shown in **FIG. 5.5**, and addition

materials with lower quality data that are shown in **FIG. S5.4**.[9] As shown in **FIG. 5.7**, the average differential strain values of the two most compact dodecaborides ($Y_{0.25}Zr_{0.5}Gd_{0.25}B_{12}$ and $Y_{0.5}Zr_{0.5}B_{12}$) fall outside of the linear trend of the other solid solutions, suggesting that the compactness of the unit cell is the major contributing factor to the high hardness.

Lastly, we studied the incompressibility of the dodecaborides by monitoring the change in volume of the unit cell as a function of pressure. The lattice constants calculated from the d-spacings are summarized in **Table S5.1** in the Supporting Information. The bulk modulus, obtained by fitting the compression data to the third-order Birch-Murnaghan EOS, is summarized in **Table 5.1**. The EOS in terms of normalized pressure and Eulerian strain can be found in **FIG. S5.5**. It is important to note that bulk modulus is a measure of elastic deformation reflecting the resistance to shape change with respect to pressure and not a measure of resistance to plastic deformation. Since all the dodecaboride solid solutions have reasonably high bulk moduli (>200 GPa), it can be concluded that the dodecaboride system possesses high incompressibility, but no obvious correlation between the compressibility and hardness was observed.

5.4 Conclusions

A family of dodecaboride solid solutions (ZrB_{12}, YB_{12}, $Zr_{0.5}Y_{0.5}B_{12}$, $Y0_{.25}Hf_{0.75}B_{12}$, $Zr_{0.5}Gd_{0.5}B_{12}$, $Y_{0.5}Gd_{0.25}Hf_{0.25}B_{12}$, $Zr_{0.5}Gd_{0.25}Hf_{0.25}B_{12}$ and $Y_{0.25}Zr_{0.5}Gd_{0.25}B_{12}$) were studied using synchrotron-based XRD under nonhydrostatic compression up to 60 GPa. Lattice specific differential strain analysis shows good consistency with Vickers hardness tests, indicating that Vickers hardness values are dominated by intrinsic hardening effects, despite the complex multiphase nature of these materials. The highest differential strain was achieved in $Y_{0.25}Zr_{0.5}Gd_{0.25}B_{12}$, which also possesses the most compact packing in the unit cell. The high hardness likely arises from the compact atomic packing of metal atoms of complimentary sizes in

the rigid boron cage network. Other anomalously compact structures were similar found to show high differential strain, and structures that were anomalously un-compacts showed lower differential strain. The hydrostatic compression curves obtained at $\varphi = 54.7°$ were also used to calculate bulk moduli by fitting to the Birch-Murnaghan EOS.

Interestingly, no correlation was found between the fraction of different metals in in the solid solution or their difference in metal atom size, as in standard solid-solution hardening. This indicates that it is not the metal itself that dominates the hardness and leads to suppressed slip, but rather how the metal atom modifies and interacts with the nature of the boron cage. With a combination of high hardness and high bulk modulus, metal dodecaborides are potentially desirable light weight materials for applications such as cutting tools and hard protective coatings. This study allows us to begin to understand the structural features that lead to enhanced hardness and how those structural features can be controlled with different dopants, thus providing new insights into the design of novel superhard materials.
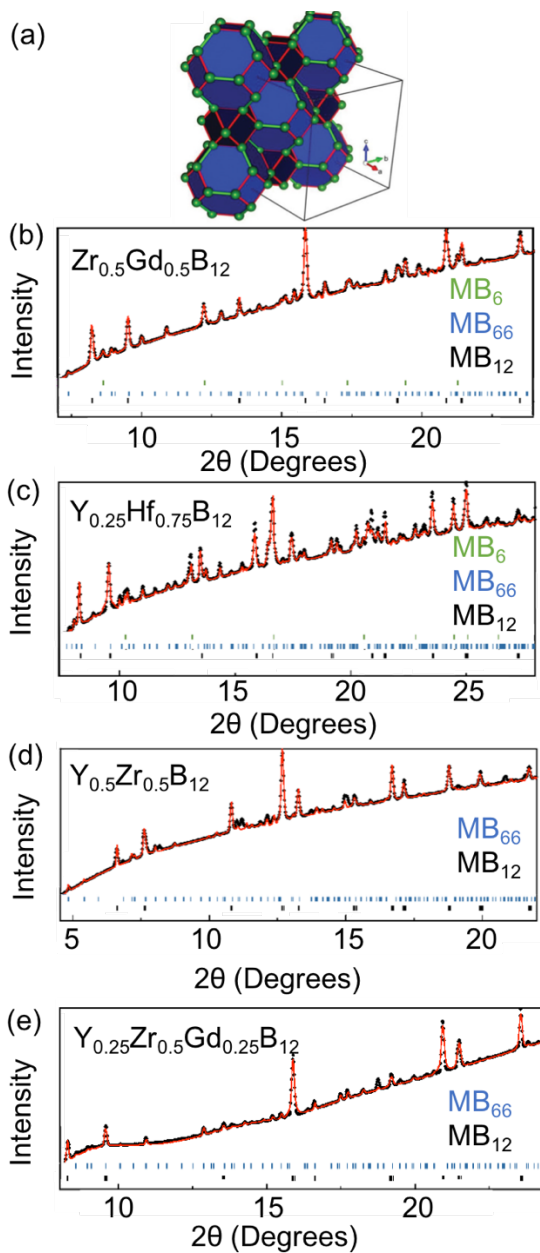
FIG. 5.1. A polyhedral view of crystal structure of (a) metal dodecaborides. Rietveld refinement of X-ray diffraction patterns to the orthorhombic structure for (b) $Zr_{0.5}Gd_{0.5}B_{12}$, (c) $Y_{0.25}Hf_{0.75}B_{12}$, (d) $Y_{0.5}Zr_{0.5}B_{12}$, and (e) $Y_{0.25}Zr_{0.5}Gd_{0.25}B_{12}$. The refinements include the parent MB_{12} phase, as well as any impurities present (MB_2, MB_6, MB_{66}, M = metal). The phases present in each sample are listed in the order of stick patterns shown at the bottom of each graph. Part (a) was reproduced with permission.[9] Copyright 2019, Advanced Functional Materials.

146
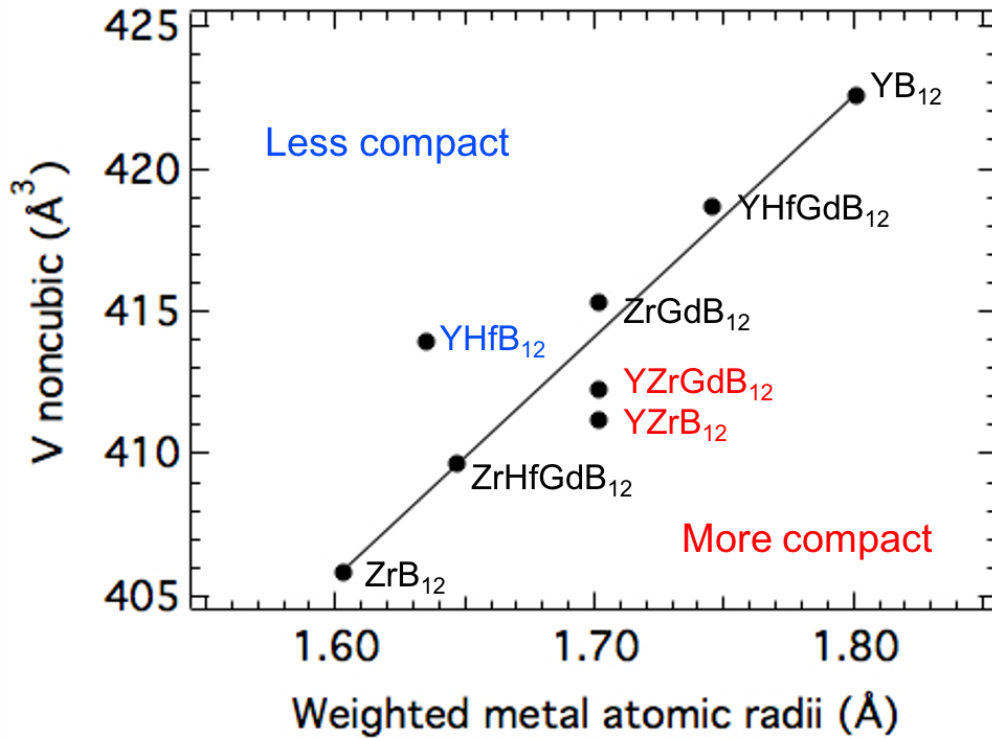
FIG. 5.2. Unit cell volume determined from Rietveld refinement plotted as a function of the weighted metal atomic radii for all MB_{12} samples (ZrB_{12}, YB_{12}, $Zr_{0.5}Y_{0.5}B_{12}$, $Y0_{.25}Hf_{0.75}B_{12}$, $Zr_{0.5}Gd_{0.5}B_{12}$, $Y_{0.5}Gd_{0.25}Hf_{0.25}B_{12}$, $Zr_{0.5}Gd_{0.25}Hf_{0.25}B_{12}$ and $Y_{0.25}Zr_{0.5}Gd_{0.25}B_{12}$). There is an almost perfect correlation between the weighted atomic size and the unit cell volume for most compounds, but a few have either a lower than expected volume (shown in red, more compact), or a higher than expected volume (shown in blue, less compact). These trends do not appear if the unit cell is forced to be cubic. The nominal composition of each MB_{12} solid solution is provided for simplicity.
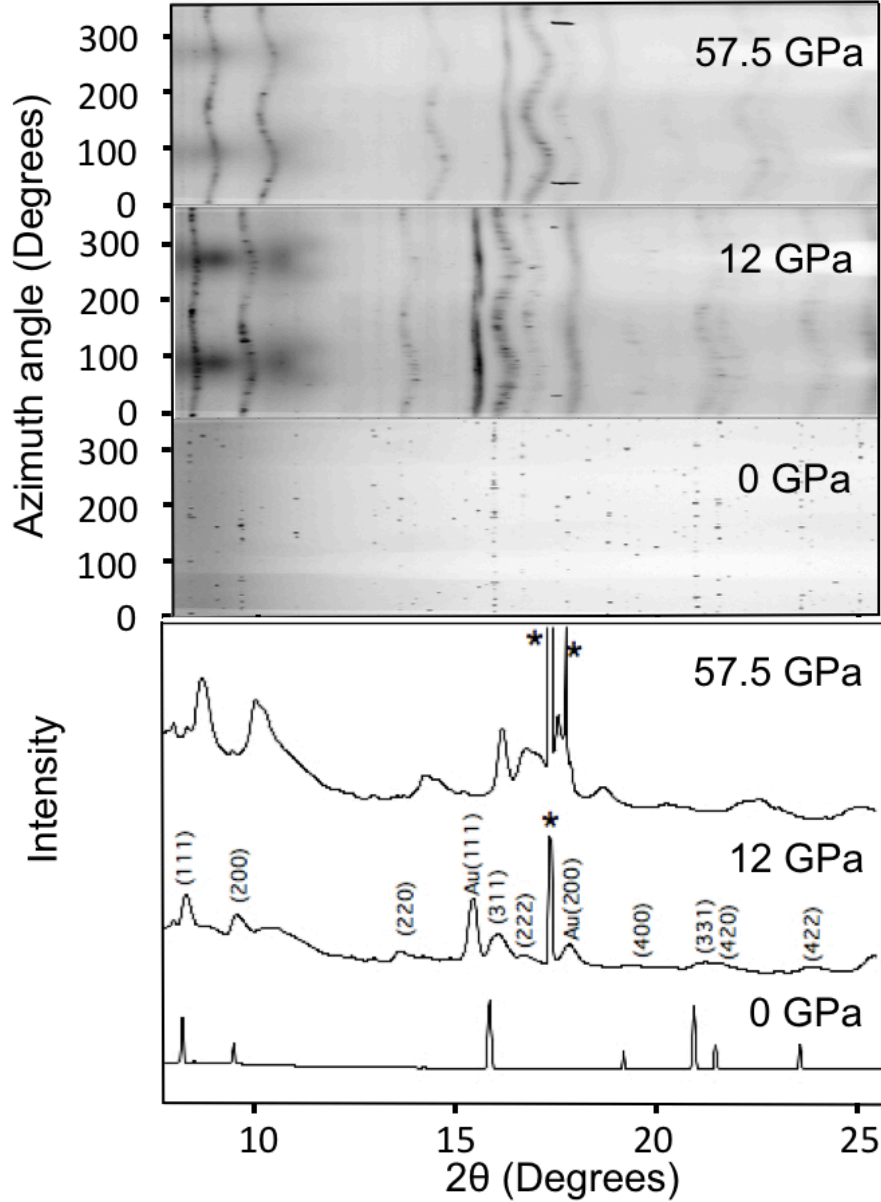
FIG. 5.3. Representative cake patterns (top) and 1-D diffraction patterns (bottom) of $Zr_{0.5}Y_{0.25}Gd_{0.25}B_{12}$ at ambient, low and high pressure. The peaks in the 1-D full integrations broaden as the pressure increases because the integration is averaging over the varying stress states within the high pressure cell. The high intensity peak marked with an asterisk stems from the strong texture of the large grains in the sample.
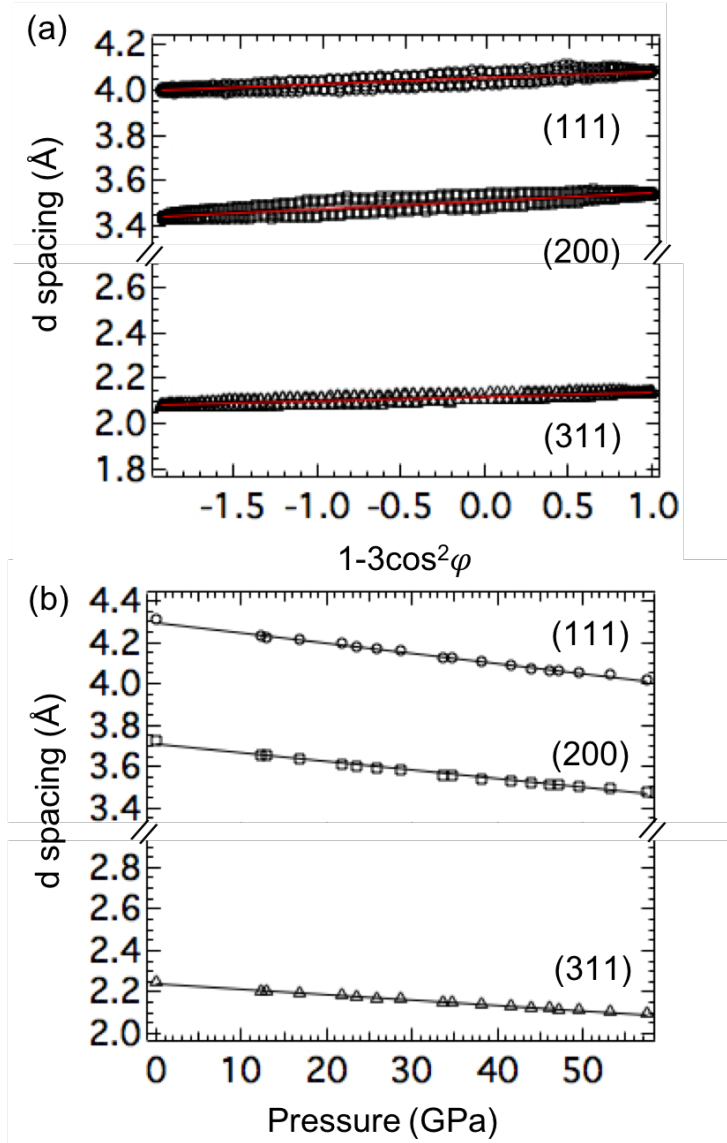
FIG. 5.4. High-pressure diffraction data for $Zr_{0.5}Y_{0.25}Gd_{0.25}B_{12}$. (a) Measured d-spacing vs. $1-3\cos^2\varphi$ at high pressure (57.5 GPa). The data at $1-3\cos^2\varphi=0$ corresponds to quasi-hydrostatic conditions, and those values can be used to generate plots like those in part (b),which plots the hydrostatic d-spacing as a function of pressure for the (111), (200), (311) lattice planes.
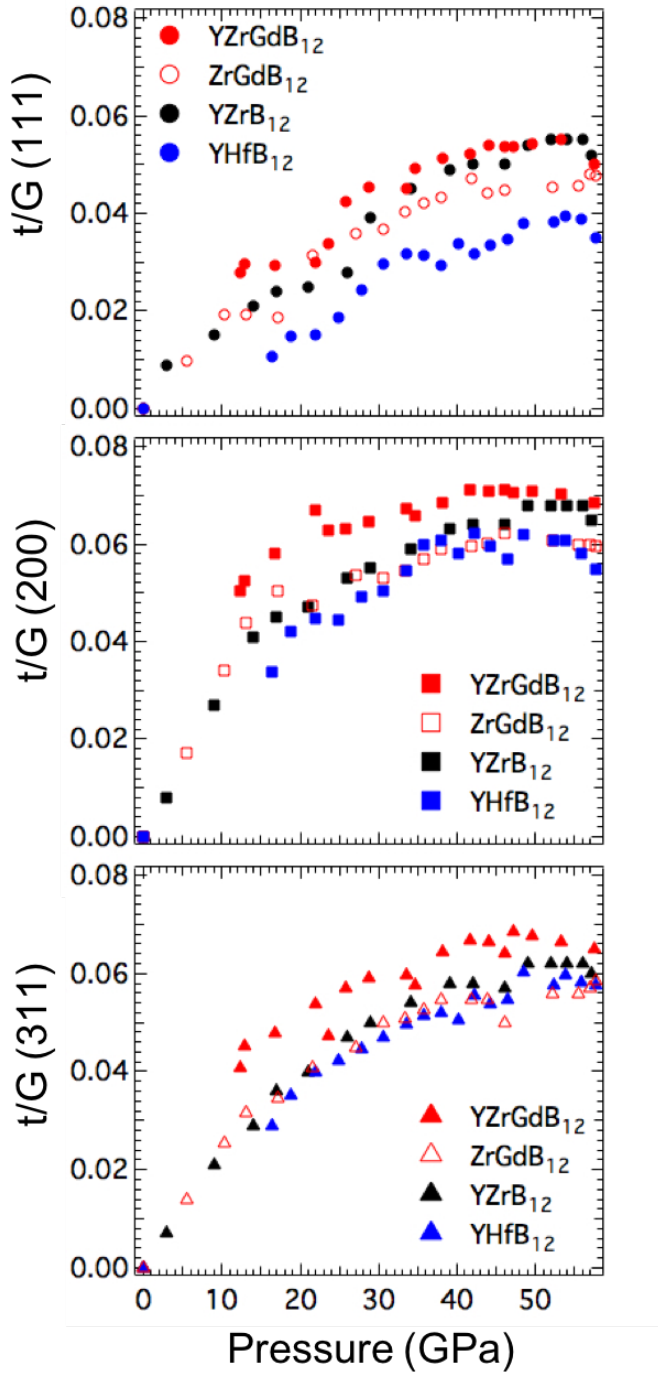
FIG. 5.5. Differential strain (t/G) as a function of pressure for $Zr_{0.5}Gd_{0.5}B_{12}$, $Y_{0.5}Zr_{0.5}B_{12}$, $Y_{0.25}Zr_{0.5}Gd_{0.25}B_{12}$, and $Y_{0.25}Hf_{0.75}B_{12}$. The nominal composition of each MB_{12} solid solution is used in the legend for simplicity. Similar trends in the plateau value of the differential strain are found in all lattice planes.
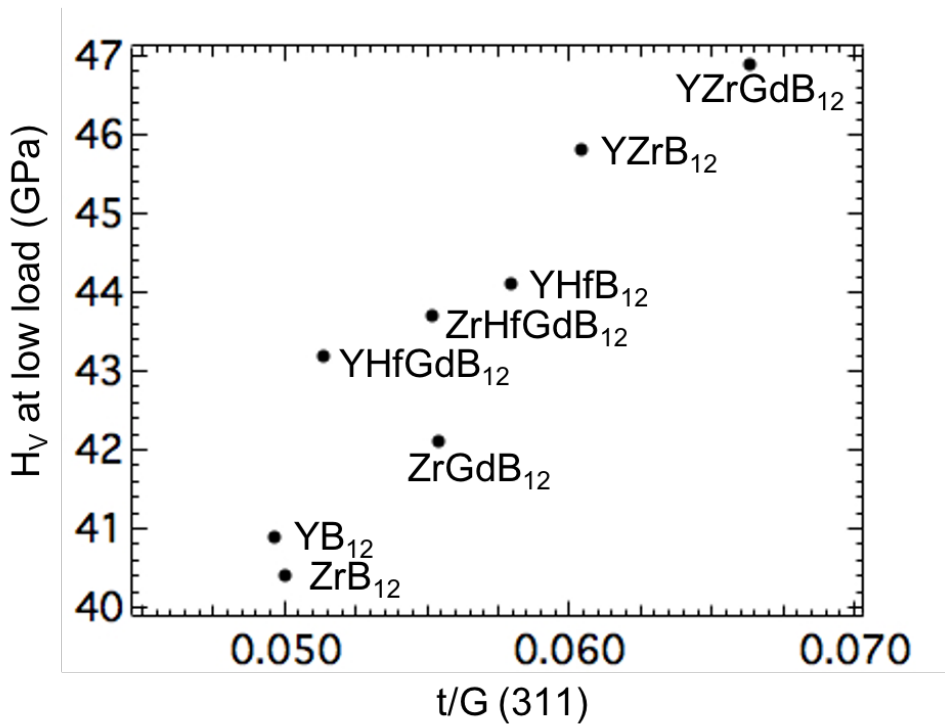
FIG. 5.6. Vickers hardness at low load (0.49 N) vs. the plateau value t/G of the (311) lattice plane for all MB_{12} samples (ZrB_{12}, YB_{12}, $Zr_{0.5}Y_{0.5}B_{12}$, $Y0.25Hf_{0.75}B_{12}$, $Zr_{0.5}Gd_{0.5}B_{12}$, $Y_{0.5}Gd_{0.25}Hf_{0.25}B_{12}$, $Zr_{0.5}Gd_{0.25}Hf_{0.25}B_{12}$ and $Y_{0.25}Zr_{0.5}Gd_{0.25}B_{12}$). The nominal composition of each MB_{12} solid solution is given for simplicity. A nearly linear correlation between plateau t/G value and Vickers hardness is observed.
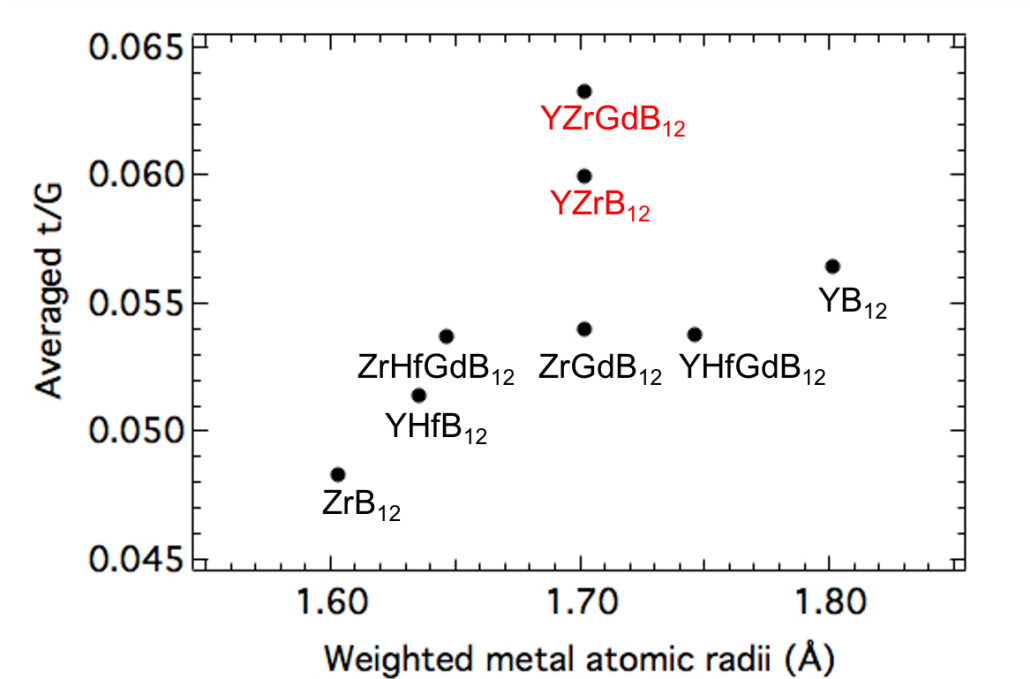
FIG. 5.7. Averaged t/G obtained using the plateau value for the (111), (200), and (311) lattice planes vs. weighted metal atomic radii for all MB_{12} materials (ZrB_{12}, YB_{12}, $Zr_{0.5}Y_{0.5}B_{12}$, $Y_{0.25}Hf_{0.75}B_{12}$, $Zr_{0.5}Gd_{0.5}B_{12}$, $Y_{0.5}Gd_{0.25}Hf_{0.25}B_{12}$, $Zr_{0.5}Gd_{0.25}Hf_{0.25}B_{12}$ and $Y_{0.25}Zr_{0.5}Gd_{0.25}B_{12}$). The nominal composition of each MB_{12} solid solution is used for simplicity.

Table 5.1. Lattice Parameters a, b, c calculated from XRD by Rietveld Refinement, Lattice Constant a Calculated from Vegard's law, Weighted Metal Atomic Radii, Bulk Modulus Calculated using the 3rd order Birch-Murnaghan Equation of State, and Vickers Hardness for all MB_{12} materials examined in this work.

	a_{XRD}[a]	b_{XRD}[a]	c_{XRD}[a]	a_{norm}[b]	Weighted metal atomic radii	Bulk modulus		Vickers Hardness (GPa) at 0.49 N load[b]
ZrB_{12}[c]	7.401(7)	7.401(7)	7.401(7)	7.408	1.603	K_0=276±7	K_0'=2±0.4	41.3±1.1
YB_{12}[c]	7.505(1)	7.505(1)	7.505(1)	7.500	1.801	K_0=238±6	K_0'=3±0.1	41.6±1.3
$Y_{0.5}Zr_{0.5}B_{12}$	7.45826(9)	7.4408(1)	7.4098(2)	7.468	1.702	K_0=320±5	K_0'=1.2±0.1	45.8±1.3
$Zr_{0.5}Hf_{0.25}Gd_{0.25}B_{12}$	7.4267(5)	7.4267(5)	7.4267(5)	7.429	1.647	K_0=294±14.6	K_0'=1.2±0.2	43.7±1.8
$Y_{0.5}Hf_{0.25}Gd_{0.25}B_{12}$	7.4759(5)	7.4511(3)	7.5159(3)	7.478	1.746	K_0=266±6	K_0'=1.96±0.13	43.2±2
$Zr_{0.5}Gd_{0.5}B_{12}$	7.46559(1)	7.46576(6)	7.45090(5)	7.468	1.702	K_0=190±1	K_0'=4	42.1±1.9
$Y_{0.25}Hf_{0.75}B_{12}$	7.4560(5)	7.4346(5)	7.4666(1)	7.409	1.635	K_0=231±2.5	K_0'=2.2±0.05	44.1±1.7
$Y_{0.25}Zr_{0.5}Gd_{0.25}B_{12}$	7.46353(6)	7.4177(2)	7.44679(7)	7.463	1.702	K_0=214±2.7	K_0'=2.7±0.09	46.9±2.4

[a] From MAUD, errors are given in brackets. [b] Adopted from Akopov *et al.* [Ref 6]. [c] Adopted from Lei *et al.* [Ref 9].

5.5 Supporting information

Table S5.1: Lattice Constants of $Zr_{0.5}Gd_{0.5}B_{12}$, $Y_{0.25}Hf_{0.75}B_{12}$, $Y_{0.25}Zr_{0.5}Gd_{0.25}B_{12}$, and $Y_{0.5}Hf_{0.25}Gd_{0.25}B_{12}$, $Zr_{0.5}Hf_{0.25}Gd_{0.25}B_{12}$ Under Pressure

$Zr_{0.5}Gd_{0.5}B_{12}$		$Y_{0.25}Hf_{0.75}B_{12}$		$Y_{0.25}Zr_{0.5}Gd_{0.25}B_{12}$	
a(Å)	P(GPa)	a(Å)	P(GPa)	a(Å)	P(GPa)
6.973(12)	57.68(9)	6.978(16)	57.59(5)	6.958(8)	57.53(6)
6.983(10)	57.01(9)	6.985(15)	55.78(5)	6.992(9)	53.22(5)
6.995(12)	55.45(9)	6.993(16)	53.83(5)	7.016(10)	49.54(5)
7.004(14)	52.24(8)	7.006(13)	52.32(7)	7.031(10)	47.27(5)
7.030(22)	46.11(9)	7.027(16)	48.44(5)	7.037(9)	46.08(5)
7.062(12)	43.91(6)	7.043(16)	46.48(5)	7.051(9)	44.03(5)
7.078(14)	41.84(7)	7.058(14)	44.20(4)	7.068(9)	41.60(5)
7.109(14)	38.03(6)	7.073(20)	42.26(4)	7.097(11)	38.16(4)
7.125(14)	35.83(7)	7.090(13)	40.22(4)	7.130(11)	34.59(5)
7.139(15)	33.31(5)	7.108(21)	37.90(4)	7.131(12)	33.56(4)
7.164(19)	30.56(5)	7.125(18)	35.77(4)	7.185(14)	28.76(5)
7.187(22)	27.15(5)	7.146(16)	33.50(4)	7.197(15)	25.78(4)
7.230(21)	21.51(6)	7.168(19)	30.50(4)	7.219(18)	23.59(4)
7.272(23)	17.23(6)	7.195(24)	27.86(4)	7.240(20)	21.85(3)
7.314(13)	13.08(4)	7.221(27)	24.97(4)	7.280(14)	16.82(3)
7.345(4)	10.37(3)	7.245(29)	21.99(4)	7.314(7)	12.89(2)
7.394(2)	5.54(3)	7.272(22)	18.74(4)	7.322(6)	12.26(3)
7.464(1)	0	7.298(19)	16.34(4)	7.455(8)	0
		7.457(3)	0		

154

Zr$_{0.5}$Hf$_{0.25}$Gd$_{0.25}$B$_{12}$		Y$_{0.5}$Hf$_{0.25}$Gd$_{0.25}$B$_{12}$	
a(Å)	P(GPa)	a(Å)	P(GPa)
7.052(26)	48.14(11)	7.079(18)	49.43(6)
7.120(163)	46.64(10)	7.105(34)	45.28(4)
7.059(38)	45.84(12)	7.121(36)	43.05(4)
7.065(59)	43.82(12)	7.148(26)	38.76(4)
7.085(52)	41.20(11)	7.186(5)	36.80(17)
7.090(75)	39.71(12)	7.196(14)	34.09(10)
7.107(42)	37.21(11)	7.207(16)	32.14(5)
7.138(28)	34.19(9)	7.292(21)	22.56(6)
7.158(17)	32.24(9)	7.315(9)	18.22(7)
7.163(34)	30.06(11)	7.360(11)	13.76(5)
7.192(20)	27.58(8)	7.402(30)	7.82(5)
7.210(20)	25.28(9)	7.429(13)	4.98(4)
7.225(15)	22.98(9)	7.476(6)	0
7.253(12)	20.19(9)		
7.275(33)	17.45(7)		
7.306(21)	13.90(8)		
7.375(4)	6.95(4)		
7.415(8)	2.25(3)		
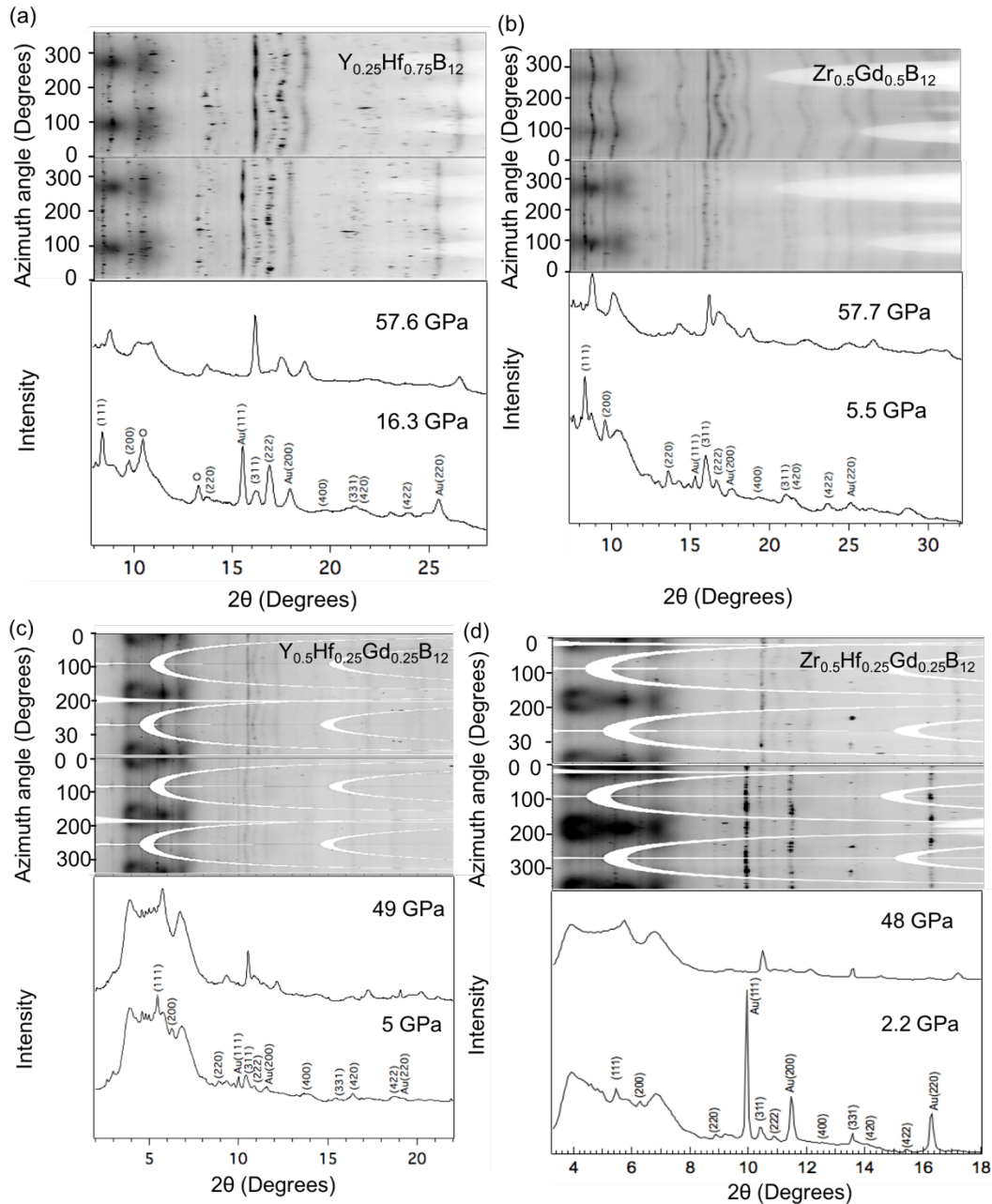
FIG. S5.1: Cake patterns (top) and full integrated 1-D diffraction (bottom) at low and high pressure for (a) $Y_{0.25}Hf_{0.75}B_{12}$, (b) $Zr_{0.5}Gd_{0.5}B_{12}$, (c) $Y_{0.5}Hf_{0.25}Gd_{0.25}B_{12}$, and (d) $Zr_{0.5}Hf_{0.25}Gd_{0.25}B_{12}$. The white arcs in the cake pattern in (c) and (d) are due to the grid lines in the Pilatus detector. Significant broadening is observed in the 1-D integrations at high-pressure due to strain anisotropy in the uniaxially compressed material.
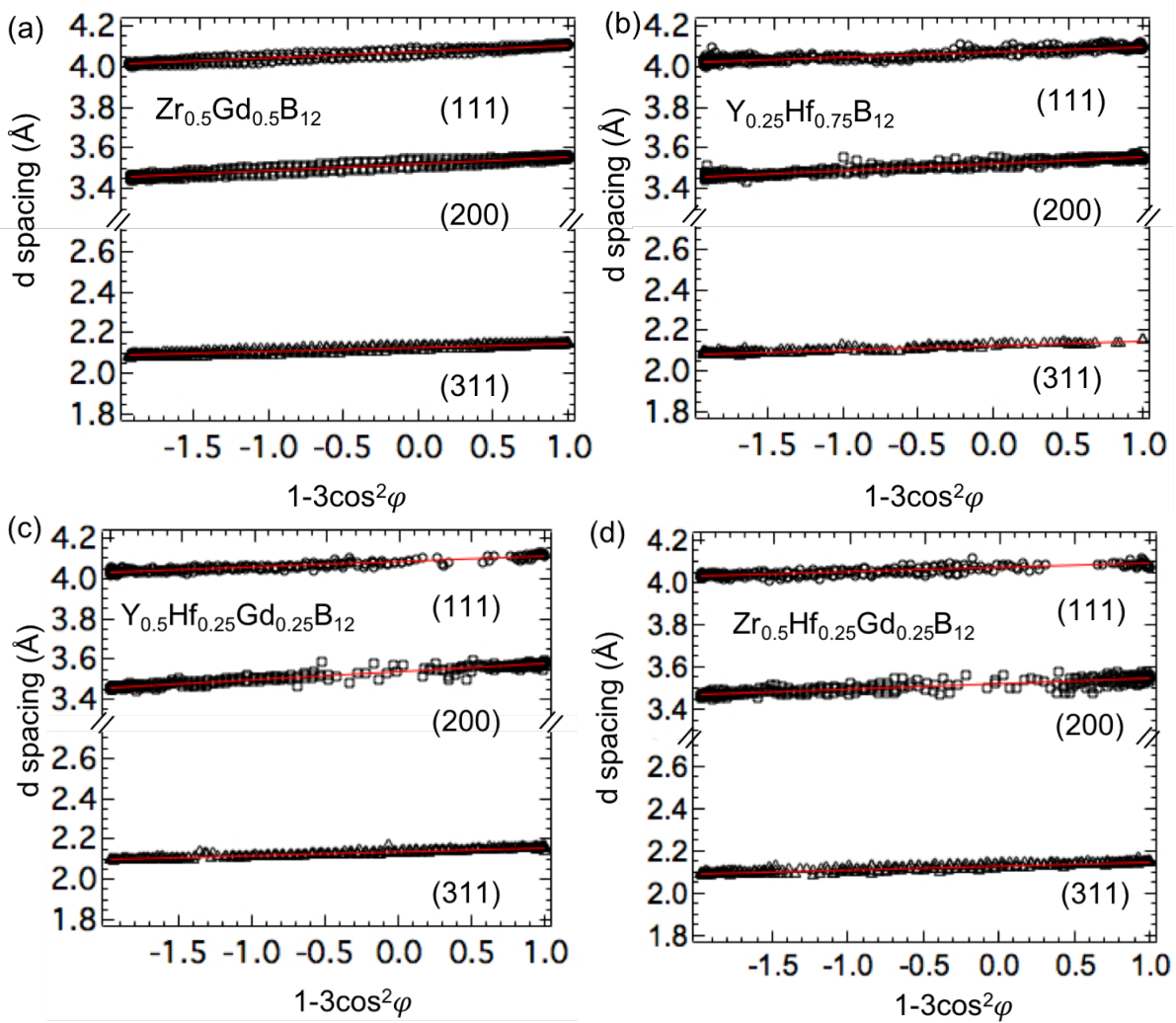
FIG. S5.2: Measured d-spacing vs. $1-3\cos^2\varphi$ at the highest pressure for (a) $Zr_{0.5}Gd_{0.5}B_{12}$, (b) $Y_{0.25}Hf_{0.75}B_{12}$, (c) $Y_{0.5}Hf_{0.25}Gd_{0.25}B_{12}$, and (d) $Zr_{0.5}Hf_{0.25}Gd_{0.25}B_{12}$.
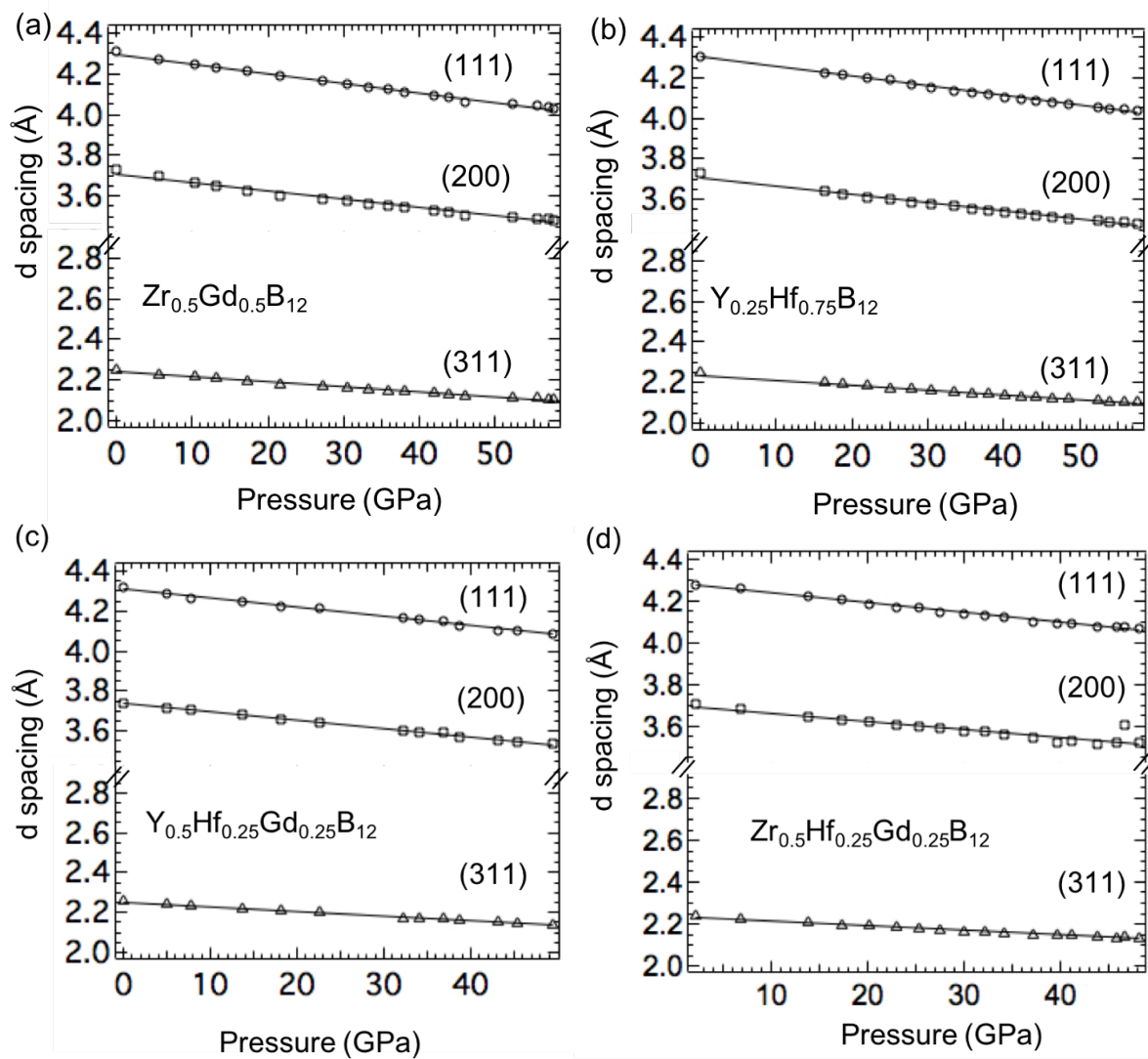
FIG. S5.3: Measured d-spacing vs. pressure for the (111), (200), (311) lattice planes in (a) $Zr_{0.5}Gd_{0.5}B_{12}$, (b) $Y_{0.25}Hf_{0.75}B_{12}$, (c) $Y_{0.5}Hf_{0.25}Gd_{0.25}B_{12}$, and (d) $Zr_{0.5}Hf_{0.25}Gd_{0.25}B_{12}$.
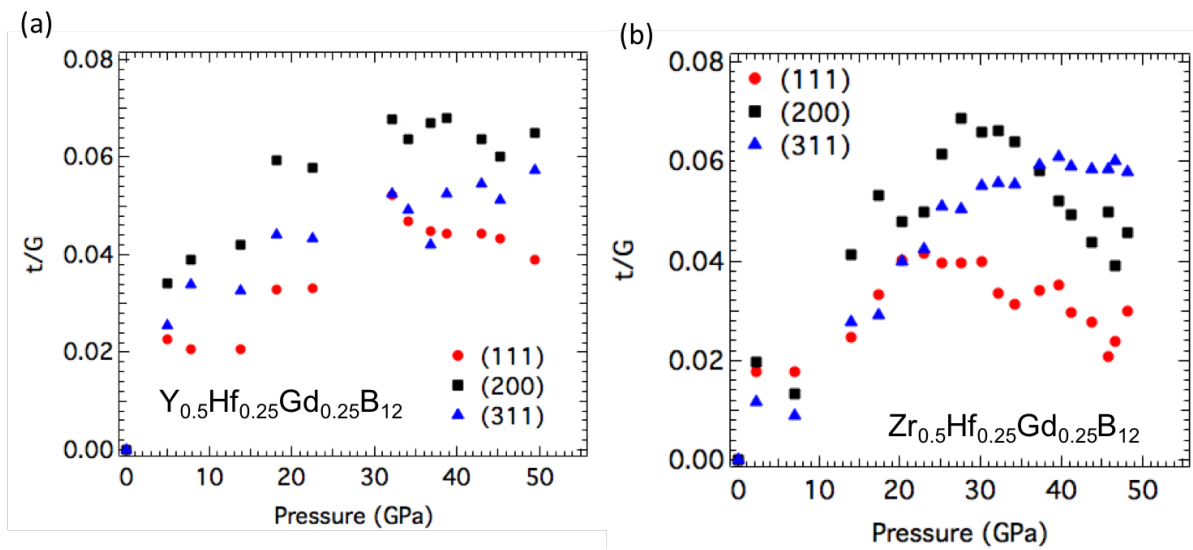
FIG. S5.4: Measure t/G vs. pressure for (a) $Y_{0.5}Hf_{0.25}Gd_{0.25}B_{12}$, and (b) $Zr_{0.5}Hf_{0.25}Gd_{0.25}B_{12}$.
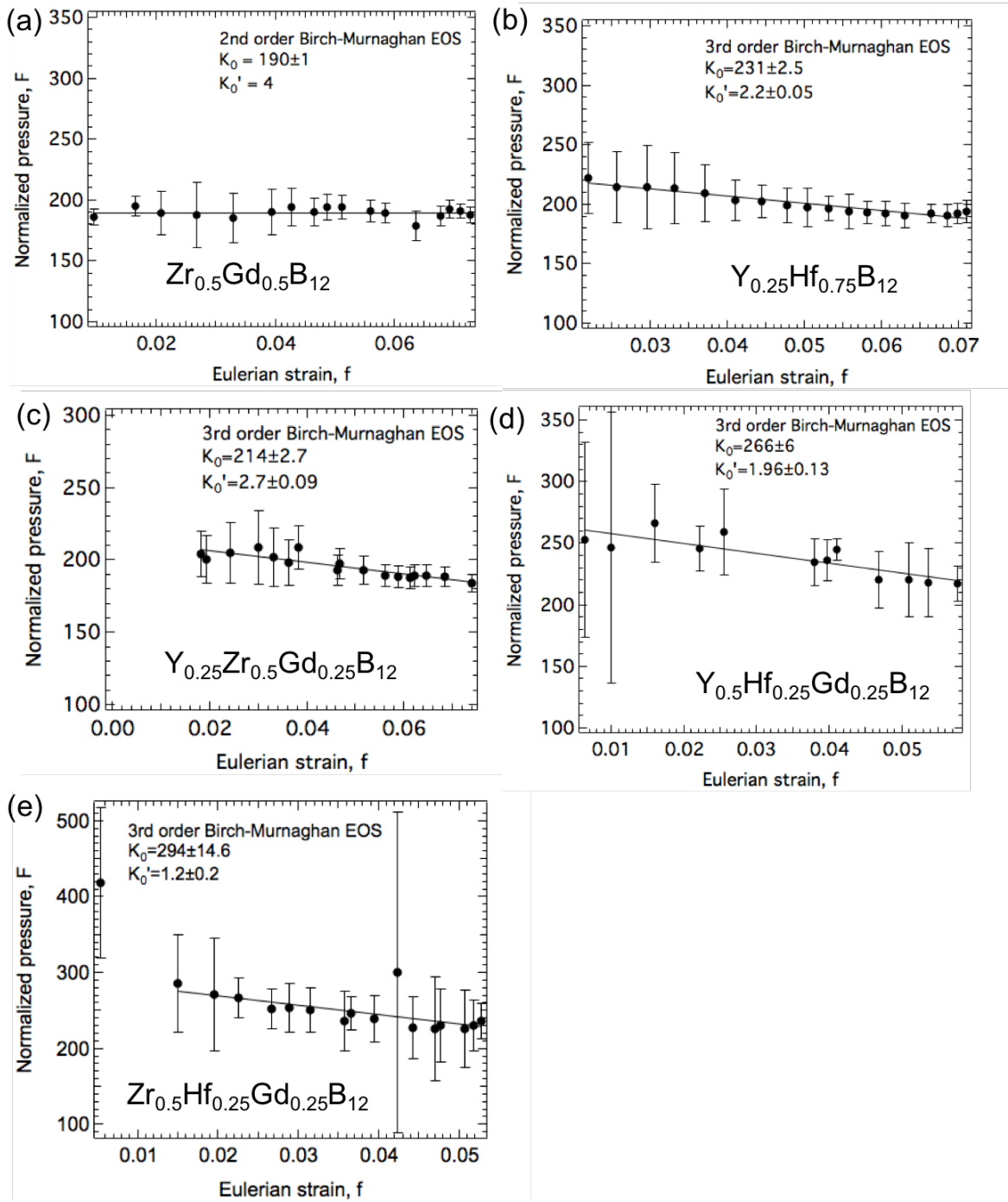
FIG. S5.5: Normalized pressure, F vs. Eulerian strain, f for (a) $Zr_{0.5}Gd_{0.5}B_{12}$, (b) $Y_{0.25}Hf_{0.75}B_{12}$, (c) $Y_{0.25}Zr_{0.5}Gd_{0.25}B_{12}$, (d) $Y_{0.5}Hf_{0.25}Gd_{0.25}B_{12}$, and (e) $Zr_{0.5}Hf_{0.25}Gd_{0.25}B_{12}$. The lines correspond to the best fit of the BM-EOS. The intercept of the line yields the ambient pressure bulk modulus (K_0) and the slope yields the pressure derivative (K_0').

5.6 References

1. Komanduri, R. & Shaw, M. C. Wear of synthetic diamond when grinding ferrous metals. *Nature* **255**, 211–213 (1975).

2. Taniguchi, T., Akaishi, M. & Yamaoka, S. Mechanical Properties of Polycrystalline Translucent Cubic Boron Nitride as Characterized by the Vickers Indentation Method. *Journal of the American Ceramic Society* **79**, 547–549 (1996).

3. Westraadt, J. E., Sigalas, I. & Neethling, J. H. Characterisation of thermally degraded polycrystalline diamond. *International Journal of Refractory Metals and Hard Materials* **48**, 286–292 (2015).

4. Levine, J. B., Tolbert, S. H. & Kaner, R. B. Advancements in the Search for Superhard Ultra-Incompressible Metal Borides. *Advanced Functional Materials* **19**, 3519–3533 (2009).

5. La Placa, S., Binder, I. & Post, B. Binary dodecaborides. *Journal of Inorganic and Nuclear Chemistry* **18**, 113–117 (1961).

6. Akopov, G., Roh, I., Sobell, Z. C., Yeung, M. T. & Kaner, R. B. Investigation of ternary metal dodecaborides (M1M2M3)B12 (M1, M2 and M3 = Zr, Y, Hf and Gd). *Dalton Trans.* **47**, 6683–6691 (2018).

7. Liang, Y. *et al.* Thermodynamic Ground States of Multifunctional Metal Dodecaborides. *Chem. Mater.* **31**, 1075–1083 (2019).

8. Matkovich, V. I., Economy, J., Giese, R. F. & Barrett, R. The structure of metallic dodecarborides. *Acta Cryst* **19**, 1056–1058 (1965).

9. Lei, J. *et al.* Radial X-Ray Diffraction Study of Superhard Early Transition Metal Dodecaborides under High Pressure. *Advanced Functional Materials* **29**, 1900293 (2019).

10. Yeung, M. T., Mohammadi, R. & Kaner, R. B. Ultraincompressible, Superhard Materials. *Annual Review of Materials Research* **46**, 465–485 (2016).

11. Vegard, L. Die Konstitution der Mischkristalle und die Raumfüllung der Atome. *Zeitschrift fur Physik* **5**, 17–26 (1921).

12. Cannon, J. F. & Farnsworth, P. B. High pressure syntheses of ThB12 and HfB12. *Journal of the Less Common Metals* **92**, 359–368 (1983).

13. Akopov, G., Yeung, M. T., Turner, C. L., Mohammadi, R. & Kaner, R. B. Extrinsic Hardening of Superhard Tungsten Tetraboride Alloys with Group 4 Transition Metals. *J. Am. Chem. Soc.* **138**, 5714–5721 (2016).

14. Singh, A. K. The lattice strains in a specimen (cubic system) compressed nonhydrostatically in an opposed anvil device. *Journal of Applied Physics* **73**, 4278–4286 (1993).

15. Singh, A. K. Analysis of nonhydrostatic high-pressure diffraction data (cubic system): Assessment of various assumptions in the theory. *Journal of Applied Physics* **106**, 043514 (2009).

16. Hemley, R. J. *et al.* X-ray Imaging of Stress and Strain of Diamond, Iron, and Tungsten at Megabar Pressures. *Science* **276**, 1242–1245 (1997).

17. He, D. & Duffy, T. S. X-ray diffraction study of the static strength of tungsten to 69 GPa. *Phys. Rev. B* **73**, 134106 (2006).

18. Merkel, S. *et al.* Deformation of polycrystalline MgO at pressures of the lower mantle: DEFORMATION OF MgO AT HIGH PRESSURE. *J. Geophys. Res.* **107**, ECV 3-1-ECV 3-17 (2002).

19. Hammersley, A. P., Svensson, S. O., Hanfland, M., Fitch, A. N. & Hausermann, D. Two-dimensional detector software: From real detector to idealised image or two-theta scan. *High Pressure Research* **14**, 235–248 (1996).

20. Ruoff, A. L. Stress anisotropy in opposed anvil high−pressure cells. *Journal of Applied Physics* **46**, 1389–1392 (1975).

21. Singh, A. K., Mao, H., Shu, J. & Hemley, R. J. Estimation of Single-Crystal Elastic Moduli from Polycrystalline X-Ray Diffraction at High Pressure: Application to FeO and Iron. *Phys. Rev. Lett.* **80**, 2157–2160 (1998).

22. Birch, F. Finite strain isotherm and velocities for single-crystal and polycrystalline NaCl at high pressures and 300°K. *Journal of Geophysical Research: Solid Earth* **83**, 1257–1268 (1978).

23. Meade, C. & Jeanloz, R. Static compression of Ca(OH)2 at room temperature: Observations of amorphization and equation of state measurements to 10.7 GPa. *Geophysical Research Letters* **17**, 1157–1160 (1990).

24. Rietveld, H. M. A profile refinement method for nuclear and magnetic structures. *Journal of Applied Crystallography* **2**, 65–71 (1969).

25. Lutterotti, L., Chateigner, D., Ferrari, S. & Ricote, J. Texture, residual stress and structural analysis of thin films using a combined X-ray analysis. *Thin Solid Films* **450**, 34–41 (2004).

26. Lutterotti, L. Total pattern fitting for the combined size–strain–stress–texture determination in thin film diffraction. *Nuclear Instruments and Methods in Physics Research Section B: Beam Interactions with Materials and Atoms* **268**, 334–340 (2010).

27. Cannon, J. F., Cannon, D. M. & Tracy Hall, H. High pressure syntheses of SmB2 and GdB12. *Journal of the Less Common Metals* **56**, 83–90 (1977).

28. Akopov, G., Sobell, Z. C., Yeung, M. T. & Kaner, R. B. Stabilization of LnB $_{12}$ (Ln = Gd, Sm, Nd, and Pr) in Zr $_{1-x}$ Ln $_{x}$ B $_{12}$ under Ambient Pressure. *Inorg. Chem.* **55**, 12419–12426 (2016).

29. Akopov, G., Yeung, M. T., Turner, C. L., Li, R. L. & Kaner, R. B. Stabilization of HfB $_{12}$ in Y $_{1-x}$ Hf $_{x}$ B $_{12}$ under Ambient Pressure. *Inorg. Chem.* **55**, 5051–5055 (2016).

30. Dubrovinsky, L. *et al.* The most incompressible metal osmium at static pressures above 750 gigapascals. *Nature* **525**, 226–229 (2015).

31. Amulele, G. M., Manghnani, M. H. & Somayazulu, M. Application of radial x-ray diffraction to determine the hydrostatic equation of state and strength of TiB2 up to 60GPa. *Journal of Applied Physics* **99**, 023522 (2006).

32. He, D., Shieh, S. R. & Duffy, T. S. Strength and equation of state of boron suboxide from radial x-ray diffraction in a diamond cell under nonhydrostatic compression. *Phys. Rev. B* **70**, 184121 (2004).

33. Kanoun, M. B., Hermet, P. & Goumri-Said, S. Structure, Elastic Stiffness, and Hardness of Os $_{1-x}$ Ru $_{x}$ B $_{2}$ Solid Solution Transition-Metal Diborides. *J. Phys. Chem. C* **116**, 11746–11751 (2012).

34. Chung, H.-Y. *et al.* Synthesis of Ultra-Incompressible Superhard Rhenium Diboride at Ambient Pressure. *Science* **316**, 436–439 (2007).

Chapter 6

Synthesis and High Pressure Mechanical Properties of Superhard Rhenium/Tungsten Diboride Nanocrystals

6.1 Introduction

As new state-of-the-art materials and metals are discovered and synthesized, the demand for materials capable of cutting, forming, and shaping those new materials grows. Diamond, the world's hardest natural material, cannot be effectively used for cutting and drilling ferrous metals because of its poor thermal stability in air and its tendency to form carbides.[1-3] Cubic boron nitride (c-BN), an alternative to diamond, is of interest because of its high hardness and excellent chemical stability,[4] but high pressure is a necessary to synthesize c-BN, which again limits its use. In 2007, rhenium diboride (ReB_2) was successfully synthesized by arc melting at ambient pressure.[5] ReB_2 shows a third order bulk modulus of 340 GPa[6] and a Vickers hardness (H_v) as high as 40.5 GPa[7] under an applied load of 0.49 N. Although its hardness value only narrowly surpasses the threshold for superhard materials (H_v >40 GPa), it is still capable of scratching a natural diamond.[8]

It has been reported that the hardness of ReB_2 can be increased to ~48 GPa *via* solid solution hardening (*i.e.* $Re_{1-x}W_xB_2$) where tungsten is added into the host lattice.[9] Interestingly, pure tungsten diboride (WB_2) has been shown to be ultra-incompressible, but not superhard,[10-15] because it takes a crystal structural that is intermediate between that of ReB_2 (*P6₃/mmc*, containing corrugated boron layers alternating with metal layers; **FIG. 6.1a**) and AlB_2 (*P6/mmm*, containing flat boron sheets, again alternating with metal layers). The WB_2 structure consists of alternating

corrugated and planar boron sheets (**FIG. 6.1b**). The presence of any planar boron sheets provides easy slip planes and significantly reduces the hardness of the material. We have previously shown that the ReB_2-type structure can be maintained with tungsten content up to 48 at. % for $Re_{1-x}W_xB_2$ solid solutions, providing a large window for solid solution based hardness enhancement. [9]

While we have found that crystal engineering to tune the intrinsic hardness of a material is an excellent method to enhance hardness, in many cases extrinsic effects, such as finite size or multiphase effects, can produce even greater enhancement. It turns out that the extremely high hardness in $W_{0.92}Zr_{0.08}B_4$ (H_v = 55 GPa) and $W_{0.99}Re_{0.01}B_4$ (H_v = 50 GPa) can be explained by morphological control and secondary phase dispersion hardening, respectively.[16,17] One would expect that a higher hardness for ReB_2 can be achieved by reducing its grain size, known as the Hall-Petch effect. Indeed, work in other nanoscale systems has shown fantastic enhancements. Chen *et al* has demonstrated that the stress-induced dislocation activity can be suppressed to a significant extent for 3 nm Ni nanocrystals.[18] Although Ni metal is not superhard, it provides insights for the potential to tune mechanical properties by changing slip systems. The challenge is that forming nanostructured superhard materials is still synthetically difficult. Mechanical grinding below the micron scale is extremely challenging for superhard materials. All reported synthetic routes to nanocrystalline superhard materials typically require applied pressure in gigapascals. Nano-twinned c-BN has been prepared under pressure of 15 GPa by using an onion-like BN as the precursor and this material showed unparalleled hardness.[19] Similarly, nano-twinned diamond was synthesized at 20 GPa and 2000 ºC using a high-energy metastable carbon as the precursor and the resultant materials had a Vickers hardness as high as 200 GPa.[20]

A bottom-up synthetic route to nanoscale transition metal borides based on $Sn/SnCl_2$ redox chemistry was recently reported.[21] Here, elemental boron and anhydrous metal chlorides were

166

mixed with Sn in a glove box and sealed in a quartz ampoule under vacuum. This was followed by heat treatment between 700-900 °C. A variety of transition metal borides with the general composition of M_xB_y (x, y = 1 - 4), where M is a 3d, 4d, or 5d element, can be made through this method, such as TaB_2, NbB_2, Mo_2B and MoB_2. Portehault *et al.* also reported a general solution route toward metal boride nanocrystals using solid metal chlorides and sodium borohydride as metal and boron sources.[22] A LiCl/KCl eutectic was chosen as the flux. Various systems ranging from hexaborides to monoborides such as CaB_6, MoB_4, NbB_2 and FeB were synthesized to demonstrate the generality of this approach. However, many of the superhard members of the metal boride families have yet to be explored.

As discussed above, all superhard nanocrystals reported to date have been synthesized under high pressure. Here, we report a synthetic approach to make nanocrystalline versions of the superhard materials ReB_2 (n-ReB_2) and $Re_{0.52}W_{0.48}B_2$ (n-$Re_{0.52}W_{0.48}B_2$) *via* molten salt flux growth at ambient pressure. We then use synchrotron-based angle dispersive X-ray diffraction (XRD) experiments in a radial geometry using a diamond anvil cell (DAC)[23] to determine the bulk modulus of these new materials and to examine the differential stress in a lattice plane specific manner up to ~60 GPa. The differential stress has been commonly considered as a good estimate of yield strength in many studies, and it is found to strongly correlate to hardness.[24-30] Differential stress can only be measured through radial diffraction, where the sample is compressed non-hydrostatically, rather than the traditional axial diffraction, where a hydrostatic pressure medium[31] is employed. Radial diffraction studies have the added benefit that very small sample volumes are needed, and that powders can be studied directly, without the need for first compacting them.

Another advantage for radial diffraction over axial diffraction is that texture in the radial geometry is sensitive to the active slip systems as well as stress,[32-34] which enables elucidation of

the microscopic deformation mechanisms controlling the plastic behavior of the material.[18,35] Through an understanding of the mechanisms by which available slip systems are tuned, we have the potential to rationally design the next generation of ultra-hard metal borides. Such ideas have been used previously for a range of superhard metal borides. For example, Yeung *et al.* found that the intrinsic yield strength of tungsten monoboride could be dramatically improved by removing the slip plane through selective substitution of the malleable tungsten bilayer with Ta.[29,30,36] This substitution pushes the originally non-superhard boride into the superhard regime, demonstrating an effective design strategy. Although there are theoretical calculations predicting the slip systems for ReB_2,[37-39] to date there are no papers where lattice preferred orientation and deformation mechanisms under high pressure are experimentally investigated.

In this work, we combine all of these ideas to examine how both finite size effects and solid-solution formation can be used to enhance hardness in a family of materials based on ReB_2. Radial diffraction is used instead of indentation hardness, because solid compacts of the nanocrystal based materials have not been fabricated and so these materials are not amenable to traditional hardness measurements. Because of the high quality of nanocrystal based powder diffraction, however, we are able to extract a much higher level of information from the radial diffraction, gaining insight into both the bulk slip systems, and the effect of atomic substitution on those slip systems. We specifically compare bulk ReB_2 with n-ReB_2 to examine size effects. We then compare bulk ReB_2 with bulk $Re_{0.52}W_{0.48}B_2$ in mechanical properties to examine how solid solutions can enhance hardness. Finally, we combine these two approaches in nanoscale $Re_{0.52}W_{0.48}B_2$ (n-$Re_{0.52}W_{0.48}B_2$) to examine the synergistic effects of using both finite size effects and solid-solution hardening. In the future, spark plasma sintering (SPS) will be adopted to produce a solid bulk compact of nanocrystals. Because of its very high heating rate, this rapid sintering process may avoid

excessive coarsening and therefore maintain the outstanding mechanical properties of these nanocrystals into practical bulk materials.

6.2 Experimental procedure

A. Synthesis of n-ReB₂

Elemental rhenium (99.99%, CERAC Inc., U.S.A) and amorphous boron (99+%, Strem Chemicals, U.S.A) powders were uniformly mixed in the molar ratio Re:B = 1:4 using an agate mortar and pestle. Note that the reaction needs the excess boron to avoid forming lower borides. We then added 100x excess NaCl (99.5%, Sigma-Aldrich, U.S.A) by weight to the mixture and ground for 30 min, followed by transferring into an alumina boat for heat treatment in a tube furnace under flowing argon. The heating profile was set as follows: ramp up to 850 ºC over 1.5 h, dwell for another 1.5 h and then cool down to room temperature over 5 h. Each sample was washed in water and centrifuged several times in order to remove the NaCl. The resulting powders were characterized by powder X-ray diffraction (PXRD), scanning electron microscopy (SEM).

B. Synthesis of bulk Re$_{0.52}$W$_{0.48}$B₂

Bulk Re$_{0.52}$W$_{0.48}$B₂ was prepared by arc melting. Tungsten and rhenium powders were mixed with amorphous boron at a molar ratio (total metal:boron) of 1:2.25 followed by pressing into pellets. Subsequently, the pellets were arc melted and cooled in argon gas. The synthesis details can be found in Ref. 9. The ingot was then crushed and ground with a Plattner's-style hardened tool-steel mortar and pestle set (Humboldt Mfg., Model H-17270). The resulting powder was sieved with a No. 635 mesh sieve (Humboldt Mfg.) to ensure its particle size is ≤~20 µm.

C. Synthesis of n-Re$_{0.52}$W$_{0.48}$B₂

Tungsten and rhenium metal powders were mixed and pre-alloyed in arc-melter. The resultant ingot was then crushed out and ground with a Plattner's-style hardened tool-steel mortar and pestle

set (Humboldt Mfg., Model H-17270). Subsequently, the metal powders were mixed with boron and NaCl following the same experimental procedure used for the n-ReB$_2$ synthesis.

D. Synthesis of bulk ReB$_2$

Bulk ReB$_2$ was prepared by arc melting. Rhenium powders were mixed with amorphous boron at a molar ratio of 1:2.05 followed by pressing into pellets. The extra 0.05 mol of boron compensates for boron evaporation during arc-melting. The pellets were then liquefied in an arc melting furnace under argon gas. The detailed description of the synthesis can be found in previous report.[8] The ingot was then crushed, and ground followed by sieving with a No. 635 mesh sieve (Humboldt Mfg.) to ensure its particle size is ≤~20 μm.

E. Radial X-ray diffraction

The *in situ* angle-dispersive X-ray diffraction experiments under non-hydrostatic pressure were carried out at synchrotron beamline 12.2.2 of the Advanced Light Source (ALS, Lawrence Berkeley National Lab). Nano-ReB$_2$, bulk Re$_{0.52}$W$_{0.48}$B$_2$ and nano-Re$_{0.52}$W$_{0.48}$B$_2$ samples were loaded individually into a sample chamber, with a hole drilled by a laser (~60 μm in diameter) in a boron disc (~400 μm in diameter and ~60 μm in thickness), which is made of amorphous boron and epoxy, subsequently embedded in a rectangular Kapton tape.[40] For most samples, a small piece of platinum foil (~15 μm in diameter) was intentionally placed on top of the sample to serve as an internal pressure standard. No pressure-transmitting medium was added to ensure the presence of non-hydrostatic stress upon compression. More technical details for the DAC may be found in Ref. 33. In this experiment, the incident monochromatic X-ray beam (25 KeV in energy, 20×20 μm in beam size) was perpendicular to the loading axis. The diffracted intensity was recorded using an MAR-345 image plate with pressure steps of ~4 GPa. Calibration of the sample-to-detector distance, beam center and detector tilt, were carried out by using a CeO$_2$ standard and the program

FIT2D.[41] The ring-like diffraction patterns were then "unrolled" into cake diffraction patterns, a plot of azimuthal angle η (with 0° and 180° the low stress directions and 90° and 270° the high stress directions as shown in **FIG. 6.1c and 6.2a,c**) *versus* 2θ. For bulk $Re_{0.52}W_{0.48}B_2$, the diffraction patterns were imported into Igor Pro (WaveMetrics, Inc.), where each diffraction line was analyzed individually. The diffraction data of n-ReB_2 and n-$Re_{0.52}W_{0.48}B_2$ were analyzed by the Rietveld refinement method[42] as implemented in the software package MAUD.[43]

The combination of radial X-ray diffraction and lattice strain theory[44,45,46] enabled us to study the stress state of samples under non-hydrostatic compression in a DAC. A set of orthogonal stress components were applied to the sample upon compression. The stress component σ_l, is parallel to the incident X-ray beam, while σ_3 coincides with the loading axis. The difference between σ_l and σ_3 is termed the uniaxial stress component or differential stress, which is limited by the yield strength of the specimen material according to von Mises yield criterion Equation (6.1):[47]

$$t = \sigma_3 - \sigma_1 \leq 2\tau = \sigma_y \qquad (6.1)$$

where τ is the shear strength and σ_y is the yield strength. The lattice strain produced by t is given by Equation (6.2):

$$[d_m(hkl) - d_p(hkl)]/d_p(hkl) = (1 - 3\cos^2\varphi)Q(hkl). \qquad (6.2)$$

This equation can be rearranged to a commonly used form as follows:

$$d_m(hkl) = d_p(hkl)[1 + (1 - 3\cos^2\varphi)Q(hkl)] \qquad (6.3)$$

where $d_m(hkl)$ denotes the observed *d-spacing* in the presence of a deviatoric stress component, while $d_p(hkl)$ is the *d-spacing* under hydrostatic pressure alone, where φ is the angle between the loading axis and the diffraction plane normal to it.[44,45,46] Note that the actual stress state of the

sample lies between the two extremes determined by the iso-strain[48] and iso-stress[49] conditions, therefore $Q(hkl)$ can be expressed as given in Equation (6.4):

$$Q(hkl) = \left(\frac{t}{3}\right)\{\alpha[2G_R(hkl)]^{-1} + (1-\alpha)(2G_V)^{-1}\}. \quad (6.4)$$

Here G_V and $G_R(hkl)$ are the Voigt shear modulus (iso-strain) and Reuss shear modulus (iso-stress), respectively. For a hexagonal system, the G_V is given by Equation (6.5)[50]

$$30G_V = 7c_{11} - 5c_{12} - 4c_{13} + 12c_{44} + 2c_{33}. \quad (6.5)$$

The expressions of $G_R(hkl)$ in terms of elastic compliance $[S_{ij}]$, can be found in Ref. 46. Approximately, the differential stress from Eq. (6.4) can be written as,

$$t = 6G < Q(hkl) >, \quad (6.6)$$

where $< Q(hkl) >$ stands for the average value over the observed crystallographic reflections and G is the aggregate shear modulus. Equation (6.3) indicates a linear relation between $d_m(hkl)$ and $(1 - 3\cos^2\varphi)$. The slope of the linear fit yields the product $d_p(hkl)Q(hkl)$, which can be used to evaluate and describe contributions of both plastic and elastic deformation.[51,52] The $d_p(hkl)$ obtained from the intercept (with x $= 0$ corresponding to $\varphi = 54.7°$) reflects compression behavior due to the hydrostatic component of stress, which can yield the equivalent hydrostatic compression curve. The zero pressure bulk modulus, K_0, and pressure derivative can then be determined by fitting the compression curve to the third order Birch-Murnaghan equation-of-state (EOS),[53]

$$P = 1.5 K_0 \left[\left(\frac{V}{V_0}\right)^{-\frac{7}{3}} - \left(\frac{V}{V_0}\right)^{-\frac{5}{3}}\right]\{1 - 0.75(4 - K_0')\left[\left(\frac{V}{V_0}\right)^{-\frac{2}{3}} - 1\right]\}. \quad (6.7)$$

Here, the pressure, P, and the unit cell volume, V, are measured at $\varphi = 54.7°$.

6.3 Results and discussion

Previous synthetic efforts have explored reactions between metal halides and sodium borohydride to produce transition metal boride nanocrystals, mainly based on redox chemistry, where the alkali borohydrides serve as both reductant and boron source.[21,22] In contrast, our synthesis of nano-ReB$_2$ and Re$_{0.52}$W$_{0.48}$B$_2$ employed elemental Re and boron to limit impurities. The operative mechanism in our synthesis is closer to the classical solid-state method, where the diffusion of boron into the metal lattice is likely assisted by the molten salt flux. In the synthesis of nano materials, the ratio of metal to boron was kept at 1:4. The excess boron is very important for the synthesis of ReB$_2$ from the elements, as diffusion of boron into the metal lattice to achieve the correct stoichiometry is driven by the presence of excess boron. Indeed, the addition of excess boron is also very common in the synthesis of bulk transition metal borides made by conventional high temperature routes, and is particularly important for superhard borides to thermodynamically drive the formation of phase pure materials. For example, WB$_4$ is typically made at a metal to boron ratio of 1:12.[17] Dodecaborides such as ZrB$_{12}$ and YB$_{12}$ are generally made at a ratio of 1:20.[54] Fortunately, in the radial diffraction experiment, differential strain is measured in a lattice specific manner, and so any extra boron content does not negatively influence the analysis.

In situ XRD studies were conducted under non-hydrostatic compression up to ~60 GPa, 43 GPa and 53 GPa for n-ReB$_2$, bulk Re$_{0.52}$W$_{0.48}$B$_2$ and n-Re$_{0.52}$W$_{0.48}$B$_2$. Two-dimensional diffraction images at low and high pressure and integration diffraction patterns obtained at the magic angle ($\varphi = 54.7°$, effectively hydrostatic conditions) at several pressures are presented for the bulk (**FIG. 6.1c,d**) and nanoscale samples (**FIG. 6.2**). Two dimensional plots evolve from straight lines at low pressure, indicating a hydrostatic stress state, to wavy lines at high pressure, indicating a well-defined high and low stress direction. Integrated diffraction patterns at the magic angle smoothly shift to higher angle (smaller lattice constant) with increasing pressure. Note that the pressure for

each compression step was derived from the equation-of-state of an internal standard,[55] using its lattice parameter at $\varphi = 54.7°$. This explains why the diffraction peaks of Pt are present in the diffraction patterns shown in Figs. 1c,d and 2c,d. A small amount of unreacted Re was found in n-ReB_2, as can be seen in **FIG. 6.2a,b**. Re is also a common pressure standard, like Pt, and its equation-of-state has been well studied.[56-59] As a result, no additional internal standard was needed for this sample.

The data show that the addition of tungsten expands the hexagonal-close-packed metal lattice because W (1.41 Å) is larger than Re (1.37 Å) in atomic size,[60] which causes the peaks to shift towards lower angles in the ambient pressure diffraction data in **FIG. 6.2d**, compared to the stick reference pattern of ReB_2 (Joint Committee on Powder Diffraction Standards Card #00-006-0541). No pure W phase peaks were observed in the patterns across the entire pressure range, suggesting that WB_2 and ReB_2 do indeed form a solid solution. All diffraction peaks for $Re_{0.52}W_{0.48}B_2$, n-ReB_2, and n-$Re_{0.52}W_{0.48}B_2$ can be cleanly indexed to the ReB_2-type structure. Note that some peaks and the amorphous humps below 10° 2θ (labeled with open stars) do not shift with pressure, and these are from the boron gasket. The background scan for the gasket alone can be found in **FIG. S6.1**. There is also a small impurity phase found in the n-$Re_{0.52}W_{0.48}B_2$ sample, which is labeled with a closed star.

All of our bulk samples are prepared by arc melting, and are polycrystalline with grain sizes in the micron regime. This results in spotty patterns due to the low grain number statistics, as can be seen in **FIG. 6.1c,d**. The spotty nature of the pattern makes peak intensities unreliable, so that the data cannot be fully refined. In contrast, the diffraction pattern for the sample prepared by NaCl flux growth is smooth, indicating a much finer particle size, which is determined to be between 40 and 150 nm, depending on the sample, as determined by SEM (**FIG. 6.3a,b**). The overall

morphology of the nano materials can be found in the SEM-EDS images with lower magnification (**FIG. S6.2 and S6.3**) showing that the nano materials are reasonably mono-dispersed and tend to form agglomerates. Size histograms extracted from the SEM images for both nanoscale samples are also include in **FIG. S6.2** to demonstrate the breadth of the size distribution. The averages size from these distributions is ~50 nm for the n-ReB_2, and ~120 for the the n-$Re_{0.52}W_{0.48}B_2$. We note that only a finite number of SEM images could be collected on more dispersed parts of the power, so the size statistics form SEM may not fully represent the sample. As a result, we use generally use sizes determined form XRD peaks widths to describe the samples.

EDS maps demonstrate that Re is found where there are powder grains, indicating that the particles in the SEM images are indeed n-ReB_2. For the n-$Re_{0.52}W_{0.48}B_2$ sample, Re and W colocalize on the EDS maps, again indicating solid solution behavior. The Si peak in the EDS spectrum of n-ReB_2 arises from the silicon substrate used in the SEM. The peak situated at 3.4 keV appears to be Sn. This is very likely an artifact resulting from the multiple scattering of backscattered electrons, an effect that is very common when performing EDS for uneven surfaces such as powders. The chlorine and sodium peaks found in the spectrum for n-$Re_{0.52}W_{0.48}B_2$ may result from residual salt flux.

The smooth diffraction patterns of n-ReB_2 and n-$Re_{0.52}W_{0.48}B_2$ enabled us to conduct Rietveld refinement, which is a whole pattern refinement technique where the experimental profile is compared with a calculated one.[42] An example of refined data is shown and tabulated in **FIG. 6.3c** and **Table S6.1**. It is known that the peak broadening can be attributed to several factors: instrumental broadening, crystallite size, and stress-induced broadening.[33,61] In our experiments, the instrumental broadening was characterized using a standard material, CeO_2. The Rietveld analysis for the peak profile from the XRD of the unstressed sample shows that the crystallite size

for n-ReB$_2$ and n-Re$_{0.52}$W$_{0.48}$B$_2$ is ~40 nm and ~30 nm with microstrain of 0.003 and 0.002 respectively, confirming that the samples are indeed nanosized. Additional broadening at high pressure can be assigned to stress. The size determined by XRD, however, appears to be smaller than that shown in the SEM. This is because SEM measures the particle size rather than the crystallite size. An SEM image of the n-Re$_{0.52}$W$_{0.48}$B$_2$ shows that its particle size is 100 -150 nm (**FIG. S6.2**) while XRD shows it is ~40 nm, which suggests that each particle seen in SEM may be composed of multiple crystalline domains. In comparison, the particle size of n-ReB$_2$ observed by SEM is close to the crystallite size determined using XRD indicating that the particles are single domains. As seen in the figure, all diffraction signals including the ReB$_2$, the unreacted Re and background were well refined in the Rietveld fitting, with the exception of the amorphous hump from the boron/epoxy gasket.

As can be seen in **FIG. 6.4a**, a linear variation between the measured *d*-spacings and orientation function $(1 - 3\cos^2\varphi)$ for the selected lattice planes is observed as expected based on lattice strain theory (eq. 6.2). The hydrostatic *d*-spacings are then determined from the zero intercept of this linear fit, plotted as a function of pressure (**FIG. 6.4b**). The *d*-spacings show a continuous, linear decrease as the pressure increases with no abrupt changes. This behavior suggests the samples are stable in the hexagonal structure upon compression and decompression up to ~60 GPa, ~43 GPa, and 52 GPa.

The lattice parameters at each pressure were calculated from the *d*-spacings and are summarized in **Table S6.2**; this data, in turn, enables calculation of the bulk modulus. As shown in **FIG. 6.5**, the hydrostatic compression curves were fitted to the third order Birch-Murnaghan equation-of-state yielding a bulk modulus as high as 314 ± 12 GPa ($K_0' = 7.1$), 349 ± 11 GPa ($K_0' = 1.7$) and 326 ± 2 GPa ($K_0' = 4.4$) for bulk Re$_{0.52}$W$_{0.48}$B$_2$, n-Re$_{0.52}$W$_{0.48}$B$_2$ and n-ReB$_2$,

respectively. The 2nd order equation-of-state in terms of normalized pressure and Eularian strain[62] can be found in **FIG. S6.4**. The bulk modulus of n-ReB$_2$ obtained here under non-hydrostatic compression is consistent with the reported third order value of 340 GPa for bulk ReB$_2$ measured under hydrostatic conditions,[6] and it also falls in the range of 317-383 GPa[63-67] obtained from both other experiments and calculations. This indicates that hydrostatic and non-hydrostatic/magic angle data give results in good agreement with each other. Moreover, the fact that the bulk modulus does not change significantly on varying the grain size indicates that the bulk modulus for ReB$_2$ is a size independent property. The fact that the bulk Re$_{0.52}$W$_{0.48}$B$_2$ shows a slightly lower bulk modulus than the ReB$_2$ can be attributed to a decrease in valence electron concentration when substituting W for Re. This decrease, however, seems less significant when determining the bulk modulus of n-Re$_{0.52}$W$_{0.48}$B$_2$, since it shows nearly the same bulk modulus value as bulk ReB$_2$. One possible reason is that the atomic structure of the surface can undergo reconstruction to compensate the energy increase when shifting the atoms from their perfect lattice positions due to the presence of surface strain. It has been found in hard materials such as SiC that the bond distance of Si-C, C-C and Si-Si at the surface of nanocrystals is different from those within the nanocrystal center, giving rise to a core-shell structure.[68] As a result, the shell shows higher bulk modulus than the inner core. The addition of W decreases the valence electron density suggesting a lower bulk modulus than ReB$_2$, however, it may also induce more bonding reconstruction at the surface of the grains, which becomes more significant at the nanoscale explaining the surprising lack of change in bulk modulus.

Generally, a high bulk modulus (*i.e.* high incompressibility) is a necessary, but insufficient prerequisite for high hardness.[69] Bulk modulus is a measure of elastic deformation, reflecting the resistance to volume change with respect to pressure, and is strongly related to the intrinsic

properties of a material, particularly valence electron count and structure.[70] Hardness, defined as the resistance to plastic deformation, is not only influenced by intrinsic factors such as the strength and directionality of bonding, but also by extrinsic factors, such as dislocation density and grain morphology. The yield strength is believed to be one of the most significant determining factors for hardness and the ratio of yield strength to shear modulus (t/G) for each lattice plane can be directly measured from the slope of the linear fit as shown in **FIG. 6.4a**. Values of t/G for selected planes are plotted as a function of pressure for bulk $Re_{0.52}W_{0.48}B_2$, n-ReB$_2$ and n-$Re_{0.52}W_{0.48}B_2$ in **FIG. 6.6a,b** and compared with data for bulk ReB$_2$ from Ref. 71. For n-ReB$_2$, the t/G ratio for each plane increases almost linearly with pressure from the beginning up to ~15 GPa. The increase rate then becomes slower and eventually plateaus, indicating the onset of plastic deformation and that t (the yield strength) has reached its limiting value.

Similar trends in t/G are observed for all samples, with some noted differences. In comparing the bulk samples, we find that the $Re_{0.52}W_{0.48}B_2$ shows a higher plateau value of t/G and reaches that value at a somewhat higher pressure than pure ReB$_2$. Similarly, both nano materials support a higher plateau value and show a higher plateau pressure, compared to their bulk counterparts. Overall, bulk ReB$_2$ shows both the lowest plateau pressure and plateau value, indicating that all methods used here are successful at improving mechanical properties. As seen in **FIG. 6.6a,b** the basal plane of the *hcp* lattice for all samples is always the lowest, implying it is very likely to be a slip plane. The $t(100)/G$, $t(101)/G$ and $t(110)/G$ values for n-ReB$_2$ are quite similar, which we also observed for bulk ReB$_2$. In contrast, the addition of tungsten seems to change the strain anisotropy. Unlike ReB$_2$, the planes for $Re_{0.52}W_{0.48}B_2$, in both bulk and nanoscale form, present a significant difference in t/G with (100) being the highest followed by the (110) and (101) planes. This may relate to the greater sensitivity of the c-axis to the addition of tungsten, as shown in **FIG. 6.2b,f**.

It is important to calculate t, in addition to t/G, when comparing yield strength of different materials, since a very low shear modulus like that found in a soft elastic material can also produce a high strain. For example, the (200) lattice plane of Au^{72} can support a similar amount of differential strain as the (004) lattice plane of ReB_2. As described in the experimental section, this conversion can be done making two different limiting assumptions. The Voigt shear modulus assumes iso-strain conditions, while the Reuss shear modulus assumes iso-stress conditions. The differential stress under Reuss and Voigt conditions for bulk and nanoscale $Re_{0.52}W_{0.48}B_2$ and ReB_2 was calculated by using the elastic stiffness constants from references 73 and 74, respectively. While the real differential stress is a weighted average of these two conditions, the correct weighting for our experimental conditions is not known, so we simply calculated both values as upper and lower limits on the actual values. As seen in **FIG. 6.7(a-c)**, both nano materials clearly show higher differential stress values than that of their bulk counterparts. For example, the (100) plane for $Re_{0.52}W_{0.48}B_2$ system is found to be the strongest plane with a plateau value of ~16-19 GPa for the bulk material and ~20-25 GPa for the nanoscale material. The (002) is always the weakest plane regardless of size and composition, again suggesting that this is a slip plane. When comparing different methods to enhance the yield strength, we found the strength for the (002) and (101) planes of n-ReB_2 is almost the same as that of bulk $Re_{0.52}W_{0.48}B_2$. However, the (100) and (110) planes of n-ReB_2 are clearly weaker than those of bulk $Re_{0.52}W_{0.48}B_2$, indicating that bulk $Re_{0.52}W_{0.48}B_2$ possesses an overall higher yield strength than n-ReB_2 and thus that solid solution effects are more beneficial than finite size effects alone in this system.

Finite size effects are significant, however, as even the weakest plane of n-ReB_2 still exhibits a higher yield strength than the strongest plane of bulk ReB_2, demonstrating that finite size effects are an effective approach to hardness enhancement for superhard metal borides. Because the

different lattice planes show more variation in t for $Re_{0.52}W_{0.48}B_2$ then for ReB_2, a clean separation of t values is not observed between bulk and nanoscale $Re_{0.52}W_{0.48}B_2$, but the nanoscale material still show a significant enhancement in t under both iso-stress and iso-strain assumptions. When the crystallite size is reduced into the nano realm, the nucleation of dislocations becomes more energetically unfavorable. Moreover, dislocations are also harder to propagate due to the high density of grain boundaries, which in turn is responsible for the higher yield strength of n-ReB_2. Solid solution effects similarly result in a higher yield strength because dislocation movement is impeded by the atomic size mismatch between tungsten and rhenium. Importantly, it appears to be possible to take advantage of both solid solution hardening and size effects in a synergistic manner, as n-$Re_{0.52}W_{0.48}B_2$ exhibits the highest differential stress of all samples studied.

In order to correlate the yield strength for a polycrystalline sample to its hardness, the yield strength for many different diffraction planes need to be considered, because many lattice planes are compressed by the diamond indenter in a polycrystalline material at the same time during the hardness test. While we never know what specific grain orientations are below any given indentation, to get a sense of the average yield strength, here we took the average of all lattice plains that we could track to get an effective average differential stress and plotted the data in **FIG. 6.7d**. For example, the differential stress of n-ReB_2 shown in **FIG. 6.7d** was obtained by taking the average of t/G for the (002), (100), (101), (102), (103), (104), (110) and (112) planes followed by multiplying by the aggregate shear modulus of 273 GPa.[74] In **FIG. 6.7d**, the differential stress for bulk $Re_{0.52}W_{0.48}B_2$ is slightly higher than that for n-ReB_2 and they are both greater than that of bulk ReB_2. This result is consistent with the hardness previously reported for both bulk materials (H_v=40.5 GPa for bulk ReB_2, H_v=47.2 GPa for bulk $Re_{0.52}W_{0.48}B_2$).[9] Since n-ReB_2 and n-$Re_{0.52}W_{0.48}B_2$ were made only in powder form, no hardness values are available. However, it is

reasonable to believe that the hardness of a compact made from n-ReB$_2$ should be higher than bulk ReB$_2$ and close to or slightly lower than bulk Re$_{0.52}$W$_{0.48}$B$_2$ based on the differential stress data, while the hardness of a compact made from n-Re$_{0.52}$W$_{0.48}$B$_2$ would likely be even higher than the bulk solid solution value.

We end by taking advantage of our ability to refine the nanocrystal diffraction patterns as a function of pressure to learn more about the available slip systems in these superhard materials. When shear stress is applied to polycrystals, individual grains deform preferentially on slip planes. This results in crystallite rotations, generating lattice-preferred orientation or texture, which manifests as changes in peak intensity with pressure.[75] Unfortunately, the diffraction pattern for the coarse-grained bulk samples (**FIG. 6.2a**) only allow us to analyze the diffraction line shifts and the evolution of the differential strain upon compression, while peak intensity variation with azimuth angles can't be correlated to the slip systems because of the low grain number statistics. As a result, in addition to the high strength, another advantage of nano-crystalline samples is that quantitative texture information can be obtained from high-pressure data through Rietveld analysis.

The orientation distribution or texture is represented using an inverse pole figures (IPF), as shown in **FIG. 6.8**, which denotes the probability of finding the poles (normal) to lattice planes in the compression direction. The texture strength (*i.e.* pole density) is measured in multiples of the mean random distribution (m.r.d.), where m.r.d. = 1 indicates a fully random distribution, and a higher m.r.d. number represents stronger texture. The n-ReB$_2$ initially exhibits a nearly random distribution at ambient pressure. The texture strength evolves with pressure and shows a maximum at (0001) at 59 GPa, indicating the (0001) lattice planes are oriented with an alignment of the *c* axis to the high stress direction. This experimental observation confirms that the (001) plane is indeed a slip plane, consistent with our differential stress data and the theoretical slip system of

(001)[1$\bar{1}$0] for ReB_2.[38] As shown in **FIG. 6.1**, the (001) planes are the planes parallel to the boron layers, and it has been reported that the puckered boron layers become more flattened with increasing pressure;[76] therefore the observed slip plane can be attributed to the lack of constrained bonding between layers.

The preferred orientation for n-$Re_{0.52}W_{0.48}B_2$ was also observed in (0001) lattice plane as can be seen in **FIG. 6.8b**, suggesting that the tungsten added did not change the primary slip system. More interestingly, the texture area (brown in color) for n-ReB_2 grows larger and larger with pressure, implying new slip systems gradually opened up with the development of the plastic deformation. This increase in the number of available slip systems may be the root of the indentation size effect, which is the phenomenon were the measured hardness decreases with increasing indentation load.[5] The indentation size effect is always strongly observed in these superhard metal borides.[9,17,29] Interestingly, the texture for n-$Re_{0.52}W_{0.48}B_2$ is more restricted at the (0001) corner. This suggests that the addition of tungsten helps suppress the formation of new slipping paths, resulting in higher yield strength, greater mechanical stability, and presumably higher hardness.

The quantitative texture strength also provides information about the microscopic deformation mechanisms controlling the plastic behavior of these material. Dislocation creep and grain boundary processes are believed to be the two main mechanisms for plastic deformation in compressed powders.[77] Dislocation creep on preferred slip systems has been reported to produce a strong texture, while grain boundary sliding and mechanical twinning usually randomize the texture.[35,75,78] Interestingly, both n-ReB_2 and n-$Re_{0.52}W_{0.48}B_2$ exhibit fairly weak texture, with an index of ~1.3 m.r.d. at the highest pressure reached in our experiment, suggesting that the dislocation mediated processes are not the dominant mechanism for plasticity. Indeed, the low

value indicates that the n-ReB$_2$ and n-Re$_{0.52}$W$_{0.48}$B$_2$ maintain a low dislocation density upon non-hydrostatic compression up to ~60 GPa, a result which also explains why the nano materials show a much higher yield strength than its coarse-grained counterparts. Importantly for the design of future compacts based on nanocrystalline super hard metal borides, these results also indicate that grain boundary strengthening is the key to enabling high hardness in practical superhard nanoscale metal borides.

6.4 Conclusions

In this paper, nanoscale ReB$_2$ and Re$_{0.52}$W$_{0.48}$B$_2$ was synthesized through a molten salt flux growth method. Their high pressure behaviors was explored and compared with coarse-grained ReB$_2$ and Re$_{0.52}$W$_{0.48}$B$_2$ using synchrotron based X-ray diffraction under non-hydrostatic compression up ~60 GPa. The equation-of-state(s) for n-ReB$_2$, Re$_{0.52}$W$_{0.48}$B$_2$ and n-Re$_{0.52}$W$_{0.48}$B$_2$ were determined using the hydrostatic volume data measured at the magic angle ($\varphi = 54.7°$). Little difference was found in the bulk modulus of n-ReB$_2$ compared with bulk ReB$_2$, while nano Re$_{0.52}$W$_{0.48}$B$_2$ was found to be more incompressible than bulk Re$_{0.52}$W$_{0.48}$B$_2$. Lattice-dependent strength anisotropy indicates that the basal planes of the samples support the least differential stress, indicating that (*00l*) is a slip plane limiting the strength of ReB$_2$. This hypothesis was further confirmed by texture analysis. Moreover, the yield strength of bulk Re$_{0.52}$W$_{0.48}$B$_2$, n-ReB$_2$ and n-Re$_{0.52}$W$_{0.48}$B$_2$ were all found to be much higher than that of bulk ReB$_2$, demonstrating that solid solution hardening and nano-structuring are two effective approaches to hardness enhancement for superhard transition metal borides. Importantly, these too effects can be synergistically combined to produce the highest yield strength in n-Re$_{0.52}$W$_{0.48}$B$_2$. Finally, the plastic deformation mechanism for n-ReB$_2$ and n-Re$_{0.52}$W$_{0.48}$B$_2$ was examined and it was found that the dislocation density remains very low level, despite compression to ~60 GPa.
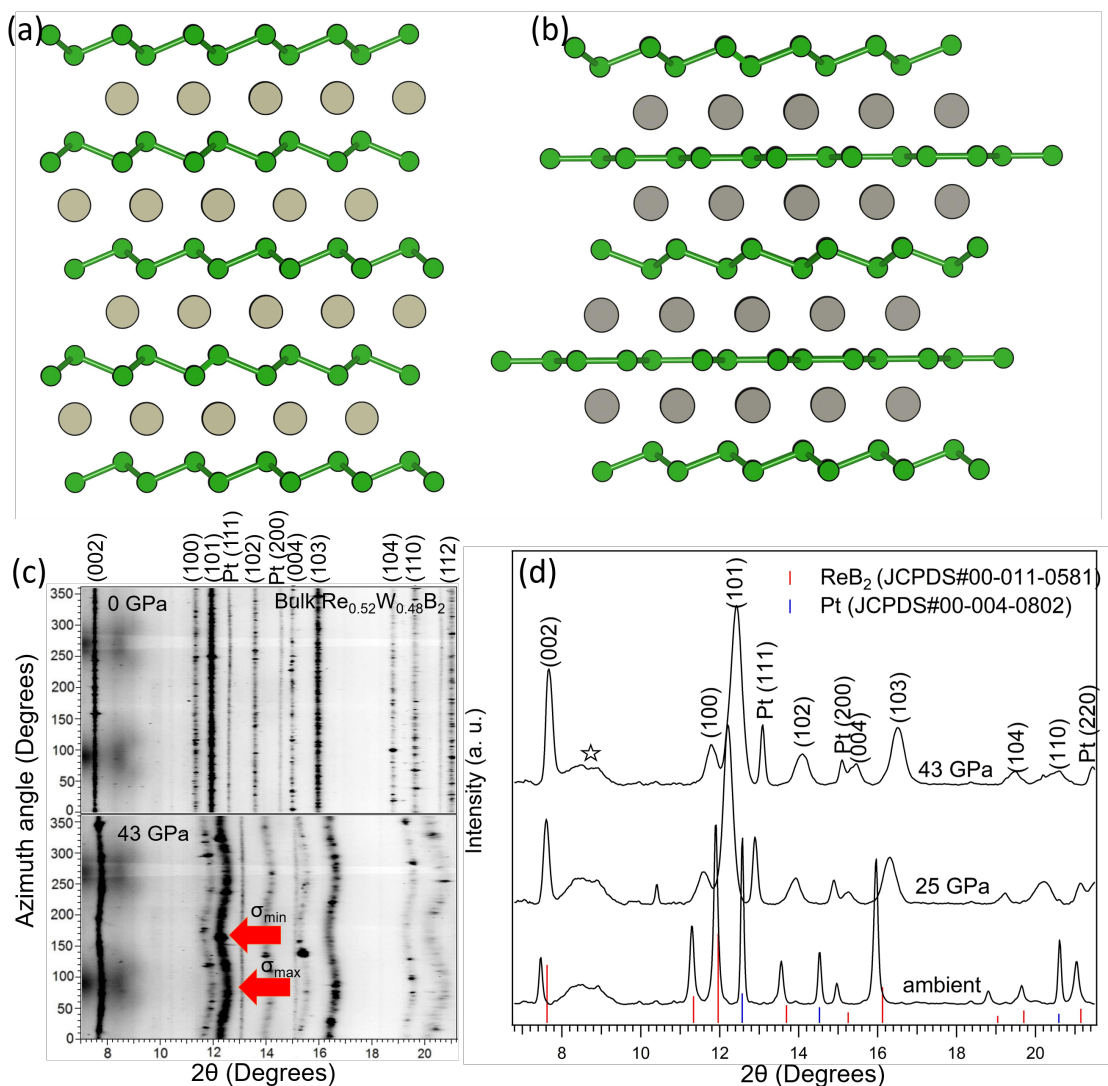
FIG. 6.1. A comparison of the structures of ReB_2 (a) and WB_2 (b). Boron and metal atoms are shown in green and gray, respectively. Representative synchrotron 2-D azimuthally unrolled patterns (c), and 1-D X-ray diffraction patterns (d) with increasing pressure for bulk $Re_{0.52}W_{0.48}B_2$. The data in part (d) were obtained by integration over an 5° slice center at the magic angle of $\varphi = 54.7°$. Indexing for relevant peaks is included on the image (note that the stick pattern is for ReB_2, not $Re_{0.52}W_{0.48}B_2$). Diffraction from the boron/epoxy gasket is indicated with an open star. All diffraction peaks other than those from the gasket shift to higher angle with increase pressure.
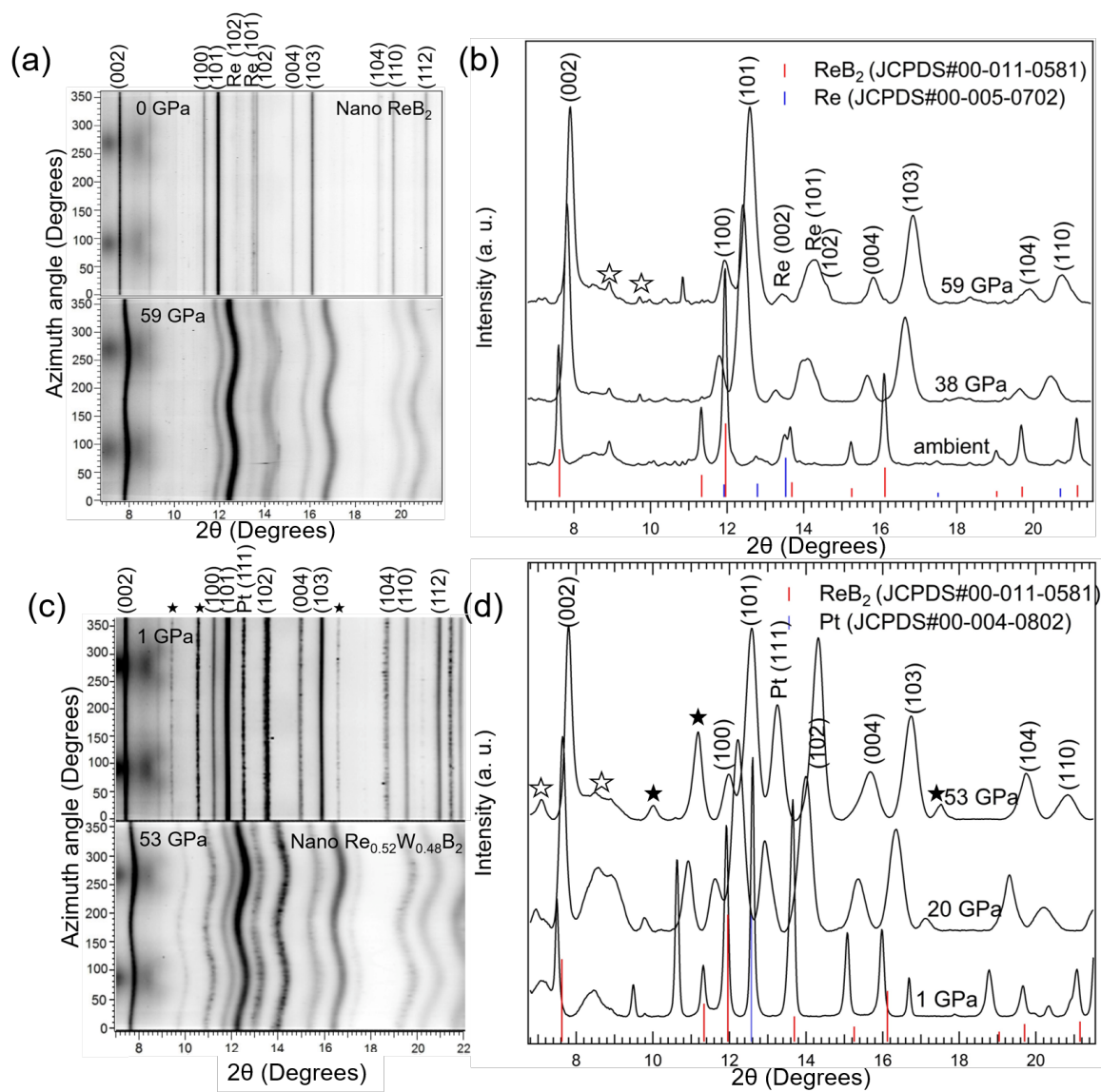
FIG. 6.2. Representative synchrotron 1-D X-ray diffraction patterns and 2-D azimuthally unrolled patterns with increasing pressure for (a),(b) nano-ReB_2 and (c),(d) nano-$Re_{0.52}W_{0.48}B_2$. The data in parts (b) and(d) was obtain by integration over an 5° slice center at the magic angle of $\varphi = 54.7°$. Indexing for relevant peaks is included on the image (note that the stick pattern is for ReB_2, in both figures). Diffraction from the boron/epoxy gasket is indicated with an open star and an impurity in the n-$Re_{0.52}W_{0.48}B_2$ is labeled with a closed star. All diffraction peaks other than those form the gasket shift to higher angle with increase pressure.
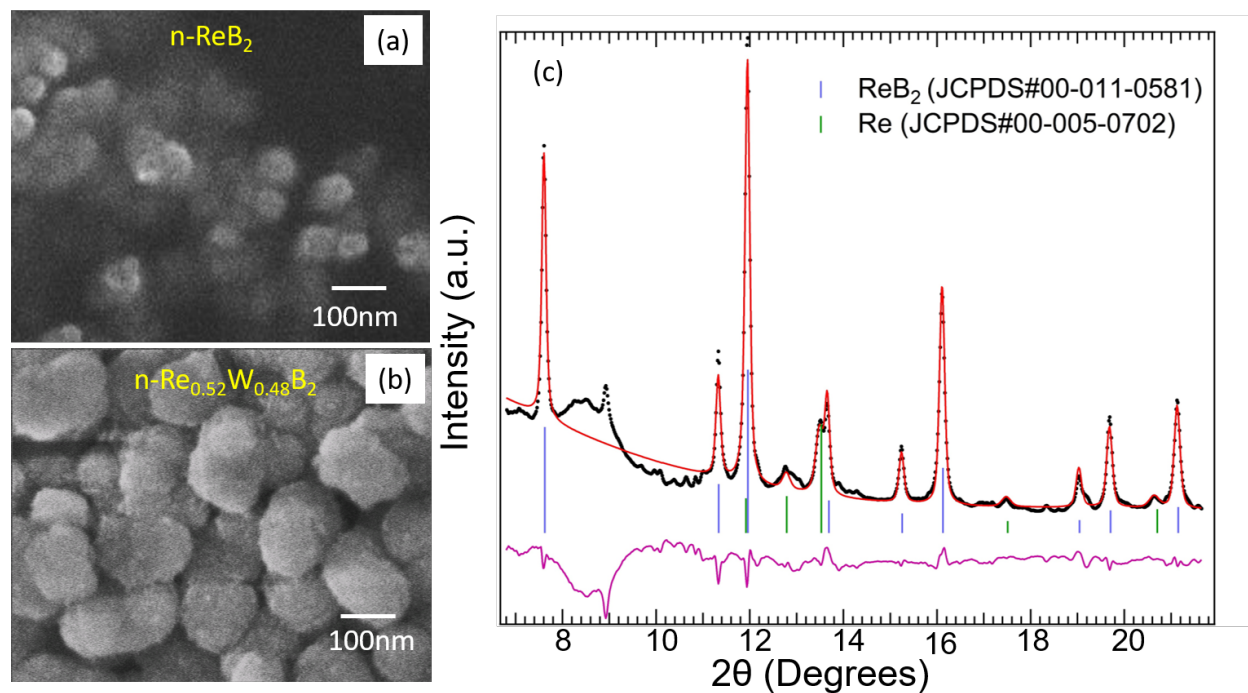
FIG. 6.3. Scanning electron microscopy images of (a) n-ReB$_2$ and (b) n-Re$_{0.52}$W$_{0.48}$B$_2$ prepared using an NaCl flux. Particle sizes range from ~40 to ~150 nm for the two samples. (c) Rietveld fitting of nano-ReB$_2$ at ambient pressure. The experimental spectrum is shown with a black dashed line, and the calculated fit is shown with a solid line in red. The difference pattern is shown in violet. Good agreement is found for all peaks other than those arising from the boron/epoxy gasket.
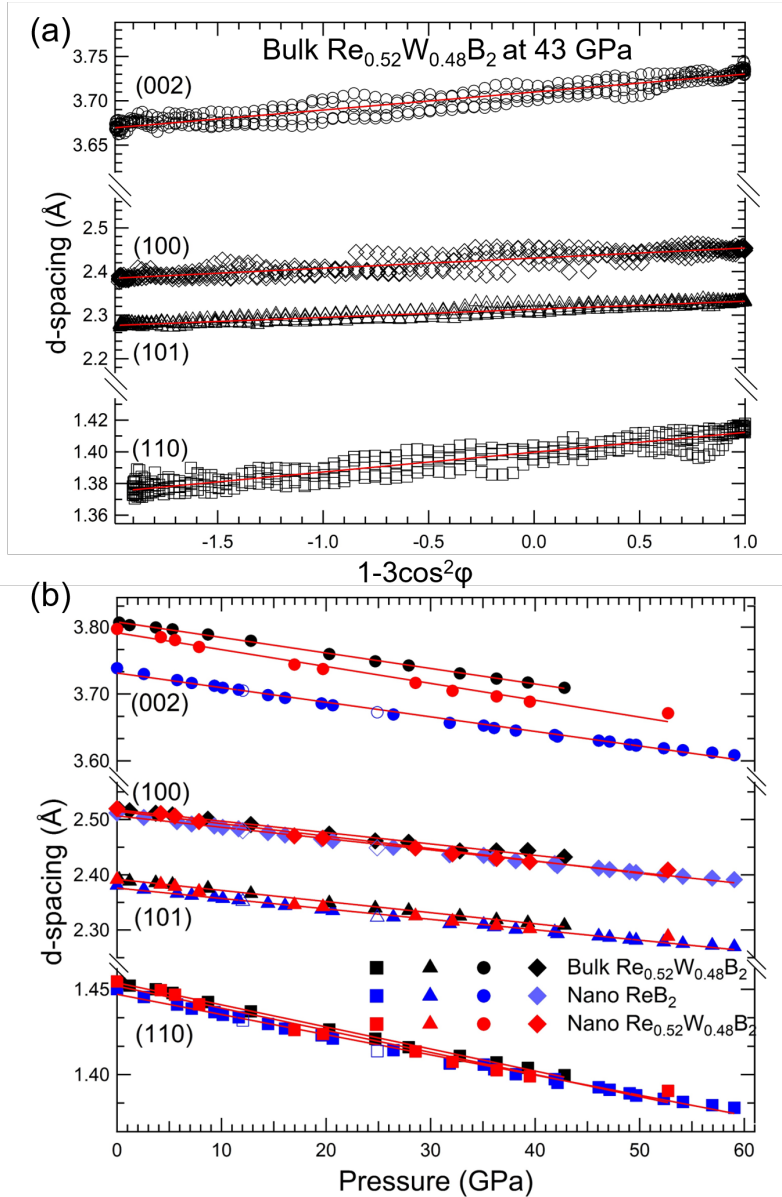
FIG. 6.4. (a) Linearized plot of *d*-spacings for $Re_{0.52}W_{0.48}B_2$ as a function of φ angle at the highest pressure reached. The solid lines are the best linear fit to the data. (b) Measured *d*-spacings for selected lattice planes as a function of pressure. Error bars that are smaller than the size of the symbols have been omitted. Data with close symbols were collected upon compression, while those with open symbols were collected upon decompression. Only the c-axis shows large changes upon addition of W to ReB_2.
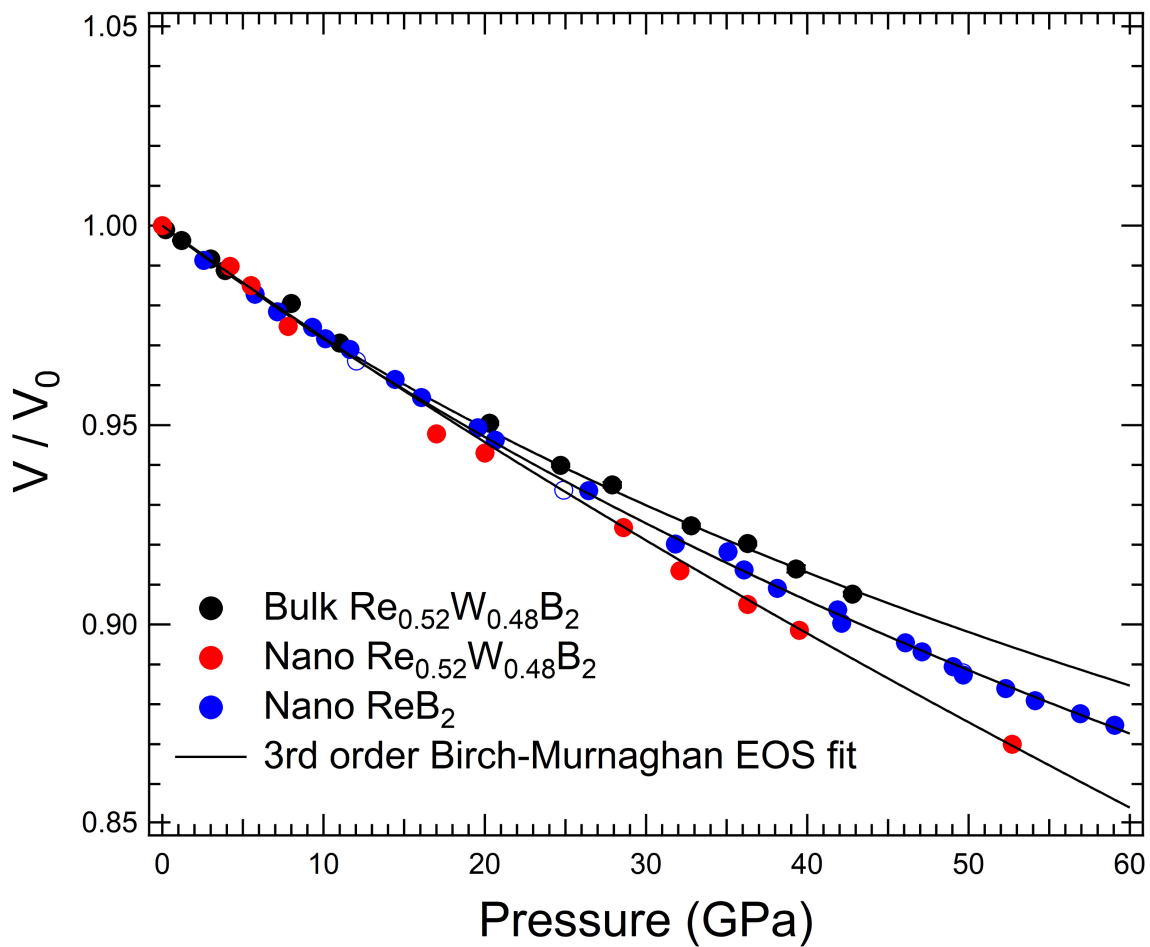
FIG. 6.5. Hydrostatic compression curves of $Re_{0.52}W_{0.48}B_2$ (black), nano-ReB_2 (blue), and nano-$Re_{0.52}W_{0.48}B_2$ (red) obtained at the magic angle, $\varphi = 54.7°$. The solid line is the best fit to the third-order Birch-Murnaghan equation-of-state.
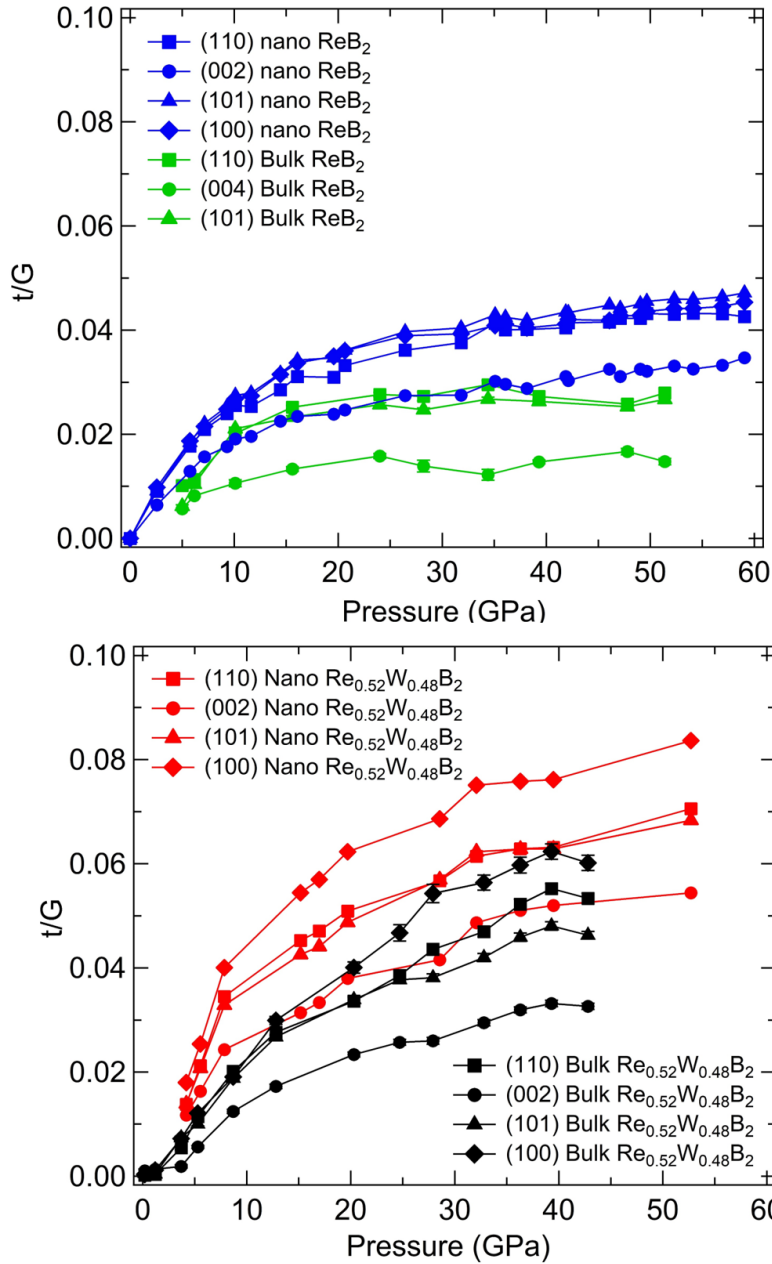
FIG. 6.6. (a) Comparison of the differential strain, given by the ratio of differential stress t to aggregate shear modulus G, as a function of pressure between nano-ReB_2 (blue) and bulk ReB_2 (green). (b) Differential strain as a function of pressure for nano-$Re_{0.52}W_{0.48}B_2$ (red) and bulk $Re_{0.52}W_{0.48}B_2$ (black).
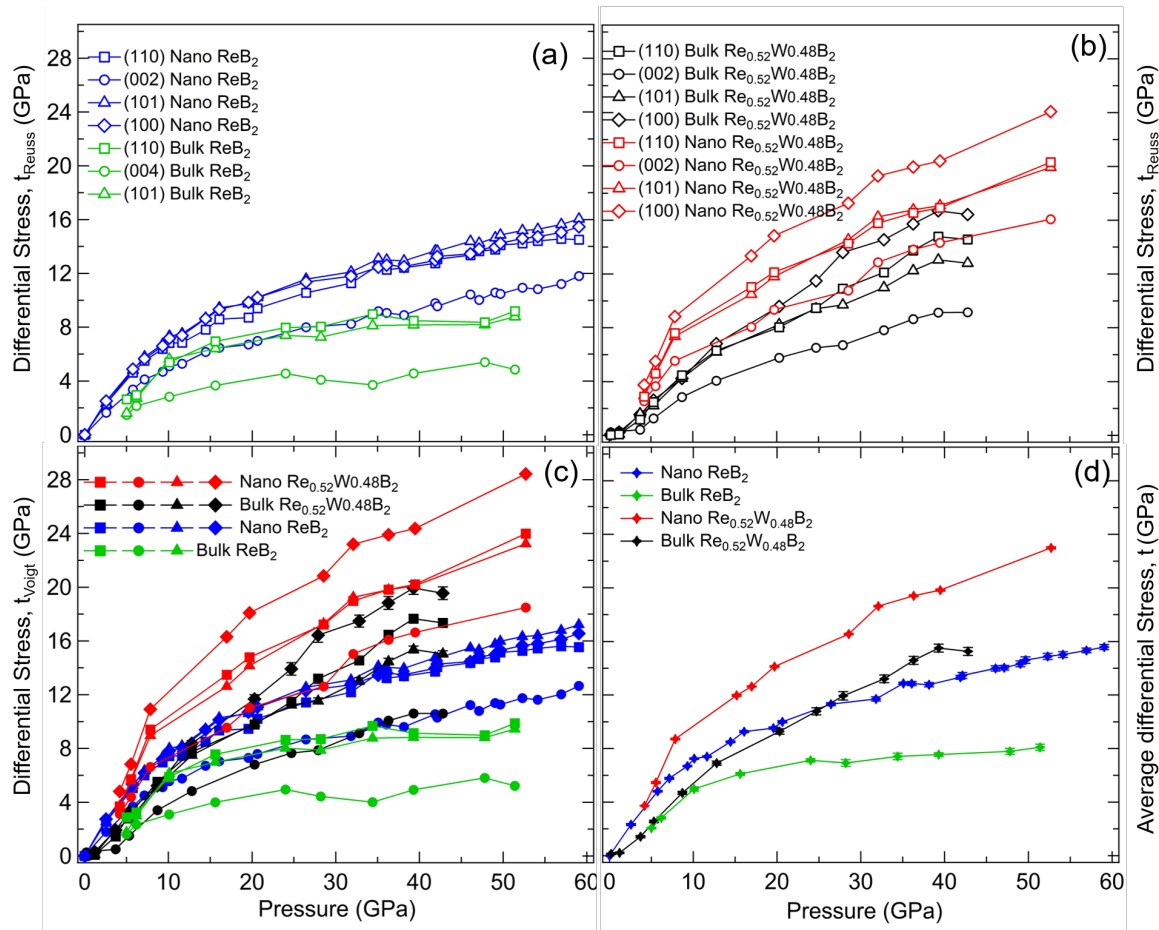
FIG. 6.7. Differential stress (t) calculated under the Reuss (iso-stress) condition (a), (b) and Voigt (iso-strain) condition (c). Part (a) compares bulk and nanoscale ReB_2, while part (b) shows bulk and nanoscale $Re_{0.52}W_{0.48}B_2$. Lattice planes are indicated on the figure. Part (c) compares all four samples, and the indexing is the same as that used in parts (a) and (b). Part (d) shows the evolution of the average differential stress over all observed lattice planes with pressure for the same four samples.
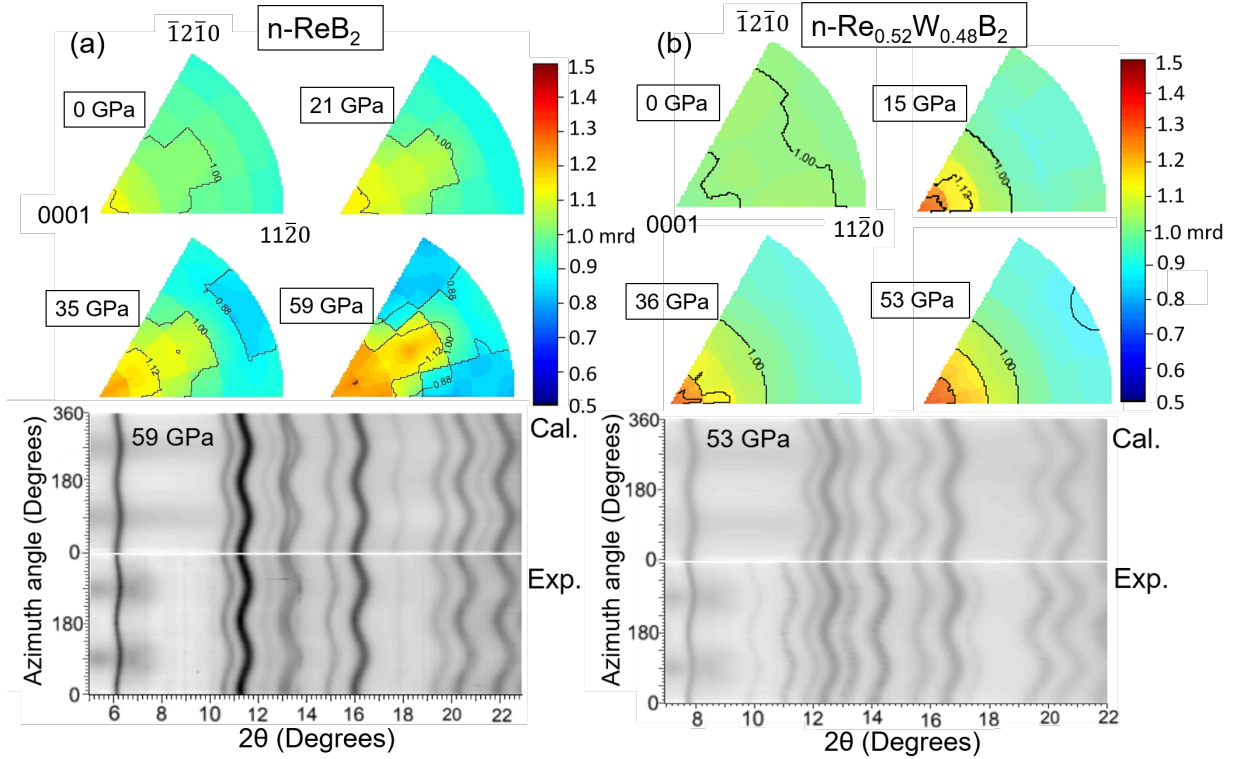
FIG. 6.8. Inverse pole figures for (a) n-ReB$_2$ and (b) n-Re$_{0.52}$W$_{0.48}$B$_{2,}$ showing texture evolution with pressure. Both samples exhibit only weak texture, even when compressed above 50 GPa. For both samples, the (00l) direction is found to be the primary slip system. In pure ReB$_2$, other slip systems become accessible at higher pressures, but these additional slip systems appear to be suppressed in the n-Re$_{0.52}$W$_{0.48}$B$_2$.

6.5 Supporting Information
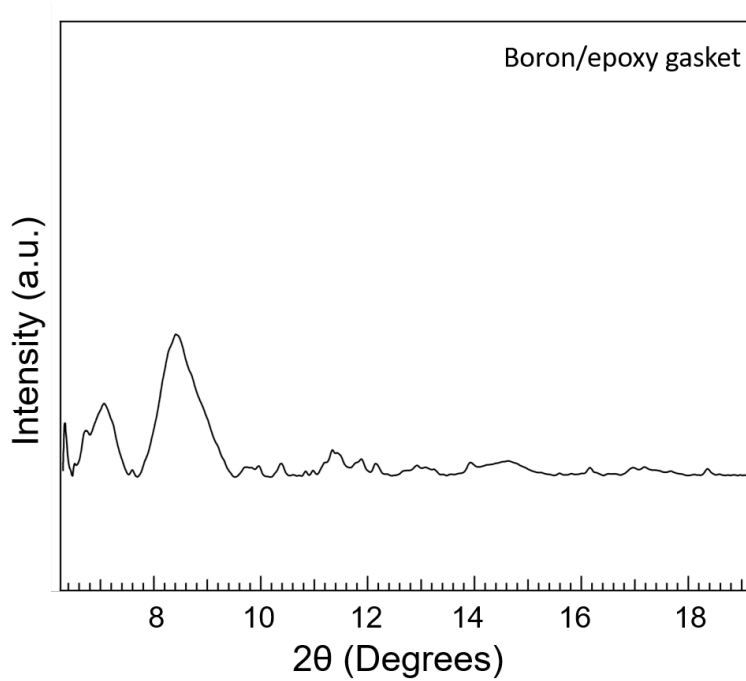
FIG. S6.1. XRD pattern of the boron/epoxy gasket.
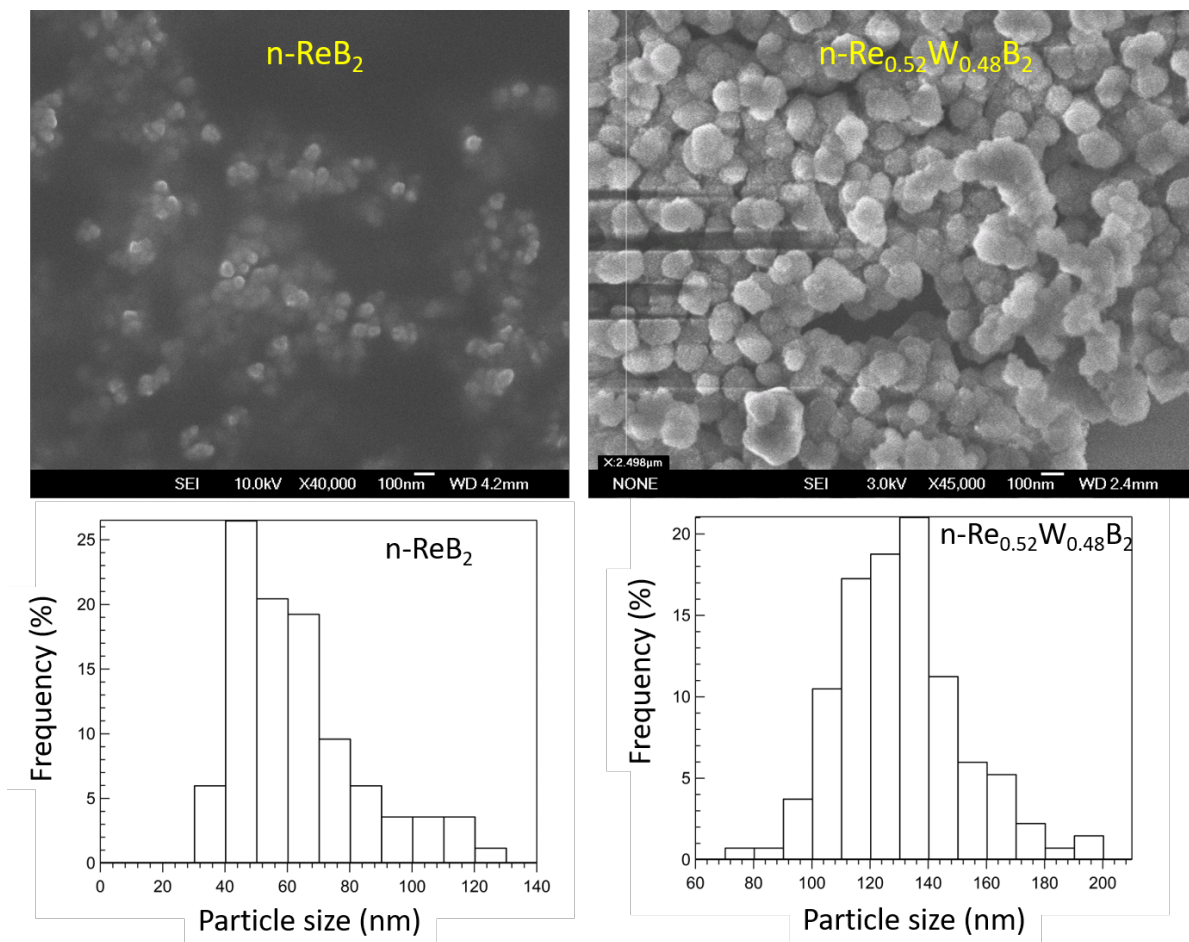
FIG. S6.2. Low magnification scanning electron microscopy (SEM) images of n-ReB$_2$ (left) and n-Re$_{0.52}$W$_{0.48}$B$_2$ (right), together with histograms generated from the images, showing the distribution of nanocrystal sizes.
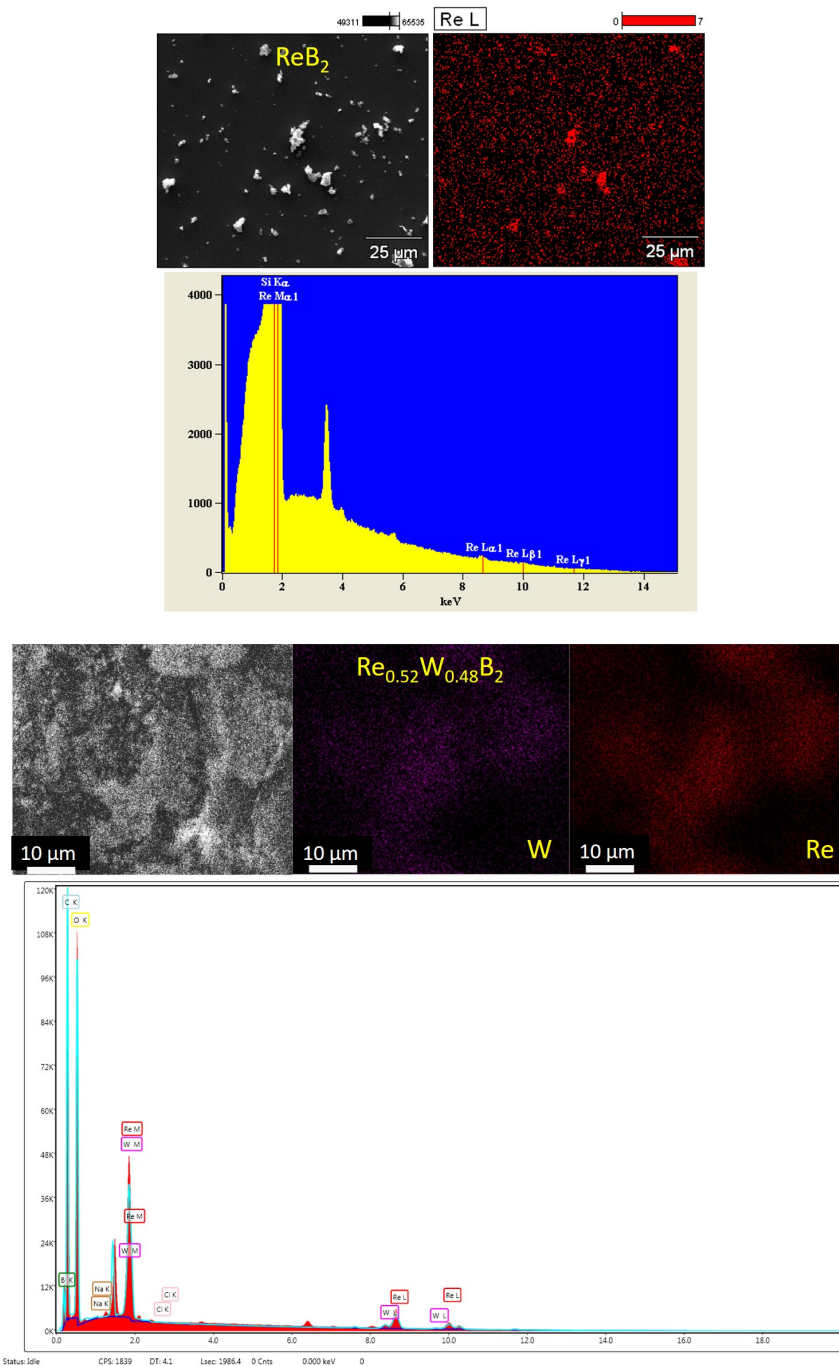
FIG. S6.3. SEM-EDS maps of ReB$_2$ and Re$_{0.52}$W$_{0.48}$B$_2$. W and Re co-localize in the elemental maps, indicating alloyed material.
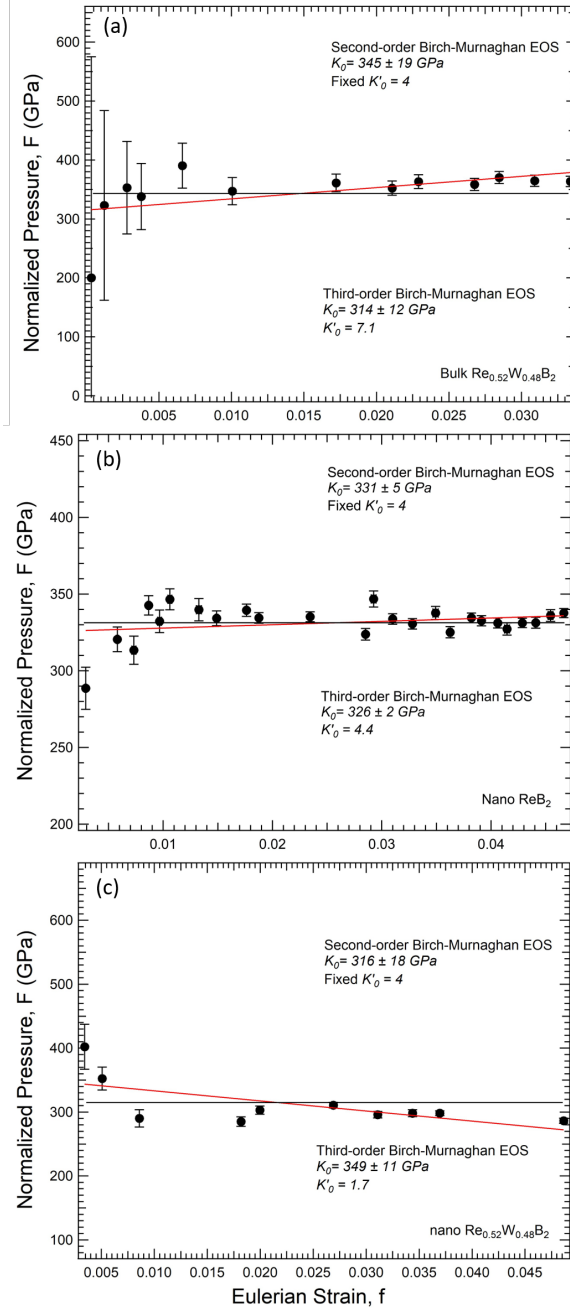
FIG. S6.4. Normalized pressure (F) *vs.* Eularian strain (f) for (a) bulk $Re_{0.52}W_{0.48}B_2$, (b) nano-ReB_2 and (c) nano-$Re_{0.52}W_{0.48}B_2$, where $F = \frac{P}{3f\,(1+2f)^{2.5}}$ and $f = \left(\frac{1}{2}\right)\left[\left(\frac{V_0}{V}\right)^{\frac{2}{3}} - 1\right]$. The intercept of the solid line yields the ambient pressure bulk modulus (K_0). The slope of the line yields the pressure derivative (K'_0)

195

Table S6.1. Lattice Parameters and d-Spacings from Rietveld Fitting of n-ReB$_2$

	Re	ReB$_2$
a (Å)	2.7666(2)	2.9003(6)
c (Å)	4.4552(8)	7.4775(7)
d_{100} (Å)	2.39597	2.51178
d_{002} (Å)	2.22761	3.73879
d_{101} (Å)	2.11018	2.38104
d_{102} (Å)	1.63144	2.08496
d_{110} (Å)	1.38331	1.45018
d_{103} (Å)	1.26227	1.76925
d_{200} (Å)	1.19799	-
d_{004} (Å)	-	1.86939
d_{104} (Å)	-	1.49964
d_{112} (Å)	-	1.35204

Table S6.2. Compression Data for $Re_{0.52}W_{0.48}B_2$, Nano-ReB_2 and Nano-$Re_{0.52}W_{0.48}B_2$

Nano-ReB_2			Bulk $Re_{0.52}W_{0.48}B_2$		
P (GPa)	a (Å)	c (Å)	P (GPa)	a (Å)	c (Å)
0	2.9003(6)	7.4775(7)	0	2.9076(5)	7.6138(3)
3.0(1)	2.8911(3)	7.4600(2)	1.0(3)	2.9051(1)	7.6064(5)
6.0(1)	2.8822(4)	7.4419(2)	3.0(2)	2.8997(9)	7.5992(4)
7.0(1)	2.8774(7)	7.4331(4)	4.0(1)	2.8965(7)	7.5938(8)
9.0(1)	2.8733(4)	7.4247(5)	8.0(3)	2.8873(3)	7.5782(7)
10.0(1)	2.8702(6)	7.4188(7)	11.0(2)	2.8762(4)	7.5596(2)
12.0(1)	2.8673(6)	7.4133(7)	20.0(4)	2.8538(4)	7.5198(2)
14.0(1)	2.8593(8)	7.3970(9)	25.0(4)	2.8420(6)	7.4982(8)
16.0(2)	2.8542(3)	7.3885(9)	28.0(3)	2.8370(9)	7.4854(1)
20.0(2)	2.8461(3)	7.3720(8)	33.0(2)	2.8258(9)	7.4620(1)
21.0(2)	2.8425(1)	7.3665(8)	36.0(4)	2.8219(7)	7.4466(4)
26.0(2)	2.8287(3)	7.3389(1)	39.0(3)	2.8144(7)	7.4346(7)
32.0(4)	2.8131(3)	7.3140(2)	41.0(3)	2.8076(5)	7.4190(1)
35.0(4)	2.8117(8)	7.3057(4)			
36.0(4)	2.8062(2)	7.2985(2)			
38.0(4)	2.8005(5)	7.2908(1)	Nano-$Re_{0.52}W_{0.48}B_2$		
41.0(4)	2.7947(9)	7.2775(3)	P (GPa)	a (Å)	c (Å)
42.0(4)	2.7904(5)	7.2729(8)	0	2.9093(4)	7.5947(1)
46.0(4)	2.7852(1)	7.2608(4)	4.0(1)	2.8991(7)	7.5704(3)
47.0(5)	2.7822(1)	7.2579(4)	6.0(1)	2.8937(9)	7.5615(4)
49.0(4)	2.7781(5)	7.2490(5)	8.0(1)	2.8826(1)	7.5409(5)
50.0(5)	2.7754(7)	7.2459(9)	17.0(2)	2.8525(2)	7.4882(9)
52.0(5)	2.7716(1)	7.2381(2)	20.0(2)	2.8477(1)	7.4750(8)
54.0(6)	2.7680(4)	7.2321(4)	29.0(2)	2.8273(1)	7.4336(8)
57.0(6)	2.7642(8)	7.2249(3)	32.0(3)	2.8151(2)	7.4097(1)
59.0(5)	2.7611(2)	7.2174(1)	36.0(3)	2.8053(2)	7.3930(9)
50.0(5)*	2.7758(2)	7.2484(7)	40.0(2)	2.7982(2)	7.3772(9)
25.0(3)*	2.8276(9)	7.3454(9)	53.0(2)	2.7606(3)	7.3382(7)
12.0(1)*	2.8636(7)	7.4104(8)			
0*	2.9003(7)	7.4801(2)			

The data labeled * were collected upon decompression.

6.6 References:

1. Levine, J.B.. Tolbert, S. H. & Kaner, R. B. Advancements in the Search for Superhard Ultra-Incompressible Metal Borides. *Adv. Funct. Mater.* **19**, 3519-3533 (2009).

2. Komanduri, R. & Shaw, M. C. Wear of Synthetic Diamond When Grinding Ferrous Metals. *Nature* **255**, 211-213 (1975).

3. Westraadt, J. E., Sigalas, I. & Neethling, J. H. Characterization of Thermally Degraded Polycrystalline Diamond. *Int J Refract Met Hard Mater.* **48**, 286-292 (2015).

4. Taniguchi, T., Akaishi, M. & Yamaoka, S. Mechanical Properties of Polycrystalline Translucent Cubic Boron Nitride as Characterized by the Vickers Indentation Method. *J. Am. Ceram. Soc*. **79**, 547-549 (1996).

5. Chung, H.-Y. *et al*. Synthesis of Ultra-Incompressible Superhard Rhenium Diboride At Ambient Pressure. *Science* **316**, 436-439 (2007).

6. Xie, M. *et al*. Exploring the High-Pressure Behavior of Superhard Tungsten Tetraboride. *Phys. Rev. B* **85**, 064118 (2012).

7. Levine, J. B. *et al*. Preparation and Properties of Metallic, Superhard Rhenium Diboride Crystals. *J. Am. Chem. Soc.* **130**, 16953-16958 (2008).

8. Chung, H.-Y. *et al*. Response to Comment on Synthesis of Ultra-Incompressible Superhard Rhenium Diboride at Ambient Pressure. *Science* **318**, 1550 (2017).

9. Lech, A. T. *et al*. Superhard Rhenium/Tungsten Diboride Solid Solutions. *J. Am. Chem. Soc.* **138**, 14398-14408 (2016).

10. Yin, S. *et al*. Hardness and Elastic Moduli of High Pressure Synthesized MoB_2 and WB_2 Compacts. *High Pressure Res.* **33**, 409-417 (2013).

11. Hao, X. *et al*. Low-Compressibility and Hard Materials Reb2 and WB2: Prediction from First-Principles Study. *Phys. Rev. B* **74**, 224112 (2006).

12. Aydin, S. & Simsek, M. First-Principles Calculations of Mnb2, Tcb2, and Reb2 within the Reb2-Type Structure. *Phys. Rev. B* **80**, 134107 (2009).

13. Lazar, P., Chen, X.-Q. & Podloucky, R. First-Principles Modeling of Hardness in Transition-Metal Diborides. *Phys. Rev. B* **80**, 12103 (2009).

14. Tu, Y. & Wang, Y. First-Principles Study of the Elastic Properties of $Os_xW_{1-x}B_2$ and $Re_xW_{1-x}B_2$ Alloys. *Solid State Commun.* **151**, 238-241 (2011).

15. Chen, X.-Q., Fu, C., Krčmar, M. & Painter, G. Electronic and Structural Origin of Ultraincompressibility of 5d Transition-Metal Diborides MB_2 (M=W, Re, Os). *Phys. Rev. Lett.* **100**, 196403 (2008).

16. Akopov, G., Yeung, M. T., Turner, C. L., Mohammadi R. & Kaner, R. B. Extrinsic Hardening of Superhard Tungsten Tetraboride Alloys with Group 4 Transition Metals. *J. Am. Chem. Soc.* **138**, 5714-5721 (2016).

17. Mohammadi, R. *et al*. Tungsten Tetraboride, an Inexpensive Superhard Material. *Proc. Nat. Acad. Sci.* **108**, 10958-10962 (2011).

18. Chen, B. *et al*. Texture of Nanocrystalline Nickel: Probing the Lower Size Limit of Dislocation Activity. *Science* **338**, 1448-1451 (2012).

19. Tian, Y. *et al*. Ultrahard Nanotwinned Cubic Boron Nitride. *Nature* **493**, 385-388 (2013).

20. Huang, Q. *et al*. Nanotwinned Diamond with Unprecedented Hardness And Stability. *Nature* **510**, 250-253 (2014).

21. Jothi, P. R., Yubuta, K. & Fokwa, B. P. T. A Simple, General Synthetic Route toward Nanoscale Transition Metal Borides. *Adv. Mater.* **30**, 1704181 (2018).

22. Portehault, D. *et al*. A General Solution Route toward Metal Boride Nanocrystals. *Angew. Chem. Int. Ed.* **50**, 3262-3265 (2011).

23. Hemley, R.J. *et al*. X-Ray Imaging of Stress and Strain of Diamond, Iron, and Tungsten at Megabar Pressures. *Science* **276**, 1242-1245 (1997).

24. He, D. & Duffy, T. S. X-Ray Diffraction Study of the Static Strength of Tungsten to 69 GPa. *Phys. Rev. B* **73**, 134106 (2006).

25. Duffy, T. S. *et al* .Lattice Strains in Gold and Rhenium under Nonhydrostatic Compression to 37 GPa. *Phys. Rev. B* **60**, 15063 (1999).

26. Shieh, S. R., Duffy, T. S. & Li, B. Strength and Elasticity of SiO_2 across the Stishovite–$CaCl_2$-Type Structural Phase Boundary. *Phys. Rev. Lett.* **89**, 255507 (2002).

27. Kavner, A. & Duffy, T. S. Elasticity and Rheology of Platinum under High Pressure and Nonhydrostatic Stress. *Phys. Rev. B* **68**, 144101 (2003).

28. He, D., Shieh, S. R. & Duffy, T. S. Strength and Equation of State of Boron Suboxide from Radial X-Ray Diffraction in a Diamond Cell under Nonhydrostatic Compression. *Phys. Rev. B* **70**, 184121 (2004).

29. Yeung, M. T. *et al*. Superhard Monoborides: Hardness Enhancement through Alloying in $W_{1-x}Ta_xB$. *Adv. Mater.* **28**, 6993-6998 (2016).

30. Lei, J. *et al*. Understanding How Bonding Controls Strength Anisotropy in Hard Materials by Comparing the High-Pressure Behavior of Orthorhombic and Tetragonal Tungsten Monoboride. *J. Phys. Chem. C* **122**, 5647-5656 (2018).

31. Lei, J. *et al*. Structural and Mechanical Stability of Dilute Yttrium Doped Chromium. *Appl. Phys. Lett.* **102**, 021901 (2013).

32. Mao, W. L. *et al*. Experimental Determination of the Elasticity of Iron at High Pressure. *J. Geophys. Res.* **113**, B09213 (2008).

33. Merkel, S. *et al*. Deformation of Polycrystalline MgO at Pressures of the Lower Mantle. *J. Geophys. Res.* **107**, ECV 3-1– ECV 3-17 (2002).

34. Merkel, S., Miyajima, N., Antonangeli, D., Fiquet, G. & Yagi, T. Lattice Preferred Orientation and Stress in Polycrystalline Hcp-Co Plastically Deformed under High Pressure. *J. Appl. Phys.* **100**, 023510 (2006).

35. Dorfman, S. M., Shieh, S. R. & Duffy, T. S. Strength and Texture of Pt Compressed to 63 GPa. *J. Appl. Phys.* **117**, 065901 (2015).

36. Lei, J. *et al.* Understanding the Mechanism of Hardness Enhancement in Tantalum-Substituted Tungsten Monoboride Solid Solutions. *J. Appl. Phys.* **125**, 082529 (2019).

37. Zhang, R. F., Legut, D., Niewa, R., Argon, A. S. & Veprek, S. Shear-induced Structural Transformation and Plasticity in Ultraincompressible Reb2 Limit Its Hardness. *Phys. Rev. B* **82**, 104104 (2010).

38. Zang, C., Sun, H., Tse, J. S. & Chen, C. Indentation Strength of Ultraincompressible Rhenium Boride, Carbide, and Nitride from First-Principles Calculations. *Phys. Rev. B* **86**, 014108 (2012).

39. Simunek, A. Anisotropy of Hardness from First Principles: The Cases of Reb$_2$ And OsB$_2$. *Phys. Rev. B* **80**, 060103 (2009).

40. Merkel, S. & Yagi, T. X-Ray Transparent Gasket for Diamond Anvil Cell High Pressure Experiments. *Rev. Sci. Instrum.* **76**, 046109 (2005).

41. Hammersley, A. P., Svensson, S. O., Hanfland, M., Fitch, A. N. & Hausermann, D. Two-Dimensional Detector Software: From Real Detector to Idealised Image or Two-theta Scan. *High Pressure Res.* **14**, 235-248 (1996).

42. Rietveld, H. M. a Profile Refinement Method for Nuclear and Magnetic Structures. *J. Appl. Crystallogr.* **2**, 65-71 (1969).

43. Lutterotti, L., Matthies, S., Wenk, H. R., Schultz, A. S. & Richardson, J.W. Combined Texture and Structure Analysis of Deformed Limestone from Time-of-Flight Neutron Diffraction Spectra. *J. Appl. Phys.* **81**, 594 (1997).

44. (44) Singh, A. K., Mao, H.-K., Shu, J. & Hemley, R. J. Estimation of Single-Crystal Elastic Moduli from Polycrystalline X-Ray Diffraction at High Pressure: Application to FeO and Iron. *Phys. Rev. Lett.* **80**, 2157 (1998).

45. Singh, A. K. the Lattice Strains in a Specimen (Cubic System) Compressed Nonhydrostatically in an Opposed Anvil Device. *J. Appl. Phys.* **73**, 4278-4285 (1993).

46. Singh, A. K., Balasingh, C., Mao, H.-K., Hemley, R. J. & Shu, J. Analysis of Lattice Strains Measured under Nonhydrostatic Pressure. *J. Appl. Phys.* **83**, 7567-7575 (1998).

47. Ruoff, A. L. Stress Anisotropy in Opposed Anvil High-Pressure Cells. *J. Appl. Phys.* **46**, 1389-1391 (1975).

48. Voigt, W. *Lehrbuch der Kristallphysik*; Teubner Verlag: Wiesbaden, Germany (1966).

49. Reuss, A. Calculation of the Centrifugal Limit of Mixed Crystals due to the Plasticity Condition for Single Crystals. *Z. Angew. Math. Mech.* **9**, 49– 58 (1929).

50. Hearmon, R. F. S. the Elastic Constants of Anisotropic Materials. *Adv. Phys.* **5**, 323-382 (1956).

51. Amulele, G. M., Manghnani, M. H. & Somayazulu, M. Application of Radial X-Ray Diffraction to Determine the Hydrostatic Equation of State and Strength of up to 60 GPa. *J. Appl. Phys.* **99**, 023522 (2006).

52. He, D.W., Shieh, S. R. & Duffy, T. S. Strength and Equation of State of Boron Suboxide from Radial X-Ray Diffraction in a Diamond Cell under Nonhydrostatic Compression. *Phys. Rev. B* **70**, 184121 (2004).

53. Birch, F. Finite Strain Isotherm and Velocities for Single-crystal and Polycrystalline NaCl at High Pressures and 300 K. *J. Geophys. Res.* **83**, 1257-1268 (1978).

54. Akopov, G. *et al*. Superhard Mixed Transition Metal Dodecaborides. *Chem. Mater.* **28**, 6605 (2016).

55. Fei, Y. *et al*. Toward an Internally Consistent Pressure Scale. *Proc. Nat. Acad. Sci.* USA **104**, 9182-9186 (2007).

56. Dubrovinsky, L., Dubrovinskaia, N., Prakapenka, V. B. & Abakumov, A. M. Implementation of Micro-Ball Nanodiamond Anvils for High-Pressure Studies above 6 Mbar. *Nat. Commun.* **3**, 1163 (2012).

57. Anzellini, S., Dewaele, A., Occelli, F., Loubeyre, P. & Mezourar, M. Equation of State of Rhenium and Application for Ultra High Pressure Calibration. *J. Appl. Phys.* **115**, 043511(2014).

58. Manghnani, M. H., Katahara, K. & Fisher, E. S. Ultrasonic Equation of State of Rhenium. *Phys. Rev. B* **9**, 1421 (1974).

59. Liu, L. G., Takahashi, T. & Bassett, W. A. Effect of Pressure and Temperature on the Lattice Parameters of Rhenium. *J. Phys. Chem. Solids* **31**, 1345-1351 (1970).

60. Egami, T. & Waseda, Y. Atomic Size Effect on the Formability of Metallic Glasses. *J. Non-Cryst. Solids* **64**, 113-134 (1984).

61. Weidner, D. J., Wang, Y. & Vaughan, M. T. Strength of Diamond. *Science* **266**, 419-422 (1994).

62. Meade, C. & Jeanloz, R. Static Compression of $Ca(OH)_2$ at Room Temperature: Observations of Amorphization and Equation of State Measurements to 10.7 GPa. *Geophys. Res. Lett.* **17**, 1157-1160 (1990).

63. Koehler, M. R., Keppens, V., Sales, B. C.. Jin, R. Y. & Mandrus, D. Elastic Moduli of Superhard Rhenium Diboride. *J. Phys. D* **42**, 095414 (2009).

64. Suzukia, Y. *et al.* Rhenium Diboride's Monocrystal Elastic Constants, 308 to 5 K. *J. Acoust. Soc. Am.* **127**, 2797 (2010).

65. Wang, Y. X. Elastic and Electronic Properties of TcB_2 and Superhard ReB_2: First-Principles Calculations. *Appl. Phys. Lett.* **91**, 101904 (2007).

66. Hao, X. F. *et al*. Low-Compressibility and Hard Materials ReB_2 and WB_2: Prediction from First-Principles Study. *Phys. Rev. B* **74**, 224112 (2006).

67. Chung, H.-Y., Weinberger, M. B., Yang, J. M., Tolbert, S. H. & Kaner, R. B. Correlation between Hardness and Elastic Moduli of the Ultraincompressible Transition Metal Diborides RuB_2, OsB_2, and ReB_2. *Appl. Phys. Lett.* **92**, 261904 (2008).

68. Palosz, B. *et al*. High Pressure X-Ray Diffraction Studies on Nanocrystalline Materials. *J. Phys.: Condens. Matter* **16**, 353-377 (2004).

69. Sung, C.-M. & Sung, M. Carbon Nitride and Other Speculative Superhard Materials. *Mater. Chem. Phys.* **43**, 1-18 (1996).

70. Yeung, M. T., Mohammadi, R. & Kaner, R. B. Ultraincompressible, Superhard Materials. *Annu. Rev. Mater. Res.* **46**, 465-485 (2016).

71. Xie, M. *et al.* Lattice Stress States of Superhard Tungsten Tetraboride from Radial X-Ray Diffraction under Nonhydrostatic Compression. *Phys. Rev. B* **90**, 104104 (2014).

72. Duffy, T. S. *et al.* Elasticity, Shear Strength and Equation of State of Molybdenum and Gold from X-Ray Diffraction under Nonhydrostatic Compression to 24 GPa. *J. Appl. Phys.* **86**, 6729 (1999).

73. Zhong, M.-M. *et al*. Phase Stability, Physical Properties, and Hardness of Transition-Metal Diborides MB_2 (M = Tc, W, Re, and Os): First-Principles Investigations. *J. Phys. Chem. C* **2**, 10643-10652 (2013).

74. Levine, J. B. *et al.* Full Elastic Tensor of a Crystal of the Superhard Compound ReB_2. *Acta Mater.* **58**, 1530-1535 (2010).

75. Chen, B. *et al.* Detecting Grain Rotation at the Nanoscale. *Proc. Nat. Acad. Sci.* USA **111**, 3350-3353 (2014).

76. Pellicer-Porres, J., Segura, A., Munoz, A., Polian, A. & Congeduti, A. Bond Length Compressibility in Hard ReB_2 Investigated by X-Ray Absorption under High Pressure. *J. Phys.: Condens. Matter* **22**, 045701 (2010).

77. Schiotz, J., Di Tolla, F. D. & Jacobsen, K. W. Softening of Nanocrystalline Metals at Very Small Grain Sizes. *Nature* **391**, 561-563 (1998).

78. Zhou, X. *et al.* Reversal in the Size Dependence of Grain Rotation. *Phys. Rev. Lett.* **118**, 096101 (2017).

Chapter 7

High-Pressure Studies of Size Dependent Yield Strength in Rhenium Diboride Nanocrystals

7.1 Introduction

Ultra-incompressible and superhard materials are good candidates for applications in cutting tools, grinding, polishing, and wear resistant coatings. The demand for superhard materials has steadily increased in the past decade as the prevalence of space-age metals and ceramics become mainstream in the marketplace. The traditional method for making synthetic superhard materials, such as diamond and cubic boron nitride, entails both high temperature and high pressure.[1,2] Additionally, diamond cannot be effectively used to cut ferrous metals due to its limited thermal stability in air and tendency to form iron carbide byproducts.[3] A decade ago, we found that transition metal borides, which can be synthesized under ambient pressure, are potential alternatives due to the low costs and appreciable mechanical properties.[4,5,6] The first example of a superhard metal boride was rhenium diboride (ReB_2, $P6_3/mmc$), which has a Vicker's hardness greater than 40 GPa under an applied load of 0.49 N and a bulk modules above 300 GPa, thereby classifying ReB_2 into both the superhard and ultra-incompressible categories.[7,8]

While the hardness of pure metal borides is quite high, a variety of methods can be used to further increase hardness. For example, A broad range of studies have shown that hardness can be enhanced via solid solution effects, where the addition of metal(s) of different atomic size(s) or number of valence electrons is added into the host lattice.[9,10,11,12,13] This addition serves to impede the slip within the lattice, which is known as dislocation pinning. For example, our group has demonstrated that the hardness of ReB_2 can be increased to ~48 GPa by substitutionally doping tungsten into ReB_2 to form a $Re_{1-x}W_xB_2$ solid solution.[14] On the other end of the spectrum, extrinsic

effects such as the finite size or multiphase effects, can also produce higher hardness.[15,16,17,18,19] Studies suggest that as the grain size is reduced, the likelihood of dislocations running into grain boundaries increases, leading to stronger barriers to dislocation movement. Works in other nanoscale metal systems have shown enhanced hardness through suppressing stress-induced dislocation.[20,21] This hardening phenomenon can be explained by Hall-Petch effect that the maximum strength in materials can be achieved by reducing grain size. As the grain size decreases, the nucleation of dislocations becomes more energetically unfavorable, leading to material hardening. Indeed, previous work from our group has shown that nanosized ReB_2 materials can be synthesized, and that such materials display evidence of the Hall-Petch effect.[22] Despite large enhancements observed in hardness, the deformation mechanism is not fully understood, particularly the size-dependent yield strength in the nanosized superhard materials, which are much more resistant to slip that soft materials like metals.[16]

In order to investigate the hardness of the nanomaterials, radial diffraction is used instead of conventional indentation tests, because indentation, whether nano- or micro-indentation can only be performed on compact solid samples.[2] Alternatively, in-situ high-pressure X-ray diffraction, directly measuring the change of bonding of the nanomaterials upon compression, gives yield strength, which is the maximum stress the material can sustain before bond breaking.[23,24] It is directly related to the hardness and can be used to compare the intrinsic hardness of nano-ReB_2 of different grain sizes. In the current study, we specifically compare the 20 nm, 50 nm, and 60 nm ReB_2 to examine size effects.

The goal here is to tune the grain size of superhard materials and investigate the plastic and elastic properties in response to external pressure, with a goal of better understanding the fundamental physics contributing to hardness. A major challenge is that mechanical grinding

below the micrometer scale is extremely difficult for superhard materials—often due to oxidation or contamination by the grinding media. To address this challenge, our group previously developed a bottom-up synthesis of nano-ReB_2 at ambient pressure based on a high temperature salt flux reaction.[22] Here, we report a synthetic approach to tune the nano-crystallite size of ReB_2 by precise control of the soak time and temperature. We then used synchrotron-based angle dispersive X-ray diffraction in a radial geometry, in a diamond anvil cell (DAC) to determine the bulk modulus and to examine the yield strength of the superhard material up to ~50 GPa.[25] Additionally, the texture (sensitive to the active slip systems as well as stress), elucidates the microscopic deformation mechanisms controlling the plastic behavior of the material.[26,27]

In this work, we present a study of the compressibility, yield strength, and texture evolution in ReB2 nanocrystals to examine size dependent hardness. In the future, spark plasma sintering (SPS) will be conducted to produce a densified bulk pellet comprised of nanocrystals, thereby allowing nano- and/or micro-indentation, providing comparison of the hardnesses with other superhard materials. Rapid sintering in SPS generally avoids excess coarsening, and should allow nano-ReB_2 to retain the mechanical properties of the isolated nanocrystals, potentially making them suitable for machining future applications.

7.2 Experimental Procedure

Synthesis of n-ReB$_2$

Elemental rhenium (99.99%, CERAC Inc., USA) and amorphous boron (99+%, Strem Chemicals, USA) powders were uniformly mixed in the molar ratio Re:B = 1:5 using an agate mortar and pestle for 60 nm and 20 nm ReB_2. Note that the reaction needs an excess of boron to avoid forming lower borides. We then added 100× and 20× excess NaCl (99.5%, Sigma-Aldrich, USA) by weight to the mixture for the syntheses of 60 nm and 20 nm ReB_2, respectively. In the

previously published paper, 50 nm ReB$_2$ was prepared by mixing elemental rhenium and amorphous boron with 1:4 ratio, followed by adding 100× NaCl by weight to the mixture.[22] The mixture was then pressed into 13mm diameter pellets under a 10-ton load using a hydraulic jack press (Carver, USA), followed by heat treatment in a tube furnace under flowing argon. The heating profile for 60 nm ReB$_2$ was set as follows: ramp from 20 °C to 1100 °C over 2 h, dwell at temperature for 2 h, and then cool to room temperature over 5 h. The heating profile for 20 nm ReB$_2$ was set as follows: ramp up to 850 °C over 50 min, dwell for 45 min at temperature, and subsequently cool to room temperature over 5 h. The heating profile for 50 nm ReB$_2$ was ramping up to 850 °C over 1.5 h, dwelling for another 1.5 h, and then cool down to room temperature over 5 h. Each sample was washed in water and centrifuged several times in order to remove the NaCl. The resulting powders were characterized by powder X-ray diffraction (PXRD).

Radial X-ray diffraction

The in-situ angle-dispersive X-ray diffraction experiments under non-hydrostatic pressure were carried out at synchrotron beamline 12.2.2 of the Advanced Light Source (ALS, Lawrence Berkeley National Lab). Each sample was loaded individually into a chamber (~60 μm in diameter and ~60 μm in thickness) in a boron gasket (~400 μm in diameter and ~60 μm in thickness), made of amorphous boron and epoxy and subsequently embedded in rectangular polyimide tape.[28] A small piece of platinum foil (~15 μm in diameter and ~10 μm in thickness, used for 20 nm and 60 nm) or rhenium foil (give specs, 50 nm) was placed on top of the sample to serve as an internal pressure standard. No pressure-transmitting medium was added to ensure the presence of non-hydrostatic stress upon compression. In this experiment, the incident monochromatic X-ray beam (25 keV in energy, 20 × 20 μm in beam size) was perpendicular to the loading axis. The diffraction

was recorded using an MAR-345 image plate at each ~4 GPa pressure step. Calibration of the

sample-to-detector distance, beam center, and detector tilt was carried out by using a CeO_2

standard and the program FIT2D.[29]

The ring-like diffraction patterns were "unrolled" and transformed to rectangular coordinates,

which are called "cake patterns". The diffraction data were analyzed by Rietveld refinement as

implemented in the software package, MAUD.[30,31] The cake pattern has azimuthal angle η (with

0° and 180° corresponding to the low-stress directions and 90° and 270° corresponding to the high

stress directions) plotted versus 2θ. The 1-dimensional diffraction patterns as a function of 2θ were

obtained at the magic angle (φ = 54.7°), which corresponds to effectively hydrostatic condition.

The stress in the sample under uniaxial compression is described by Equation (7.1):

$$\sigma = \begin{bmatrix} \sigma_1 & 0 & 0 \\ 0 & \sigma_1 & 0 \\ 0 & 0 & \sigma_3 \end{bmatrix} = \begin{bmatrix} \sigma_p & 0 & 0 \\ 0 & \sigma_p & 0 \\ 0 & 0 & \sigma_p \end{bmatrix} + \begin{bmatrix} -t/3 & 0 & 0 \\ 0 & -t/3 & 0 \\ 0 & 0 & -2t/3 \end{bmatrix} \tag{7.1}$$

where σ_1 is the minimum stress, σ_3 is the maximum stress, σ_P is the hydrostatic stress component,

and t is the differential stress.[23,32] The d-spacing is calculated by:

$$d_m(hkl) = d_p(hkl)[1 + (1 - 3\cos^2\varphi)Q(hkl)] \tag{7.2}$$

where d_m is the measured d-spacing, d_p is the d-spacing under hydrostatic condition, φ is the angle

between the diffraction normal and axial compression direction, and $Q(hkl)$ is the lattice strain

under the uniaxial stress condition. The differential stress, t, is directly related to the differential

strain, $t(hkl)/G(hkl)$, by:

$$t(hkl) = 6G(hkl)Q(hkl) \tag{7.3}$$

where $G(hkl)$ is the shear modulus of the specific lattice plane. Note that the actual shear modulus

lies between the two extremes determined by the iso-strain (Voigt)[33] and iso-stress (Reuss)[34]

conditions. For a hexagonal crystal, the expression of G_{Voigt} and $G_{Reuss}(hkl)$ in terms of elastic compliance can be found in references [35] and [36].

Incompressibility can be determined using the third-order Birch-Murnaghan equation-of-state (EOS)[37] as following:

$$P = \frac{3}{2}K_0 \left(\left(\frac{V_0}{V}\right)^{7/3} - \left(\frac{V_0}{V}\right)^{5/3} \right) \left(1 + \frac{3}{4}(K_0' - 4)\left(\left(\frac{V_0}{V}\right)^{2/3} - 1 \right) \right) \quad (7.4)$$

where P is the pressure, K_0 is the bulk modulus at ambient pressure, V is the volume, V_0 is the undeformed unit cell volume, and K_0' is the derivative of K_0 with respect to P. Equation (7.4) can be simplified to second-order by fixing $K_0' = 4$. The Birch-Murnaghan equation-of-state can also be rewritten in terms of normalized pressure (F) and Eulerian strain (f),[38] as shown in the following:

$$F = \frac{P}{3f(1+2f)^{5/2}} \quad (7.5)$$

$$f = \frac{1}{2}\left(\left(\frac{V_0}{V}\right)^{2/3} - 1 \right) \quad (7.6)$$

Equations (7.5) and (7.6) can be combined to give a linear regression, where the zero-intercept yields the bulk modulus at ambient pressure (K_0) and the slope gives the pressure derivatives of the bulk modulus (K_0').

Texture analysis is carried out by the software package MAUD.[31] The inversed pole figures, representing the variations of intensities along different stress directions, reveal the grain texture and signify the primary slip planes. The texture strength is measured in multiples of the mean random distribution (M.R.D.), with random texture at M.R.D. = 1 and stronger texture at higher M.R.D. values.

7.3 Results and discussion

In our previous work, we showed that nano-ReB$_2$ could synthesized by a flux reaction, where the formation of ReB$_2$ from the pure elements could occur at high temperature in a molten salt.[22] Here, we worked to tune the particle size through control of nucleation and growth rates with precisely controlled temperature profiles and variation in the precursor-to-salt ratio. In the synthesis of nano-ReB$_2$, excess boron ensures complete formation of borides with the desired stoichiometry. Previously published, 50 nm particles were prepared with excess NaCl, whose liquid phase serves as diffusion medium as the temperature reaches above its melting point (850 °C).[22] The nucleation of nanoparticles occurs above the melting point of NaCl and the prolonged soaking time ensures the crystal growth. In the current study, larger particles are synthesized with higher temperature and longer soaking time to ensure the full growth of nanoparticles. Smaller particles are synthesized with a higher precursor-to-salt ratio, lower temperature, and shorter soaking time. With a higher precursor-to-salt ratio, nanocrystal nucleation is facilitated, thus initiating the growth of many nanocrystals at once. Faster ramp rates to above the melting temperature of NaCl further facilitates rapid nucleation of nanoparticles. Efficient nucleation is then accompanied by limited growth, which is achieved using short soak times and that lowest temperatures that produce phase pure material to limit grain growth. This combination produces nanocrystals that are significantly smaller than those produced previously.

The peak width was used to determine the average grain sizes of the nanoparticles. In our experiment, the calibration material, CeO$_2$, was used to determine the instrumental broadening. Rietveld analysis for the peak profile from the XRD of the unstressed nano-samples shows crystallite sizes of ~20 nm, ~50 nm and ~60 nm. Overlaying the diffraction patterns of nano-samples, the peak width of the diffraction pattern from the 20 nm particles is much wider, and the

50 nm particles have very similar peak width to 60 nm particles. This is consistent with the particle size estimation from Rietveld refinement (**FIG. 7.1**).

In-situ high-pressure XRD experiments were conducted under non-hydrostatic compression up to 50 GPa for 20 nm, 50 nm, and 60 nm-ReB_2. The "cake" patterns recorded at the lowest and highest pressures and the integrated 1-dimensional diffraction patterns for the 20 and 60 nm materials are shown in **FIG. 7.2**. At low pressure, the diffraction lines are almost straight due to the hydrostatic stress state, while at high pressure, the diffraction lines deviate to higher 2θ values (smaller d-spacings) in the high stress direction ($\varphi = 0°$) and to lower 2θ values (higher d-spacings) in the low stress direction ($\varphi = 90°$).[24] The sinusoidal variation of each diffraction line indicates the lattice-supported strain. The peak broadening in the high-pressure 1-D integrations is thus due to strain inhomogeneity.

Quasi-hydrostatic high-pressure diffraction patterns can also be obtained at the magic angle $\varphi = 54.7°$, and all peaks in these patterns can be indexed to the ReB_2 crystal structure throughout the measured pressure range. This magic angle data can be used to track the change in lattice spacing upon compression (**FIG. 7.3**); as expected, all peaks shift to higher 2θ values with increasing pressures, but the shift is not identical for different sizes of nanocrystals.. The peak positions at $\varphi = 54.7°$ are used to determine the lattice parameters and volume, as summarized in **Table S7.1**. The pressure for each compression step was determined from the equation-of-state of a Pt standard, using its d-spacing at $\varphi = 54.7°$. As shown in **FIG. 7.2**, the diffraction patterns are very smooth, indicating high grain number statistics due to fine particle size. Therefore, Rietveld refinement can be conducted on the high pressure data, where an entire diffraction pattern can be fit to produce a calculated pattern in an iterative fashion. An example of refined data is shown in **FIG. S7.1**.

As previously mentioned, the d-spacings show a continuous, linear decrease without abrupt changes upon compression, suggesting no phase transition occurs and the hexagonal structure is maintained as pressure increases. With the lattice parameter determined from the d-spacings, bulk modulus can be calculated. Note that the bulk modulus (K_0) is sensitive to the choice of pressure derivative (K_0'), so that large variations inbulk modulus can result from slight variations in K_0'.[37] As shown in **FIG. 7.4**, a fit to the third-order equation of state in terms of normalized pressure and Eulerian strain (red line) yields a bulk modulus of 355±8.8 GPa (K_0'=0) and 393±14.4 GPa (K_0'=5.1) for 60 nm- and 20 nm-ReB$_2$, respectively. The second-order equation of state with fixed K_0' = 4 (black line) yields a bulk modulus of 304±8.3 GPa and 406±6.5 GPa for 60 nm- and 20 nm-ReB$_2$, respectively, but the quality of the fit for the second-order equation is clearly inferior, particularly for the 20-nm nanocrystals. As shown in **FIG. 7.5**, the hydrostatic compression curves, fit to the third-order equation-of-state, shows higher incompressibility in 20 nm-ReB$_2$, compared to 50 or 60-nm materials. The unit cell volume of the smaller particle changes less upon compression and the trend in compressibility is monotonic with size. Similar trends were observed in titania nanoparticles, where it was found that bulk modulus increases with decreasing particle size in tens of nanometer-scale.[39] In that system, it was hypothesized that as the particle size decreases, dislocation pileups become more prevalent due to increasing interaction of the dislocations with interfaces, thus shielding intervening regions from the external pressure.

It is true that a high bulk modulus is often observed in hard materials, however, it is not the primary factor in determining materials strength.[9,40,41] Bulk modulus, a measure of elastic deformation, reflects a material's resistance to volume change with respect to pressure. Indeed, a number of mechanically soft materials have high bulk moduli.[42] Yield strength, on the other hand, defined as the resistance to plastic deformation, is directly related to the hardness of the material.[43]

In the current study, the plastic deformation mechanism was studied using the evolution of the differential stress (t) as a function of pressure in a lattice specific manner. This is an ideal way to study hardness, as the plateau value of the differential stress corresponds to the yield strength.

As described in the Experimental section, differential stress (t) can be calculated from differential strain (t/G), given the shear modulus (G). It is important to note that shear modulus (G) is weighted average between the Voigt shear modulus (iso-strain) and the Reuss shear modulus (iso-stress). The differential stress under both conditions was calculated using the elastic stiffness constants.[44,45] In **FIG. 7.6**, differential stress under iso-stress (t_{Reuss}) and iso-strain (t_{Voigt}) conditions are plotted separately for three different sizes of nano-ReB$_2$ (20 nm, 50 nm,[22] 60 nm) and bulk ReB$_2$ in a lattice-specific manner. Note that differential stress increases linearly with pressure and then appears to level off. The linear increase is associated with elastic behavior, and the plateau is interpreted to imply that the lattice plane can no longer sustain additional stress, and presumably indicates the onset of plastic deformation. The plane with the lowest differential stress plateau value supports the least deformation, while planes with higher differential stress plateau values resist more shear and dislocation movement. Bulk ReB$_2$ supports much lower differential stress compared to the nano-samples in all three lattice planes studied, suggesting that an enhanced resistance to shear is likely due to the dislocation-grain boundary interaction in the boundary-rich nano samples. Comparing the differential stress among the nano-ReB$_2$ samples, we found that 20 nm-ReB$_2$ has the highest plateaued value, and the 50 nm-ReB$_2$ has very similar trends in differential stress to the 60 nm-ReB$_2$. This suggests that as the particle size gets significantly smaller, the grain boundary concentration increases, leading to a higher energy barrier for lattice dislocations to propagate through grain boundaries. This phenomenon is known as the Hall-Petch effect, and it states that the strength is inversely proportional to the grain size.[46,47] As the grain size

decreases, the nucleation of dislocations becomes more energetically unfavorable, leading to material hardening.

Interestingly, the size dependent effects are not the same for all lattice planes. The basal plane of the hexagonal closed packed crystal structure, (002), has the lowest plateaued differential stress, implying it is very likely to be the major slip plane. This plane shows the largest size dependent increase in differential stress, a fact that should translate to large changes in measured hardness in a nanocrystal compact. The (101) and (110) planes, which both cut through the boron and metal layers, support higher plateau values of differential stress. The (101) plane shows very similar differential stress data for all three nanocrystal sizes, though the 20-nm samples appears to be slightly higher. For the (110) plane, all three sizes are initially very similar, but above 40 GPa, there is a dramatic change in the (110) differential stress this change corresponds to the point where the (002) plane begins to slip, and thus the increase may be a strain hardening effect.

Further information about slip systems in these nanocrystal samples comes from texture analysis, where a direct map of accessible slip systems is derived from the peak intensity variation with stress directions in the radial diffraction geometry. When shear stress is applied to polycrystals in the DAC, individual grains tend to deform preferentially on slip planes, inducing grain rotation to collapse at the lattice-preferred orientation. Such orientation distributions are represented by inverse pole figures (IPF), as shown in **FIG. 7.7** and in other literature.[22] In the inverse pole figure, the color scheme indicates the probability of finding the poles to the lattice planes in the compression direction, with a random distribution corresponding to mean random distribution (m.r.d.) =1, and stronger preferred orientation at higher m.r.d. values.

In **FIG. 7.7**, the IPFs show the evolution of texture for both 20 nm- and 60 nm-ReB_2 as a function of pressure. The texture (contrast in m.r.d. intensities) gets stronger as the pressure

increases. The trends for the 60 nm ReB$_2$ is very similar to that observed previously for 50 nm ReB$_2$, with are m.r.d. intensity concentrated at the (0001) corner at high pressure. This indicates that the (0001) lattice planes are preferentially orientated perpendicular to the high-stress direction, and thus that (0001)/(001) slips easily. This confirms that (000l) is indeed the slip plane, in good agreement with the differential strain analysis discussed above and the theoretical slip system of (001)[1$\bar{1}$0] for ReB$_2$.[48] Interestingly, 20 nm-ReB$_2$ does not show the same monotonic increase in texture. It exhibits decreasing texture from 35 GPa to 41 GPa, followed by increasing texture to 55 GPa. This finding is in good agreement with the strain hardening observed in **FIG. 7.6**. A plateau in the differential stress indicates slipping of a lattice plane, whereas an increasing differential stress value indicates resistance to the slip. The significant increase in differential stress for the (110) lattice plane of 20 nm-ReB$_2$ from 35 GPa to 41 GPa suggests a greater ability of smaller particles to resist slipping at the basal plane, which results in a weaker texture. At the highest pressure (55 GPa), nanoparticles eventually fail to resist slip, and therefore, stronger texture was observed. As shown in the IPF at 55 GPa, higher m.r.d intensities are again more concentrated at the (0001) corner, as expected for basal plane slip.

Comparing the data for the 20 nm- and 60 nm- ReB$_2$ at the highest pressure (42 GPa) collected for the 60 nm- sample show significant differences. At a similar pressure (41 GPa), 20 nm-ReB$_2$ has weaker texture, especially at the (0001) corner, implying that slip systems are suppressed in the smaller crystallites, which results in higher differential stress. Similar size dependence of texture has been observed in a number of metal nanocrystal systems.[49,50,21] In the nickel nanocrystals, for example, nano-Ni with smaller grain sizes shows weaker texture, indicating that dislocation becomes less active with decreasing grain size.[21] Since ReB$_2$ is much tougher than soft materials like Ni, the dislocation creep on preferred slip systems is less significant, and therefore

the texture is much weaker, with an m.r.d valude of only ~1.3 at the highest pressure in our experiment, but the same trend of size-dependent texture follows. The texture results, together with strain analysis, suggest that grain boundary effects are key to impeding dislocation, thus influencing the plastic deformation mechanism in the nanosized superhard metal borides.

7.4 Conclusions

In this paper, methods to produce nanoscale ReB_2 ranging is size from 20 nm- and 60 nm using a molten salt flux growth method can control of nanocrystal nucleations. In-situ high-pressure radial XRD was performed under nonhydrostatic compression up to ~50 GPa. The equation-of-state for nano-ReB_2 samples were calculated from d-spacings under hydrostatic condition ($\varphi = 54.7°$) and the bulk moduli were obtained. The results indicate that the bulk modulus was significantly increased in the smaller crystallites. Lattice-specific differential strain analysis was performed on 20, 50, and 60 nm-ReB_2 and the results were compared with bulk ReB_2. The yield strength was found to be inversely proportional to grain size, in good agreement with the Hall-Petch effect. The basal planes of the samples supporting the least differential stress confirming that (00l) is the slip plane controlling deformation in all sizes of ReB_2. Texture analysis confirmed the slip system and showed a size dependence to the development of texture in nano-ReB_2; weaker texture was observed in the smaller nanocrystals. This fact, coupled with the strong correlation between yield strength and texture, indicate that grain boundaries in these superhard materials can dramatically reduce dislocation-induced plastic deformation. While this fundamental study was only performed on powders, and not on solid compacts, the result have exciting implications for the potential enhanced hardness of nanostructured ceramics that may eventual be produced from these precursors.
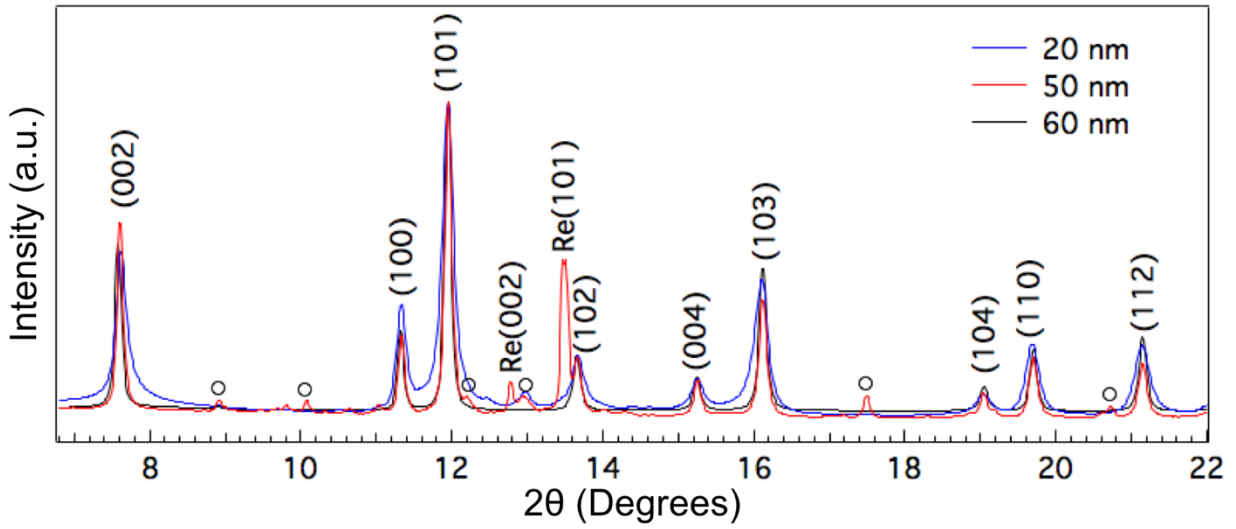
FIG. 7.1: 1-D diffraction patterns for 20 nm-, 50 nm-, and 60 nm-ReB$_2$ at ambient pressure. The impurity in the 50 nm-ReB$_2$ is labeled with open circle.
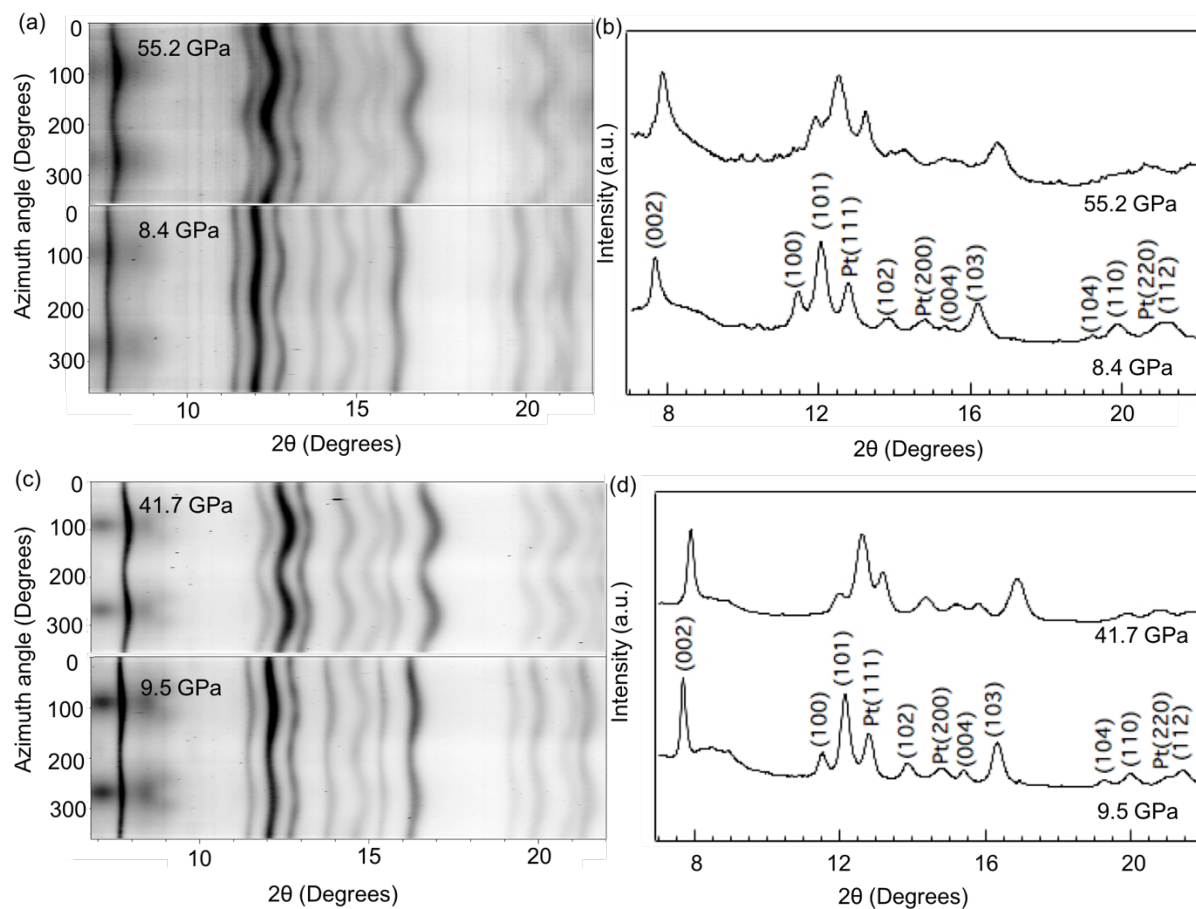
FIG. 7.2: Representative synchrotron cake pattern and 1-D X-ray diffraction patterns integrated at the magic angle ($\varphi = 54.7°$) for (a,b) 20 nm-ReB$_2$ and (c,d) 60 nm-ReB$_2$. The indexing for the relevant peaks is included on the image.
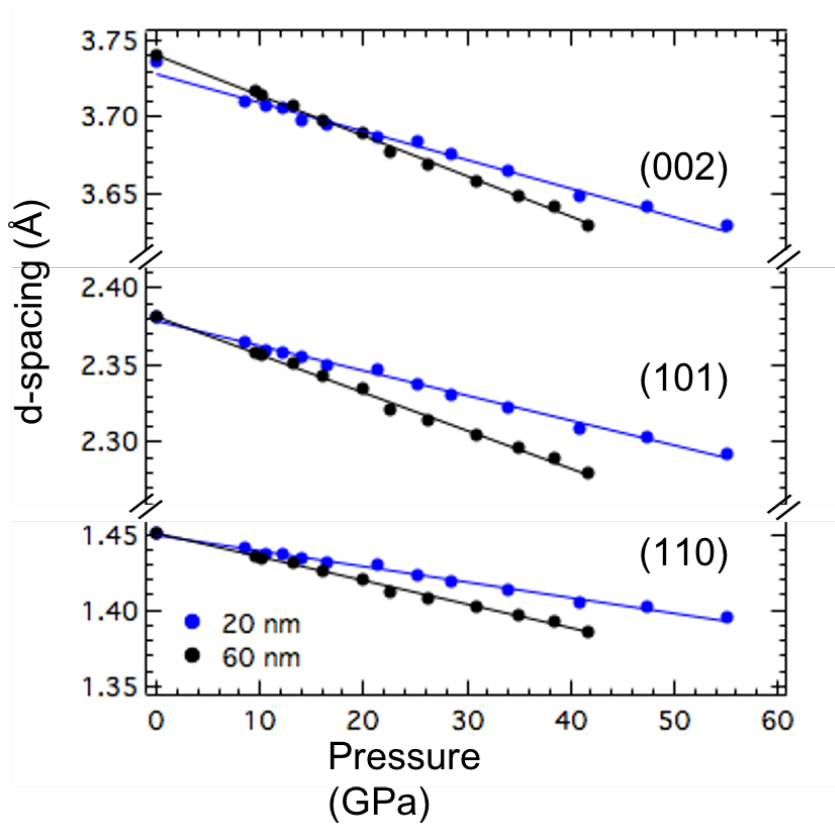
FIG. 7.3: Measured d-spacings for selected lattice planes of 20 nm- and 60 nm-ReB$_2$ as a function of pressure.
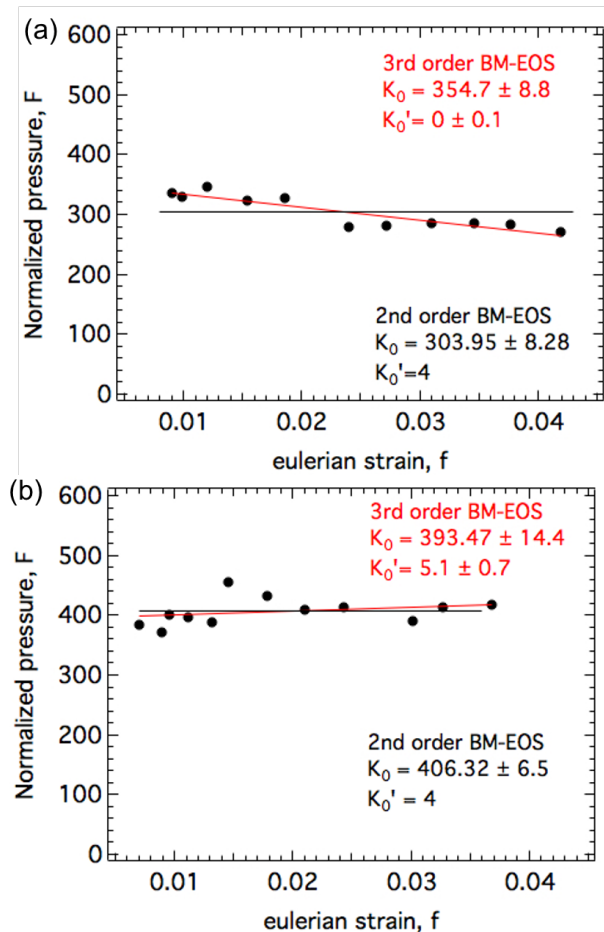
FIG. 7.4: Normalized pressure (F) *vs.* Eularian strain (f) for (a) 60 nm-ReB$_2$ and (b) 20 nm-ReB$_2$.

Data points are fit separately to a second-order (black) and a third-order (red) Birch-Murnaghan

equation-oof-state. The intercept of the solid line yields the ambient pressure bulk modulus (K_0).

The slope of the line yields the pressure derivative (K_0').
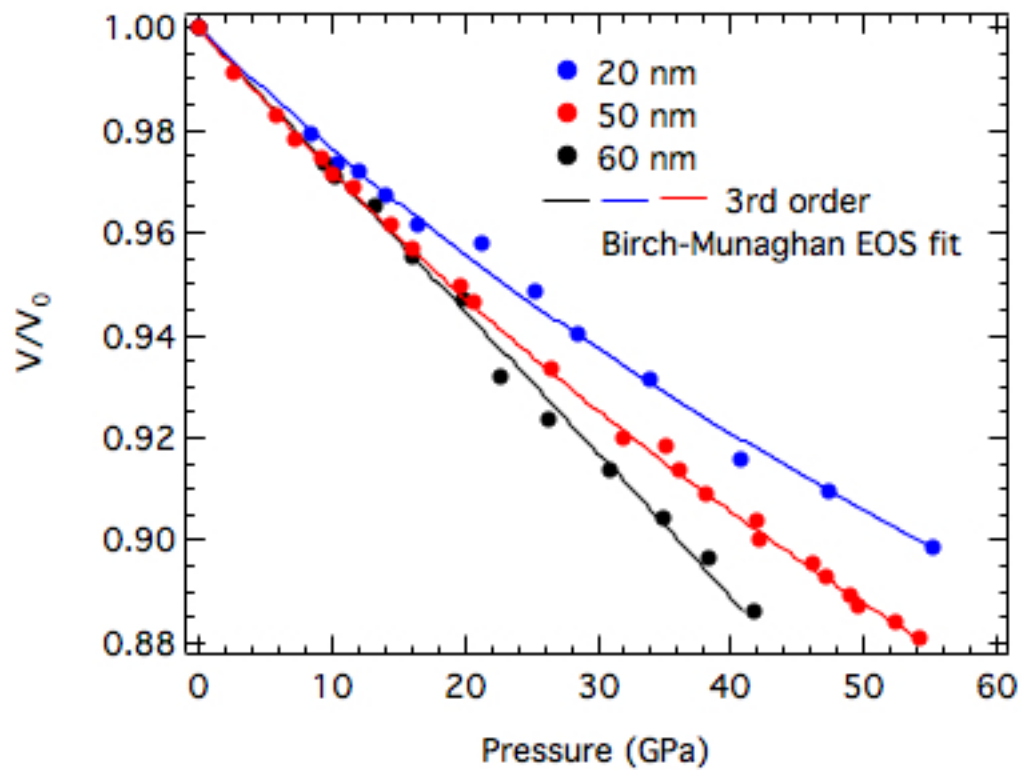
FIG. 7.5: Hydrostatic compression curves of 20 nm-, 50 nm- and 60 nm-ReB$_2$ obtained at the magic angle ($\varphi = 54.7°$). The solid line is fit to the third-order Birch-Murnaghan equation-of-state.
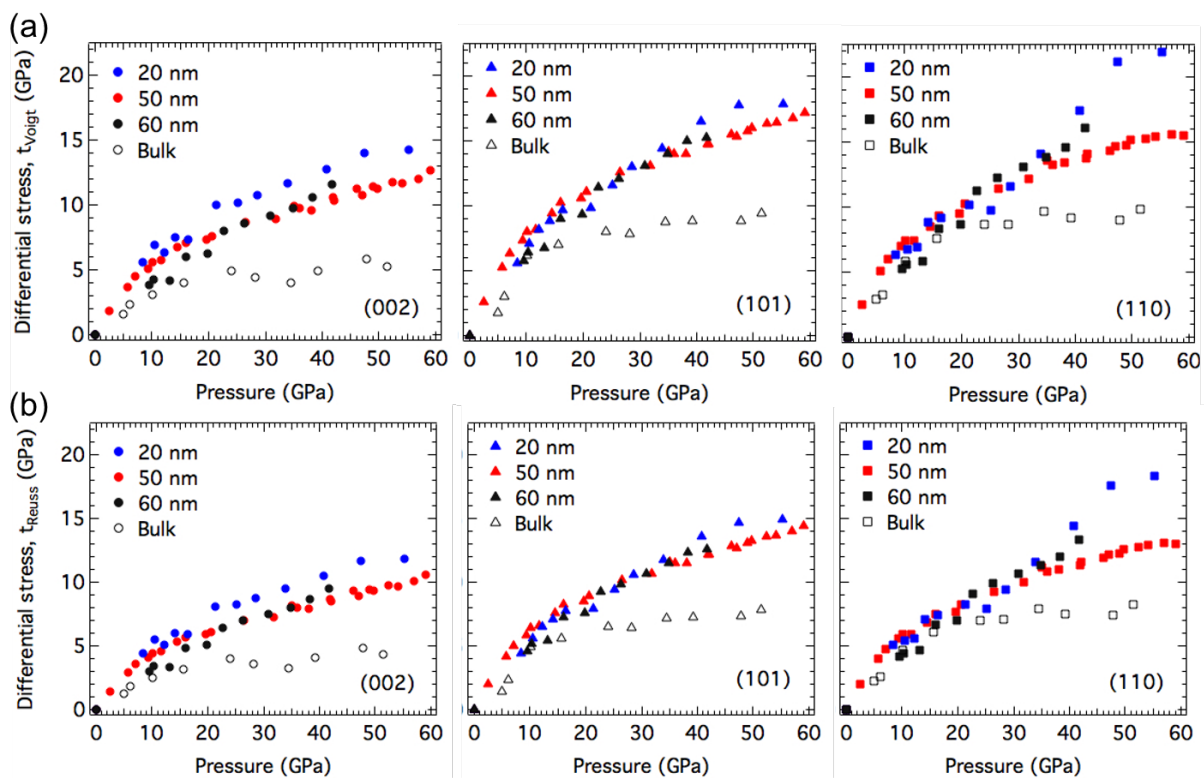
FIG. 7.6. Comparison of the differential stress (t) under (a) iso-strain (t_{Voigt}) and (b) iso-stress (t_{Reuss}) conditions as a function of pressure for 20 nm-, 50nm-, 60nm- and bulk-ReB_2 in the (002), (101) and (110) lattice planes. [Ref 22]
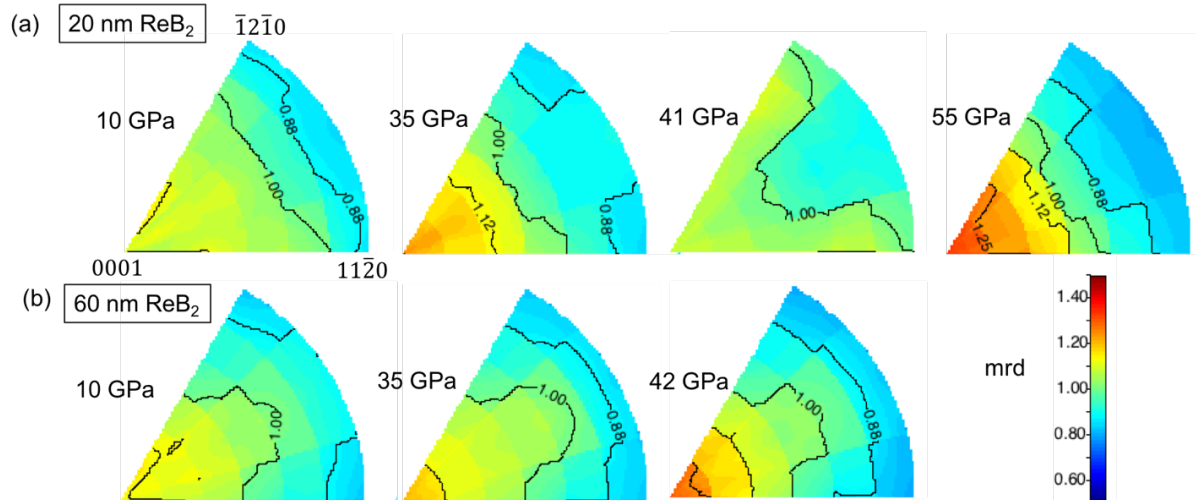
FIG. 7.7. Inverse pole figures for (a) 20 nm- and (b) 60 nm-ReB$_2$ as a function of pressure. For both samples, (00l) direction is found to be the primary slip system.

7.5 Supporting information

Table S7.1. Lattice parameters for 20 nm- and 60 nm-ReB$_2$

20 nm		
P (GPa)	a (Å)	c (Å)
55.2(11)	2.7924(9)	7.255(4)
47.4(18)	2.8039(8)	7.281(3)
40.8(10)	2.8113(8)	7.295(3)
34.9(15)	2.8283(7)	7.328(3)
28.5(3)	2.8371(7)	7.351(3)
25.2(10)	2.8470(7)	7.367(3)
21.3(11)	2.8594(10)	7.374(4)
16.5(5)	2.8618(9)	7.390(4)
14.0(5)	2.8694(8)	7.396(4)
12.1(3)	2.8729(8)	7.411(3)
10.5(5)	2.8748(7)	7.415(3)
8.4(4)	2.8819(10)	7.420(4)
0	2.9020(3)	7.473(1)

60 nm

P (GPa)	a (Å)	c (Å)
41.7(6)	2.7726(8)	7.257(3)
38.4(6)	2.7844(8)	7.281(3)
34.9(6)	2.7938(8)	7.297(3)
30.8(6)	2.8041(8)	7.316(3)
26.2(6)	2.8154(8)	7.336(3)
22.6(8)	2.8250(12)	7.352(5)
19.9(6)	2.8421(8)	7.380(3)
16.1(6)	2.8518(8)	7.397(3)
13.2(7)	2.8627(11)	7.414(4)
10.2(5)	2.8689(7)	7.427(3)
9.5(5)	2.8717(6)	7.433(2)
0	2.9011(1)	7.480(0)
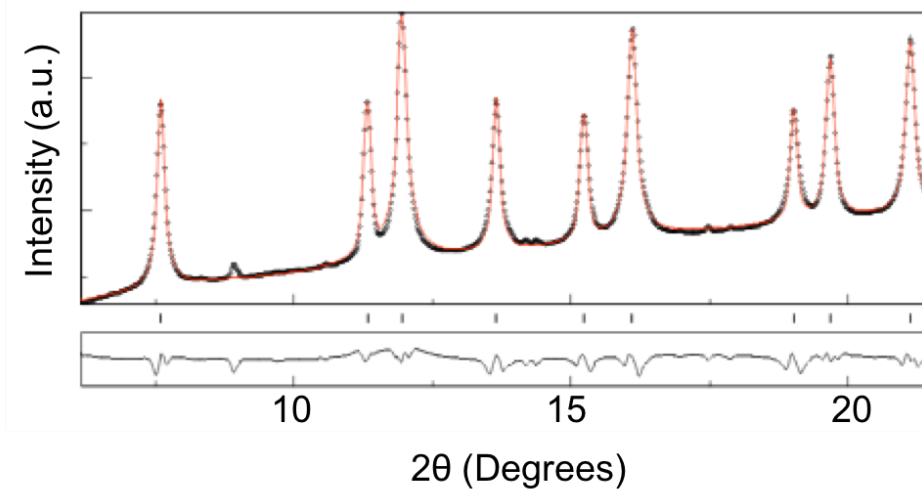
FIG. S7.1: Rietveld refinement of 60 nm-ReB$_2$ crystallites at ambient pressure. The experimental

spectrum is shown with a black dashed line and the calculated fit is shown with a solid line in red.

The residuals are shown in the small box at the bottom.

7.6 References

1. Komanduri, R. & Shaw, M. C. Wear of synthetic diamond when grinding ferrous metals. *Nature* **255**, 211–213 (1975).

2. Taniguchi, T., Akaishi, M. & Yamaoka, S. Mechanical Properties of Polycrystalline Translucent Cubic Boron Nitride as Characterized by the Vickers Indentation Method. *Journal of the American Ceramic Society* **79**, 547–549 (1996).

3. Westraadt, J. E., Sigalas, I. & Neethling, J. H. Characterisation of thermally degraded polycrystalline diamond. *International Journal of Refractory Metals and Hard Materials* **48**, 286–292 (2015).

4. Levine, J. B., Tolbert, S. H. & Kaner, R. B. Advancements in the Search for Superhard Ultra-Incompressible Metal Borides. *Advanced Functional Materials* **19**, 3519–3533 (2009).

5. Chung, H.-Y. *et al.* Synthesis of Ultra-Incompressible Superhard Rhenium Diboride at Ambient Pressure. *Science* **316**, 436–439 (2007).

6. Kaner, R. B., Gilman, J. J. & Tolbert, S. H. Designing Superhard Materials. *Science* **308**, 1268–1269 (2005).

7. Levine, J. B. *et al.* Preparation and Properties of Metallic, Superhard Rhenium Diboride Crystals. *J. Am. Chem. Soc.* **130**, 16953–16958 (2008).

8. Xie, M. *et al.* Exploring the high-pressure behavior of superhard tungsten tetraboride. *Phys. Rev. B* **85**, 064118 (2012).

9. Yeung, M. T., Mohammadi, R. & Kaner, R. B. Ultraincompressible, Superhard Materials. *Annual Review of Materials Research* **46**, 465–485 (2016).

10. Xie, M. *et al.* Exploring hardness enhancement in superhard tungsten tetraboride-based solid solutions using radial X-ray diffraction. *Appl. Phys. Lett.* **107**, 041903 (2015).

11. Pangilinan, L. E. *et al.* Superhard Tungsten Diboride-Based Solid Solutions. *Inorg. Chem.* **57**, 15305–15313 (2018).

12. Akopov, G., Roh, I., Sobell, Z. C., Yeung, M. T. & Kaner, R. B. Investigation of ternary metal dodecaborides (M1M2M3)B12 (M1, M2 and M3 = Zr, Y, Hf and Gd). *Dalton Trans.* **47**, 6683–6691 (2018).

13. Mansouri Tehrani, A. *et al.* Atomic Substitution to Balance Hardness, Ductility, and Sustainability in Molybdenum Tungsten Borocarbide. *Chem. Mater.* **31**, 7696–7703 (2019).

14. Lech, A. T. *et al.* Superhard Rhenium/Tungsten Diboride Solid Solutions. *J. Am. Chem. Soc.* **138**, 14398–14408 (2016).

15. Li, Y., Bushby, A. J. & Dunstan, D. J. The Hall–Petch effect as a manifestation of the general size effect. *Proceedings of the Royal Society A: Mathematical, Physical and Engineering Sciences* **472**, 20150890 (2016).

16. Huang, Q. *et al.* Nanotwinned diamond with unprecedented hardness and stability. *Nature* **510**, 250–253 (2014).

17. Sumiya, H. & Irifune, T. Hardness and deformation microstructures of nano-polycrystalline diamonds synthesized from various carbons under high pressure and high temperature. *Journal of Materials Research* **22**, 2345–2351 (2007).

18. Huang, C., Yang, B., Peng, X. & Chen, S. Plastic Deformation and Hardening Mechanisms of a Nano-twinned Cubic Boron Nitride Ceramic. *ACS Appl. Mater. Interfaces* **12**, 50161–50175 (2020).

19. Zhao, B. *et al.* Enhanced strength of nano-polycrystalline diamond by introducing boron carbide interlayers at the grain boundaries. *Nanoscale Advances* **2**, 691–698 (2020).

20. Chen, Bin. Texture of Nanocrystalline Nickel: Probing the Lower Size Limit of Dislocation Activity. https://www.science.org/doi/10.1126/science.1228211 doi:10.1126/science.1228211.

21. Zhou, X. *et al.* High-pressure strengthening in ultrafine-grained metals. *Nature* **579**, 67–72 (2020).

22. Lei, J. *et al.* Synthesis and High-Pressure Mechanical Properties of Superhard Rhenium/Tungsten Diboride Nanocrystals. *ACS Nano* **13**, 10036–10048 (2019).

23. Ruoff, A. L. Stress anisotropy in opposed anvil high−pressure cells. *Journal of Applied Physics* **46**, 1389–1392 (1975).

24. Singh, A. K. Analysis of nonhydrostatic high-pressure diffraction data (cubic system): Assessment of various assumptions in the theory. *Journal of Applied Physics* **106**, 043514 (2009).

25. Hemley, R. J. *et al.* X-ray Imaging of Stress and Strain of Diamond, Iron, and Tungsten at Megabar Pressures. *Science* **276**, 1242–1245 (1997).

26. Merkel, S., Miyajima, N., Antonangeli, D., Fiquet, G. & Yagi, T. Lattice preferred orientation and stress in polycrystalline hcp-Co plastically deformed under high pressure. *Journal of Applied Physics* **100**, 023510 (2006).

27. Dorfman, S. M., Shieh, S. R. & Duffy, T. S. Strength and texture of Pt compressed to 63 GPa. *J. Appl. Phys.* **117**, 065901 (2015).

28. Merkel, S. & Yagi, T. X-ray transparent gasket for diamond anvil cell high pressure experiments. *Review of Scientific Instruments* **76**, 046109 (2005).

29. Hammersley, A. P., Svensson, S. O., Hanfland, M., Fitch, A. N. & Hausermann, D. Two-dimensional detector software: From real detector to idealised image or two-theta scan. *High Pressure Research* **14**, 235–248 (1996).

30. Rietveld, H. M. A profile refinement method for nuclear and magnetic structures. *J Appl Cryst* **2**, 65–71 (1969).

31. Lutterotti, L., Matthies, S., Wenk, H.-R., Schultz, A. S. & Richardson, J. W. Combined texture and structure analysis of deformed limestone from time-of-flight neutron diffraction spectra. *Journal of Applied Physics* **81**, 594–600 (1997).

32. Singh, A. K. The lattice strains in a specimen (cubic system) compressed nonhydrostatically in an opposed anvil device. *Journal of Applied Physics* **73**, 4278–4286 (1993).

33. Voigt, Woldemar. *Lehrbuch der Kristallphysik (mit Ausschluss der Kristalloptik)*. (1966).

34. Reuss, A. Berechnung der Fließgrenze von Mischkristallen auf Grund der Plastizitätsbedingung für Einkristalle . *ZAMM - Journal of Applied Mathematics and Mechanics / Zeitschrift für Angewandte Mathematik und Mechanik* **9**, 49–58 (1929).

35. Singh, A. K., Balasingh, C., Mao, H., Hemley, R. J. & Shu, J. Analysis of lattice strains measured under nonhydrostatic pressure. *Journal of Applied Physics* **83**, 7567–7575 (1998).

36. Hearmon, R. F. S. The elastic constants of anisotropic materials—II. *Advances in Physics* **5**, 323–382 (1956).

37. Birch, F. Finite strain isotherm and velocities for single-crystal and polycrystalline NaCl at high pressures and 300°K. *Journal of Geophysical Research: Solid Earth* **83**, 1257–1268 (1978).

38. Meade, C. & Jeanloz, R. Static compression of Ca(OH)2 at room temperature: Observations of amorphization and equation of state measurements to 10.7 GPa. *Geophysical Research Letters* **17**, 1157–1160 (1990).

39. Chen, B. *et al.* Size-dependent elasticity of nanocrystalline titania. *Phys. Rev. B* **79**, 125406 (2009).

40. Sung, C.-M. & Sung, M. Carbon nitride and other speculative superhard materials. *Materials Chemistry and Physics* **43**, 1–18 (1996).

41. Kenichi, T. Bulk modulus of osmium: High-pressure powder x-ray diffraction experiments under quasihydrostatic conditions. *Phys. Rev. B* **70**, 012101 (2004).

42. Dubrovinsky, L. *et al.* The most incompressible metal osmium at static pressures above 750 gigapascals. *Nature* **525**, 226–229 (2015).

43. He, D., Shieh, S. R. & Duffy, T. S. Strength and equation of state of boron suboxide from radial x-ray diffraction in a diamond cell under nonhydrostatic compression. *Phys. Rev. B* **70**, 184121 (2004).

44. Zhong, M.-M. *et al.* Phase Stability, Physical Properties, and Hardness of Transition-Metal Diborides MB_2 (M = Tc, W, Re, and Os): First-Principles Investigations. *J. Phys. Chem. C* **117**, 10643–10652 (2013).

45. Levine, J. B. *et al.* Full elastic tensor of a crystal of the superhard compound ReB2. *Acta Materialia* **58**, 1530–1535 (2010).

46. Hall, E. O. The Deformation and Ageing of Mild Steel: III Discussion of Results. *Proceedings of the Physical Society of London Section B* **64**, 747–753 (1951).

47. Petch, N. J. The Cleavage Strength of Polycrystals. *J. Iron Steel Inst.* **174**, 25–28 (1953).

48. Zang, C., Sun, H., Tse, J. S. & Chen, C. Indentation strength of ultraincompressible rhenium boride, carbide, and nitride from first-principles calculations. *Phys. Rev. B* **86**, 014108 (2012).

49. Schiøtz, J., Di Tolla, F. D. & Jacobsen, K. W. Softening of nanocrystalline metals at very small grain sizes. *Nature* **391**, 561–563 (1998).

50. Chen, B. *et al.* Detecting grain rotation at the nanoscale. *Proceedings of the National Academy of Sciences* **111**, 3350–3353 (2014).

Chapter 8

Future work

8.1 Non-equimolar High Entropy Alloys

In this study, a broad range of phases with different boron content (WB_2, ReB_2, WB_4, MB_{12}) have been examined to understand the role of the covalent boron network and of metal boron bonding. We examined the intrinsic hardening of WB_2 solid solutions. High-pressure radial X-ray diffraction reveals that bond strengthening, especially the bonding between the metal-boron interlayer, contributes to enhanced hardness from 29.5 ± 1.7 GPa to 45.7 ± 2.5 GPa at 30% doping ($W_{0.7}Mo_{0.3}B_2$). Another system that we studied is ReB_2. The hardness of ReB_2 increases to 47.4 ± 1.5 GPa with 2 at. % Os doping and 43.0 ± 2.8 GPa with 2 at. % Ru doping. $Re_{0.98}Os_{0.02}B_2$ shows greater resistance to shear (differential strain) than pure ReB_2 in all lattice planes. In $Re_{0.98}Ru_{0.02}B_2$, similar trends to ReB_2 are observed, except for the strengthening in (002) plane. Overall, solid solution effects are significant, as even 2 at. % dopant substitution can change strain anisotropy and enhance the differential strain in the ReB_2 system.

In addition, we conducted high-pressure experiments to probe the difference in dopant-cage interaction by doping WB_4 with boron-like light elements (carbon) and transition metal (zirconium) in order to understand how dopant position influences chemical bonding that contributes to the intrinsic hardness. The carbon-doped WB_4 resists the highest degree of shear force before undergoing plastic deformation among other solid solutions, especially bonding in c axis is significantly strengthened. On the other hand, doping Zr results in a decrease in shear resistance as the pseudo-cage structure is disrupted due to the weakening in c axis from doping Zr. In another cage structure system, a wide range of dodecaboride solid solutions and high-entropy alloy have been studied. High-pressure experiment, combining with structural analysis by Rietveld

refinement, suggests enhanced hardness likely arises from compact atomic packing with metal atoms of complimentary sizes in the rigid boron cage network.

In future studies, we need to consider exploring a broader range of high-entropy dodecaborides, especially non-equimolar high entropy alloys. In previous work, we have synthesized equimolar high entropy dodecaboride ($Y_{0.2}Gd_{0.2}Ho_{0.2}Hf_{0.2}Zr_{0.2}B_{12}$), which shows Vicker's hardness above 40 GPa at 0.49N load. According to our theory, the unit cell expansion or contraction should be closely related to the mix and match of metal atomic sizes in the solid solution formation. In fact, most solid solutions and HEA follow a linear trend in the plot of unit cell volume vs. weighted metal atomic radii. The linear trend indicates continuous unit cell expansion as the overall metal size increases, which confirms the solid solution formation in accordance with Vegard's law. The fact that the hardest dodecaborides have the smallest unit cells than predicted perfect solid solutions suggests that the distortion of boron cage to optimize atomic packing to form a more compact unit cell contributes to higher hardness. We thus propose to explore other non-equimolar HEAs, potentially having more compact unit cell packing, and investigate dislocation-mediated deformation under high pressure.

Currently, we have only studied high entropy dodecaboride containing five elements in even concentrations. In the future, we should take attempts to synthesize HEAs with 6 or more elements, as the increasing number of elements in the alloy allows the entropy of mixing to overcome the enthalpies of the formation and thereby stabilizes the solid solutions. More attention needs to be focused on synthesizing HEAs with high density, low-oxygen impurity and refined microstructure that can be potentially used for machining applications.

8.2 Nanostructured superhard materials

In this study, we have also investigated the extrinsic hardening in nano-ReB$_2$ system. Significant enhancement of yield strength in nanostructured materials is due to the high density of grain boundaries.[1] We have also found that as the grain size is reduced, the likelihood of dislocation running into grain boundaries increases, leading to stronger dislocation barrier and hence higher hardness, which is in good agreement with Hall-Petch effect.[2] More importantly, radial diffraction can provide quantitative information on slip planes within a material through texture analysis. When an anisotropic shear stress is applied to a polycrystalline material, slip along specific lattice plane generates lattice-preferred orientation, which is reflected in varying peak intensity with azimuth angles under pressure. We have found that the texture strength of nanocrystal ReB$_2$ shows a maximum at (0001) at high pressure, signifying that dislocation is primarily governed by the basal slip system. In the inverse pole figure for the 20 nm-ReB$_2$, the preferred orientation is more concentrated at the (0001) corner, suggesting that the increased grain boundary content suppresses the formation of non-basal slips, a fact that explains the observed higher yield strength. By measuring the main slipping planes and the size dependence of texture, we can design the new superhard materials by suppressing slip system or by tuning grain size.

In the future, we propose to nanoengineer other boride systems, such as WB$_2$ and WB$_4$. We have demonstrated the molten salt flux synthesis of ReB$_2$ in Chapter 6 and 7. Similar methods can also be used to synthesize nano-W$_{0.5}$Ta$_{0.5}$B$_2$ by pre-alloying the two metals first and then using the molten salt method. We thus propose to use radial diffraction studies to provide lattice specific measurement of elastically supported strain and to identify slip systems in a range of nanostructured W$_x$Ta$_{1-x}$B$_2$ solid solution, with a goal of understanding how solid-solution formation enhances hardness in a system with a comparatively soft parent phase. While we have not yet achieved a broad range of size control in the W$_x$Ta$_{1-x}$B$_2$ system, the ability to systematically

237

tune composition in a fine-grained material that is amenable to Rietveld analysis should provide insight into the evolution of slip systems with changing solid-solution composition.

Finally, we aim to synthesize nanocrystals of WB_4, which is by far the hardest metal boride phase that we have made. Unfortunately, unlike lower borides, WB_4 is not easy to form, and stoichiometric mixtures of the elements produce a mixture of WB_4, lower borides, and excess boron. Indeed, we must use a 1:12 W:B ratio to drive the formation of bulk WB_4 in bulk solid-state reactions, and this high boron content is not amenable to nanocrystal synthesis. Recently, however, we have found that by mixing W with Ta, the WB_4 phase can be stabilized with a 1:4.5 metal to boron ratio.[3] We propose first to use radial diffraction studies on bulk $W_xTa_{1-x}B_4$ to understand the effect of Ta doping on the evolution of slip systems. Using the $W_xTa_{1-x}B_4$ system, we will then synthesize nanocrystals using salt-flux methods similar to those described above. We will use Rietveld refinement of high-pressure data and directly observe the changing of slip system with pressure, allowing us to compare the evolution of slip systems with increasing pressure in layered versus cage structured metal borides.

8.3 References:

1. Lei, J. *et al.* Synthesis and High-Pressure Mechanical Properties of Superhard Rhenium/Tungsten Diboride Nanocrystals. *ACS Nano* **13**, 10036–10048 (2019).

2. Li, Y., Bushby, A. J. & Dunstan, D. J. The Hall-Petch effect as a manifestation of the general size effect. *Proceedings of the Royal Society A: Mathematical, Physical and Engineering Sciences* **472**, (2016).

3. Akopov, G. *et al.* Effects of Variable Boron Concentration on the Properties of Superhard Tungsten Tetraboride. *J. Am. Chem. Soc.* **139**, 17120–17127 (2017).